MICROCOPY RESOLUTION TEST CHART
NATIONAL BUREAU-OF STANDARDS-1963-A

AD-A159 299

AFWAL-TR-84-4165
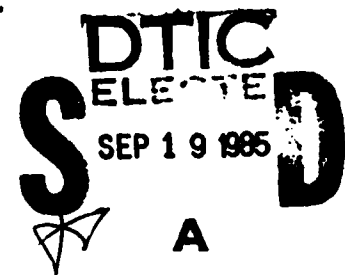
EFFECTS OF CHEMISTRY AND PROCESSSING ON THE FRACTURE RELATED PROPERTIES . OF P/M ALUMINUM ALLOY CT91

W. M. GRIFFITH
Structural Metals Branch

August 1985

DTIC
SELECTE
SEP 1 9 1985
S   D
A

Final Report for Period Sep 80 - May 84

APPROVED FOR PUBLIC RELEASE; DISTRIBUTION UNLIMITED

DTIC FILE COPY

MATERIALS LABORATORY
AIR FORCE WRIGHT AERONAUTICAL LABORATORIES
AIR FORCE SYSTEMS COMMAND
WRIGHT-PATTERSON AIR FORCE BASE, OHIO 45433-6533

85 09 19 011

NOTICE

When Government drawings, specifications, or other data are used for any purpose other than in connection with a definitely related Government procurement operation, the United States Government thereby incurs no responsibility nor any obligation whatsoever; and the fact that the government may have formulated, furnished, or in any way supplied the said drawings, specifications, or other data, is not to be regarded by implication or otherwise as in any manner licensing the holder or any other person or corporation, or conveying any rights or permission to manufacture use, or sell any patented invention that may in any way be related thereto.

This report has been reviewed by the Office of Public Affairs (ASD/PA) and is releasable to the National Technical Information Service (NTIS). At NTIS, it will be available to the general public, including foreign nations.

This technical report has been reviewed and is approved for publication.

WALTER M. GRIFFITH
Structural Metals Branch
Metals & Ceramics Division

GAIL E. EICHELMAN
Chief, Structural Metals Branch
Metals & Ceramics Division

FOR THE COMMANDER

TERENCE M.F. RONALD
Technical Area Manager,
Aluminum Group
Structural Metals Branch
Metals & Ceramics Division

"If your address has changed, if you wish to be removed from our mailing list, or if the addressee is no longer employed by your organization please notify AFWAL/MLLS, W-PAFB, OH 45433 to help us maintain a current mailing list".

Copies of this report should not be returned unless return is required by security considerations, contractual obligations, or notice on a specific document.

SECURITY CLASSIFICATION OF THIS PAGE

AD-A159 299

REPORT DOCUMENTATION PAGE

1a. REPORT SECURITY CLASSIFICATION UNCLASSIFIED	1b. RESTRICTIVE MARKINGS
2a. SECURITY CLASSIFICATION AUTHORITY	3. DISTRIBUTION/AVAILABILITY OF REPORT Approved for public release; distribution unlimited.
2b. DECLASSIFICATION/DOWNGRADING SCHEDULE	
4. PERFORMING ORGANIZATION REPORT NUMBER(S) AFWAL-TR-84-4165	5. MONITORING ORGANIZATION REPORT NUMBER(S)

6a. NAME OF PERFORMING ORGANIZATION AFWAL	6b. OFFICE SYMBOL (If applicable) MLLS	7a. NAME OF MONITORING ORGANIZATION AFWAL/MLLS
6c. ADDRESS (City, State and ZIP Code) AFWAL/MLLS WPAFB, OH 45433		7b. ADDRESS (City, State and ZIP Code) AFWAL/MLLS WPAFB, OH 45433
8a. NAME OF FUNDING/SPONSORING ORGANIZATION	8b. OFFICE SYMBOL (If applicable)	9. PROCUREMENT INSTRUMENT IDENTIFICATION NUMBER
8c. ADDRESS (City, State and ZIP Code)		10. SOURCE OF FUNDING NOS.

11. TITLE (Include Security Classification) See Block 16	PROGRAM ELEMENT NO. 62102F	PROJECT NO. 2418	TASK NO. 241802	WORK UNIT NO. 24180207

12. PERSONAL AUTHOR(S)
W.M. Griffith

13a. TYPE OF REPORT Final	13b. TIME COVERED FROM SEP 80 TO MAY 84	14. DATE OF REPORT (Yr., Mo., Day) August 1985	15. PAGE COUNT 334

16. SUPPLEMENTARY NOTATION
Effects of Chemistry and Processing on the Fracture Related Properties of P/M Alloy CT91.

17	COSATI CODES		18. SUBJECT TERMS (Continue on reverse if necessary and identify by block number)
FIELD	GROUP	SUB. GR.	Aluminum Alloys, Powder Metallurgy, CT91, 7091, Low Cycle Fatigue, Microstructure

19. ABSTRACT (Continue on reverse if necessary and identify by block number)

With the single exception of fatigue crack propagation resistance, the development of high strength powder metallurgy (P/M) aluminum alloys has been very successful. CT91, an example of this class of alloy, has been studied to determine the effect of chemistry (Co content), deformation processing (38% and 64% uniaxial upset forging), and stress relief on engineering and fracture related properties. Stress relief by compression after solution heat treatment was found to have little effect on the properties studied and made no apparent change in the microstructure. A slight reduction in strength and slight improvement in fatigue crack propagation (FCP) resistance was noted in material that had been stress relieved. Co content had the largest effect of all program variables on strength - the 0.4% Co alloy exhibits a 28 MPa (4 ksi) increase in both ultimate and yield strength compared to the 0% Co alloy. No effect of Co content on fracture toughness or FCP resistance was observed. Changing the uniaxial forging deformation from 38% to

20. DISTRIBUTION/AVAILABILITY OF ABSTRACT UNCLASSIFIED/UNLIMITED ☒ SAME AS RPT. ☐ DTIC USERS ☐	21. ABSTRACT SECURITY CLASSIFICATION UNCLASSIFIED
22a. NAME OF RESPONSIBLE INDIVIDUAL W.M. GRIFFITH	22b. TELEPHONE NUMBER (Include Area Code) 513-255-4249	22c. OFFICE SYMBOL AFWAL/MLLS

DD FORM 1473, 83 APR EDITION OF 1 JAN 73 IS OBSOLETE. UNCLASSIFIED

SECURITY CLASSIFICATION OF THIS PAGE

64% produced no measureable effect on strength, toughness, or FCP resistance. There was a marked increase in scatter in the fracture related properties at the lower forging strain. This is attributed to the reduced degree of breakup and distribution of oxides found at the prior powder particle boundaries which provides sites for easy crack propagation. None of the major program variables had a significant effect on the LCF behavior of the alloy. Only single slope Coffin-Manson behavior was observed with β ranging from 1.017 to 1.344. These β's are considerably higher than values reported for similar alloys in different proudct forms. This also is attributed to the inability of the forging process to adequately break up and distribute the oxide associated with the prior particle surfaces. TEM analysis of LCF indicated homogeneous deformation for all cases. In addition, for $\Delta\varepsilon_p <0.3\%$, fine slip band formation was occasionally observed. Results of LCF testing indicate that CT91 forgings do not conform to the LCF-based models of FCP behavior in the range of plastic strains studied.

TABLE OF CONTENTS

Accesion For

NTIS CRA&I

DTIC TAB

Unannounced

Justification

By

Distribution/

Availability Codes

Avail and/or

Dist Special

A-1

DTIC COPY INSPECTED

LIST OF TABLES

LIST OF FIGURES

LIST OF FIGURES (continued)

Today a significant amount of Al is used in aircraft structures. In fact, high strength aluminum alloys such as 7075 and 2024 are often termed "workhorse" materials because they can make up 90% of the structural weight of aircraft. This position is being eroded by the introduction of graphite-epoxy composites into aircraft. This is seen clearly in Figure 1 where material usage for current new aircraft design is compared to future design. Note that a high percentage of structural weight may be either Al or composites, depending solely on the outcome of material development programs currently underway. The failure of high strength Al P/M alloys to demonstrate improved FCP resistance will almost surely result in increased composites usage [14].

What is responsible for the unacceptable FCP behavior of the P/M Al alloys? There is considerable speculation dating back to the original realization that FCP resistance was not improved. What is certain is that our understanding of the fracture and crack growth characteristics of this new class of Al alloys is not complete. In fact, several ongoing basic research programs [15-18] and uncounted Independent Research and Development (IRAD) programs continue to investigate the issue.

The research described in this dissertation addressed the effect of chemistry and processing variations on the microstructure and properties of CT91 forgings. It is hoped that the results and discussion that follow will add significantly to our understanding of the phenomena of crack initiation, crack growth, and fracture in P/M Al alloys in general, and in forgings specifically.

3

eventually terminated because of its inability to produce acceptable products from less than fully dense forging preforms. This was the first realization that the P/M aluminum alloys were "different" in the sense that extra deformation is required to break up and distribute the surface oxides that form when the powders are exposed to oxygen.

Another disappointment of the P/M alloys - and perhaps the most significant - was their fatigue crack propagation (FCP) resistance, which was no better than that of other high strength Al alloys, and in many cases worse! Although thought initially [4] to possess superior FCP resistance, these improvements were shown to be due solely to residual quenching stresses [5]. The realization that FCP was not improved led many designers to suggest that the full potential of 7090 and 7091 could not be achieved - that is, the additional strength, toughness, and corrosion resistance could not be used because the equally important design property of FCP resistance limited the applications where P/M Al could be considered. The full impact of this was realized at the first Aerospace/Aluminum Strategy Assessment Workshop held in Dayton, Ohio in July 1981 [12]. Aerospace contractors almost unanimously agreed that without additional improvements in FCP resistance, 7090 and 7091 would not find widespread application. In spite of this, enough interest remained for 10 aerospace companies to participate in the Round Robin Assessment [13] that resulted from that original meeting. More than two years later and after estimated total expenditures of $1M the results indicate that the FCP characteristics of the P/M Al alloys, as expected, will limit their use. The 2nd AF Industry Strategy Assessment Meeting [14] held in September 1983 provided a few interesting details of the Round Robin testing. Among these is the finding that although the P/M Al alloys have average FCP resistance in constant amplitude testing, they excel when more realistic spectrum fatigue loading is used. In addition, at this meeting Alcoa announced the introduction of a "2nd Generation" of high strength Al P/M alloys purported to have even higher strengths and perhaps improved FCP resistance.

2

1.0 Introduction

Beginning in the late 1960's Alcoa, under sponsorship by the Army's Frankford Arsenal [1, 2] began developing a series of 7000-series Al alloys using a powder metallurgy process. The Army was particularly interested in developing an armor material that was strong and tough but also lightweight. Subsequently, after examining more than 30 compositions, the alloys MA67 and MA87 were chosen as the best alloys - the former being the stronger alloy, the latter being the tougher. Since this re-introduction of Al P/M by the Army, this technology has piqued the interest of the aerospace industry. It is termed a "re-introduction" because a decade earlier Roberts [3], under WADC sponsorship, reported similar alloy development experiments. Under more recent Air Force sponsorship [4-11] the two Alcoa alloys were redesignated CT90 and CT91 respectively as they proceeded from an experimental to a semi-commercial status. In 1980 Alcoa petitioned the Aluminum Association for commercial designations and the alloys were assigned X7090 and X7091. When the alloys were finally accepted in 1982 the X's were dropped.

. The P/M approach was originally pursued for several reasons, as indicated in Section 2.1 that follows. Primarily, it was thought that the fine, homogeneous structures resulting from the P/M process would have a beneficial effect on properties. This proved to be the case; for example, compared to the best 7000-series ingot alloys 7091 is about 10% stronger with superior toughness, corrosion resistance and fatigue crack initiation resistance. In spite of all the success these alloys have enjoyed there were several significant failures that have lessened the enthusiasm of initially optimistic observers. Because a 2-3X cost premium is incurred by using P/M it is important to reduce the "buy to fly" ratio - that is, to optimize scrap losses to a minimum. To accomplish this a program to develop precision forging methods was undertaken [7]. The program was less than successful and was

1

LIST OF SYMBOLS continued

RA	Reduction in Area
r_p	Monotonic plastic zone size
r_p'	Cyclic plastic zone size
ρ	Parameter related to process zone size
S	Distance
σ_a	Stress amplitude
σ_i	Stress opposing dislocation motion
σ_{yc}'	Cyclic compressive yield stress
σ_{ys}	Tensile yield stress
$\Delta\sigma$	Stress range
T	Dislocation line tension
$\Delta\tau_o$	Increase in shear strength due to particles
U	Hysteretic energy per unit area of crack
ΔW	Calculated value of plastic work per cycle

$\bar{g}$	Reflecting vector
K	Stress intensity factor
K_C	Critical stress intensity factor
K_{IC}	Plane strain fracture toughness
K_{max}	Maximum stress intensity
K_{op}	Stress intensity required to open a crack
ΔK	Stress intensity range
ΔK_{app}	Apparent stress intensity range
ΔK_{eff}	Effective stress intensity range
ΔK_o	Threshold stress intensity range
ℓ	Process zone size parameter
$\delta L/L$	Engineering strain
M	Schmid Factor
m	Paris Law exponent
N_f	Cycles to failure
N_i	Cycles to initiation
n	Strain hardening exponent
n'	Cyclic strain hardening exponent
ν	Poisson's ratio
ΔP	Load drop
R	Stress ratio
R_ϵ	Strain ratio

LIST OF SYMBOLS

A	Paris Law constant
ΔA	Area reduction
A_{ϵ}	Strain ratio
a	Crack length
α	Modified Coffin-Manson equation exponent
$\textbf{B}$	Burger's vector
β	Coffin-Manson exponent
C_t	Triaxiality factor
D	Particle or grain diameter
da/dN	Crack growth rate
E	Young's modulus
el	Elongation
ϵ	Strain
ϵ_a	Strain amplitude
ϵ_f'	Fatigue ductility coefficient
$\dot{\epsilon}_t$	Strain rate
$\Delta\epsilon_e$	Elastic strain range
$\Delta\epsilon_p$	Plastic strain range
$\Delta\epsilon_t$	Total strain range
η	Incoherent $MgZn_2$
η'	Partially coherent $MgZn_2$
f_c	Volume fraction of constituents
G	Shear modulus

FIGURE   PAGE

LIST OF FIGURES (continued)

FIGURE   PAGE

2.0 Literature Survey

2.1 Powder Metallurgy (P/M) Aluminum Alloy Processing

There are several comprehensive reviews of this subject currently available [19-25] to which the reader is directed for a detailed discussion. Interest in P/M aluminum increased dramatically in the early 1970's because improvements in ingot metallurgy (I/M) alloys through compositional and processing improvements had plateaued by that time [19]. Through P/M processing the shortcomings of I/M could be overcome and the unique advantages of P/M exploited.

2.1.1 Advantages of Rapidly Solidified P/M Alloys

The advantages commonly attributed to rapidly solidified P/M Al Alloys include:

- extension of solubility limits
- improvements in chemical homogenity
- refinement of second phase particles
- decrease in grain size.

The plateau in properties of I/M aluminum was due in part to the limited number of alloying elements that have significant solubility in aluminum. In I/M, where equilibrium conditions are approached because of the slow cooling rates associated with cooling large masses from the liquid state, only eight elements exhibit solubility limits in excess of 1 atomic percent. These elements are Zn, Mg, Ga, Si and Ge which surround Al on the periodic chart and Li, Cu, and Ag. In the P/M approach, because of the rapid solidification from the liquid state, substantially greater solubility can be obtained for at least 20 additional elements. This fact is quantified in Table 1 for seven elements [26]. The advent of P/M has provided the possibility of

4

exploiting new alloy systems. Alloy systems currently under United States Air Force consideration [27] include Al-Fe-Ce and Al-Fe-Mo, which have been demonstrated to possess significant percentages of room temperature strength past 500°F. The Air Force Wright Aeronautical Laboratories Materials Laboratory is currently applying the concept of rapid solidifiication to examine the additions of other refractory and rare-earth metals to aluminum [28].

The great advantage of Al P/M lies in providing chemical homogeneity and unique alloy compositions as demonstrated in Figure 2 for the CU78 (Al-Fe-Ce) alloy. The microstructures on top are from a button melt on a water cooled copper plate and shows a second phase which is coarse and cannot be redistributed by heat treatment. In the powder product in Figures 2c and 2d a very fine dispersion of second phase is present along with areas that are probably supersaturated solid solution [29].

The grain refinement possible using P/M rather than I/M is illustrated in Figure 3 for two die forgings made from 7000 series alloys [64]. This is important for improvement of properties such as strength, fatigue initiation, and corrosion resistance. The low stress corrosion resistance of an I/M die forging due in part to the grain flow at the flash plane, is remedied by the fine structure of a part produced using the P/M approach (Figure 4) [63].

The development of P/M Al alloys, with mechanical properties superior to conventional I/M alloys, is a good example of a technology being "pulled" by the aircraft industry's need for higher performance [19]. The current I/M Al alloys most used are represented by the 2000- and 7000-series alloys. The I/M 2000-series alloys are typified by relatively low strengths but good damage tolerance characteristics. The I/M 7000-series alloys are stronger, but designers are unable to take full advantage of the peak strength because of reduced resistance to stress corrosion or exfoliation. Therefore, various overaged tempers are used which degrade strength by as much as 20%, resulting in

higher weight and consequently increased operating costs or decreased performance levels. The attraction of the developing P/M alloys is their superior property combinations compared to the state-of-the-art I/M aluminum alloys.

2.1.2 P/M Processes

Figure 5 is a flow chart of the typical P/M process in use today to produce commercial products for aerospace applications [33]. Powder is made through a combination of melting, alloying, and atomization (or other appropriate method to produce particulate). The loose powder is collected, sized and usually packaged in drums for shipment. In the process known commonly today as the Frankford Arsenal-Alcoa Process [34] the powder is cold isostatically pressed into a cylindrical shape, canned, and hot vacuum degassed. After sealing, the can is preheated to the consolidation temperature and vacuum hot pressed (usually in an extrusion press against a "blind" die). After consolidation the can is machined away and the billet is processed as any other aluminum billet. These processing steps and some common modifications are discussed in detail below.

2.1.2.1 Powder Making

There are a variety of methods by which powder can be made. These are generally characterized by that with which the molten metal interacts and by the environment in which the powder is made and collected. The methods important for Al P/M include:

a) Gas atomization [20, 30] - occurs when a molten metal stream is forced through a nozzle and impinged upon by a stream of gas, breaking it into fine droplets. This method accounts for the greatest percentage of aluminum powder made today. It may be called inert gas atomization or ultrasonic gas atomization depending upon the type of gas or the character of the gas velocity [20]. Reported cooling rates

6

during solidification for gas atomization range from 10^3 to 10^6 K/s [20]. The process can result in relatively smooth spherical powder when using inert gas atomization or in irregular nodular shaped powders when using air atomization, as seen in Figure 6. Varying process parameters can yield a wide range of particle size distributions. Higher solidification rates and finer microstructural features are associated with smaller powder particles [20, 31].

b) <u>Centrifugal atomization</u> [32] is characterized by the molten stream of metal impinging on a rapidly rotating disk. This process is commonly associated with Pratt and Whitney (the RSR Process) and uses recirculated He gas as a coolant. Cooling rates of 10^4 to 10^6 K/s are reported [20, 32]. The powder particles are relatively large and smooth, as seen in Figure 6.

c) <u>Splat quenching</u> [20, 24] involves propelling gas atomized droplets of molten metal onto a cold surface resulting in a flat flake-like "splat" product. This process can result in higher cooling rates than with conventional gas atomization [20]. The splats can vary in size, thickness, and cooling rate because of variation in droplet size and the quenching process [2]. Other disadvantages of this process include handling difficulties due to the low packing density (7-15% theoretical density) and difficulty in pouring and sizing by screening [20].

Environments for aluminum powder making and collecting are normally air or inert gas, depending upon the desire to control or reduce oxidation. The atomizing environment has a dramatic effect on the shape and surface characteristics of aluminum powders as indicated in Figure 6. Air environments tend to produce a rougher and more irregular shaped powder particle compared to inert environments such as helium or nitrogen. Alcoa often uses an oxygen depleted gas mixture designated synthetic flue gas (0.0% O_2, 2.0% H_2, 12.6% CO_2, 0.6% CO,

7

balance N_2) to control oxidation of reactive materials such as the Al-Fe-Ce alloys [34].

2.1.2.2 Powder Conditioning

The apparent density (pour density) of aluminum powders is generally 50% theoretical or less depending on the powder making process (size and shape) [35]. In addition, if the powder has been exposed to air and/or moisture a deleterious hydrated oxide will have formed [36]. To prepare the powder for consolidation one or more of the following conditioning steps is performed.

a) Cold compaction is carried out to make powder handling safer (i.e., to reduce the explosion hazard) and easier [19], and it also increases the yield [25]. It is normally carried out to less than 80% of theoretical density to preserve interconnected porosity for degassing. Typically [25] it is carried out in an isostatic press using a wet bag system and 30 ksi pressure. An alternative to CIP'ing is vibration or jolting [2] to increase pouring density to improve yield.

b) Degassing is normally carried out to remove hydrogen and water to prevent porosity and blistering that may form in high temperature processing operations such as solution heat treatment [25]. Degassing usually improves bonding of the particles and has been shown to improve the transverse properties--particularly ductility and toughness [25]. It is known that the surface of aluminum alloys forms an oxide that readily absorbs water to form an Al-hydroxide [36]. Upon heating in vacuum the hydroxides decompose to Al-oxide according to the reactions in Table 2 [37-40]. The basic reactions of importance are the reduction of the tri-hydrate to the mono-hydrate to pure γ-Al_2O_3 according to [37, 40, 41]:

$$Al_2O_3 \cdot 3H_2O \xrightarrow[150°C]{175\text{-}310°C} Al_2O_3 \cdot H_2O \xrightarrow[600\text{-}900°C]{530\text{-}550°C} \gamma\text{-}Al_2O_3 \quad (1)$$

310-500°C

8
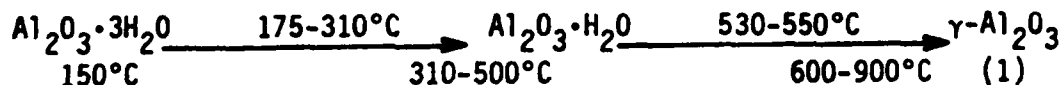
In the case of alloy 7091 which contains highly mobile and reactive Mg ($\sim$ 2.5 atomic %), the following reaction is also possible [36]:

$$Mg + H_2O \rightarrow MgO + H_2 \qquad (2)$$

In addition to Al-hydroxides, Al_2O_3 and MgO, physically absorbed gases (H_2O and/or O_2) are also present on the powder surface. Neutron activation analyses [42, 43] showed a reduction in the oxygen level (0.6 wt% $\rightarrow$ 0.3 wt %) when 7091 powder is cold compacted and degassed at 520°C (970°F) for 6 hr. The hydrogen level was reduced to the order of 1 ppm for small billets through degassing [43]. Kim, et. al. [36] postulate that the degassing "dries up" the surface oxide layer. The average thickness of the oxide film is < 4 nm as estimated by Transmission Electron Microscope (TEM) observations [36] which agrees with other reports [6, 44]. Failure to adequately remove the gases and hydroxides by appropriate vacuum degassing treatments can lead to blistering, porosity, or weak particle bonding forming during subsequent processing [2, 25, 33, 36]. The degassing temperature must be chosen to approximate the solutionizing temperature in precipitation hardened systems [19].

On the other hand, in dispersion strengthened systems such as Al-Fe-Ce or Al-Fe-Mo, holding for long times at high temperatures can cause irreversible coarsening to dispersoids responsible for strength, thereby causing a loss in strength that cannot be recovered. The criticality of the degassing step for a sound product is generally accepted.

2.1.2.3 Hot Compaction

Generally, conditioning is followed by hot compaction to a dense billet to raise the hot ductility of the compact sufficiently to permit hot working [25]. This billet may then be processed into a wrought product in a manner similar to an I/M billet. Using 7091 as an example, [19] the powder is generally canned and degassed above the

9

solution heat treatment temperature, which is about 950°F. The degassed compact is then extruded against a blind die to essentially a 100% dense billet at pressures as low as 30 ksi [25]. These billets can now be produced as product weighing up to 350 lb. [19]. The dense billet can be further processed by extruding, forging, or rolling at a typical temperature of 750°F. The Air Force is currently funding a program to produce large billets--3,000 to 20,000 lb.--so that rolling may take place on commercial rolling mills. Some surface must be removed from the hot pressed compact to prevent cracking during forging [25] and to remove canning material.

2.1.2.4 Hot Working

Compacts are typically hot worked at 550-750°F [25]. Compacts, even when preheated, degassed, and hot pressed using good practices have low ductilities in comparison to forgings and extrusions [25]. Hot deformation in which substantial metal flow occurs is required to raise the ductility of 7000-series P/M products [25]. This is probably due to the need to break-up and distribute the particle surface oxides [36] as discussed in the next section.

2.1.3 Oxide Break-up and Dispersion

As previously discussed, cold isostatic pressing at pressures up to 207 MPa (30 ksi) compacts loose powders up to 80% theoretical density. This results in some minor damage to the surface oxide layer [36]. In addition the plastic nature of the wet, predominantly amorphous surface oxide layer apparently protects itself from extensive damage [36]. Hot pressing after degassing fully densifies the product, but the extent of deformation at the powder particle surface is minimal and depends on the powder particle shape, size, and surface roughness [36]. Thus the hot pressing operation can easily break up the oxide surface film but cannot adequately redistribute it. When poorly degassed the

oxide film is less susceptible to breakup by hot pressing [45]. After hot pressing the broken oxides are present along the powder particle surfaces forming prior powder particle boundary (PPB) arrays. Forging elongates and flattens powder particles which are more or less round after hot pressing. Any such shape change will increase the surface area, thus the PPB area also increases as does the oxide break up spacing [36]. In forgings, the oxide stringers that form remain continuous and interconnected throughout the material. Crack initiation and propagation will be easier along the stringers and through oxide dense regions [36, 44].

This behavior is not observed in material that is severely extruded. For example, an extrusion with a 24:1 extrusion ratio and 8:1 aspect ratio shows almost completely discrete oxides that are not associated with PPB's or grain boundaries [45]. In fact, PPB's are no longer observed. These observations lend credence to the suggestion of a "critical extrusion ratio" by Billman, et. al., [46] above which the transverse toughness of P/M Al alloy extrusions is equivalent to the longitudinal toughness. Billman et. al., [46] found this ratio to be 12:1. Voss [47] also predicted good properties for P/M extrusions extruded above about 10:1 as did Gurney and Abson [48]. There appears to be no such critical parameter for forgings [36] which maintain PPBs and oxide stringer continuity even at high forging reductions.

2.1.4 Families of P/M Aluminum Alloys [19]

There are three families of P/M aluminum alloys receiving significant attention and the U. S. Air Force is currently funding development of all three. These include the high strength corrosion-resistant alloys, the low density alloys, and the dispersion strengthened elevated temperature alloys. The goals of these three thrusts are shown in Table 3. Each of these three families will be discussed in turn. The nominal compositions of alloys in each family are shown in Table 4 and typical properties in Table 5.

11

2.1.4.1 High Strength Corrosion-Resistant Alloys [19]

The high strength alloys--such as 7090 and 7091--were developed for their good strength/corrosion resistance combination. They also have good fatigue initiation resistance. These alloys are somewhat disappointing because their constant amplitude fatigue crack growth resistance is considered by many not sufficiently improved to warrant replacement of high strength I/M alloys on a broad scale. However, very recent results indicate that the performance of P/M alloys relative to I/M alloys is improved when the crack growth testing is done under certain spectrum conditions (e.g., the FALSTAFF spectrum), which is closer to the "real world" situation [50, 51]. Telesman [192] has reported that crack growth resistance is no better, and perhaps worse when the spectrum is dominated by tensile overloads.

It has been suggested that this class of alloy will not find the wide application of the alloys discussed in the next sections. However, interest in this class remains high as evidenced by the participation of ten airframe companies in the High-Strength Aluminum PM Alloy Cooperative Structural Assessment (Round Robin) organized in 1982 by the AFWAL Materials Laboratory [13]. It is expected that specialized applications of these alloys will result from this study. Independent of this study, Boeing has identified two forgings for 757 type aircraft that saves 14 lb./aircraft [52, 60]. Typical properties of this class of alloy are given in Table 5. Alcoa has recently announced the development of second generation high strength aluminum P/M alloys which are to be available during 1984 [62].

2.1.4.2 Low Density-High Modulus Alloys [19]

The low density-high modulus alloys are being developed against goals of 20%-30% higher specific modulus (E/p) up to 20% higher strength, and up to 10% lower density. Lithium-containing aluminum alloys are most commonly included in this category because they exhibit

12

improvements in both parameters. The I/M and P/M approaches to Al-Li alloy development are both being pursued in AF sponsored programs [53, 54] and under independent research programs throughout the airframe industry. Current results [54] indicate short term goals can be realized using an I/M approach. The P/M approach does offer several advantages including refined microstructures and extension of solubility for major and minor alloying additions. Refined microstructure is expected to impact the long time problem of poor ductility and toughness in this class of alloys. P/M may also be used to produce compositions that can not be produced otherwise in second generation Al-Li alloy development. Finally, th. P/M process is one solution to casting difficulties recently reported for I/M Al-Li alloys [55].

The payoff that can be attained if program goals are met has created unparalleled interest in Al-Li alloy development. Studies [53, 54] have shown that a one-for-one replacement of current aluminum alloys would reduce structural weight by 10% or more. Even more significant is that, by considering redesign, Al-Li alloys can be made competitive on a cost and weight basis with graphite/epoxy composites [53, 54] Typical properties of alloys under development are given in Table 5.

2.1.4.3 Elevated Temperature Aluminum Alloys [19]

This is the first class of aluminum alloys considered that fully exploits the capability of Rapid Solidification Technology (RST) to produce compositions that cannot be cast using current ingot technology. Here the approach is to add alloy additions such as the transition metals which form a thermally stable dispersion characterized by low solid solubility and low diffusion rates. The goals of AF sponsored research [56] are shown in comparison with conventional I/M alloys and Ti alloys in Figure 7 [56, 65]. Basically the goal of the alloy development program is to maintain usable properties at temperatures 200°F-400°F higher than currently possible. Realization of

13

program goals will allow application of this class of alloy in hot airframe structure (replacing Ti alloys), in low compression sections of gas turbine engines, and in skin and structure of many missile systems. Weight savings from 8%-35% have been reported depending upon the specific application and significant cost savings relative to titanium alloys are generally anticipated. Typical properties are shown in Table 5. Note that the excellent room temperature strength and modulus may make this class of alloy competitive with metal matrix composites for some room temperature applications.

2.1.4.4 Cost Effective Processing [19]

Presently the cost of P/M aluminum mill products is 2-3 times that of conventional I/M product [13]. While the enhanced mechanical property behavior of all three alloy families will ensure that they are used in demanding applications, a cost parity with the conventional alloys would result in even further use. Consequently the Air Force is aggressively investigating the possibility of decreasing the number of steps required to produce a P/M mill product. Ideally it would be possible to go directly from powder to final mill product. However in practice this is not always possible. It should be remembered that direct processing, at least for soft (non-hardenable) alloys, has been a commercial entity for many years [57]. Possibilities include direct rolling to sheet, strip or thin plate, direct extrusion and spray deposition to near net shapes such as forging preforms, sheet, strip or thin plate. Integrated into these processes must be control of the oxide nature and distribution since this so strongly influences the mechanical properties. Possibilities include concepts such as open-tray degassing [61] rather than the conventional degassing of the less than 100% dense cold pressed billet.

The Air Force is currently considering several efforts that could substantially reduce the cost of producing Al P/M products. The approaches include direct rolling of sheet [11], producing billets

14

using canless processes [9, 58], and a spray deposition (forming) process [59]. Integrated into these processes is a concern for the control of oxide nature and distribution.

2.2 7000-Series Aluminum Alloys

Under the Aluminum Association's aluminum alloy designation system, 7000-series alloys are those whose major alloying element is Zn. Generally 7000-series alloys refers to classes of Al-Zn-Mg alloys, particularly those containing copper. Along with Al-Cu (2000-series) alloys, these alloys are used extensively by designers of airframe structure because of their relative high strength and low density. As seen in Figure 1, the amount of Al in aircraft structures is significant. The advent of graphite-epoxy composites is predicted to erode the favorable position of aluminum alloys somewhat, but even conservative estimates place aluminum at up to 50% of the structural weight of aircraft designed for the late 1990's.

2.2.1 Microstructure

The 7000-series aluminum alloys are precipitation strengthened. Mondolpho [82] and others [88-104] report the age hardening sequence of Al-Zn-Mg alloys as:

$$SSS \rightarrow \text{Guinier-Preston (GP) Zone} \rightarrow \underset{(\eta')}{\text{intermediate}} \rightarrow \underset{(\eta)}{\text{final precipitate.}} \quad (3)$$

Most often GP zones are reported to be spherical and approximately 50Å in diameter for maximum strengthening [86] although various authors will report this diameter as small as 20Å [96] and as large as 80Å [84]. GP zones nucleate homogeneously and proceed to a spherical coherent form with a hexagonal structure [83].

15

The intermediate transition phase, η' has an hcp structure with a = 4.68Å and c = 8.68Å and is semi-coherent (7% disregistry) [84]. η' precipitates are $MgZn_2$ plates approximately 50Å thick and 200-500Å long [67, 84]. Peak strength is usually associated with a fine distribution of η', yet small amounts of the equilibrium phase η may be present. η is a rod or lath-like $MgZn_2$ and also has an hcp structure with a = 5.15Å and c = 8.48Å [84]. In the transition from GP zones to η during aging, the matrix-precipitate coherency progressively disappears. GP zones are coherent, η' is semi-coherent and η is incoherent [84]. Because they are not coherent, η' and η can heterogeneous nucleate on subgrain boundaries and dislocations or grain boundaries respectively during quenching and aging [85].

Addition of Cu stimulates uniform precipitation, reduces the precipitate free zone (PFZ) width at the grain boundary [84] and increases Stress Corrosion Cracking (SCC) resistance, toughness and peak strength [82]. As Cu content increases up to 2.1% by weight, cyclic strain resistance is improved in 7000-series alloys [86]. Sanders and Staley [84] report that the Cu enters into hardening precipitates to form $Mg(CuAl,Zn)_2$.

The highest strength commercial wrought alloys contain 3.5-6% Zn, 2-3% Mg, and 1-2.5% Cu as principal alloying elements [105]. Minor alloying elements may include Cr,Zr,Mn, and/or Ti. 0.1-0.4% Cr and Mn significantly change the quench rate effect on properties after aging by accelerating GP zone growth. This is accomplished by Cr in solid-solution causing an increase in vacancy retention during quenching [95].

2.2.2 Precipitate Free Zones

A zone free of precipitates is commonly found adjacent to grain boundaries in precipitation strengthened aluminum alloys. These zones are of two types [107]: those arising from depletion of vacancies and

16

those arising from depletion of solute. Since the circumstances from which each type is formed is separate and specific, the zones need to be described more rigorously than simply using terminology such as "denuded" or "precipitate-free" [107]. In the first case, vacancy depletion occurs near grain boundaries (which act as sinks) and diffusion of solute, required to form precipitates, is inhibited. In the second case depletion of solute due to the formation of heterogeneously nucleated $MgZn_2$ at grain boundaries prevents formation of the fine hardening precipitate adjacent to the grain boundaries [87-90]. The PFZ width depends on the rate of quenching from the solution heat treatment temperature [88]. SCC [89, 90] and embrittlement phenomena [91] have been explained in terms of preferential deformation in the PFZ [89]. UTS and yield strength are not significantly affected by increasing PFZ width [88]. Lynch [92] has observed localized deformation in PFZ's in age hardened Al-Zn-Mg alloys.

2.2.3 Second Phase Particles

Three distinct types of second phase particles significantly affect the properties of 7000-series alloys [67, 106]. These include:

1. Small (.01-.05 µm) solute rich strengthening phases previously discussed.

2. Intermediate (.02-.5 µm) dispersoids rich in Mn,Cr,Zr or Co that precipitate during elevated temperature ingot homogenization treatments. These are incoherent $Al_{12}Mg_2Cr$ (in 7075) and Al_3Zr (in 7050). The primary role of dispersoids is to prevent recrystallization and limit grain growth during processing. The P/M analogy is Co_2Al_9, a spherical precipitate formed during solidification. Without Co_2Al_9 a very thin, elongated grain structure is formed in forgings; with Co_2Al_9 a decrease in subgrain size is reported [94]. A majority of Co_2Al_9 is in the grains. It is appropriate to include in this classification the

17

creates a separate set of problems related to test control, strain measurement, temperature control, and specimen design [159, 160].

6. Environment - It is often desirable to conduct tests in environments other than lab air, either for enhanced control (i.e., to avoid variations in humidity) or to include evaluation of behavior in corrosive or inert environments. Again, use of an aggressive environment often complicates the test set-up since delicate measuring equipment must be protected.

Typical data derived from strain controlled LCF tests includes [154]:

1. Total, plastic and elastic components of axial and/or diametral strain. Strain is generally measured by use of a contact type sensor referred to as an extensometer. This small transducer senses the deflection (either axial or diametral) in the gage section.

2. Stress range or amplitude as a function of imposed cycles; this determines whether cyclic hardening or softening is observed and can be used with other data to derive a cyclic stress-strain curve.

3. Cycles to failure.

4. Cycles to crack initiation. The definition of initiation is arbitrary, usually depends on the sensitivity of the load measuring device, and has not been standardized [155]. Suggested definitions [155] include presence of the smallest crack detectable either unaided or with magnification, a crack long enough to cause a significant decrease in load carrying capability (e.g., 5% load drop), or a crack sufficient to cause fracture. Because of the fact that in many metals crack propagation is a significant fraction of fatigue life [161], generally greater than 75% for Al [162], cycles to initiate has become a more important LCF parameter than cycles to failure.

graphically. The cyclic stress-strain response described in Equation 10 will determine the stress range.

2. Mean Strain - defined as the algebraic mean of the maximum and minimum strain values in one cycle, i.e., $(\epsilon_{max} + \epsilon_{min})/2$. Other definitions that help describe the strain controlled cycle are identified by the letters R and A:

$$R_\epsilon = \frac{\epsilon_{min}}{\epsilon_{max}} \tag{11}$$

$$A_\epsilon = \frac{\epsilon_a}{\epsilon_{mean}} = \frac{\epsilon_{max} - \epsilon_{min}}{\epsilon_{max} + \epsilon_{min}} = \frac{1 - R}{1 + R} \tag{12}$$

3. Cycling Frequency - is the reciprocal of the cycle time. Frequency (f) is typically selected to provide a constant strain rate for all tests. Strain rate is related to frequency through:

$$\dot{\epsilon}_t = \frac{strain\ amplitude}{cycle\ time/4} = 2f\Delta\epsilon_t \tag{13}$$

4. Wave Form - The triangular wave form shown in Figure 11 is typical for many simple test programs, but other, often complicated, wave forms are possible. These include triangular with hold times which is used when time dependent processes are studied and dual slope which is also used when creep or environmental factors are important.

5. Temperature - when thermally activated processes are not studied, the most common test temperature is room temperature. Elevated temperature LCF testing is commonly carried out on materials used in rotating components of gas turbine engines where fatigue-creep interactions become important. Testing at elevated temperatures

30

plastic strain exceeds the elastic strain. The distinguishing feature of LCF is that peak stresses exceed the tensile yield stress and the strains induced have a measurable plastic component [154]. It is generally accepted today that plastic strain is the parameter that controls microstructure-dislocation mechanisms and thus strain controlled LCF is the most widely used technique to study fatigue deformation mechanisms [111, 155-157].

Morrow [158] has described the cyclic stress-strain response as:

$$\frac{\Delta\epsilon_t}{2} = \frac{\Delta\epsilon_e}{2} + \frac{\Delta\epsilon_p}{2} = \frac{\sigma_a}{E} + \epsilon_f' \frac{\sigma_a}{\sigma_f'}^{1/n'} \qquad (10)$$

where

$\Delta\epsilon_t$ = total strain range

$\Delta\epsilon_e$ = elastic strain range

$\Delta\epsilon_p$ = plastic strain range

σ_a = stress amplitude

E = Young's Modulus

ϵ_f' = Fatigue Ductility coefficient

σ_f' = Fatigue strength coefficient

n = cyclic strain hardening exponent

Conditions of the strain-controlled test [154] is typically characterized by:

1. Strain Amplitude - when ϵ is the controlled variable the specimen is deformed within the same strain limits in each cycle. Total strain is generally controlled by some type of closed-loop controller most often in a servo hydraulic testing machine. Using a triangular wave form as an example, Figure 11 defines strain amplitude

29

Sanders et. al., argue that when r_p is substantially larger than a given microstructural feature, e.g., grain size or interparticle spacing, that feature should have relatively little effect on FCG resistance; the microstructure essentially behaves as a continuum obeying relationships calculated from linear elastic fracture mechanics [5]. Yoder et. al., [265-267] found that the transition from structure-sensitive to structure-insensitive crack growth resistance occurred when the cyclic plastic zone was equal to the average Widmanstätten pack size in titanium alloys. At low ΔK where r_p is small, large grains [140] or constituent particles [85] may divert cracks from the preferred crack growth path normal to the applied stress. In large grained I/M aluminum alloys crystallographic crack growth may serve to significantly reduce measured FCGRs at low ΔK levels. The fine structure of P/M aluminum alloys is still small relative to r_p and offers no features to divert the crack from the macroscopic growth direction. Somewhat higher FCGRs are observed for P/M materials below 5 MPa√m. At higher stress intensity values when the r_p values are larger, both I/M and P/M microstructures act similarly and display similar FCGRs. These arguments assume a deflection mechanism and do not address the interactions occuring within the plastic zones which certainly affect the way in which damage is accumulated. As will be discussed in the next section processes such as precipitate reversion can substantially alter the properties of the material. The interaction of precipitates and dispersoids inside the plastic zones can determine the nature of slip and hence affect FCP. Typical FCP curves for 7000-series alloys are shown in Figure 10.

2.4 Low Cycle Fatigue (LCF)

Low cycle fatigue is often defined as the cyclic application of stress or strain such that specimen failure occurs before some specified number of cycles, usually between 10^4 and 10^5 cycles [111, 154-156]. A better definition is testing such that the magnitude of observed

28

strain fragmented oxides but had little effect on Co_2Al_9 dispersoids in CT91. Oxides act as nucleation sites for precipitation. Fragmented oxides are strung out along grain and subgrain boundaries in deformed materials, therefore precipitation is more continuous along these boundaries. Fatigue cracks follow the semicoherent or noncoherent precipitation regions [105]. In this region the microstructures of both I/M and P/M act as a continuum and the FCGRs are similar. Kim and Bidwell [120] have reported dramatic decreases in crack growth rates of P/M Al alloy X7091 as a result of increasing grain size from 3 to 300 microns.

Stage III crack growth is characterized by static mode mechanisms (cleavage, intergranular, fibrous) and is influenced by microstructure, mean stress and specimen thickness [140]. There is little influence of environment. The Stage III FCP behavior is controlled to a large degree by fracture toughness.

Sanders et. al., [5] compared the monotonic plane strain plastic zone size, r_p, to pertinent structural features to help understand the FCG behavior of high strength 7000-series aluminum alloys. An estimate [152] of r_p can be obtained from:

$$r_p = \frac{1}{6\pi}\left(\frac{K_{max}}{\sigma_{ys}}\right)^2 \tag{9a}$$

where K_{max} = max. stress intensity during a fatigue cycle
σ_{ys} = yield strength.

A more appropriate comparison may have been the cyclic plastic zone size, r_{pc} which is one-fourth the size of the monotonic zone:

$$r_{pc} = \frac{1}{24\pi}\left(\frac{K_{max}}{\sigma_{ys}}\right)^2 \tag{9b}$$

27

fine microstructure to diffuse crack-tip cyclic strain and to create a tortuous crack path. As a result crack growth proceeds unobstructured causing the fracture to appear featureless.

Stage II crack growth is generally considered to follow the Paris-Erdogan equation [151].

$$da/dN = A\Delta K^m \qquad (8)$$

where A and m are material constants. Stage II is generally characterized by a continuum mechanism (striation formation) and often is said to show little influence of microstructure, mean stress, dilute environment and thickness [140, 263]. In fact there is increasing evidence that a microstructure does play a role in influencing crack growth resistance. In this region factors which increase resistance of 7000-series alloys to SCC, i.e., overaging and increasing Cu content, increased resistance to FCP [85]. The effect of dispersoid type was not significant [85]. Truckner et. al., [106] report that for Al alloys 7050 and 7075, increasing the degree of precipitation, higher Cu content, lower volume % constituent particles, and lower humidity reduced Stage II FCPRs, while dispersoid type and distribution and grain size (5-65000 grains/mm^3) had no effect. There is evidence that coarsening grain size in steels and titanium alloys can decrease crack propagation rates [140]. Edwards and Martin [264] report that for an Al-Mg-Si alloy at low and intermediate values of ΔK the crack growth rate decreased as the volume fraction of dispersoid increased. Changing the frequency from 20 Hz to 2 Hz gave a lower Fatigue Crack Propagation Rate, (FCPR) in high humidity and higher FCPR in low humidity. This was reported to be due to increased corrosion activity per cycle which blunts the crack and/or builds up corrosion residue increasing crack closure forces which retard crack growth. It is generally accepted [105] that thermomechanical treatments have little effect on FCP of I/M wrought aluminum alloys. Deformation did have an effect on P/M materials. Antes [105] reports that increasing forging

26

2.3.3 Fatigue Crack Propagation (FCP)

The key parameter controlling fatigue crack propagation rate (FCPR) is the stress intensity range $(K_{max} - K_{min})$ [139]. Figure 9 schematically shows the variation of crack growth rate with ΔK. It is seen that three regimes of crack propagation may be defined [140]: a) near-threshold where ΔK approaches ΔK_0; b) midgrowth-rate region and; c) the high growth-rate region where K_{max} approaches K_{IC}.

The fatigue limit or other value of critical stress describes the threshold conditions for microcrack initiation. The threshold condition for subsequent propagation as a macrocrack depends on a critical value of stress intensity, the threshold stress intensity or ΔK_0 [140]. Stage I crack growth occurs as ΔK approaches ΔK_0. It is characterized by non-continuum mechanisms and shows a large influence of microstructure, mean stress and environment [140]. The primary microstructural parameters include yield strength and grain size (which are interdependent). As strength increases and grain size decreases the initiation resistance of a material generally increases but resistance to near threshold crack growth decreases dramatically [141-145]. In aluminum alloys the underaged tempers are fractionally better than peak and overaged tempers [140]. Filler [146] has observed that replacing Cr in 7000-series alloys with Zr improves Stage I FCP but that increased purity (lower Fe and Si) was detrimental. Environmental effects can be dramatic. Testing in vacuum increases ΔK_0 significantly in steels [147], titanium [148, 149] and aluminum [150]. There is also a marked dependence of near-threshold FCP on mean stress which is not generally noted in Stage II. Studies indicate that, for a wide range of steels and nonferrous alloys tested in air, ΔK_0 is substantially decreased as the load ratio $(R = K_{min}/K_{max})$ is increased from 0 to 0.9 [140]. Similar tests in vacuum showed no such dependence suggesting an environmental interaction effect. The relationship between aluminum P/M microstructure and FCP is incomplete [5]. Higher FCPRs in P/M compared to I/M at low ΔK is associated with the reduced ability of the

25

through the control of grain size and by the fact that they impede intergranular fracture. Coarse particles (constituents) were not a factor in grain size dependent K_{IC} data from center-cracked panels, but did appear to lower K_{IC} in compact tension specimens which were thought to be more sensitive to matrix properties [128]. Grain length to aspect ratio also was important, with high aspect ratio being detrimental. Cu variations had no effect when compensated for the grain size effect. Aging had no strong effect but it was thought that minor toughness improvements can be realized through optimization of multiple step aging if not offset by a degradation of SCC resistance [128]. Long term homogenizing treatments-required for slowly cooled ingots-can be detrimental because they result in larger intermediate precipitates (dispersoids) and coarsen grain size which more than offsets the benefits of increased dissolution of coarse particles [128]. This is contradicted by Hyatt [129] who indicates that if complete homogenization can be attained more efficient utilization of solute elements leads to relatively higher strengths, higher ductility and higher toughness. Improved toughness through the reduction in second phase particles has been demonstrated by a number of other studies [77, 79, 130-135]. These studies have led to a reduction in the allowable Fe and Si in most of the recently introduced 7000-series aluminum alloys, including 7475, 7175, 7050 and 7049 [129]. Thermomechanical treatments (TMTs) during ingot homogenization and fabrication have been shown to improve toughness [68, 129, 134] by breaking up intermetallic particles and by decreasing diffusion distances between dendrite arms of the cast structure. TMTs described by Ostermann and Reimann [80], Waldman et. al., [119] and DiRusso et. al., [127] involve an aging treatment interrupted by cold rolling. Such treatments have a favorable effect on fracture toughness [80, 119, 127, 138]. Hyatt has attributed this to retention of work hardening with uniform dis.   on structure giving rise to increased ductility by permitting more homogeneous deformation. Rosenfield et. al., [128] attribute the improvements in toughness to the refined grain size usually associated with this type of TMT.

24

them and hence that for void nucleation. Decreasing both f_c and D improves toughness by delaying void coalescence. In regions of intense shear between large and growing voids smaller particles nucleate small voids which coalescence and link up with large voids and effectively limit the improvement in the plane strain fracture toughness, K_{IC}, due to the lowering f_c [123, 126]. Hahn and Rosenfield [124] relate K_{IC} to f_c as:

$$K_{IC} = (A\sigma_{ys}ED)^{1/2} f_c^{-1/6} \qquad (7)$$

where K_{IC} = plane strain fracture toughness
   A = numerical constant
   σ_{ys} = yield strength
   E = Young's modulus
   D = particle size
   f_c = volume fraction of constituents

Reducing the size and amount of dispersoid precipitates does not improve K_{IC} as effectively as reducing f_c because the resulting larger grain size promotes intergranular failure and lower K_{IC} [125]. Alloy 7050 uses Zr instead of Cr as a dispersoid former which produces a finer dispersoid that improves toughness [126]. The size of hardening precipitates can be lowered by underaging but this improves toughness at the expense of strength and resistance to SCC and exfoliation attack [122, 129, 136]. Judicious control of impurities (Fe, Si) and dispersoid forming elements (Mn, Cr, Zr, Co) and a proper choice of heat treatment are necessary to produce a cost effective alloy with an optimum property mix [122].

In general, fracture toughness decreases with increasing yield strength [119, 127]. Rosenfield et. al., [128] studied microstructural effects on toughness. They report a Petch effect, i.e., fracture toughness varied linearly with the reciprocal square root of grain size. The intermediate precipitates had the strongest effect on K_{IC}

23

exhibit a grain size dependence contained a well defined, recovered substructure and an intense fiber texture. The degree to which the grain size affects strength in artificially aged 2024 products is reduced as the hardening precipitate's resistance to shearing increases. Voss [47], in a study of I/M and P/M 7075 reports a low dependence of yield strength on grain size. Waldman [19] showed that grain sizes from 15 to 112 μm have only a minor effect on yield strength for 7075-T6 plate.

This low dependence of yield strength on grain size in 7075 is attributed to the combined effect of the Cr dispersoid and the partially coherent η' intermediate precipitate particles. These particles reduce the slip length and promote homogeneous slip within the grains, thereby reducing the influence of the grain boundary. The fact that Lutjering's alloys [117] did not contain a dispersoid forming addition indicates that the absence of a yield strength dependence on grain size is not dependent on homogeneity of deformation. Kim and Bidwell [120] varied the grain size of Al P/M alloy X7091 from 1 μm to more than 1000 μm through thermomechanical treatment with a corresponding drop in yield strength of about 10%. The alloy was insensitive to grain size changes in the range of about 100 μm to 1000 μm.

2.3.2 Fracture Toughness

The fracture of high strength aluminum alloys generally occurs by a ductile or fibrous mode. The presence of dimples gives the fracture surface a fibrous appearance [121]. Close examination of a typical fracture discloses two sets of dimples [70]: large dimples with the spacing equal to the spacing of constituents ($\sim$ 10 μm) and small dimples that connect larger voids. The large dimples are initiated at cracked constituent particles (which can usually be seen at the center) [70]. Decreasing the volume fraction of constituents (f_c) increases the large dimple spacing and permits more growth of large voids [122]. Decreasing the particle size (D) increases the stress required to crack

22

of more Cu can affect the precipitation process, decreasing the coherency of the precipitate when aged to peak strength. Excess Mg also participates in solid solution strengthening [115].

Grain size has a measurable effect on mechanical properties of most alloys; at room temperature, hardness, yield strength, tensile strength, fatigue strength and impact resistance all increase with decreasing grain size [116]. The grain size effect is most pronounced in properties related to the early stages of deformation when grain boundary barriers are most effective; hence yield strength is more dependent on grain size than tensile strength [116]. Complex dislocation interactions occurring within grains control the strength in the latter stages of deformation when grain size is not a controlling variable [116]. For most metals the yield stress is related to grain size by [116]:

$$\sigma_{ys} = \sigma_i + K_y \, D^{-\frac{1}{2}} \tag{6}$$

where σ_{ys} = yield stress
   σ_i = friction stress opposing motion of a dislocation
   K_y = measure of extent to which dislocations are piled up at barriers
   D = grain diameter

K_y can be determined from a plot of σ_{ys} versus the reciprocal of the square root of grain diameter.

   Lutjering et. al., [117] studied grain size variations between 30 and 200 μm in a 7000-series alloy. Although reducing grain size improved tensile fracture properties and fatigue properties, there was no apparent affect on yield strength. Voss and Bunk [118] report that, for I/M and P/M naturally aged 2024, recrystallized P/M extrusions as well as large grained recrystallized I/M extrusions do not show a strength-grain size relationship. The P/M extrusion products that

21

where F = average maximum force which a particle can withstand before shearing

F' = measure of relative particle strength with F = F'D/b

Sanders [111] normalized Equations 4 and 5 by the factor $\Delta\tau_0 b^2/2TF^{\frac{1}{2}}$ and plotted that factor versus D/b on a log-log scale. This plot is shown in Figure 8. From this plot it is noted that particle looping (Orowan mechanism) shows a linear dependence with a negative slope while the shearing mechanism has a positive slope. The intersection of these two curves is a measure of critical radius for looping. The position of the intersection along the Orowan curve is a measure of particle strength, i.e., its inability to deform [111]. The intersection of the two curves is also a measure of the critical radius for looping [111]. Figure 8 also indicates experimental results for several alloy systems including Al-Zn-Mg alloys. Precipitation hardening is most effective when particles are small and coherent with the matrix lattice because a strain is created in the matrix which interacts with the dislocation strain fields to cause a repulsion [112, 113]. Overaging is softening resulting from extended aging and in aluminum alloys it appears concurrently with loss of coherency [113]. As aging progresses the precipitates grow, but the number decreases. Maximum hardening (strengthening) is associated with an optimum small size and a corresponding large number of particles; overaging is associated with a few relatively large particles [113]. Dramatic strength increases accompany the presence of G.P. zones; slip dislocations cut through zones because of their combination of coherency, small size (10 to 100 Å) and high density (10^{18} per cm^3) [114]. The recovery process of cross-slip and climb allow dislocations to avoid some precipitate particles [112].

Chemistry variations can have an effect on strength in 7000-series alloys, although small compared to precipitation strengthening. Cu additions considerably increase the strength of Al-Zn-Mg alloys [115]. Up to 1% Cu does not alter the basic precipitation mechanism and the Cu is thought to add a component of solid solution strengthening. Addition

20

microstructure which can be described [105, 5] as a fine, mostly unre-crystallized structure with a grain/subgrain size of 1 to 5 μm; no coarse constituents are found but a fine inhomogeneous distribution of oxides and Co_2Al_9 is found; and the structure is relatively insensitive to Co content and processing.

2.3 Monotonic Properties

2.3.1 Strength

Mechanical properties in 7000-series alloys are determined prima-rily by dislocation-particle interactions [108]. As previously dis-cussed these alloys are precipitation (strengthen). Noncoherent parti-cles act as impenetrable barriers to dislocation motion. The particles are looped in a process described originally by Orowan [109, 110]. Strength increases due to looping can be expressed by [111]:

$$\Delta\tau_0 = \frac{2T}{bD} \cdot \frac{f^{\frac{1}{2}}}{2} \tag{4}$$

where $\Delta\tau_0$ = increase in shear stress due to the particles

   T = dislocation line tension

   f = volume fraction of particles

   D = particle radius

   b = Burger's vector

Since the slip systems of the precipitates and the matrix are generally coincident, coherent and partially coherent particles may be penetrated by dislocation [111]. These precipitates deform plastically and are sheared by dislocations. Strength increases for particle shearing as given by [111]:

$$\Delta\tau_0 = \frac{F}{b^2} \cdot \frac{F'}{2T} \cdot \frac{F}{2} \cdot \frac{D^{\frac{1}{2}}}{b} \tag{5}$$

19

oxide particles inherent in P/M. When properly processed the MgO and Al_2O_3 are dispersed uniformly and can have an effect on grain structure [36].

3.   Coarse (1-30 μm) constituent particles are formed during solidification by separation of impurity elements Fe and Si. In addition this class may include non-metallic inclusions trapped during ingot casting. Because of rapid solidification the powder alloys contain no large metallic constituent particles. The most common compositions reported are Al_7Cu_2Fe and Mg_2Si. Because Fe is tied up in Co_2Al_9 as $(Co,Fe)_2 Al_9$, the formation of even fine Al_7Cu_2Fe is suppressed in cobalt containing alloys. During ingot breakdown the brittle constituents are cracked and often found in stringers aligned in the principal direction of working. This lowers toughness, especially in the short transverse direction [69]. The particles may also participate in void formation by cracking early in the deformation process [70]. Fatigue cracks can initiate at constituents [71-75]. Constituent particles also lower strength by tying up solute elements normally available for precipitation during aging. Researchers have recently sought to improve 7000 series alloys by reducing the amount of second phase constituent particles. Antes, et. al. [77], Singh and Flemings [78], and Mulhern and Rosenthal [79] have used high purity materials (Fe and Si <.01%) and extended homogenization anneals to improve both strength and toughness of 7000-series alloys. Properties of 7000-series alloys have been improved by maintaining a high Zn:Mg ratio, increasing Cu content and by slight overaging [76]. Thermomechanical processing has also been studied in an attempt to break up these particles [69, 80, 81].

The structure of a typical wrought I/M material can be described [5] as a partially recrystallized, duplex structure with fine subgrains (5 μm) and larger recrystallized grains which may be greater than 200 μm in the principal direction of working; constituent particles (approx. 1% by volume) are generally 2-20 μm in size; and the structure is variable with processing conditions. This is in contrast to the P/M

18

In a typical LCF test, strain and load are plotted continuously. Periodically, hysteresis loops are recorded thus preserving a detailed accounting of the stress-strain behavior in a given cycle. Figure 12 is a schematic of the quantities associated with a generalized hysteresis loop [163]. σ_a, $\Delta\epsilon_p$, $\Delta\epsilon_t$ can be measured directly from the loops. In strain control LCF tests stress is monitored and plotted as a function of cycle number. The microstructure's response to the imposed cyclic straining is observed by noting the stress and strain for each progressive cycle: increasing stress indicates hardening, decreasing stress indicates softening and unchanged stress indicates a stable condition, referred to as saturation, has been reached.

Softening is often attributed to reversion of precipitates by repeated cutting by dislocations [87, 178-181]; each time the precipitate is sheared its radius is decreased, eventually below some critical value and it dissolves. Softening has also been attributed to an over-aging mechanism [183-186] due to enchanced diffusion and reduced local elastic strains as a result of dislocation interaction with coherent and semi-coherent precipitates. Laird and Thomas [187] concluded that reversion does not occur in high purity 7000- and 2000-series alloys but relate softening to crack nucleation in soft regions like PFZs.

Calabrese and Laird [182, 188] attribute softening of age-hardenable Al-4Cu to decay of order in precipitates by repeated dislocation cutting. Wilhelm et. al., [189] reported that destruction of order cannot be the only mechanism responsible for softening in age-hardened alloys having observed a strong reduction of particle size in Persistent Slip Blands (PSB's) in Al-5Zn-1Mg alloys. Cyclic hardening can be attributed to the effective pinning of dislocations by microstructural features as in any work hardening operation, i.e., increase in dislocation density. Cyclic stability indicates that the rate of hardening and softening are equivalent. By plotting the stress-strain combinations representing the types of stable hysteresis loops from specimens cycled at different strain amplitudes a cyclic

32

stress-strain curve can be generated [164]. Plotting Log $\Delta\sigma$ vs. log $\Delta\epsilon_p$ will also yield the cyclic strain hardening exponent, n' in Equation 10. In general, materials that are initially soft will exhibit cyclic hardening and materials that are initially hard will probably exhibit cyclic softening. All metals with a ultimate strength to yield strength ratio greater than 1.4 will cyclically harden; cyclic softening will occur when the σuts/σys ratio is less than 1.2; both hardening and/or softening will be observed in the intermediate range [154].

There have been several investigations on the cyclic stress-strain behavior of a variety of age hardened aluminum alloys [85, 108, 111, 169, 174-176]. Sanders [11] reported cyclic hardening for Al-Zn-Mg ternary alloys and 7050 with an increasing tendancy to stability as heat treatment temperature and time increase, thus increasing the size and incoherency of $MgZn_2$ precipitates. Walker [108] reports hardening for 7091-T7 at strains of 0.7% but softening at strains of 0.2%. Santner [176] reports initial hardening for Al-Cu alloys followed by stability or softening. Santner [169] also reports hardening in 7075-T6 and TMP 7075; again followed by softening in the 7075-T6 alloy. Walker [108] attributed similar behavior to the formation of micro-cracking. Kuo [174] reports hardening followed by saturation in various combinations of I/M and P/M 7091, both processed commercially stable. Laird [168] reports that both conventional 7075 and Al-Zn-Mg ternaries shows regular hardening behavior. Benson and Hancock [170] report cyclic softening for 7075-T651, but add that the softening is so slight the material could be described as cyclically stable. For strain controlled fatigue experiments, log-log plots of $\Delta\epsilon_p$ vs. N_f are usually linear. This has given rise to the empirical Coffin-Manson [170, 171] relationship:

$$N_f^\beta \, \Delta\epsilon_p = C \tag{14}$$

33

Where N_f = cycles to failure
          $\Delta\epsilon_p$ = plastic strain range
          β, C = material constants

Many investigators [84, 85, 87, 108, 111, 155, 175, 169, 174-186] have reported that a single slope Coffin-Manson plot doesn't adequately describe the behavior of age hardened aluminum alloys. This is generally reported to be due to a change from homogeneous deformation (wavy slip) to non-homogeneous deformation (planar slip) [85, 108, 111, 140, 155, 157, 167, 169, 174, 177, 190, 191]. Figure 13 represents dual slope behavior for a variety of aluminum alloys. One theory for this behavior is that at low strains cross slip is not activated within the matrix, deformation is localized and the measured macrostrain is lower than in regions of concentrated plastic strain [155]. Any microstructural features that maintain homogeneous deformation should avert this shift to lower life at low strains.

Overaging 7000-series alloys is an effective way to overcome strain localization in the matrix since this heat treatment produces incoherent, large, widely spaced $MgZn_2$ precipitates that are bypassed by dislocation looping mechanisms [185]. Rapid work hardening occurs due to the greater number of geometrically necessary dislocations generated to accommodate the matrix-precipitate interface as compared to underaged alloys. Dowling [161] suggests that dislocation looping disperses co-planar flow thereby reducing the intensity of persistent slip bands (PSB) at the barriers. Increased dislocation mobility and more frequent interaction also allows more uniform distribution of strain. Since overaging reduces the static strength of these alloys it may be more advantageous to add a small volume fraction of fine, non-coherent dispersoid sized particles which should be conducive to homogeneous deformation [111, 160]. The presence of dispersoids along grain boundaries and subgrain boundaries acts to prevent grain growth and thus indirectly homogenizes slip by limiting the slip distance of PSBs. Preventing grain growth in recrystalized regions and reducing

34

reducing grain size will delay crack initiation by reducing the stress concentrations at grain boundaries [155]. Smaller grain sizes allow a large volume fraction of material to deform homogeneously due to increased grain boundary area where multiple slip occurs.

2.5 FCP Models

Each of the several reviews [198-202] describing models of fatigue crack propagation classifies the models into categories to simplify comparisons on an equal basis [198]. For example, the recent review by Bailon and Antolovich [202] proposes three categories: phenomenological models, dislocation based models and models based on a microcrack tip LCF process. These classifications provide a concise and descriptive categorization that will be used in the following discussion of some of the more important models:

a). Phenomenological Models

These models are developed on an empirical basis. They can be thought of as macroscopic models in which the bulk properties are used to fit a modified Paris equation. Models utilizing crack tip opening displacement (CTOD) are also representative of this class. Some of the better known examples include:

1. Paris and Erdogan [151]

$$da/dN = C\Delta K^m \qquad (15)$$

where da/dN = crack growth per cycle

C, m = material constants

ΔK = stress intensity parameter range

The constants must be determined experimentally. The exponent m varies from metal to metal [151, 211-217]. Unless other classes of

models are considered there is no way to derive numerical values for constants from microstructures and microdeformation at the crack tip [212]. Freudenthal [213] reports that the value of m falls between 2 and 10. High values, $5 < m < 10$, are characteristic for metals of high strength as well as for crack propagation under fully developed plastic conditions of ductile metals. Low values, $2 < m < 5$, represent propagation against elastically restrained plastic resistance. Antes [105] reports that m is related to fracture toughness such that a lower m indicates higher fracture toughness. He calculated m for CT91 forgings of varying strain. For $\epsilon = 0$, $m = 5.7$. Increasing forging strain to $\epsilon = 0.5$ and $\epsilon = 0.7$ gives an m of 3.6 and 3.9 respectively. The constant C varied from 4 to 631 to 513 in/cycle for the same variations in ϵ. The Paris equation describes only part of the experimentally determined da/dn vs. ΔK curve; the existence of two asymptotes is incompatible with Equation 15.

The shortcomings of the Paris equation have led to numerous modifications, a few of which are described below.

2. Forman's Equation [203]

$$da/dN = \frac{C\Delta K^m}{(1-R)K_c - \Delta K}$$

(16)

where $R = K_{min}/K_{max}$
and K_c = fracture toughness for the thickness at which the test is being done

This equation was developed specifically to address the acceleration of crack growth rates at the upper end of the power law region of the da/dN vs. ΔK curve [201]. The Forman equation is in fair agreement for many aircraft structural materials, especially aluminum alloys [198, 202]. Schutz [198] reports that C and m can be determined from a few tests at one stress amplitude and mean stress (i.e., R) and

36

that these values can be used for other mean stresses with reasonable accuracy so long as R > 0. For R < 0 the constants must be determined from new tests at R < 0.

The original Forman equation was not appropriate for near threshold crack growth and has been modified as seen below.

3. Frost/Dixon Equation [204]

$$da/dN = \frac{C}{\sigma_{ys}E} [\Delta K - \Delta K_o]^2 [1 + \frac{\Delta K}{K_{IC} - K_{max}}] \qquad (17)$$

where σ_{ys} = yield strength

E = Young's modulus

ΔK_o = the threshold stress intensity below which no crack propagation occurs

K_{IC} = plane strain fracture toughness

and K_{max} = the maximum applied stress intensity

4. Elber Equation [206]

$$da/dN = C (K_{max} - K_{op})^m \qquad (18)$$

where K_{op} = the stress intensity that opens the crack. If $K_{op} < K_{min}$ then K_{min} replaces K_{op} in Equation 18. The Elber equation assumes that no damage contributing to crack propagation can occur until the crack is open.

Phenomenological models are based on the Paris equation which in turn was proposed on a purely empirical basis [202]. The primary usefulness of these models is to provide data correlation and a convenient means to represent FCP data. These are equations of form and not of prediction and do not provide information useful for alloy design [202]. The dimension of C in Equation 15 must depend on the value of m.

b). Dislocation-Based Models

These are microscopic in nature and dislocation deformation processes are incorporated. Examples include:

1. Weertman's Model [207]

$$da/dN = A \, \Delta K^4 / G \sigma_{ys}^2 U \tag{19}$$

where A = a dimensionless constant depending on the strain hardening behavior of the material
  G = shear modulus
  U = plastic work done to create a unit area of fatigue crack

Fine and co-workers [259-261] have used strain gages attached near the crack path to estimate the energy term U. For aluminum alloys, steels and Ni-7Al values of A have been determined experimentally to be 1.6 to 6.3 x 10^{-3} which is 2 to 10 times lower than predicted from the model.

Lankford et. al., [262], by measuring cyclic strain at a point ahead of the crack tip through stereoimaging have calculated the corresponding energy dissipated in crack growth. They have correlated this energy term with U in Equation 19 and demonstrated that U is not independent of ΔK, suggesting a more general form should be employed:

$$da/dN = A \, \frac{\Delta K^4}{\sigma_{ys}^2 G \, U_0 (\Delta K)^m} = \frac{A \Delta K^{4-m}}{\sigma_{ys}^2 G \, U_0} \tag{19a}$$

where U_0 is an empirically determined constant.

2. Yokobori's Model [208]

$$da/dN \propto \frac{\Delta K}{\sigma_{ys} \sqrt{s}}^{\, 2n'(p+1)^2/(1+n')(p+2) \, + \, 1/1+n'} \tag{20}$$

38

where σ_{cy} = initial cyclic yield stress

S = a distance ahead of the crack tip

n' = the cyclic strain hardening exponent

and p = the exponent on stress in the equation for dislocation velocity

This model is discussed in Reference 202 and summarized in Reference 208. The analysis is based on a treatment of the instability of dislocation emission from the crack tip and on dislocation group dynamics [202]. The model assumes blunting always occurs spontaneously when a cracked body is pulled in tension; it then assumes that since FCP is related to CTOD it is also related to the number of dislocations generated at the crack tip. The model excludes damage cumulated ahead of the crack due to strain reversals [210]. From Equation 20 it can be concluded that the Paris exponent, m, should depend on fundamental deformation behavior as characterized by the strain rate exponent, p, and the strain hardening behavior of the material [202]. For p = 4 to 10 and n' = 0.08 to 0.3 calculated values of m range from 0.6 to 5 [202].

In approaches to life prediction based on dislocation considerations the crack advance mechanisms are highly idealized and the assumptions necessary to obtain solutions are often over simplified [202]. Weertman's model requires the plastic zone to be perfectly circular and sizes are estimated from equations that assume plane stress conditions when in reality most FCP tests results are representative of plane strain conditions. Models such as Yokobari's appear too simplistic in as much as there is no provision for reversed straining occurring during the compressive stroke [202]. The existence of the reversed plastic zone ahead of the crack tip is ignored and the models don't take into account the oscillating motion of dislocations occurring during fatigue cycling [202]. The models do predict that m is a material constant depending on basic properties of dislocation motion.

39

c. Models Based on a Micro-Crack-Tip LCF Process.

In considering models of this type, FCP is assumed to be the result of damage accumulation ahead of the crack. The crack advances when sufficient damage has been accumulated, the distance generally referred to as the "process zone" where the micro LCF process operates [202]. McClintock [218] originated the concept without reference to the significance of the process zone. Examples of LCF-based models include:

1. Antolovich/Saxena/Chanani Model [209]

$$da/dN = \frac{C}{(\sigma'_{yc}\epsilon'_f E)^{1/\beta}} \cdot \frac{1}{\ell^{1/b-1}} \cdot \Delta K^{2/\beta} \tag{21}$$

where σ_{yc} = cyclic yield strength
ϵ'_f = fatigue ductility
β = Coffin-Manson Law exponent
ℓ = process zone size parameter

The model [209] assumes the fatigue process occurs in a region ℓ units ahead of the crack tip and that the crack advances ℓ units in ΔN cycles according to a modified Coffin-Manson equation.

A reasonable initial test of the model is the comparison of the FCP exponent with the predicted value and to use the experimental value of C and the measured mechanical properties to compare ℓ with actual microstructural parameters. Antolovich et. al., [209] have done this for a variety of materials with good agreement. For 2024-T6 aluminum the value of ℓ was 55A which is on the order of the distance between hardening precipitates. The model is limited in application to the regime where crack growth is discontinuous and not controlled by CTOD processes. The original model used cycles to failure in the Coffin-Manson equation while cycles to initiate cracks is more realistic since

40

failure of a macroscopic LCF specimen integrates a considerable amount of crack propagation [202].

2. Lanteigne and Bailon Model [210]

$$da/dN = \frac{4}{\rho^{1/\beta-1}} \frac{0.2(1-\nu^2)(\Delta K^2-\Delta K_0^2)}{\pi\sqrt{3} \; C_t \; E \; \sigma_{ys} \; \epsilon_f'} \tag{22}$$

where ν = Poisson's ratio, approximately 0.3

C_t = triaxiality factor, approximately 2.7

ρ = parameter related to process zone size

This model was developed to incorporate the threshold stress intensity, ΔK_0. It assumes the crack tip is a semicircular notch of radius ρ and the incremental crack growth occurs within a distance 4 ρ ahead of the crack tip in N_f cycles. N_f is given by the Coffin-Manson relation (Equation 14). As with the previous model, the value of the Paris Law exponent, m, can be approximated by $2/\beta$ if the model is appropriate. The model can be used to correlate experimental data for low FCPR or for ΔK_0 [210]. This was done for a variety of materials with reasonable agreement ($\sim$ order of magnitude). The model is valid only for R = 0 and assumes a perfectly elastic-plastic material [202]. This model is only valid for slow crack growth (requiring damage accumulation) and which cannot be deduced from CTOD (i.e., one striation implies one load application). As in the previous model, the number of cycles to failure is used in the Coffin-Manson relationship rather than the more realistic cycles to initiate.

3. Chakrabortty Model [211]

41

$$da/dN = 2 \sum_{n=1} \bar{\rho}_n' \left(\frac{\Delta\epsilon_{pn}}{2\epsilon_f'}\right)^{-1/\beta} \tag{23}$$

where $\Delta\epsilon_{pn}$ is given by

$$\Delta\epsilon_{pn} = \int_{x=r_{n-1}}^{r_n} x^{\frac{1}{2}} \cdot \Delta\bar{\epsilon}_p \cdot dx \quad \int_{x=r_{n-1}}^{r_n} x^{\frac{1}{2}} dx \tag{24}$$

$$x = \frac{A}{(\Delta\bar{\epsilon}_p)^{n'} + \frac{k'}{E}(\Delta\bar{\epsilon}_p)^{2n'}}$$

and where $\Delta\epsilon_{pn}$ = plastic strain range for the nth echelon

$\bar{\rho}_n'$ = average size of the microstructural deformation zone (MDZ) in the nth echelon

x = dimension in the direction of crack growth

r_n = distance between crack tip and the end of the nth echelon

In this model the FCPR is related to cyclic flow stress and the cyclic ductility of materials by means of a ductility exhaustion mechanism [211]. The author purports the model to calculate the absolute rate of FCP from first principles using no adjustable parameters and thus to be a unique contribution to understanding crack propagation from which microstructural effects can be unambiguously determined. Close examination of the assumptions used show this is not the case and the model can be shown to be a restatement of concepts in the literature. For example, the plastic strain distribution is approximated by using the concept of the MDZ (microstructural deformation zone) over

42

which the assumed analytical expression for the strain distribution is averaged. The essentials of this concept have been invoked elsewhere [209, 219, 220]. A Coffin-Manson failure criterion along with Miner's Law is used to compute the rate of crack advance. This first step has also been used prior to the appearance of this model in the literature [208, 218-220] as has use of a cumulative damage equation [218-220]. The model actually represents only a minor refinement for the purpose of understanding microstructural effects. Furthermore, use of a Miner's Law constant equal to unity is clearly not universally applicable especially when different mechanisms of deformation are operative at different strain levels. Finally, use of cycles to failure instead of cycles to initiation in the Coffin-Manson Law is clearly a conceptual error which is common in most LCF based FCP models. This is not a serious error if the model is to be used in evaluating the relative effects of microstructure; however, when used to calculate absolute FCP rates, as claimed, this becomes a significant error and any agreement between the model and absolute FCP rates is probably fortuitous for this reason alone. The model is claimed [211] to have no adjustable parameters, but the microstructural parameter, ρ, can easily be interpreted as a "fitting parameter" to force agreement. The MDZ is similar, if not identical, to the process zone used in the previous two models discussed.

In models based on LCF considerations the Paris Law exponent is related to the Coffin-Manson exponent through the equation

$$m = 2/\beta \tag{25}$$

Thus the validity of these models for various alloy systems is easily checked. This approach is intermediate in its degree of fundamentalism between the more macroscopic models and the dislocation-based models, and as such is a phenomenological rather than a mechanistic representation [202]. The correlation of the fatigue damage process in an LCF

43

test and a FCP test depends to a high degree on factors such as temperature, Stacking Fault Energy (SFE), strain rate, and purity among others. The models are limited to the regime in which crack growth is discontinuous and not controlled by CTOD processes. In addition, initiation, not failure, must be used for the Coffin-Manson analysis since there is considerable crack propagation in a typical LCF failure. The usefulness of these models is not as a method of predicting to a high degree of precision FCP properties, but as a method to evaluate the importance of factors that affect FCP.

3.0 Experimental

3.1 Variables

3.1.1 Material

Two compositions based on aluminum P/M alloy CT91 differing only in Co content were selected for study. The material used in this investigation was purchased from the Aluminum Company of America. The compositions are shown in Table 6. CT91 is now designated 7091 by the Aluminum Association; because of improvements in powder production and collection since these alloys were prepared, the designation CT91 is now used to designate alloys made before improvements were completed.

Details of powder production and billet compaction are given in Reference 4. A schematic of the powder process is shown in Figure 5. The powders were produced using air atomization. Powder size and distribution data provided by the supplier are given in Table 7. Each powder lot was cold isostatically pressed at 207 MPa (30 ksi) in a wet bag system to form 66 Kg (145 lb.) cylindrical compacts 18.7 cm (7.4 in.) in diameter by 109.2 cm (43 in.) long. Each compact was canned and preheated to 521°C (970°F) under a dynamic vacuum level of 10 μm of Hg. The evacuation line was then sealed and the compact was consolidated by hot pressing in a closed end compaction cylinder (i.e., an

44

extrusion press using a blank die) at a nominal axial pressure of 621 MPa (90 ksi) during a one minute dwell. The hot pressed billets, essentially 100% dense, were scalped to 18.4 cm (7.25 in.) diameter x 26 inches for shipping, as shown in Figure 14.

3.1.2 Material Processing

Two additional program variables included forging deformation and stress relief during heat treatment.

3.1.2.1 Forging. In preparation for forging, the as-received billets were cut into small cylindrical sections approximately 94 mm (3.7 in.) high and identified as shown in Figure 14. From each of these sections five forging blanks were rough cut and machined into the configuration shown in Figure 15. These blanks were forged in the AFWAL Materials Laboratory's Experimental Processing Laboratory on a Lombard 500 ton hydraulic forging press at 371°C (700°F) in the channel dies shown in Figure 16. An upper die plate that allowed the final forging height to be 0.6 inches was used. In this way the final true forging strain of 0.5 or 1.0 (based on height reduction) was controlled by the original height of the forging blank.

These true forging strains represent deformation based on upsets of 38% and 64% respectively. The approximate final product configuration is illustrated in Figure 17. The forgings were cut in half before heat treatment. Channel die forging was selected to provide uniform deformation (and thus microstructure) across the forging. In many hand forgings the variability in strain from point to point would cause variations in properties [105]. To demonstrate the uniformity, tensile and toughness tests were conducted across the width and length of several forgings.

dispersoid is homogeneously distributed and has the effect of reducing the grain size slightly. Although generally referred to as Co_2Al_9, the dispersoid is more correctly $(Co,Fe)_2Al_9$ because Fe has a high affinity to substitute for Co in the crystal. Lawley and Koczak [49] have studied the effect of Co variation on microstructure. They report that percent recrystallization increases with Co content; this implies that the 0.4% Co variant would have a slightly more recrystallized structure. They also report that there were no systematic differences detected in grain size or grain morphology as a result of Co content, but that subgrain size decreased with increasing cobalt. Additional discussion of the cobalt containing dispersoid is found in Section 4.1.2.

Comparison of Figures 30(a), (c), (e) and (g) (not stress relieved) with Figures 30(b), (d), (f) and (h) (stress relieved) clearly indicates there is no effect of stress relief on the optical microstructure.

Other microstructural features normally found in high strength aluminum alloys such as constituent particles (Al_7Cu_2Fe, Mg_2Si) and large soluble precipitates $(MgZn_2)$, are not resolvable on the optical scale.

4.1.2 Transmission Electron Microscopy

4.1.2.1 VhP Billet

Figure 32 shows the structures of Co-free and Co-containing CT91 respectively. The variations in powder particle size are seen in both. The areas between particles contain a high concentration of oxides which are broken up but not displaced significantly from their original locations [36]. Also seen is evidence of fine constituents and coarse soluble precipitates. Figure 33 shows the distribution of the Co_2Al_9 dispersoid, which outlines the dendrites that have since been eliminated by heating and working.

59

the forgings is smaller than of the VHP billets. The grains are generally equiaxed and their size depends on the original powder particle size [36] and forging reduction. The grains range in size from 10 μm in 38% forgings and 7 μm in 64% forgings in large powder particles down to as small as a fraction of a μm in small powder particles. The smallest grains are not easily observed in optical micrographs because of heavy etching due to the high density of oxides associated with small powder particles on which they are found. TEM observation is required to adequately characterize the structure. The grain structure is about an order of magnitude smaller than that found in conventionally processed I/M forgings [105, 229] and is confined within the original powder particles. The nature of oxide breakup and distribution in P/M forgings (described below) develops what has been described as a bamboo structure [36] (see Figure 31). The grain size is influenced by all the second phase particles including Co_2Al_9 dispersoids, oxides and coarse soluble precipitates (η). Paris and Hafeez [6] report that the oxide content had a stronger influence on grain size than dispersoids because it is finer and more inhomogeneous. Kim et. al., [36] also report a strong influence of oxide distribution on grain structure. The final grain structure depends both on dynamic recovery and recrystallization processes in hot working and static recovery and recrystallization processes during solution heat treatment (SHT) [6]. Static processes depend on strain localization during hot working and the source of the strain is deformation near coarse, hard particles. In CT91, the Co_2Al_9 and soluble $MgZn_2$ (η) phases are coarsened during billet compaction and reheating during fabrication [6]. The optimum size for effectiveness as nuclei for recrystallization is approximately 1 μm - larger than most particles available in CT91 [6]. This is consistent with reports that microstructures in CT91 are essentially unrecrystallized [36, 49, 174, 228, 230, 231].

Figures 30c, d, g, and h show the microstructures of the Co-containing variants. On the optical scale the cobalt containing

58

little deformation [36, 49]. The same observations can be made for the 0.4% Co variant shown in Figure 29(b). In addition evidence of the fine Co_2Al_9 dispersion can be seen.

There have been few studies of the microstructure of VHP billets reported, but those available [36, 49, 105, 108] are in general agreement with the above observations. Antes [105] suggests that darkly etching areas are denser with surface oxides. This is equivalent to saying that dark etching areas contain small powder particles because the oxide concentration can be related to surface area [36]. Walker and Starke [108] have measured the average grain volume of powder particles before and after compaction as 1640 μm^3 and 158 μm^3 respectively, indicating a grain size reduction due to the VHP process. The usefulness of assigning a single calculated parameter to such a complex microstructure is questionable.

4.1.1.3 Forgings

Figures 30(a)-30(h) show the optical microstructures for the forgings in all eight conditions studied. Comparing Figure 30 with Figure 29, the forging deformation is clearly evident, but the individual powder particles are still observable, especially in the 34% forgings (Figures 30(a)-(d)). The powder particles are elongated in the direction of material flow (L), the amount of elongation proportional to the forging reduction. It has been reported that increasing forging deformation improves particle bonding [7, 36, 227] and improves toughness and ductility [7].

No attempt to calculate an average grain size for the forgings was made for two reasons: 1) a single number does not adequately describe the wide variation in grain sizes observed and 2) it is difficult to distinguish between grains and subgrains at the optical scale [36, 230]. The term grain is used throughout this discussion without differentiating between high and low angle boundaries. The grain size of

4.0 Results and Discussion

4.1 Microstructure

4.1.1 Optical Characterization

4.1.1.1 Etching

It was apparent from initial attempts to optically characterize the microstructure of P/M aluminum alloys that Keller's etchant, generally used for aluminum alloys [225], was not adequate to completely disclose fine structure [226]. A study [226] of several etchants including Keller's, boiling nitric, phosphoric, and Graff-Sargent [224] was undertaken. The results clearly indicated that the Graff-Sargent etchant was ideal to reveal the fine grain structure of 7000-series P/M alloys. Figure 28 shows a comparison of similar structures etched with Keller's and Graff-Sargent. Figure 28(a) and 28(b) indicate the Keller's etchant reveals only very chemically active boundaries such as previous powder particle boundaries. As shown in the SEM photomicrograph (Figure 28), very little attack at grain boundaries and subgrain boundaries is present. The Graff-Sargent etchant appears to attack all boundaries uniformly and thus reveals the fine grain/ subgrain structure of the P/M alloys. Because of this, the Graff-Sargent etchant was used throughout this study.

4.1.1.2 Vacuum Hot Pressed (VHP) Billet

Figure 29 shows the optical microstructure of the as-received VHP billet. Figure 29(a) is the Co-free variant. The original powder particles are easily identifiable; they show little deformation with perhaps a slight elongation. The size distribution of the powder particles determines the inhomogeneity of the billet microstructure [108]. Grains are visible in the large powder particles. These grains are reasonably equiaxed and relatively large (up to 20 μm) which suggests

56

at $A_\epsilon < 1.0$ allows preservation of the fracture surface for later examination. Tests were run on all conditions at four plastic strain ranges, nominally $\Delta\epsilon_p$ = 0.6%, 0.1%, 0.05% and 0.025%. These values were chosen based on a Coffin-Mason analysis of LCF data available for other Al alloys in order to space cycles to initiation equally between 50 and 5000 cycles on a log scale. During the test the plastic strain range was maintained constant by manual adjustment of the span control. The test was allowed to continue until the specimen failed (i.e., separated into two parts).

2. A_ϵ = 0.95, Plastic Strain Control, Test Stopped At Initiation

A series of tests were run as above except that the test was discontinued when a load drop was observed on the strip chart. The specimens were removed for SEM examination of gage surface cracks. Tests were run at nominal plastic strain ranges of 0.6% and 0.025% on the nonstress relieved conditions only. This was done to conserve material. Stress relief will have the least effect of the variables under consideration in an LCF test because the effect is negated after the first few cycles of the test.

3. A_ϵ = ∞, Total Strain Control

A series of tests were run on the stress relieved conditions using the MTS controller to maintain a completely reversed constant total strain range, nominally ±1.4%, ±1.0%, ±0.95%, ±0.7% and ±0.6%. These tests were run to document any mean stress effect in these alloys.

55

$10^3 sec^{-1}$. Load and strain were plotted on strip chart recorders as a function of time. Periodically, hysteresis loops were recorded using an X-Y recorder. For all tests initiation was defined as the first measurable load drop on the strip chart.

All the LCF specimens were polished prior to testing using the following procedures:

1. Rough polish by hand through 600 grit SiC papers. All scratches in the longitudinal direction - i.e., no circumferential scratches.

2. Electropolish in a solution of 50 parts methanol, 30 parts ethylene glycol monobutylether (butyl cellusolve) and 4 parts $HClO_4$ (60%) maintained between 0 and 10°C. Best results are obtained by setting voltage at 30-35V (amperage = 2-2.5 amps) and stirring solution. Except for the reduced gage section the entire specimen is painted with a lacquer. The sample is rotated during electropolishing to insure uniform metal removal. The typical current density is 17 amps/cm^2 (110 amps/$in.^2$). Typical polishing time is one minute.

3. Samples are checked optically at 10× magnification. If radial scratches are present, the specimen is repolished. Good samples are stored in a dessicator.

Three types of LCF tests were run as follows:

1. A_ϵ = 0.95, Plastic Strain Control

This represents the majority of tests. This condition most close-ly correlates to the conditions ahead of the crack tip in a fatigue crack growth situation. Because the purpose of these tests was to try to understand fundamental material behavior and to present data in terms of $\Delta\epsilon_p$, it follows that $\Delta\epsilon_p$ should be held as nearly constant as possible to minimize the effect of interactions. In addition, testing

shows that ΔK is relatively insensitive to crack length changes over a wide range of crack length.

The samples were tested on a closed-loop MTS machine at 20 Hz in lab air. The specimens were loaded by positioning the ring between two parallel plates attached to the ram and the platten. A small flat was machined on the outside of the ring to allow proper positioning of the notch on an imaginary line perpendicular to the face of the ram. Pre-cracking was undertaken at the lowest ΔK possible, always starting at the ΔK at which the test was to be run. Initial difficulty in pre-cracking was observed but this was alleviated in most cases by rema-chining the notch tip using an electrodischarge machining (EDM) pro-cess. Before testing the surface of each ring specimen was polished to facilitate measurement of the crack length.

3.3.4 Low Cycle Fatigue (LCF)

All LCF testing was conducted on a closed-loop MTS machine using the specimen shown in Figure 25. This sample has a cylindrical gage section (as opposed to hour-glass) to maximize the volume of material undergoing deformation, allowing the microstructure to determine the site of initiation.

The test set-up is shown in Figures 26 and 27. The specimens were threaded into an extension bar connected to the load cell. A lock washer and lock nut were used to remove the misfit in the threads. A Wood's Metal pot attached to the ram was used to insure good alignment thus avoiding bending stresses. A double knife-edge longitudinal MTS extensometer was used to measure strain. The extensometer was placed on two strips of masking tape to avoid notching the specimen and was carefully attached by two springs. A plastic bag was placed around the MTS frame to allow the test to be run in dry Argon (dewpoint = - 62°C - 80°F) or approximately 12 ppm H_2O [223]). All tests were run under strain control using a triangular wave form at a strain rate of

53

the failure load could reasonably be assumed to be P_{max} it was possible to measure a_f and calculate a K_Q. Although not a valid test per ASTM Standard E399, it was deemed acceptable for the purposes of these tests, i.e., to confirm or deny material variability.

As a result, a final set of specimens were tested using only the precracking set-up. Samples were cycled between 22.7 Kg (50 lbs) and 227 Kg (500 lbs) until failure. a_f was measured and 227 Kg (500 lbs) was assumed to be the failure load. K_Q was calculated using the equations of ASTM Standard E399-78.

3.3.3 Fatigue Crack Propagation (FCP)

Fatigue crack propagation tests were run for each condition. The purpose of this testing was two-fold: firstly to characterize the crack growth rates in the Paris region, and secondly to provide material deformed by a propagating crack under controlled conditions from which to extract thin foils for TEM examination. In a standard crack growth test the stress intensity range, ΔK, changes with increasing crack length [221]:

$$\Delta K = \Delta\sigma\sqrt{\pi a}\ F\left(\frac{a}{w}\right)$$

(26)

Where $\Delta\sigma$ = stress range

   a = crack length

   $F\left(\frac{a}{w}\right)$ = a function of crack length and specimen geometry

Because of the desirability to maximize the volume of material available for SEM and TEM examination, a constant ΔK test was run using the specimen shown in Figure 24. The ring specimen provides a convenient means for closely approximating constant stress intensity range test conditions when cycled between fixed load limits [222]. Figure 24 also

52

b) The center slice of the remaining forgings was used to insure no significant variations occurred during the forging operation and heat treatments that would significantly change the sample metallurgically as evidenced by unacceptable tensile properties. All tensile tests were run with an extensometer in place for approximately the first 1% of total strain, after which it was removed and elongation was measured using crosshead displacement.

3.3.2 Toughness Tests

To add confidence to the degree of variability measured using tensile tests fracture toughness tests were carried out in accordance with ASTM Standard E399-78 using precracked Charpy specimens (Figure 23) in 3-point bend. Specimen Layout is shown in Figure 22.

In the standard test, samples are precracked by fatigue loading to develop a sharp crack. Precracking was started at $0.4K_{IC} \leq K < 0.9 K_{IC}$ at a frequency of 30Hz. For the toughness test itself, a crosshead rate of 1.27 cm/min. (0.5 in./min.) and a ram travel of 3.8 mm (0.15 in.) were selected so as to break the specimen but leave the specimen halves connected and preserve the fracture surfaces. Precracking and testing was performed on a closed-loop electroservohydraulic MTS machine. Load and displacement data were accurately acquired by a Datronics LVDT and a Hewlett-Packard X-Y recorder.

Difficulty in obtaining a straight precrack was encountered from the outset. Typical options (check alignment, razorblade notch tip, shim uncracked side, etc.) were exercised with little success. Residual stresses were suspected to be the problem and selected samples were submitted for measurement of residual stresses.

It was noted that samples which failed during precracking always had an acceptably straight crack front. It was also noted that since

51

3) Measure the angular distance of the diffracted spot with respect to the tilt axis and note the quadrant in which the spot appears.

4) Using tracing paper over a Wulff net, plot the two-beam spot as indicated in Figure 19.

5) Continue this process at both positive and negative tilts until several spots have been plotted.

6) A complete stereographic projection can be deduced by measuring angles between the plotted points and using the angular relationships on the fcc standard projections, Figure 20.

7) Using this projection, any arbitrary plane can be brought into a 2-beam condition by rotating (and/or tilting) the appropriate number of degrees to bring the plotted spot to the edge of the net. If two spots are on the edge simultaneously a multi-beam condition will exist; multibeam conditions are usually avoided since they result in all dislocations being visible.

3.3 Mechanical Behavior Evaluation

The specimen layout for all tests is shown in Figure 21.

3.3.1 Tensile Tests

These tests were carried out in accordance wtih ASTM Standard E8-72 using the specimen design shown in Figure 22. Two sets of tensile tests were run as follows:

a) Three forgings (S1, S3, and S4) were sectioned entirely for tensile tests. The purpose of these tests was to demonstrate that the tensile properties of the material did not vary significantly across the forging and further to demonstrate that tensile properties of different forgings of the same composition did not vary significantly.

50

6. Use acetone to remove the lacquer and rinse the foil in pure ethanol. Store the foil in vacuum dessicator until examination in the TEM.

3.2.3.2 In-Situ Grain Orientation

The following procedure allows for precise in situ crystallographic orientations of the grains of interest in thin foils.

a. Tilt Axis Determination - A grid is scribed on the phosphorescent screen of the microscope as in Figure 18. This enables the operator to determine the angular relationship of the diffraction spots to the tilt axis of the specimen holder. This grid is positioned precisely with respect to the tilt axis. The tilt axis position is determined by taking a series of electron micrographs at progressively increasing tilt angles. By determining the direction of motion of Kikuchi line intersections the tilt axis is established as a line perpendicular to this motion.

Scribe marks are placed at 10° intervals on the screen away from the tilt axis. Also scribed on the screen are two semi-circles which are used as references to identify planes of various d-spacings.

b. Crystallographic Orientations - A grain (crystal) of interest is oriented as follows:

1) Place tilt axis at 0° tilt.
2) Tilt on the primary axis until a 2-beam diffraction condition arises (although not necessary, the active spots can be easily identified by comparing spot locations relative to the semi-circles with previously examined easily recognizable low index diffraction patterns).

3.2.3.1 Sample Preparation

The following procedure was used to prepare thin foils for examination of LCF samples:

1. A 0.25 mm (0.01 in.) thick wafer is cut from the gage section using a low deformation diamond saw cut on both sides. A slow feed rate and ample coolant prevented specimen heating.
2. Thin to 0.127 mm (0.005 in.) by gently grinding both sides on 300 grit SiC paper. Rinse clean in acetone and gently dry.
3. Using a specially designed punch, make two or three punchings 3 mm (0.12 in.) diameter.
4. Electro-chemically thin using a 20% HNO_3 (conc) and 80% Methanol bath at -40°C, 25 volts and 50 milliamps.
5. After perforation, rinse in pure ethanol and store in vacuum dessicator until examination in TEM.

The following procedure was used to prepare thin foils near the fracture surface of FCP samples:

1. Cut a thin slice, 0.25 mm (0.01 in.), just below the fracture surface.
2. Grind the fracture surface until just before evidence of the fracture is gone.
3. Grind the opposite side until thin enough to punch a 3mm (0.12 in.) disk.
4. Electropolish in a jet polisher just long enough (approximately 1 min.) to remove grinding layer.
5. Mask the fracture side with lacquer and continue electropolishing on the opposite side only until perforation occurs.

48

identities of several blanks were lost. These blanks were numbered consecutively and checked for cobalt content by electron microprobe. These samples maintained this numerical identification throughout and cannot be traced to the original billet or blank location.

3.2 Metallographic and Fractographic Characterization

3.2.1 Optical Microscopy

Standard Metallographic techniques were used to polish and etch samples from each of the eight conditions. It was determined that Keller's etchant, the etchant used almost universally for 7000-series aluminum alloys, did not give a satisfactory result with the fine-grained Al P/M alloys. The Graff-Sargent etchant [224] was found to give the best results. Similar sections of CT-91 forgings were polished and subsequently etched in each etchant. These were examined both optically and by SEM.

3.2.2 Scanning Electron Microscopy (SEM)

The SEM was used to examine the as-fractured surface of failed LCF and FCP specimens. In addition, the surfaces of initiated but unfailed LCF samples were documented. Samples were stored in a vacuum-dessicator until examination.

3.2.3 Transmission Electron Microscopy (TEM)

TEM was used to characterize the fine microstructural features of the P/M alloys and to determine the active deformation mechanisms in cyclic tests.

47

3.1.2.2 Heat Treatment

Solution heat treatment was carried out in an air circulating furnace at 493°C (920°F) for 2 hours. One half of each forging was quenched into a Blue-M quench tank containing water at 18°C (64°F) and placed directly into a freezer held at -18°C (0°F) to delay room temperature aging. The second half of each forging was stress relieved after quenching by reforging at room temperature in the same dies with a die plate thick enough to allow 1-5% additional permanent deformation. The stress relieved product was immediately placed in a freezer. Before final heat treatment the forgings were aged at room temperature for five days. They were than placed in a Blue-M air circulating furnace and aged for 24 hours at 121°C (250°F). A second step age of 4 hours at 163°C (325°F) was immediately applied and the forgings were allowed to air cool. The processing and heat treatment procedures are summarized in Table 8.

3.1.3 Nomenclature

Two levels each of forging strain (ϵ = 0.5,1.0), Co content (wt% Co = 0, 0.4) and stress relief (no, yes) are the major variables in this program for a total of eight conditions. It is convenient to represent the condition of any particular sample by a three digit number using a "zero" to represent the low value and a "one" to represent the high value of each variable. The conditions are listed in Table 9 for the convenience of the reader.

Each sample was identified by the original forging blank from which it was cut. For example, LCF specimen D5-2 came from the fifth forging blank of slice D of the original billet (see Figures 14, 15, 17). It was the second specimen tested from D5. An R, such as D5R-2, indicates that the sample came from the half of the forging that was stress relieved. Thus each sample can be traced to its original billet location. Unfortunately, during machining of the forging blanks the

4.1.2.2 Forgings

The fine structure of P/M forgings not easily resolvable in the optical scale can be easily studied using TEM. Three primary areas will be discussed: fine powder particles and grains; intermetallic dispersoids, precipitates and constituents; and oxides.

a) Fine powder particles and grains. Figures 33-36 illustrate the type of fine microstructures found in the forgings in this study. As discussed earlier, the small grains are difficult to resolve optically because of their association with the surface oxides which etch heavily. Since the grain size depends not only on the amount of forging reduction but also on the original powder particle size [36], a combination of TEM and optical microscopy is required to adequately characterize the grain structure of CT91 forgings. Figure 33 shows the variation in powder particle and grain size possible in a relatively small volume of material. Although this is shown in only two cases, it is characteristic of all conditions examined. The relationship between powder particle size and grain size is illustrated by Figure 34. Preferential etching is seen; this due to oxides at prior particle boundaries (PPBs). Although this may be considered an artifact, it is useful in that it accurately differentiates between PPBs and other grain/subgrain boundaries. Kuo and Stacke [174] have described all PPBs as high angle boundaries. The low angle boundaries visible in the large grain are subgrain boundaries; this was determined by comparing the crystallographic orientation of each subgrain and determining there was only minimal orientation change. Figure 35 is a typical microstructure in the ST plane for 0% cobalt forgings. The original powder particles are still visible indicating that even the higher forging deformation examined (64%) was not sufficient to break up the VHP structure. This is even more evident in Figure 36 where an almost circular powder particle is seen, indicating very little deformation in this particle.

60

b) Intermetallic dispersoids, precipitates and constituents. Figure 37 (a)-(f) illustrate the types of dispersoids, precipitates and constituents found in CT91 forgings. Figure 37(a) contains most of the elements of the typical microstructure. This is an area of grain/subgrain size of 1-2 μm. Inhomogeneously nucleated $\eta(MgZn_2)$ line the grain boundaries. A large Co_2Al_9 (∿ 0.5 μm) pins the grain boundary, and a second one lies on the subgrain boundary. A constituent (∿ 0.75 μm) probably Mg_2Si, is also present. The small precipitates that give the grains a mottled appearance are the semi-coherent hardening precipitate $\eta'(MgZn_2)$. The photomicrographs in Figure 38 illustrate the presence of constituents; these are only occasionally seen. The Al_7Cu_2Fe is not seen in the Co-containing alloy. When Co is present, Fe is tied up to form $(Co,Fe)_2Al_9$ [6, 174]. Walker and Starke report observing a uniform distribution of Co_2Al_9 dispersoids in CT91 extrusions [230]. Clearly from Figure 39 this is not the case for CT91 uniaxial forgings. Figure 39(a) shows the Co_2Al_9 dispersoids outlining what were dendrites in the original powder that have been eliminated by processing. Figure 10(b) is an adjacent area of the same thin foil showing almost no Co_2Al_9 present. The dispersoids present in Figure 39 are very small (∿ 0.1 μm). The presence of Co_2Al_9 in powder depends on the cooling rate and therefore the powder particle size [230]. They continue to precipitate during compaction and fabrication. Since the smaller powder particles experience faster cooling rates, the early precipitation is suppressed and finer dispersoids result. The fact that no grain growth is evident in these areas indicates the heavy oxides associated with fine powder particles clearly dominate the dispersoids in controlling structure in these areas. The Co_2Al_9 dispersoids are essentially spherical and range in size from 0.005 to 0.5 μm in diameter. The dispersoids are not deformed or fractured during fabrication and interact with dislocations (Figure 40) and grain boundaries (Figure 37). Although no measurements were made in this study, Kuo and Starke calculated the theoretical volume percent of Co_2Al_9 as 1.16% in CT91 assuming 0.2% solubility at 930°K [174]. This agrees very well with measurements made by Paris and Hafeez [6] who

61

report 1.18 vol.% Co_2Al_9 in a similar alloy containing 0.4% Co; a 0% Co variant of the same alloy contained 0.12 vol.% Al_7Cu_2Fe.

c) Oxides. Kim et. al., [36] have recently completed the first definitive study of surface oxide breakup and distribution in P/M aluminum alloys. Their key findings include:

1. Hot pressing is the major breakup stage of processing. It crumbles the 50Å thick surface oxide film into Al_2O_3 chips and Al_2O_3-MgO clusters and separate MgO crystallites, all of which are present in the powder particle boundaries (PPBs) as dense arrays.

2. Subsequent processing redistributes the oxide arrays into aligned stringers.

3. A simple uniaxial forging results in continuous stringers always associated with PPBs and grain boundaries. Even after forging 64% the stringers are continuous and possibly cause an easy crack path.

4. Oxide stringers strongly pin grain boundaries prohibiting lateral growth. Increasing forging reduction reduces inter-oxide stringer spacing and accordingly grain size. At least up to forging upsets of 64%, oxide stringers are always associated with grain boundaries and grain size is non-uniform (1-10 μm).

Based on a weight % O_2 of 0.33%, the oxide volume fraction has been calculated to be approximately 0.5% for an average particle diameter of 13-15 μm [6]. Figures 41-43 show the morphology of the oxides observed in this study. These observations are typical for all conditions tested. Figure 41(a)-(c) shows the nature of the surface oxide in areas of small powder particles. The broken oxide film is distributed near the particle surfaces and forms a continuous array. The

62

arrays may be up to 0.5 μm thick [Figure 41(b)]. Figure 42 shows isolated oxide arrays with oxide "chips" up to .025 μm. Figure 43 shows a thick array (0.5 μm thick). It is not difficult to envision this region either participating in the initiation or propagation of a fatigue crack. Note the large soluble precipitates that nucleated on the oxide (marked η). The Co_2Al_9 dispersoids present are approximately 0.2 μm for comparison of sizes. Figures 43 and 44 show the oxide pinning grain boundaries. The curvature of the boundaries of the central grain(s) in Figure 44(a) would indicate this is a powder particle that has undergone very little deformation. Figure 45 shows particularly dense oxide arrays up to 1.5 μm across. This site would be especially susceptible to fatigue initiation because of the weakness of the powder particle bonding here [232].

A large volume fraction of closely space GP zones and η' precipitates promote the high strength attained in 7000-series alloys but also promote localized planar slip [84]. The microstructure also tends to minimize crack nucleation at constituents (through refinement) and produce homogeneous deformation during fatigue [233]. The optical and TEM micrographs presented show a very small constituent content and a relatively fine grain size. The fine grain size promotes homogeneous deformation by limiting slip band development; slip bands are blocked by grain boundaries, thus their extent is limited, making them unlikely sites for crack initiation [233]. In addition the Co_2Al_9 dispersoids may be beneficial in homogenizing deformation by acting as sites for dislocation generation [233]. The same would be true for oxides if they were uniformly distributed, as in the case of extrusion; but the nonuniform distribution of oxides in uniaxial forgings, forming arrays in some cases thicker than 1 μm, is likely to assist in crack initiation and propagation [36].

4.2 Monotonic Properties

4.2.1 Tensile Properties

Forgings S1, S3 and S4 were completely sectioned for tensile tests to demonstrate the variation in tensile properties to be expected due to variations inherent in the forging process. These variations include differences in material flow, uncontrollable slight temperature variations and quenching conditions. Table 10 shows the average tensile properties for the three forgings in stress relieved (R) and unstress relieved conditions. Note that less than 7 MPa difference was measured between stress relieved and unstress relieved forgings in the longitudinal direction for any one forging. Slightly more variation is seen in the transverse direction (ranging from 9 to 20 MPa) although the larger variations were measured with no replication. The range of longitudinal strength measured for all three forgings was 542 to 566 MPa (78.5 to 82.0 ksi) for yield strength and 584 to 611 MPa (84.6 to 88.6 ksi) for ultimate tensile strength. These values are slightly higher than most values reported for similar materials shown in Table 11.

These data were also used to evaluate the effect of position in the forging on tensile properties. This was done in order to eliminate specimens from further consideration if large property variations were noted as a function of position. Figure 46 is a plot of yield and ultimate tensile strength vs. location. As is seen, there appears to be no significant effect of location on longitudinal or transverse strength and all the forging was used in subsequent tests.

The center slice of the remaining forgings was tested to insure no significant variations occured during the forging operation and heat treatments that would significantly change the sample metallurgically as evidenced by unacceptable tensile properties. Table 12 shows the results of these tests for all eight conditions. Figures 47-49 show

64

the effect of the major program variables on strength. The largest effect results from differences in Co content (Fig. 47), where 0.5% Co increases both yield and ultimate strengths by about 28 MPa. Figure 48 shows that the stress relief operation reduces yield and ultimate strength slightly while Fig. 49 shows no measurable effect of forging reduction between 38 and 64%. Lawley and Koczak [49] studied the aging response of CT91 using differential scanning calorimetry (DSC) and report that the presence of Co increases the amount of precipitation of GPZ. The 0.4% Co alloy contains a larger amount of hardening precipitates compared to the Co-free [234]. The high strength of all the alloys tested is due to a large volume fraction of closely spaced GP zones and η' [233] although in the overaged condition studied the strengthening precipitate is primarily η' (90%) [234]. It has been reported [235] that plastic deformation by compression, such as experienced during the stress relief operation, decreases tensile yield strength and increases compressive yield strength. Although small grain/subgrain variations were noted earlier, this is not expected to have an effect on strength [49, 108, 119, 174, 236, 237]. The yield strength shows only a small dependence on grain size in the range studied. Only when the grain size approaches the magnitude of dispersoid spacing will the grain boundary play a more significant role in strengthening [49]. Walker [108] suggests that for P/M alloys, variations in grain size and shape and in oxide distribution is expected to have little effect on strength.

4.2.2 Fracture Toughness

Toughness testing was carried out to add confidence to the assumption that variations in properties due to factors other than the main variables were minimal. The precracked Charpy specimen was chosen because of material lmitations. Others [241, 245] have reported success in using this type of specimen for high strength alloys. Difficulty in obtaining a straight precrack was encountered as shown in Figure 50. Occasionally a sample failed during precracking and, as

65

shown in Figure 51, these samples would exhibit a straight crack front, indicating that the precrack evened up before failure. By using the crack length at failure and the maximum load used for precracking a non-valid K_Q was calculated and found to be in the range of expected values.

To determine the applicability of using this technique to evaluate the variation described above, two forgings, DD3R and 43R, were machined into specimens as shown in Figure 52. These specimens were cycled between 345 and 3450 MPa (50 and 500 lbs). By precracking to failure, the measured crack length at failure and P_{max} were used to calculate the K_Q's shown in Table 13. The values are reasonably consistent, but are higher than expected. This is due to the fact that the crack tip develops a plastic zone during precracking that inhibits catastrophic crack extension. Thus additional energy is required to force the crack through the plastic zone and measured toughness values are artificially high. Since absolute values of fracture toughness were not the objective of toughness testing, this is not considered a major drawback.

Two samples in each condition were tested using the described technique. Measured fracture toughness (K_Q) values are shown in Table 14. The number of data points is not adequate to statistically analyze the effects of main program variables but some observations can be made. Examining Table 14, it can be seen that there is less than 10% Difference between replicates for all but two conditions. The largest amount of scatter is found in the low strain forgings. Addition of Co may have a slight negative effect, while stress relief and increased forging strain appear to have a slight positive effect. It must be emphasized that these are trends and that the effects are only on the order of 1 to 2 MPa$\sqrt{m}$. A similar effect of dispersoids on fracture toughness was reported by other investigators [4, 6]. As discussed in Section 2.3.2, fracture occurs by the link up of dimples that form at

66

dispersoid particles. Adding 0.4% Co increases the volume fraction of dispersoids from 0.12% to 1.18% [6] and the size and spacing of the dimples is smaller; therefore a reduction in toughness is expected. Otto [4] reports that the effect of hot work sequence is minimal in going from single axis to triple axis upset forgings. There is not a simple correspondence of forgings in Otto's work to those in this study, but the three axis forging can be assumed to be more heavily worked than the single axis; thus, for small changes in forging strain no significant changes in toughness is expected. Antes [105] does report increasing toughness with increasing forging strain, but bases this on the observation that the Paris exponent (calculated from FCP testing) decreases.

The largest effect observed in this study is an orientation effect. The L-T values are on the order of 50% higher than the T-L which is consistent with the data in Table 11. This effect is typical of all high strength aluminum alloys and is attributed to the ease of crack propagation in the direction of grain elongation (L) contrasted with the numerous grain boundary intersections when the crack grows across the elongated grains (T) [4, 105].

The difficulty in obtaining a straight precrack in Al P/M is not unique to this study [246]. The most likely explanation for this is residual surface stresses acting to clamp the crack closed at the surface. If the residual stresses are not balanced then the crack may grow faster on one side of the specimen as pictured in Figure 50. To confirm the presence of surface stresses, samples were supplied to AFWAL/FIBWE and to G. Chanani at Northrop Aircraft for measurement of residual stresses using Fastress and Rigaku [249] X-ray techniques respectively. The results of these measurements are shown in Table 15. The Fastress unit measured significant compressive surfaces stresses, but showed no imbalance. The magnitude of the stresses may be misleading due to improper equipment calibration [247] but the presence of compressive stresses is confirmed. The Rigaku unit measured much more

67

modest stresses and also discloses the imbalance that can result in uneven cracking. Rigaku is the newer and more sophisticated unit and the results of Rigaku measurements are more reliable [248].

The origin of these stresses can be mechanical or thermal [116]. The mechanical residual stresses are due to machining and other processes that deform the material nonuniformly [116]. Thermally induced residual stresses are due to inhomogeneous cooling during quenching. This produces compressive residual stresses at the surface and tensile residual stresses at the interior [5, 116, 250, 251].

4.3 Fatigue Crack Propagation (FCP)

The L-T FCP data taken from ring specimens are listed in Table 16. Approximately half the tests were considered invalid as indicated in Table 16. The principal reasons for disregarding these data included formation of large shear lips (Figure 53), growth out of plane (Figure 54,), and eccentric crack front (Figure 55). The formation of shear lips such as those pictured in Figure 53 is typical of samples tested under high loads [252]. The crack growth rates measured in these samples were in most cases within the range of acceptable data and a careful review of testing procedures failed to produce any questionable practices. No explanation for the shear lip formation is available and the data was eliminated from the analysis. Cracks growing out of plane, as in Figure 54, are commonly reported for the high strength P/M alloys [5, 17]. Eccentric or uneven crack fronts, such as those pictured in Figure 55, were also observed in Charpy specimens used for fracture toughness testing. The ring specimens were only 0.64 cm (0.25 in.) thick and were machined from the center of the forging thickness. This combination should have reduced the effect of residual quenching stresses if they existed. There is evidence that the precracking difficulties experienced with the rings are related to surface conditions. The principal difficulty experienced was starting a precrack; this was overcome by electrodischarge machining the ring notches. At the tip of

68

the EDM notch is a molten zone that is free of mechanical deformation such as might be found at the surface due to conventional machining. This region is seen in Figure 56. In addition it was noted that when a specimen was polished on one side only there was a tendency for the crack to grow faster on that side, indicating the offending deformed layer was removed. This layer was not visible metallographically. Eccentric cracking has been reported by others [5, 253]. Sanders, et. al., [5] attributed this behavior to residual stresses and reported reducing specimen thickness to 0.64 cm (0.25 in.) was helpful in obtaining a straight crack front.

Table 17 lists the acceptable data from the ring tests and Figures 57-59 are plots of the data in terms of the major program variables. Table 18 lists the Paris Law parameters calculated assuming all the data falls within the Paris Law Region. The data indicates almost no effect of forging deformation in the range studied on fatigue crack growth rate. A small effect of Co content is noted, but the relatively few data points considered makes this questionable.

Surprisingly, there is an obvious effect of stress relief. It can be clearly seen in Figure 59 that the stress relieved samples have a slower FCP rate than the unstress relieved. This is surprising because the sample thickness is only 0.64 cm (0.25 in.) and no residual stress effect was anticipated. No observable microstructural changes can be attributed to stress relief. Finally, in previous studies of these alloys, unstress-relieved samples exhibited slower crack growth rates due to residual stresses clamping the crack tip closed, producing a $\Delta K_{eff} < K_{app}$ [4, 5, 6].

In an attempt to verify the limited data obtained from the non-standard ring specimen, four compact tension specimens were machined from forgings in the four stress relieved conditions. These T-L specimens were run in accordance with ASTM Standard E647. The crack growth rates obtained from these specimens is plotted in Figures 60-63 with

69

the L-T ring data superimposed. Paris Law constants were calculated from the range of ΔK = 5.5 to 11 MPa$\sqrt{m}$ (5 to 10 Ksi$\sqrt{in}$.) and are listed in Table 18. The FCP rates determined from the CT specimens show little or no effect of the main program variables (i.e., forging strain and cobalt content).

The advantage of the ring specimens is that they provide a significant amount of fracture surface characteristic of a single ΔK, while in CT specimens ΔK is constantly changing as a function of crack length. This allows characterization of fracture without concern for position. The ring also provides a significant volume of material deformed under similar conditions for SEM and TEM analysis. The disadvantage, at least as far as this study is concerned is the sensitivity to sample preparation (notch preparation, surface polish, etc.) It has not been determined that the shear lip formation is due to the ring specimen.

Figure 64 shows the typical crack path through the microstructure for the ring specimens. It is clear that the microstructure influences the crack path. In large powder particles it can be seen that the crack grows transgranularly (as in regions marked A). In other areas (marked B) it appears that the crack path follows prior powder particle boundaries (PPBs). As previously discussed, in forgings the PPB structure is not completely broken up and as a result the boundaries are heavily decorated with oxides. Kim et. al., [36] have suggested these boundaries are weaker and are sites for easy crack initiation and propagation. Lawley and Koczac [49] attribute faster crack growth and change of plane to the presence of weak interfaces due to oxides through which the crack has a strong tendency to propagate.

The values of FCP rates measured in this study are representative of values reported by other investigators [5, 49, 108, 174, 253] for similar Al P/M alloys, as seen in Table 19. Several investigators [5, 16, 174, 23] have compared the fatigue crack growth behavior of CT91

70

type alloys to ingot (I/M) alloys. In general, the FCP resistance of the P/M alloys is equal to or inferior to I/M alloys with notable exceptions. 7091 (CT91) closely resembles the behavior of 7075 [174, 233], but is inferior to 7050 except in the high ΔK regime where toughness is a major factor [174]. McEvily [16] reports that above the near threshold region the FCPRs in P/M alloys are higher than in I/M alloys due to lower closure levels in P/M alloys. Sanders, et. al., [5] conclude that at low ΔK P/M is equivalent to I/M, at intermediate ΔK P/M is inferior and at high ΔK P/M is superior. Wei and Pao [174] attribute the poorer FCPRs of P/M to the finer grain'subgrain structure which reduces slip reversability and produces less "zig-zag" in the crack path. At high ΔK the effect of grain size diminishes and FCPRs are comparable. This is consistent with the findings of others [47, 140, 190]. The influence of microstructural features on FCP is closely related to the relative size of the plastic zone, r_p, at the crack tip and the size of these features. When the microstructural elements are significantly larger than r_p, the material behaves as a continuum and linear elastic fracture mechanics applies. When r_p is significantly larger the effect of the microstructure is maximized. The plane strain monotonic plastic zone size can be calculated from [254]:

$$r_p' = \frac{1}{24\pi}\left(\frac{K_{max}}{\sigma_{ys}}\right)^2 \qquad \begin{array}{l}\text{where } k = 6 \text{ for monotonic} \\ k = 24 \text{ for cyclic}\end{array} \qquad (27)$$

Table 20 lists the calculated plane strain cyclic plastic zone size for values of strength and stress intensity range typical of those found in this study. Recalling that the grain size of the forgings ranged between ∿ 1 and 10 μm it can be seen that the microstructure will influence the FCPR for all ΔK's tested. The wide variation in grain size observed indicates that even at higher ΔK's some grains will be larger than the plastic zone and some grains will be smaller and thus no clear cut material behavior can be assumed. When the crack is in

71

the vicinity of small grains slip reversability will be limited and FCPR will be increased [49].

Figures 65-72 are typical L-T ring specimen fractographs from fractured fatigue specimens. Figure 65 shows fractographs at the three ΔK's tested. Note the equiaxed appearance of the fracture surface is similar to the equiaxed grain structure of the TS plane, i.e., the fracture plane. Figure 66 is similar but at higher magnification. In general the fracture is ductile with evidence of dimples (D) and striations. Striations are visible on the ring fracture surfaces for all ΔK's tested. Note the striation spacing increases with ΔK as expected. Occasionally areas of brittle fracture are observed as in Figure 66b. Also, secondary cracking is observed in all conditions tested.

In Figure 67, small (< 0.1 μm) particles are visible on the smooth striated surfaces. These particles (see arrows) were referred to as "white dots" by Hirose [227] and identified by Walker [108] as η, the equilibrium form of $MgZn_2$. Evidence of oxide influencing the crack path is seen in Figure 68. The brittle appearance is clearly not typical of the fracture in general, but is observed in each condition. This represents the weak interface described by Kim, et. al., [36] and by Lawley and Koczak [49]. The oxide is distributed nonuniformly and presents an easy crack path at prior particle boundaries. Evidence of intergranular failure at prior particle boundaries is also seen in Figure 69. The ridge (arrow) is a transition from transgranular to intergranular fracture. Hirose [227] and Wei and Pao [17] report primarily transgrannular fracture in CT91 type alloys. This is typical of all high strength aluminum alloys fractured in fatigue [17]. Although the more rapid FCPRs have been attributed to the fact that flat fracture (due to small grains) precludes crack closure [16]. Occasionally evidence of mechanical interference (expected if closure occurs) is observed. As seen in Figure 70 the dark areas are probably an abraided oxide. In Figure 70b the deformation typical of the first band is seen. In Figure 70c it can be seen that the deformed band is associated with a change in fracture path that allows interference.

Figures 71 and 72 show the fracture surfaces typical of the compact tension specimens. Note that at ΔK's of 5.5 and 7.7 MPa√m̄ the elongated structure of the LS plane (the fracture plane) is clearly visible. At ΔK = 11 MPa√m̄ this is not the case and the fracture features appear equiaxed. This was the case for all four CT specimens tested. This would imply that microstructural effects are present at the lower ΔK's tested but not at higher ΔK's. Figure 72 is the same as Figure 71 at higher magnification. Striations are rarely visible on the CT fractures and the fracture has a more brittle appearance than seen with the ring specimens. These differences may be due to the difference in orientation or the differences in specimen type or both. No report of similar observations has been encountered in the literature.

4.4 LCF

4.4.1 A_ϵ = 0.95, Plastic Strain Control

4.4.1.1 Cyclic Stress Strain Response (CSSR)

The CSSR as evidenced by cumulative glide plots is shown in Figures 73(a)-(h). All conditions exhibit strain hardening. This is to be expected since this is typical of overaged precipitation strengthened aluminum alloys [85, 108, 111, 155, 159, 165, 169, 176]. All the specimens tested reached an almost totally saturated state by half-life providing evidence of the effectiveness of the CT91 microstructure in preventing inhomogeneous deformation after saturation is reached. It would appear that the fine unrecrystallized structure is just as effective as the Co dispersoid in dispersing slip since the 0%-cobalt variant exhibits the same hardening behavior as the 0.4% variant. Logarithmic plots of cyclic stress amplitude versus plastic strain range made to determine the cyclic strain hardening exponent can be found in the Appendix. Typical values of n' calculated from a least squares analysis are listed in Table 20. These values range from 0.05 to 0.09 which indicates a slight tendency to harden cyclically. Other
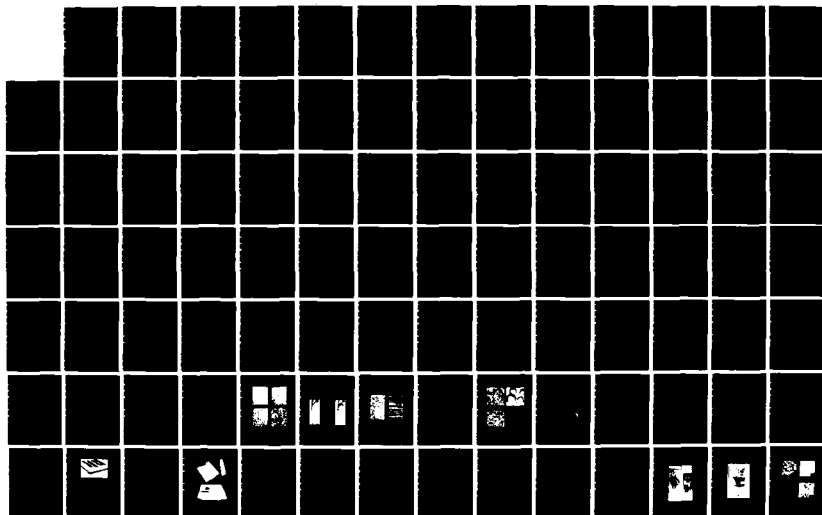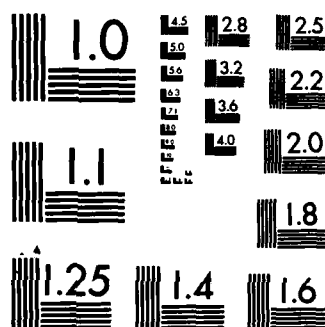
MICROCOPY RESOLUTION TEST CHART

NATIONAL BUREAU OF STANDARDS-1963-A

investigations [108, 111, 155, 169, 174] on similar materials report strain hardening exponents ranging between 0.05 and 0.12. This data is particularly good agreement with the data of Kuo [174] who reports n' = 0.09 for CT91 alloy plate. Other investigations [108, 192] of CT91 extrusions report considerably higher values of n' in limited testing; Telesman [192] reports n' = 0.26 (derived from single hysteresis loop) while Walker reports n' = 0.12. These were the highest values found in the literature for 7000-type aluminum alloys, with most other data ranging from 0.05 to 0.09. As can be seen from the data in Table 21, comparisons of the degree of forging strain and of the chemistry differences show little or no effect of the major program variables on cyclic stress strain response of the alloys tested.

4.4.1.2 Coffin-Manson Behavior

Logarithmic plots of cycles to initiate a fatigue crack versus plastic strain range provide a linear representation of the LCF data as typified by Figure 74. Emperically this can be represented as

$$N_i^{\beta} \Delta\epsilon_p = C \tag{28}$$

where N_i = the number of cycles required to initiate a fatigue crack

$\Delta\epsilon_p$ = the imposed plastic strain range

β, C = material constants.

Although it is common in the literature to find Log N_i plotted as the abscissa, the more correct method is to plot Log N_i as the ordinate because it is the dependent variable.

Coffin-Manson plots were made for all conditions tested in addition to combinations of conditions that represent the various Co and forging levels. These plots were made using the AFWAL PRIME Computer System using the program QEP. Statistical analysis was performed on

74

the same system using the program POLY. All of the plots are found in the Appendix. Tabular representation of the data is found in Table 21.

In this investigation the values of the Coffin-Manson exponent for $A_\varepsilon = 0.95$ LCF tests varied between 1.110 and 1.328. These values are higher than those reported for similar alloys [108, 111, 155, 169, 174] Kuo [174] and Walker [108] reporting on alloys of the same composition (CT91) reported values for β of 0.74 and 0.69 respectively. The most logical explanation for these differences is the inability of the forging process to break up and distribute the surface oxides inherent on the original powder particle, i.e., a microstructural effect. Kuo's work was on plate and Walker's on extrusions; both of these processes introduce considerably more deformation into the material than forgings. Kim et. al., [36] have noted that extrusion is a particularly efficient process for redistributing oxides. Of the three product forms tested the extrusion had the smallest β (0.69) and would empirically have the longest life. Another important consideration in this investigation is that although there is no apparent trend in the value for the major program variables, there was considerably more scatter in the 38% forging compared to the 64% forging as evidenced by the coefficient of determination. This is attributed to even poorer oxide distribution in the 38% forgings. Pockets of oxide, particularly at what had been originally triple points, making ideal sites for initiation [36].

Morrow [193] suggested that the Coffin-Manson Law can be derived by multiplying the plastic work per cycle, ΔW, by the cycles to failure N_f:

$$N_f (\Delta W) = C' \tag{29}$$

where C' is a material constant. This is a total energy criterion. Saxena and Antolovich [172, 173] made a first order modification to

75

take into account that as the slip mode changes the fraction of the total plastic work stored as fatigue damage also changes:

$$N_f \cdot (\Delta W)^\alpha = C \tag{30}$$

where α and C are constants that depend on material and slip mode. The area enclosed in the hysteresis loop represents the plastic work per unit cycle, but not all the work done is stored as damage. Substituting an initiation criterion for failure, using the procedure suggested by Figure 75 to calculate ΔW and substituting the result in Equation 30 yields:

$$N_i \, (\Delta \epsilon_p)^{(1 + n')\alpha} = C_1 \tag{31}$$

where C_1 is a new constant including terms other than C in Equation 30, comparing Equations 32 and 28 gives:

$$\beta = \frac{1}{(1 + n')\alpha} \tag{32}$$

ΔW was calculated using the expression

$$\Delta W = \frac{\Delta \epsilon_p \Delta \sigma}{(1 + n')} \tag{33}$$

and recorded in the Appendix. A logarithmic plot of Ni vs. ΔW is linear with slope $-\alpha$; using α together with n' from experimental data, β can be calculated from Equation 32. As can be seen from the results of these calculations in Table 21, they are in excellent agreement with $\beta_{expt.}$, indicating the data generated in this investigation are consistent with Saxena and Antolovich's improvement of Morrow's model.

4.4.2 $A_\epsilon = \infty$, Total Strain Control

In a completely reversed strain control test ($A_\epsilon = \infty$) the mean strain is zero. The previously discussed tests did not have a compression strain (A = 0.95) and therefore the mean strain was greater than

76

zero. The $A_\varepsilon = \infty$ tests were run to evaluate what differences, if any, could be associated with a mean stress effect. It should also be noted that completely reversed straining is typical of testing used in

similar investigation of 7000-series aluminum alloys [84, 108, 155, 157, 169, 174, 192].

4.4.2.1 Cyclic Stress-Strain Response

Cumulative glide plots for $A_\varepsilon = \infty$ tests are shown in Figure 76. The behavior is similar to that seen previously in $A_\varepsilon = 0.95$ tests, i.e., saturation or very slight hardening is seen in all samples. One obvious difference is the rapidity at which stresses approaching the saturation stress are reached, especially at low stresses. This is most likely due to the fact that the $A_\varepsilon = \infty$ tests were run in total strain control ($\Delta\varepsilon_t$ constant for entire test) while the $A_\varepsilon = 0.95$ tests were run in plastic strain control ($\Delta\varepsilon_t$ continuously increasing until saturation, then constant). Thus, lower stresses would be expected at the beginning of a plastic strain control test.

Values of the cyclic strain hardening exponent, n' are listed in Table 22. The CSSR is essentially identical for the $A_\varepsilon = \infty$ and $A_\varepsilon = 0.95$ tests, indicating no effect of mean stress on cyclic stress strain response.

4.4.2.2 Coffin-Manson Behavior

The cyclic properties of the conditions tested for $A_\varepsilon = \infty$ are listed in Table 22. There does not appear to be any significant variations in these values between the $A_\varepsilon = \infty$ and $A_\varepsilon = 0.95$ but the following observations can be made.

a) Both sets of data predict higher β's (i.e., shorter predicted life) for the 101 condition (64% strain, 0% cobalt) than for the other

conditions. The high value of β in the $A_\epsilon = \infty$ test is probably due to the fact that the specimen lives were not well distributed on the abscissa but instead tended to bunch around long lives. This coupled with the fact scatter tended to be greater in specimens run at low strains would lead one to believe the $A_\epsilon = 0.95$ is more correct. This poor dispersion of data is somewhat corrected by adding in the 111 data or the 001 data to examine the 64% forging data or the 0% cobalt data respectively.

b) The calculated values of β from the $A_\epsilon = 0.95$ tests tend to be higher than the values from the $A_\epsilon = \infty$ tests. β calculation is relatively insensitive to n' in the range reported so this observation is related to the values of α determined from plots of log ΔW vs. log N_i. The value of α is related to the slip mechanism and has been shown to vary with SFE [172, 173]. Since no such change in SFE is expected here it must be assumed the slight increase in α observed in the $A_\epsilon = \infty$ tests is indeed related to a mean stress effect, which is essentially related to slip mode.

c) There is a trend for β to be highest in the high strain forgings and in the zero Co chemistry in the $A_\epsilon = \infty$ test. Although the same trend is observed in the $A_\epsilon = 0.95$ data, the differences are much more subtle and could be said to be within the scatter of the experiment. The implication is the $A_\epsilon = \infty$ test is more sensitive to microstructural variation.

4.4.3 Initiation Characterization

Research on fatigue mechanisms has as a direct or underlying objective the development of fundamental information relating microstructures to fatigue initiation resistance. It has become quite common to define the failure criterion, N_f, in the Coffin-Manson law in terms of some occurrence other than separation of the specimen into two pieces. Unfortunately, the definition of initiation is arbitrary and often

78

depends on the sensitivity of the measuring device used [155]. Most definitions are couched in terms of the "smallest detectable crack," a crack "long enough" to cause a significant decrease in load carrying capability or a crack "sufficiently long" to precipitate failure [155]. Many investigators prefer to use total failure as the criterion, but this is not recommended if microstructural concerns are of importance; failure in LCF consists of two different processes, crack initiation and propagation. Often, developments to improve one of these factors will have an adverse affect on the other. For example, the development of the fine structure in P/M Al alloys has improved fatigue initiation resistance at the expense of fatigue crack propagation resistance, particularly at low stress intensities [13, 14, 15, 47, 227]. The process of crack propagation can occupy a considerable portion of total fatigue life - generally greater than 75% in the high stress range of fatigue [162]. Maiya and Busch [194] suggest plotting surface crack length vs. cycles imposed and extrapolating back to a_0, a crack length on the order of the grain size. N_0, the cycles associated with a_0 would be the failure criterion. James and Morris [195] suggest that the cycles to initiate a fatigue crack are determined by imposing a fracture criterion determined by the nature of the cracking site, i.e., each fracture mode requires its own initiation criterion.

In this work the failure criteria was taken to be the first detectable load drop on the strip charter recording load from the load cell. A fifty pound load drop was easily detectable. Assuming this is the result of elastic considerations, Young's Law can be written in terms of:

$$\Delta P = \frac{\delta E}{L} \Delta A \tag{34}$$

where ΔP is load drop

δ/L is elastic strain

E   is Young's Modulus

79

and ΔA is the reduction required to cause load drop ΔP. Assuming $\Delta P = 23$ Kg (50 lbs.), $\delta/L = 10\%$ and $E = 69$ MPa (10×10^6 psi), ΔA is approximately 3×10^{-4} cm^2 (50×10^{-6} in^2). Assuming the crack depth is 10 times its length then the crack length at $\Delta P = 23$ Kg (50 lbs.) is about 600 μm. This is a sizable crack relative to the grain size (4 μm) and indicates the failure criterion may not be adequate to solely describe crack initiation.

Several $A_\varepsilon = 0.95$ tests were stopped at the first indication of load drop. The surfaces of these specimens were examined in the SEM. Figures 77-83 are examples of the surface cracks found in this manner. Surfaces are favorable sites for initiation because they are exposed to the ambient environment, mechanical properties are altered by surface oxides and there is a partial absence of constraint upon deformation [195]. Fatigue cracks are known to initiate at or near singularities on or just below surfaces of metals [140]. These singularities include inclusions, embrittled grain boundaries, sharp scratches, pits or slip bands. In this study no surface irregularities were associated with surface cracks. There is a significant amount of debris visible in the cracks. Much of this debris appears to charge in the electron beam indicating it is nonconductive, probably in an oxide. It is impossible to determine whether the oxides were present before the cracking occurred or it is the result of surfaces rubbing together causing abrasion, i.e., fresh surface oxides. In most cases the surfaces of failed specimens did not indicate abrasion had occurred thus making it more likely that this debris was present before initiation occurred.

The fractures of the $A_\varepsilon = 0.95$ test specimens were extensively characterized by SEM analysis. As illustrated in Figure 84 initiation sites can be classified into three main types: a) grain or powder particle boundaries, b) large particles at or near the surface and c) subsurface particles. Examples of grain and powder particle boundary

80

are given in Figures 85-98. The salient features of these fractographs can be summarized as follows:

a) Multiple initiations were often observed at positions around the periphery that indicate alignment was good.

b) At high plastic strains initiation sites are more difficult to locate. At low strains a significant region of crack propagation results which emanates from the initiation site making it easier to locate.

c) Boundary initiations are characterized by flat, featureless regions near the origin of initiation which transition into flat regions with striations indicating crack propagation is occurring.

d) The area near initiation is often decorated with debris that shows no unusual elemental presence under x-ray analysis. These areas are thought to be large pockets of oxide that either participate in initiation or early stages of crack extension.

Initiations at large particles are illustrated in Figures 79-103. The pertinent conclusions regarding these initiations include:

a) No subsurface particle initiations were observed above $\Delta\epsilon p =$ 0.1%. This would indicate the boundary weaknesses were exploited early by high loads and strains but defects associated with particles built up over a period of time until a critical defect was formed in conjunction with a particle.

b) In general, the particle initiations did not lower life significantly. The exceptions are shown in Figures 79 and 103.

c) Most particles were high in Fe or Si. Fe-containing particles often had other refractory elements associated with them indicating

81

their most likely origin was the powder making process. Si-containing particles are assumed to be SiO_2 or Mg_2Si.

d) Calcium is often associated with particles found on fracture surfaces but usually not as the major element present. The exception is shown in Figure 99 where Ca makes up the greatest part of the sur- face particle.

e) Fractures initiating from particles near the surface tend to have the same fracture features as boundary type initiations (Figure 101).

f) It is interesting to note that the fracture shown in Figure 103 has only one observable initiation site, at the Mg_2Si particle near the center. If one assumes the 50 μm circular area around the particle is the initiation site and calculates a load drop due to just that area reduction using Equation 34, that load drop is on the order of 207 KPa (30 lbs.) This is approximately the minimum load drop measurable on the strip chart.

g) Subsurface particles identified with initiation are relatively large compared to other microstructural features. Si-containing parti- cles generally ranged in size between 20 and 100 μm. Fe-containing particles were generally smaller, usually 2-20 μm; however at least one Fe-containing particle was on the order of 100 μm long.

These findings are in good agreement with other investigations. Santner [197] also reports boundary initiation which he refers to as enriched areas of grain boundary aluminum. He also identifies aluminum rich inclusions with traces of Si, S, or Ca and transition metal inclu- sions (e.g., Fe, Zn) as sits of initiation. Walker [108], Kuo and Starke [174], and Lin [177] all report fatigue crack initiation occurring at grain boundaries for a range of strains tested.

82

4.4.4 TEM Evaluation of LCF

Thin foils were prepared for TEM evaluation from the gage section of LCF specimens. The following procedure was used to characterize the deformation:

a) Foils were examined to locate grains of interest; these grains were generally chosen far enough from the perforation to preclude thickness fringes and bend contours.

b) Grains of interest were oriented using the technique described previously (Section 3.2); the sample was tilted and the angles at which 2-beam conditions were observed were noted as well as the angle the diffraction spots fall from the tilt axis and the quadrant of the grid in which the spots were observed. This information was plotted on a Wulff net and a sterographic projection prepared making use of the angular relationships measured on the net. Locations of missing planes are easily deduced. An example is shown in Figure 19.

c) The active slip system is identified by calculating the Schmid Factor, M. This is accomplished by measuring the angle between <111> planes and the tensile axis which is in the center of the Wulff net and between <110> directions, lying on a given {111} and the tensile axis. Using the equation

$$M = COS\theta_{\{111\}}COS\theta_{<111>}$$ (35)

the Schmid factor is calculated for each set of systems and the active slip system is taken to be the one with the largest M. Note that M may vary between 0 and 0.5 for a given system.

d) Using the stereographic projection as a guide, the active slip plane is tilted until its pole is located on the circumfrerence of the projection - this is equivalent to examining the plane edge. Note that

83

since the active {111} plane is 90° from the associated <110> direction that $\bar{g} \cdot \bar{b} = 0$ and dislocation debris will not be in sharp contrast. However residual image contrast will exist for all but pure screw dislocations and faint slip bands will be visible if they exist.

e) If slip bands were observed, using the sterographic projection as a guide, the foil was rotated and/or tiled to bring up a reflection not 90° from the <110> directions but maintaining the active {111} plane near edge on. In this way a sharper contrast of the dislocations on the plane is obtained.

f) If slip bands were observed another {111} type plane (i.e., m) was used to form the diffraction vector. This plane was chosen (using the sterographic projection) so that when examined edge on the active {111} plane would be oblique. In this way the active plane may be examined to determine the nature of the dislocation debris in the slip bands.

g) If slip bands were not observed a similar set of experiments was carried out to characterize the nature of the dislocation debris.

Results of these experiments are shown in Figures 104-111. Figures 104 and 105 illustrate the deformation structure observed at high plastic strain amplitude. The homogeneous deformation seen in these figures is typical of all conditions tested at high plastic strains (> 0.3%). Figure 107 illustrates the inhomogeneous deformation and fine slip band formation typical of all conditions tested at low plastic strains (< 0.3%). These results agree well with results of similar testing on 7000-series alloys [108, 111, 155, 157, 174, 192]. In their work on 7050 and Al-Zn-Mg ternaries Sanders and Starke [111, 157] report that when large incoherent precipitates are present (as is the case in this study) precipitates cannot be sheared and must be bypassed. At high plastic strain amplitudes (PSA) the precipitates are most likely bypassed by a cross-slip mechanism. This is reasonable

since aluminum alloys have a relatively high stacking faulty energy which allows for easy cross-slip. Sanders and Starke [2, 5, 111, 157] also suggested that the formation of cells is further support for this assumption. Figure 107 illustrates the type of cell formation found in this study at high PSA. Figure 108 suggests the formation of cells between the slip bands at low PSA as well. This is also seen in Figure 109 where, by appropriate tilting and rotating, the nature of the slip bands on the active {111} plane is seen to be cells. At low strain amplitudes cross-slip may not always be energetically favorable and precipitates must be bypassed by another mechanism, such as Orowan looping which is less localized and leads to the formation of coarse slip bands. They also attribute the dual slope Coffin-Manson behavior to this change in deformation mechanism. Others have reported similar explanations for the behavior of 7075 [84, 155, 169], 7050 [84], and P/M alloys [108, 174]. Kuo and Starke [174] report homogeneous fine slip in CT91 alloy plate prepared by commercial methods. Telesman [45] reports observing only homogeneous slip in CT91 extrusions and coarse slip bands in similar tests on 7050. All except Santner (overaged 7075) [169] report dual slope behavior for these alloys (Telesman [192] did not report the Coffin-Manson behavior). In general, past studies have associated the dual-slope Coffin-Manson behavior with a change in defomation mechanism as witnessed by the observation of slip bands in the microstructures at low strains and their absence at high strains.

Single slope Coffin-Manson behavior was observed for all conditions in this study. The Coffin-Manson exponent was measured to be approximately 1.0 compared to 0.75 for similar alloys in other studies. This translates into a shorter life in the LCF regime. Faint slip bands were observed in all conditions tested at aplastic strain amplitudes below about 0.3%. A cell structure was observed at both high and low plastic strain amplitudes indicating that cross slip was operating in all cases [111, 157]. The nature of the observed slip was faint slip lines coexisting with homogeneous deformation. This would indicate that two deformation mechanisms may be operating simultaneously.

36. Y-W. Kim, W. M. Griffith, and F. H. Froes, "The Breakup and Distribution of Surface Oxides Through Processing of P/M Aluminum Alloy 7091," to be published in the Proceedings of ASM Metals Congress on New Developments for Aluminum Applications, Philadelphia, (Oct. 1983).

37. A. I. Litvintsev and L. A. Arbuzova, Sov. P/M and Met. Cer., 1, (1967) p 1.

38. R. C. Svedberg, Westinghouse, Pittsburgh, PA, unpublished research (1981).

39. J. M. Walker, Alcoa Laboratories, Alcoa, PA, unpublished research (1982).

40. J. T. Morgan, H. L. Gegel, S. M. Doraivelu, and L. E. Matson, Proceedings of AIME Symposium on "High Strength Powder Metallurgy Aluminum Alloys,", Dallas, TX, February 17-18, 1982, p. 193.

41. S. I. Berman, V. I. Zalesskii, Kh. I. Imanov, and V. A. Shelamov, Poroshkovaya Metallurjiya, No. 12, 84, p. 14 (1969).

42. J. W. Bohlen, S. G. Roberts, and G. R. Channani, "Ivestigation of Improved Methods for Consolidating Rapidly Solidified Aluminum Alloy Powder," Northrop Corporation Technical Report, NOR82-4, June 1982.

43. F. R. Billman, J. C. Kuli, Jr., G. J. Hildeman, J. I. Petit, and J. A. Walker, Proceedings of the 3rd Conference on Rapid Solidification, National Bureau of Standards, Gaithersburg, MD, December 6-8, 1982.

44. G. Staniek, "Observations of Oxide Skin in Powder Metallurgy Aluminum Alloys," Air Force Wright Aeronautical Laboratories, Technical Report, (1983) (in press).

26. H. Jones, "Developments in Aluminum Alloys by Solidification at Higher Cooling Rates," Aluminum, Vol. 54 (1978) p. 274.

27. "Elevated Temperature Aluminum Alloy Development," USAF Contract F33615-81-C-5096, Lockheed California Co., Burbank, CA, W. M. Griffith, AFWAL/MLLS, Wright-Patterson AFB, OH. (1981).

28. S. Savage, Internal Research, AFWAL/MLLS, (1983).

29. J. J. Kleek and F. D. Mullins, unpublished research, AFWAL Materials Laboratory, AFWAL/MLLS, (1983).

30. A. Lawley, "Preparation of Metal Powders," Ann. Rev. Mater. Sci., (1978) p. 49.

31. W. M. Griffith, S. Mazdiyasni, and M. M. Cook, "Evaluation of Aluminum P/M Sources," unpublished internal report, AFWAL/MLLS, WPAFB, OH, (1982).

32. A. R. Cox, J. B. Moore, and E. C. VanReuth, "Rapidly Solidified Powders, Their Production, Properties and Potential Applications," AGARD-CP-256 (1978).

33. O. R. Singleton, "Manufacturing Technology for High-Strength, Aluminum, P/M Mill Products," in Review of Government Sponsored Work on P/M Aluminum Alloys, Ed. by L. R. Bidwell and B. A. Kosmal, (1980).

34. R. E. Sanders, Jr., and G. J. Hildeman, "Elevated Temperature Aluminum Alloy Development," AFWAL-TR-81-4076, (1981).

35. S. D. Kirchoff and W. M. Griffith, ongoing research, AFWAL/MLLS, WPAFB, OH, (1983).

18. J. Lankford, D. L. Davidson, G. R. Leverant, J. E. Hack, and R. M. Arrowood, "Study of Fatigue Mechanisms in Aerospace Structural Materials," Annual AFOSR Scientific Report on Contract F49620-78-C-0022, (1982).

19. W. M. Griffith and F. H. Froes, "Advances in Aluminum P/M Aerospace Structural Alloys," Presented at WESTEC, Los Angeles, CA, March 1983.

20. T. E. Tietz and I. G. Palmer, "Advanced P/M Aluminum Alloys," Advances in Powder Technology, Ed. G. Y. Chin, ASM, (1982), p. 189.

21. F. H. Froes and J. R. Pickens, "Powder Metallurgy of Light Metal Alloys for Demanding Applications," Journal of Metals, 36(1), (1984), p. 14.

22. J. A. Vaccari, "The New Frontiers of Powder Metals," American Machinist Special Report 754, American Machinist, May 1983, p. 121.

23. W. E. Quist and G. H. Narayanan, "Powder Metallurgy (P/M) Aluminum Alloys for Aerospace Use," Presented at the 1983 SAMPE Meeting, Anaheim, CA, April 1983.

24. J. R. Pickens, "Aluminum Powder Metallurgy Technology for High-Strength Applications," Journal of Material Science, 16 (1981), p. 1437.

25. J. P. Lyle, Jr., and W. S. Cebulak, "Fabrication of High-Strength Aluminum Products from Powder," Powder Metallurgy for High Performance Applications, Syracuse Press, (1972), p. 231.

9. O. R. Singleton and H. M. Edwards, "High Strength, P/M, Aluminum Mill Products - Phase II: Sinter Seal Process Scale-Up," Sixth Interim Report on AF Contract F33615-79-C-5161, (1982).

10. "High Strength Al Billet, Plate and Sheet Fabrication," USAF Contract F33615-82-C-5063, AFWAL/MLTM, Wright-Patterson Air Force Base, Ohio (1983).

11. D. H. Ro, "Direct Rolling of Aluminum Powder Metal Strip," Final Report AFWAL-TR-82-4008 on USAF Contract F33615-80-C-5161, (1982).

12. "Proceedings - Aerospace/Aluminum Industry Strategy Assessment Workshop," Ed. by D. Voss, Dayton, Ohio, 30-31 July, 1981.

13. J. Petrak, M. Malas, and W. M. Griffith, Report on Cooperative Testing Program (Round Robin Assessment) of P/M Aluminum Alloys 7090 and 7091, in preparation, to be published in 1984.

14. "Proceedings - Aluminum Strategy Assessment Workshop," Ed. by T. M. F. Ronald, Dayton, Ohio, 13-15 September, 1983.

15. M. E. Fine, "Fatigue Crack Initiation and Propagation in High Strength Aluminum P/M Alloys," Final Report on AFOSR Grant AFOSR-78-3732 (1981).

16. A. J. McEvily, "The Fatigue of Powder Metallurgy Alloys," Annual Report on AFOSR Grant AFOSR-81-0046, (1982).

17. R. P. Wei and P. S. Pao, "Mechanisms of Corrosion Fatigue in High Strength I/M and P/M Aluminum Alloys," Technical Report No. 2 on AFOSR Contract No. F49620-81-K-0004, (1983).

6.0 References

1. W. S. Cebulak and D. J. Truax, "Program to Develop High Strength Aluminum Powder Metallurgy Products, - Phase III - Scale-Up A," Final Report on U. S. Army Frankford Arsenal Contract DAAA 25-70-C-0358, (1972).

2. W. S. Cebulak, "Program to Develop High Strength Powder Metallurgy Products: Phase II - P/M Alloy optimization - Phase IVB, Scale-Up to 1545 Kg. Billet," Final Report FA-TR-76-67 on U. S. Army Contract No. DAAA-25-72-C-0593, (1977).

3. S. G. Roberts, "Powder Fabrication of Aluminum Alloys," WADC Report 56-481 (1957).

4. W. L. Otto, Jr. "Metallurgical Factors Controlling Structure in High Strength P/M Products," Final Report AFML-TR-76-60, USAF Contract No. F33615-74C-5077, (1976).

5. R. E. Sanders, Jr., W. L. Otto, Jr., and R. J. Bucci, "Fatigue Resistant P/M Alloy Development," Final Report AFML-TR-79-4131 on AF Contract F33615-77-C-5174, (1979).

6. H. G. Paris and A. Hafeez, "Cobalt-Free High Strength Aluminum P/M Alloys," Final Report AFWAL-TR-83-4002 on USAF Contract F33615-80-C-5098, (1983).

7. R. Pishko, "Precision Aluminum Alloy Powder Metallurgy Structural Components," Final Report AFWAL-TR-83-4013 on USAF Contract F33615-77-C-5129, (1983).

8. J. C. Kuli, Jr. and F. R. Billman, "Low Cost Manufacturing Methods for High Strength P/M Aluminum Wrought Products," Final Report AFWAL-TR-82-4071, on USAF Contract F33615-79-C-5053, (1982).

pockets. No subsurface particle initiations were observed above $\Delta\varepsilon_p$ = 0.1% indicating powder particle boundary weaknesses near the surface were exploited early by high loads and strains but defects associated with particles built up over a period of time until a critical defect was formed in cojunction with a particle. In general, particle initiation did not shorten life although exceptions were observed.

12. TEM evaluation of thin foils taken from near the fracture surface of LCF specimens indicated homogeneous deformation is present in all conditions tested. In specimens tested at $\Delta\varepsilon_p$ < 0.3%, fine slip band formation is also observed. The fact that only single slope Coffin-Manson behavior was observed indicates that homogeneous deformation is the predominant deformation mode at all plastic-strain ranges tested. Although not substantiated by exhaustive experimentation, it appears that the inhomogeneous deformation at low strain amplitudes is found only in the larger grains.

13. The LCF-based FCP models are not valid for the alloys and conditions tested. Using the criterion that $m = 2/\beta$ and assuming the Paris Law exponent (m) to be 3.0, the value of $\beta = 0.67$ is required for agreement with the models. This value is very close to those reported for other product forms, indicating the degree of oxide breakup may be responsible for this behavior.

14. Using the true fracture strain, ε_f, as a point on the Coffin-Manson plot provides a dual slope behavior with $\beta = 0.71$ for high plastic strain amplitudes. This indicates the LCF based models would be valid in this regime. Using the model proposed by Antolovich, et. al., the process zone size parameter is approximately 8 μm, which is on the order of the powder particle size.

94

Paris Law exponent that ranges from 2.78 to 3.23 for tests using the L-T orientation indicating very little effect of the major program variables.

7. There was little effect of the major program variables on the cyclic stress strain response of the P/M Al alloys. All conditions exhibit slight cyclic hardening, with n' ranging from 0.068 to 0.107.

8. Coffin-Manson analysis of the LCF data indicated only single slope behavior is observed with β ranging from 1.017 to 1.344 for A = 0.95 tests and 0.779 to 1.437 for A_ε = ∞ tests. These values of β are 30-50% higher than those reported for similar alloys in other product forms (extrusions, plate). This difference is attributed to the inability of the forging process to break up and distribute the oxides inherent on the original powder particle surfaces.

9. An analysis of the LCF data using hysteretic energy per unit volume, ΔW, provided calculated values of β which are in excellent agreement with experimental values. This indicates the data generated in this study is consistent with Saxena and Antolovich's improvement of Morrow's derivation of the Coffin-Manson Law.

10. No significant variations in material behavior between A_ε = 0.95 and A_ε = ∞ LCF tests were observed, indicating little or no mean stress effect.

11. Three types of initiation were observed in LCF tests: a) surface boundary, b) surface particle, and c) subsurface particle. Surface boundary initiations were observed in most cases and are characterized by flat, featureless regions near the origin of initiation which transitions into flat regions with striations indicating crack propagation is occuring. The area near the origin is often decorated by debris that is thought to be the remnants of large oxide

93

4. The average tensile strength of the conditions tested ranges from 558.9 to 620.0 MPa (81.0 to 88.4 ksi); the average yield strength ranges from 509.2 to 558.9 MPa (73.8 to 81.0 ksi). There is no systematic effect of location in the channel die forgings. The largest effect observed results from differences in Co content; the 0.4% Co alloy shows a 28 MPa (4 ksi) increase in both ultimate and yield strength compared to the 0% Co alloy. The stress relief operation reduces ultimate and yield strength slightly while there is no measurable effect of forging reduction between 38% and 64% upset.

5. Difficulty in obtaining a straight precrack in Charpy specimens was encountered, preventing obtaining the correct initial conditions for a valid fracture toughness test. Samples precracked to failure _always_ showed a straight precrack. Using the crack length at failure in these specimens a K_Q was calculated which was consistently higher than expected based on K_{IC}'s reported elsewhere. This is attributed to the added energy required for the crack to propagate through a larger plastic zone than normally present. The values of K_Q in the L-T orientation generally fall between 31 and 35 MPa$\sqrt{m}$ (28 and 32 Ksi$\sqrt{in.}$). Only slight differences, 1 to 2 MPa $\overline{m}$, were observed between main program variables. The largest observed effect was due to orientation where the L-T values were on the order of 50% higher than the T-L values. The largest amount of scatter was found in the low strain forgings, presumably due to the poorer oxide distribution.

6. Difficulty was encountered in starting a precrack in FCP specimens. This was overcome by using an EDM starter notch. Much of the FCP data collected was not included in the analysis due to eccentric cracking, shear lip formation, and/or cracks growing out of plane. Little effect of forging amount or Co content was observed although there was a slight improvement in FCP in those samples that were stress relieved. Applying a Paris Law analysis to the FCP data provides a

5.0 Conclusions

High strength Al P/M alloy CT91 was investigated in order to characterize the effects of chemistry (0% and 0.4% Co), forging reduction (38% and 64% upset) and heat treatment (stress relieved and un-stress relieved). The conclusions drawn from this study are:

1. Keller's etchant, used extensively for Al alloys, does not provide a uniform grain boundary attack in the fine grained P/M Al alloys studied. Graff-Sargent etchant provides a uniform attack and thus reveals the fine grain/subgrain structure of these alloys.

2. An increasing amount of deformation is observed in the optical microstructures of the VHP billet, 38% upset forging, and 64% upset forging respectively. The grain/subgrain size of the forgings ranges from a fraction of a micron to over 10 μm. The "grains" are generally equiaxed and their size depends on the original powder particle size. Original powder particle boundaries can be seen in all products studied. The powder particles are essentially undeformed in the VHP billet and are flattened in the direction of upset and elongated in the direction of flow in the forgings. Occasionally, small undeformed powder particles are seen in the forgings.

3. Oxides associated with the powder particle surfaces are easily observed using transmission electron microscopy. The broken oxide film is distributed near the powder particle surfaces and the distribution is enhanced by increasing the degree of deformation. In the VHP billet the oxide forms a continuous array. As the deformation is increased from 38% upset to 64% upset the array thickness is decreased and the distance between oxide residue increases. In all products examined, large pockets of oxides were observed, presumably associated with triple points from the original VHP billet.

91

Using the estimate for C found in Reference 164 this can be rewritten

$$R = 4 \left[\frac{0.7A}{\sigma'_{yc} \epsilon'_f \, E} \right]^{1/\beta} \frac{1}{\ell^{\,1/\beta - 1}} \qquad (41)$$

Approximating $A = \frac{1}{24\pi}$ and solving for ℓ gives

$$\ell = \left[\frac{4}{R} \right]^{\beta/1-\beta} \left[\frac{0.7}{24\pi \, E\sigma'_{yc} \, \epsilon'_f} \right]^{\beta/1-\beta} \qquad (42)$$

Using $R \sim 7 \times 10^{-9}$ in/cycle, $E = 10^4$ ksi, $\sigma'_{yc} \sim 80$ ksi, $\epsilon'_f \sim .20$, $\beta \sim 0.71$ and substituting into Equation (42) gives $\ell \sim 8$ μm, which is on the order of powder particle sizes, especially in the plane of fracture.

alloys studied the break in slope would be detected by the plastic strain ranges selected. One final check of the models can be made if one assumes the true fracture strain, ϵ_f, measured from the tensile test can be plotted on the Coffin-Manson plot at $N_f = N_i = 0.5$. ϵ_f can be calculated from:

$$\epsilon_f = \ln \frac{100}{100 - \%RA} \tag{37}$$

For the alloys under consideration $\%RA \sim 20\%$ and $\epsilon_f \sim 0.18$. If one also assumes that the point $\Delta\epsilon_p = 0.006$, $N_i = 200$ is also on the same curve, then the slope calculated using these two points alone is $\beta = 0.71$ which is consistent with the LCF based model prediction. The only microstructural feature that could account for this behavior is the oxide distribution in the forgings.

Using a value of $\beta = 0.71$ the microstructural related "process zone size" can be estimated. Recall the model of Antolovich et. al., [164]:

$$da/dN = \frac{C}{(\sigma'_{yc}\epsilon'_f E)^{1/\beta}} \cdot \frac{1}{\ell^{1/\beta - 1}} \cdot \Delta K^{2/\beta} \tag{38}$$

where σ'_{yc} = cyclic yield strength
  ϵ'_f = fatigue ductility
  β = Coffin-Manson Law exponent
  ℓ = process zone size parameter

Noting that this takes the form of the Paris equation

$$da/dN = R \, \Delta K^m \tag{39}$$

where

$$R = \frac{C}{(\sigma'_{yc}\epsilon'_f E)^{1/\beta}} \cdot \frac{1}{\ell^{1/\beta - 1}} \tag{40}$$

89

behavior and cannot be accounted for in the model. The higher values of β measured indicate that initiation and/or failure would occur sooner than anticipated based on the FCP model. Other studies [108, 174] on CT91 extrusions and plate have reported values of β ranging from 0.69 to 0.74, close to the range predicted by the models. These values are for 12.4:1 extrusions and plate (89% reduction) respectively which agree well with values reported for other 7000-series alloys [111, 155]. Kim, et. al., [36] have demonstrated a significant difference in the degree of oxide break-up between forgings and extrusions. The more effective breakup and distribution in extrusions may be assumed to also be the case for plate, particularly if the rolling stock has been previously forged or extruded as is the normal practice for small experimental billets rolled at Alcoa Technical Center [196], the source of plate studied in Reference 174. Thus the bonding between PPBs in forgings is weaker than for other product forms and premature initiation unrelated to deformation mode is the result. The high values of β are the direct result of the improperly distributed oxides.

The second possible explanation for the failure of the LCF based models in this study may be related to the first. Several of the studies cited in Section 4.4.4 reported dual slope Coffin-Manson behavior [108, 155, 174] with the break reported to occur at plastic strain ranges of 0.1 to 0.2% corresponding to 800 to 7000 reversals ($A_\epsilon = \infty$) to failure. For example, data [155] generated for 7075 in peak strength condition shows a break in the Coffin-Manson plot at a plastic strain amplitude of approximately 0.2% corresponding to a failure at about 1500 reversals. When overaged, the 7075 plot broke at about 0.1% and 7000 reversals. Below the break, β is estimated to be about 2. Similar results are obtained from examination of Kuo's data [108]: $\beta \sim 1.92$. Both of these values of β are significantly higher than the β observed from this study, thus it is difficult to assume, based on these data, that the data generated in this study falls below some critical value of $\Delta\epsilon_p$. Also, based on the results of these studies it was anticipated that if dual slope behavior were to occur in

88

especially in light of Kim and Bidwell's [120] report that FCP resistance in CT91 type alloys can be improved by increasing the grain size.

4.5 Evaluation of FCP Models

The data generated in this study can be used most appropriately to evaluate LCF-based FCP models discussed in Section 2.5. As previously discussed, the validity of these models for a particular system is easily checked since the Paris Law exponent, m, is related to the Coffin-Manson exponent, β, through the equation

$$m = 2/\beta \tag{36}$$

For all the conditions tested, the value of m ranged between 2.76 and 3.51 for the L-T orientation. The average value of 2.97 would suggest a value of β = 0.65 if the LCF-base models are valid. The value of β ranges between 0.619 and 0.719 for model agreement. The m values for the T-L orientations have not been considered because all the LCF specimens were of the longitudinal orientation which results in the crack initiation taking place on the TS plane, the same plane on which fracture occurs for L-T FCP specimens.

Based on this evaluation the LCF-based models would not be valid for the alloys and conditions under study. The values of β determined experimentally from A = 0.95 LCF tests ranged from 1.017 to 1.344. There are two possible explanations for the failure of these models to adequately describe the behavior observed.

The models are based on the assumption that the deformation mechanisms representative of the LCF β parameter are responsible for FCP behavior in addition to a microstructural parameter, ℓ, that may also relate to the deformation mechanism. The first explanation of the model failure is based on the assumption that the weakness of the prior powder particle boundary (PPB) has a significant effect on the LCF

87

The fact that no break in the Coffin-Manson plots is observed would indicate that cross-slip is the dominant mechanism. The most likely reason for this single slope behavior is the homogenization of deformation by the fine grain size of the powder alloy. It has been well documented that lower grain size homogenizes slip [47, 190, 255-258] by reducing the slip length. Calnan and Clews [255] suggest that multiple-slip systems need only operate in the vicinity of the grain boundary while in the body of the grain slip may occur on duplex or single systems. Thus a reduced grain size would lead to a larger volume fraction of material deformed by multiple slip and therefore more homogeneous deformation overall. It is interesting to note that the only reported single slope behavior of 7075 in the literature [169] was from an investigation of thermomechanically processed material; although the grain size was not reported it is expected that it was considerably smaller than the commercially processed material showing dual slope behavior.

Although slip bands were never observed at plastic strain amplitudes (PSA) great than 0.306%, neither were they always observed at low PSA. In fact, slip band formation was not observed in the majority of grains studied. Figure 110 illustrates the typical deformation structure at low PSA when slip bands were not observed. The deformation structure is similar to that observed for high PSA, indicating the single slope Coffin-Manson behavior observed could be expected. One observation worthy of note is that slip band formation tends to occur only in the larger grains and subgrains, i.e., greater than approximately 5 μm (Figure 111). The average grain size of these forgings is 2-3 μm which is consistent with the relatively low frequency of slip band occurence if grain size makes an important contribution. This point has not been studied in detail because of the difficulty in controlling grain size in forgings, but warrants further study in follow-on programs. The existence of a critical grain size above which dual slope Coffin-Manson behavior exists would be an important finding

86

45. Y-W. Kim, "Surface Oxides, Their Distribution and Effects on Properties in Al P/M 7091," submitted to Met. Trans. for publication (1983).

46. F. R. Billman, J. I. Petit, R. E. Sanders, Jr., and H. G. Paris, "Microstructure/Processing Control for Aluminum P/M Wrought Products," U.S. Army Armament Research and Development Command, Technical Report ARSCD-CR-83001, June 1983.

47. D. P. Voss, "Structure and Mechanical Properties of Powder Metallurgy 2024 and 7075 Aluminum Alloys," EOARD-TR-80-1, (1979).

48. F. J. Gurney, D. J. Abson, and V. DePiere, "The Influence of Extrusion Consolidation Varialdes on the Integrity and Strength of the Product from Prealloyed 7075 Aluminum Powder," Powder Metallurgy, V. 17, No. 33, (1974), p. 46.

49. A. Lawley and M. J. Koczak, "A Fundamental Study of Fatigue in Powder Metallurgy Aluminum Alloys," Final Report, Grant AFOSR77-3247 (1981).

50. P. E. Bretz, "Spectrum Fatigue Behavior in 7XXX Aluminum P/M Alloys," in "Advanced Aluminum P/M and I/M Alloys," 1983 WESTEC, Los Angeles, CA, March 1983.

51. W. R. Garver, "Comparison of Spectrum Fatigue Resistance in High-Strength P/M Aluminum Alloys," in "Advanced Aluminum P/M and I/M Alloys," 1983 WESTEC, Los Angeles, CA, March 1983.

52. L. Wingert, Aerospace Aluminum Industry Strategy Assessment Meeting, Stouffer Dayton Plaza, Dayton, OH, Sept. 1983.

53. AF Contract F33615-78-C-5203, Lockheed Missiles and Space Co., Palo Alto, CA, Dr. T. M. F. Ronald, AFWAL/MLLS, Wright-Patterson Air Force Base, OH, (1983).

54. AF Contract F33615-81-C-5053, "Low Density Aluminum Alloy Dev.," Boeing Co., Seattle, WA, Dr. T. M. F. Ronald, AFWAL/MLLS, Wright-Patterson Air Force Base, OH, (1983).

55. R. R. Sawtell, Aerospace Aluminum Industry Strategy Assessment Meeting, Stouffers Dayton Plaza, Dayton, OH, Sept 1983.

56. S. L. Langenbeck, G. G. Wald, E. J. Himmel, R. F. Simenz, G. J. Hildeman, C. M. Adam, D. Hilliard and J. Bjeletich, "Elevated Temperature Aluminum Alloy Development," LR 29977, AF Contract F33615-81-C-5096, 1st Interim Report, Oct. 1981.

57. O. R. Singleton, Reynolds Metals Co., personal communication, October 1982.

58. AF Contract F33615-83-C-5132, "Direct Powder Processing," Pratt and Whitney, 1Lt. J. Y. Adkins, AFWAL/MLLS, Wright-Patterson Air Force Base, OH, (1983).

59. AF Contract F33615-83-C-5023, Lockheed, "Direct Powder Processing," 1Lt. J. Y. Adkins, AFWAL/MLLS, Wright-Patterson Air Force Base, OH, (1983).

60. J. M. Arnold, Press Release, Alcoa Public Relations Department, Pittsburgh, PA, 15 Nov. 1982.

61. W. M. Griffith and I. A. Martorell, ongoing research, AFWAL Materials Laboratory, WPAFB, OH, 1984.

62. R. H. Graham, "Putting More Muscle in Aluminum Alloys," Machine Design, January (1984), p. 128.

63. Ibid, p. 127.

64. W. M. Griffith, "Fundamentals of Aluminum," Powder Seminar for AFWAL Flight Dynamics Laboratory, 4 June 1982.

65. S. L. Langenbeck, et. al., "Elevated Temperature Aluminum Alloy Development," 2nd Interim Report L30180, AF Contract F33615-80-C-5096, April 1982.

66. E. H. Spuhler, "Alcoa Alloy X-2020," Alcoa Green Letter, July 1962.

67. J.T. Staley, Properties Related to Fracture Toughness, (1976), ASTM STP 605, p. 77.

68. S.N. Singh and M.C. Flemings, Trans TMS-AIME, Vol 245, 1969, p. 1803.

69. E. DiRusso, M. Conserra, M. Buratti, and F. Gatto, Mat Sci. Enrg., 14 (1974), p. 23.

70. R.H. Van Stone, R. H. Merchant, and J. R. Low, Jr., in "Fatigue and Fracture Toughness-Cryogenic Behavior," ASTM STP 556, (1974), p. 93.

71. J.C. Grosskreutz and G.G. Shaw, "Fracture", Ed by P.L. Pratt, 1969, p. 620.

72. C.Q. Bowles and J. Schijve, Int. J. Frac., Vol. 9, (1923), p. 171.

73. R.M. Pelloux, Trans ASM Quart, Vol 57, (1964), p. 511.

74. S.M. El-Soudani and R.M. Pellous, Met Trans, Vol. 9, (1973), p. 519.

75. R.J.H. Wanhill and G.F.J.A. Van Gestel, Aluminum, 6A, (1976), p. 653.

76. M.V. Hyatt, W. E. Quist, and J. T. Quinlivan, Met. Prog. 111 (3), (1977), p. 56.

77. H.W. Antes, S. Lipson, and H. Rosenthal, Trans TMS-AIME, 239, (1967), p. 1634.

78. Singh and Flemings, Ibid, Vol. 245, (1969), p. 1181.

79. J.H. Mulhern and H. Rosenthal, Met Trans, Vol. 2, (1971), p. 427.

80. F.G. Osterman and W.H. Reimann, "Achievement of High Fatigue Resistance in Metals and Alloys", ASTM STP 467, (1970), p. 169.

81. F. Osterman, Met Trans, 2, (1971), p. 1897.

82. L.F. Mondolfo, N. A. Gjostein, and D. W. Levinson, "Structural Changes During Aging in an Al-Zn-Mg Alloy," Trans AIME 206, (1956), p. 1378.

83. C.E. Lyman and J.B. Vander Sande, "A TEM Investigation of the Early Stages of Precipitation in an Al-Zn Mg Alloy," Met Trans, 7A, Aug. 1976, p. 1211.

84. T.H. Sanders and J.T. Staley, "Review of Fatigue and Fracture Research on High-Strength Aluminum Alloys," in "Fatigue and Microstructure," ASM 1979, pp. 467-522.

85. T.H. Sanders,R. R. Sawrtell, J. T. Staley, R. J. Bucci, and A. B. Thakker, "Effect of Microstructure on FCG of 7XXX N00019-76-C-0482, NADC, (1978).

86. L.F. Mondolfo, "Metallurgical Review", Metals and Materials, No. 153, June 1971.

87. M.E. Fine, "Precipitation Hardening of Aluminum Alloys," Met Trans., 6A, (1975), p. 625.

88. M. Abe, K. Asano, and A. Fujiwara, Met. Trans., 4A, (1973), p. 1499.

89. A.J. Sedricks, P. W. Slattery, and E. N. Pugh, "Deformation Within Precipitate-Free Zones in an Aged Al-Zn-Mg Alloy," ASM Trans Qrtly, 62, (1969), p. 815.

90. G. Thomas and J. Nutting, J. Inst. Metals, 88, (1959-60), p. 81.

91. P.C. Varley, J. Inst. Metals, 88, 1957-58, p. 337.

92. S.P. Lynch, Met. Sci. 5, Vol. 9 (1975), p. 401.

93. J.P. Lyle and W. S. Cebulak, Met. Trans., 6A, (1975), p. 685.

94. M.J. Koczak and A. Lawley, AFOSR-77-3247 Drexel, Philadelphia, PA, April 1980.

95. K.R. Van Horn, Aluminum, ASM, Vol. 1, 1968, p. 175.

96. H.Y. Hunsicker, "The Metallurgy of Heat Treatment", in Aluminum Vol. I, Ed. by K.R. Van Hor, ASM, (1971), p. 109.

97. I.J. Polmear and P.S. Young, "The Aging Characteristics of Two Commercial Alloys Based in Al-Zn-Mg. System", J. Inst. Metals, 87, (1958-59), p. 65.

98. A. Kelly and R.B. Nicholson, Progress Material Sci., 15, (1963), p. 95.

99. V.P. Spiridonor, Metal Sci. Heat-Treat., Metals, 7, (1966), p. 607.

100. L.F. Mondolfo, N. A. Gjostein, and D. W. Levinson, Trans. AIME, 206, 1956, p. 1378.

101. H. Schmalzried and W. Geral, Z. Metallkunde, 59, 1958, p. 291.

102. R.B. Nicholson et. al., J. Inst. Metals, 87, (1958-59), p. 429.

103. R. Graf and B. Gentry, "Properties des Joints de Grains", Paris (Presses Universitaires), 1961, p. 47.

104. K. Asano and K. Hirano, Trans. Japan Inst. Metals, 9, 1968, p. 24.

105. H.W. Antes, Ph.D. Thesis, Drexel University (1979).

106. W.G. Truckner, J. T. Staley, R. J. Bucci, and A. B. Thakker, "Effects of Microstructure on Fatigue Crack Growth of High Strength Al. Alloys, AFML-TR-76-169, (1976).

107. E. A. Starke, Jr., "The Causes and Effects of 'Denuded' or 'Precipitate-Free' Zones at Grain Boundaries in Aluminum-Based Alloys," J. Metals, Jan. (1970) p. 54.

108. J.A. Walker, "The Microstructure and Properties of Extruded P/M CT91-T7 x 151," MS Thesis, Georgia Institute of Technology, 1980.

109. E. Orowan, in Symposium on Internal Stress in Metals and Alloys, Inst. Metals, London, (1948), p. 451.

105

110. E. Orowan, <u>Dislocations in Metals</u>, Ed, M. Cohen, New York, (1954).

111. T.H. Sanders, Jr., "The Relationship of Microstructure to Monotonic and Cyclic Straining i Two Al-Zn-Mg Precipitation Hardening Alloys," Ph.D. Thesis, Georgia Institute of Technology, (1974).

112. H.W. Hayden, W.G. Moffatt and J. Wulff, <u>The Structure and Properties of Metals</u>, Mechanical Behavior, Vol. III, Wiley and Sons, New York, (1965).

113. R.E. Reed-Hill, <u>Physical Metallurgy Principles</u>, D. Van Nostrand and Company, Princeton, 1967.

114. S.D. Harkenss and J.J. Hren, "An Investigation of Strengthening by Spherical Coherent G.P. Zones", Met Trans, $\underline{1}$, 1970, p. 43.

115. E.A. Starke, Aluminum Workshop presented at AFWAL/MLLS, Wright-Patterson Air Force Base, OH, May 1982.

116. G.E. Dieter, Jr., <u>Mechanical Metallurgy</u>, McGraw Hill, New York, 1961.

117. G. Lutjering, T. Hanajima, and A. Gysler, "Influence of Grain Size on the Fracture of Aluminum Alloys", Fracture 1977, Vol. 2, ICF4, Waterloo, Canada, June 19-24, 1977.

118. D.P. Voss and W. Bunk, "The Structure of Rapidly Solidified, Age Hardenable Aluminum Alloy Powder Products", Proceedings of the 7th International Light Metals Conference, Vienna, 1981.

119. J. Waldman, H. Sulinski, and H. Markus, Met Trans, $\underline{5}$, (1974), p. 573.

120. Y-W. Kim and L. R. Bidwell, "Effects of Microstructure and Aging Treatment on the Fatigue Crack Growth Behavior of High Strength P/M Alumium Alloy X7091," in High Strength Powder Metallurgy Aluminum Alloys, Ed. M. J. Koczak and G. J. Hildeman, TMS-AIME, (1982) p. 107.

121. G.T. Hahn and A.R. Rosenfield, Met Trans, Vol. 6A, (1975), p. 653.

122. K.K. Sankaran, "Structure and Properties of Splat Quenched 2024-Type Aluminum Alloys Containing Lithium,"Ph.D. Thesis, MIT, 1978.

123. D. Broek, Prospects of Fracture Mechanics, Ed by G.C. Sih, H.C. Van Elst, and D. Broek, Noordhoff Int., Leyden, (1974), p. 19.

124. G.T. Hahn and A.R. Rosenfield, Paper Pl-II-211, Third International Conf. on Fracture, Munich, (1973).

125. D.S. Thompson, Met Trans., 6A, (1975), p. 671.

126. J.S. Santner, AFML-TR-76-200, (1977).

127. E. DiRusso, M. Conserva, F. Gatto and H. Markus, Met Trans., 4, (1973), p. 1133.

128. A.R. Rosenfield, C.W. Price and C.J. Martin, AFML-TR-74-129, Part I, (1974).

129. M.V. Hyatt, AFML-TR-73-224, (1973).

130. C.M. Carman, W.E. Quist and W.A. Anderson, Metallurgical Society Conference, Vol. 31, AIME, (1966), p. 227.

131. C.M. Carman, D.F. Armiento and H. Markus, Proceedings of the First International Conference on Fracture, Sendai, Japan, Vol. 2, (1965), p. 995.

132. C.J. Peel and P.J.E. Forsyth, "The Fracture Toughness of Al-Zn-Mg-Cu-Mn Alloys to DTD 5024-Effect of Iron Content", Royal Aircraft Establishment Technical Report 70162, (1970).

133. S.N. Singh and M.C. Flemings, TMS AIME, 245, (1969), p. 1811.

134. H.W. Antes and H. Markus, "Homogenization Improves Properties of 7000-Series Aluminum Alloys", Metals Engineering Quarterly, 10, (1970), pp. 9-11.

135. S.A. Levy, "Homogeneous High Strength Aluminum Alloys", presented at TMS AIME, Las Vegas, Nevada, May 1970.

136. M.O. Speidel and M.V. Hyatt, "Stress-Corrosion Cracking of High Strength Aluminum Alloys", in Advances in Corrosion Science and Technology, 2, Ed. M.G. Fontana and R.W. Stachle Plenum Press, New York, 1972, pp. 115-335.

137. S.N. Singh and M.C. Flemings, "Influence of Ingot Structure and Processing on Mechanical Properties and Fracture of a High Strength Wrought Aluminum Alloy", Trans Met Soc AIME, 245, (1969), p. 169.

138. W.H. Reimann and A.W. Brisbane, "Improved Fracture Resistance of 7075 Through Thermomechanical Processing", Engineering Fracture Mechanics, 5, (1973), pp. 67-78.

139. R.W. Hertzberg, Deformation and Fracture Mechanics of Engineering Materials, John Wiley and Sons, 1976, p. 476.

140. M.E. Fine and R.O. Ritchie, "Fatigue-Crack Initiation and Near-Threshold Crack Growth", Fatigue and Microstructure, ASM, (1979), p. 245.

141. R.O. Ritchie, "Environmentally-Sensitive Fracture of Engineering Materials", Z.A. Foroylis, Ed, TMS-AIME, 1978.

142. J.F. Knott and A.C. Packard, Met Sci, 11, (1977), p. 399.

143. J. McKittrick, MS Thesis, Northwestern University. (1979).

144. J.L. Robinson and C.J. Beevers, Met. Sci. J. 7, (1979), p. 153.

145. G.R. Yoder, L.A. Cooley, and T.W. Crooker, J. of Eng. Mat'ls and Tech. Trans. ASME H, 101, (1979) p. 86.

146. L.C. Filler, MS Thesis, Northwestern University, (1981).

147. R.J. Cooke, P.E. Irving, G.S. Booth, and C.J. Beevers, Eng. Fract. Mech. 7, (1975), p. 69.

148. P.E. Irving and C.J. Beevers, Met. Trans. 5A, (1975), p. 391.

149. A. J. McEvily and J. Groeger, "Fracture 1977", Proceedings 4th International Conference on Fracture, Waterloo, Canada, June 1977, Ed. D. M. R. Taplin, Vol. 2, p. 1293, Univ. Waterloo Press.

150. C. Bathias, A. Pinean, J. Pluvinage and P. Rabbe, IBID, ref. 11.

151. P. D. Paris and F. Erdogan, J. Basic Engr. Trans. ASME, 89, 1967, p. 528.

152. G. R. Irwin, "Plastic Zone Near a Crack and Fracture Toughness", Proceedings, Seventh Sagamore Conference, 1960, p. 1.

153. R. M. Hart, "Wrought P/M Aluminum Alloys X7090 and X7091," Alcoa Green Letter, Aluminum Company of America, Alcoa Technical Center, August 1981.

154. J. B. Conway, R. H. Stentz, and J. T. Berling, "Fatigue, Tensile and Relaxation Behavior of Stainless Steels," Mar-Test, Inc., Cincinnati, OH, (1975).

155. T. H. Sanders, Jr., J. T. Staley, and D. A. Mauney, "Strain Control Fatigue as a Tool to Interpret Fatigue Initiation of Aluminum Alloys," Fundamental Aspects of Structural Alloy Design, Ed. R. I. Jaffee and B. A. Wilcox, Plenum Publishing Corp., (1977), p. 487.

156. C. E. Feltner and M. R. Mitchell, "Basic Research on the Cyclic Deformation and Fracture Behavior of Materials," Manual on Low Cycle Fatigue, ASTM STP 465, ASTM, (1969), p. 27.

157. T. H. Sanders, Jr., and E. A. Starke, Met. Trans. 7A (1976) p. 140.

158. J. Morrow, "Cyclic Plastic Strain Energy and Fatigue of Metals," Internal Friction, Damping and Cyclic Plasticity, ASTM STP 378, ASTM (1968) p. 4.

159. C. H. Wells, "Elevated Temperature Testing Methods," Manual on Low Cycle Fatigue, ASTM STP 465, ASTM (1969) p. 87.

160. D. C. Lord and L. F. Coffin, "High Temperature Material Behavior", Ibid, p. 129.

161. N. E. Dowling, "Crack Growth During Low-Cycle Fatigue of Smooth Axial Specimens," Cyclic Stress-Strain and Plastic Deformation Aspects of Fatigue Crack Growth, ASTM, STP 637, (1977) p. 97.

162. R. G. Boettner, C. Laird, and A. J. McEvily, Jr. "Crack Nucleation and Growth in High Strain-Low Cycle Fatigue," Trans. Met. Soc. AIME, 223 (Feb. 1965) p. 379.

163. B. I. Sandor, Fundamentals of Cyclic Stress and Strain, Univ. of Wisconsin Press, Madison, WI (1972).

164. D. T. Raske and J. Morrow, "Mechanics of Materials in Low Cycle Fatigue Testing," Manual on Low Cycle Fatigue, ASTM STP 465, ASTM (1969) p. 1.

165. S. S. Manson and M. Hirschberg, Fatigue - An Interdisciplinary Approach, Syracuse Press, Syracuse, NY (1964) p. 133.

166. R. Smith, M. Hirschberg and S. S. Manson, "Fatigue Behavior of Materials Under Strain Cycling in Low and Intermediate Life Range," Report NASA-TN-D-1574, National Aeronautics and Space Administration, April 1963.

167. E. A. Starke and T. H. Sanders Jr., "The Effect of Microstructure on the Properties of High Strength Aluminum Alloys," AFOSR Annual Scientific Report, February 1981, Grant No. AFOSR-718-3471, Fracture and Fatigue Research Laboratory, Georgia Institute of Technology, Atlanta, GA.

168. C. Laird, "The General Cyclic Stress-Strain Response of Aluminum Alloys," Cyclic Stress-Strain and Plastic Deformation Aspects of Fatigue Crack Growth, ASTM STP 637, ASTM, (1977) p. 3.

169. J. .S. Santner, "The Effect of Alloy Chemistry and Heat Treatment on the Low Cycle Fatigue Behavior of 7000 Series Aluminum Alloys," Met. Trans. A, 12A, (1981) p. 1823.

170. S. S. Manson, "Behavior of Materials Under Conditions of Thermal Stress", National Advisory Committee for Aeronautics, Technical Note 2933, 1953.

171. L. F. Coffin, Jr., A Study of the Effects of Cyclic Thermal Stresses on a Ductile Material, Trans. ASME, 76 (1954) p. 931-950.

172. A. Saxena, Ph.D. Thesis, University of Cincinnati, (1974).

173. A. Saxena and S. D. Antolovich, "Low Cycle Fatigue, Fatigue Crack Propagation and Substructures in a Series of Polycrystalline Cu-Al Alloys," Met. Trans. A, 6A, (1975) p. 1809.

174. V. W. C. Kuo and E. A. Starke, "The Effect of ITMT's and P/M Processing on the Microstructure and Mechanical Properties of the X7091 Alloy," Met. Trans. A, 14A, (1983) p. 435-447.

175. R. E. Pinckert, "Damage Tolerance Assessment of F-4 Aircraft," AIAA Paper 76-904, Presented at AIAA Aircraft Systems and Technology Meeting, Dallas, TX, September 1976.

176. J. S. Santner, Ph.D. Thesis, Northwestern University, (1975).

177. F. S. Lin, "Low Cycle Corrosion Fatigue and Corrosion Fatiague Crack Propagation of High Strength 7XXX Aluminum Alloys," Ph.D. Thesis, Georgia Institute of Technology, (1978).

178. I. J. Polmear and I. F. Bainbridge, Phil. Mag. 4 (1959) p. 1293.

179. A. J. McEvily, J. B. Clark, E. C. Utley, and W. H. Herrstein, Trans. Met. Soc. AIME, 227 (1963) p. 1093.

180. C. A. Stubbington, Acta Met. 12 (1964) p. 931.

181. C. A. Stubbington and P. J. E. Forsyth, Acta Met., 14, (1966) p. 5.

182. C. Calabrese and C. Laird, Matl. Sci. Eng., 13, (1974) p. 141.

183. R. F. Hanstock, J. Inst. Metals, 83 (1954-55).

184. T. Broom, J. A. Mazza, and V. N Whittaker, J. Inst. Metals, 86, (1957-58), p. 17.

185. J. B. Clark and A. J. McEvily, Acta Met., 12 (1964) p. 1359.

186. B. L. Averback, Trans. Amer. Soc. Metals, 41, (1949), p. 262.

187. C. Laird and G. Thomas, Int. J. Fracture Mech., 3 (1967), p. 81.

188. C. Calabrese and C. Laird, Met. Trans., 5 (1974) p. 1785.

189. M. Wilhelm, M. Nageswararao, and R. Meyer, "Factors Influencing Stage I Crack Fatigue Crack Propagation in Age-Hardened Alloys," Fatigue Mechanisms,ASTM, STP 675, (1979) p. 214.

190. E. A. Starke and G. Lutjering, Cyclic Plastic Deformation and Microstructure, Fatigue and Microstructure, ASM, (1979) p. 205.

191. C. Laird, "Mechanisms and Theories of Fatigue," Fatigue and Microstructure ASM (1979) p. 205.

192. I. Telesman, M. S. Thesis, University of Cincinnati, p. 149.

TABLE 7
POWDER SIZE AND DISTRIBUTION [4]

Billet No.	US Std Screen Analysis (Wt%)				Avg Particle Diameter μm
	-50 +100	-100 +200	-200 +325	-325	
452	trace	1.2	5.2	93.4	12.6
453	0.2	1.2	10.6	87.6	14.6

TABLE 8
PROCESSING AND HEAT TREATMENT

Forge:	38% or 64% height reduction (ϵ = 0.5 or 1.0) 371°C (700°F)
Cut in half	
Solutionize:	493°C (920°F), 2 hours
Quench:	Cold Water 18°C (64°F)
Stress Relieve:	RT, 1-5% permanent deformation
Natural Age:	RT, 5 days
Artificial Age:	121°C (250°F), 24 hours + 163°C (325°F), 4 hours + Air Cool

TABLE 6

COMPOSITIONS OF ALLOYS STUDIED

	Wt% Alcoa Melt Analysis [4]		Wt% Check Analysis (*)		Billet No.
	452	453	452	453	
	6.36	6.40	6.5	6.55	Zn
	2.48	2.37	2.5	2.55	Mg
	1.51	1.47	1.5	1.55	Cu
	-	0.40	-	0.35	Co
	0.06	0.07	0.07	.07	Si
	0.06	0.07	0.05	.05	Fe
	N/A	N/A	<.01	<.01	Mn
	N/A	N/A	<.01	<.01	Ti
	N/A	N/A	<.002	<.002	B
	N/A	N/A	0.79	0.79	O
	BAL	BAL	BAL	BAL	AL

*average of top and bottom of 2 billets each

126

TABLE 5

TYPICAL PROPERTIES FOR Al P/M AND I/M ALLOYS [20]

Alloy	Temp** °C	YS MPa (ksi)	UTS MPa (ksi)	% el	E GPa (Msi)	Density g/cc
		HIGH STRENGTH ALLOYS				
7090-T7E71	RT	586 (85)	627 (91)	10	73.8 (10.7)	2.85
7091-T7E69	RT	545 (79)	593 (86)	12	72.4 (10.5)	2.82
P/M 64	RT	627 (91)	655 (95)	13	-	-
I/M 7075-T6	RT	600 (87)	682 (99)	10	71.7 (10.4)	2.80
I/M 7075-T73	RT	503 (73)	552 (80)	12	71.7 (10.4)	2.80
		LOW DENSITY ALLOYS				
Al-Cu-Mg-3Li*	RT	571 (83)	583 (84.5)	5	85.0 (12.3)	2.52
Al-Cu-Mg-2.5Li*	RT	373 (54.1)	483 (70.1)	10	83.5 (12.1)	2.59
I/M 2020	RT	531 (77.0)	579 (84.0)	7	76.0 11.1	2.71
		HIGH TEMPERATURE ALLOYS				
Al-8Fe	RT	504 (73.1)	572 (83.0)	5	81.4 (11.8)	-
	232	260 (37.7)	280 (40.6)	10	55.2 (8.0)	-
	343	148 (21.4)	172 (24.9)	12	40.0 (5.8)	-
Cu 78	RT	445 (64.5)	550 (79.8)	9	-	-
(Al-Fe-Ce)	232	367 (53.3)	395 (57.3)	6	-	-
	343	152 (22.0)	176 (25.5)	7	-	-

*See Table 4 for complete composition

**Exposure time > 100 hours where applicable

TABLE 4
NOMINAL COMPOSITIONS FOR Al P/M ALLOYS [20, 66]

Wt%

Alloy	Zn	Mg	Cu	Si	Fe	O	Mn	Cr	Zr	Co	Ce	Li	Developer
						HIGH STRENGTH ALLOYS							
7090	7.7	2.5	1.0	<.12	<.15	0.35	-	-	-	1.5	-	-	Alcoa
7091	6.3	2.5	1.5	<.12	<.15	0.35	-	-	-	0.4	-	-	Alcoa
P/M 64	7.0	2.3	2.0	-	-	-	-	0.1	0.2	0.2	-	-	Kaiser
I/M 7075	5.6	2.5	1.6	0.40	0.50	-	0.30	0.23	-	-	-	-	-
I/M 7050	6.2	2.3	2.3	0.12	0.15	-	0.10	0.04	0.12	-	-	-	-
						LOW DENSITY ALLOYS							
Al-Li#1	-	1.1	3.4	-	-	-	0.6	-	-	-	-	3.2	MIT
Al-Li#2	-	1.7	3.1	-	-	-	0.6	-	-	-	-	2.5	Lockheed
I/M 2020	-	-	4.5	-	-	-	0.5	-	0.2 Cd	-	-	1.1	Alcoa
Cu 78	-	-	-	-	8.0	-	-	-	-	-	4.0	-	Alcoa

124

TABLE 3

AIR FORCE GOALS FOR P/M [1]
ALUMINUM ALLOY FAMILIES

Alloy Families	Goals
A. High strength, high toughness, corrosion resistant	1. 10%-20% higher strength 2. 20%-40% higher fatigue resistance
B. Decreased density, increased modulus, increased specific strength	1. 20%-30% higher modulus/density 2. 20% higher strength/density
C. Increased temperature capability	1. Density modified strength equivalent to Ti-6Al-4V to 230°C (450°F) and above

123

TABLE 1

INCREASED LIMITS OF SOLID SOLUBILITY IN ALUMINUM BINARY

ALLOYS DUE TO RAPID SOLIDIFICATION [8]

Element	Maximum solubility at equilibrium, (a/o)	Maximum reported increased solid solubility, (a/o)
Cr	0.4	6
Co	0.01	5
Fe	0.02	6
Ni	0.02	8
Si	1.6	16
Mo	0.08	1
Ce	0.01	2

TABLE 2

DECOMPOSITION REACTIONS OF Al-HYDROXIDES [18]

$$Al_2O_3 \cdot 3H_2O \longrightarrow Al_2O_3 + 3H_2O \tag{1}$$

$$Al_2O_3 \cdot 3H_2O \longrightarrow Al_2O_3 \cdot H_2O + 2H_2O \tag{2}$$

$$2Al + 6H_2O \longrightarrow Al_2O_3 \cdot 3H_2O + 3H_2 \tag{3}$$

$$Al_2O_3 \cdot H_2O \longrightarrow Al_2O_3 + H_2O \tag{4}$$

$$2Al + 3H_2O \longrightarrow Al_2O_3 + 3H_2 \tag{5}$$

$$Al_2O_3 \longrightarrow \gamma\text{-}Al_2O_3 \tag{6}$$

122
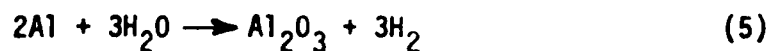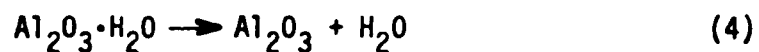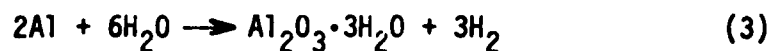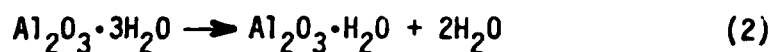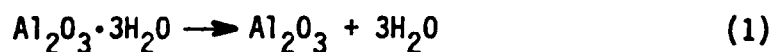
263. G. Sertour and C. Bathias, "Influence of Microstructure on the Growth of Fatigue Cracks," AGARD Report No. 610, Metallurgical Aspects of Fatigue and Fracture Toughness, Dec. 1973, p. 77.

264. L. Edwards and J. W. Martin, "Effect of Dispersoids on Fatigue Crack Propagation in Aluminum Alloys," Metal Sciencel, 17, (1983) p. 511.

265. G. R. Yoder, L. A. Cooley, and T. W. Crooker, Met. Trans. 8A, 1977, p. 1737.

266. G. R. Yoder, L. A. Cooley, and T. W. Crooker, Titanium 80, H. Kimura and O. Izuci, eds., Vol. 3, AIME, Warrendale, PA, 1980, p. 1865.

267. G. R. Yoder, L. A. Cooley, and T. W. Crooker, ASTM STP 791, Vol. I, 1983, p. I-348.

251. M. V. Hyatt and M. O. Speidel, "High Strength Aluminum Alloys," in <u>Stress-Corrosion Cracking in High Strength Steels and in Titanium and Aluminum Alloys</u>, Ed. B. F. Brown, Naval Research Laboratory, Washington, DC (1972).

252. J. Cammett, Metcut, Personal Communication (1982).

253. G. G. Wald, D. J. Chelman, and S. L. Langenbeck, Advanced Aluminum Alloys, Lockheed Report LR 30415, (1983) p. 5.507.

254. F. A. McClintock and G. R. Irwin, ASTM STP 381, 1965, p. 84.

255. E. A. Calnan and C. J. B. Clews, Phil. Mag., <u>42</u>, (1951) p. 616.

256. R. E. Sanders, Jr., and E. A. Starke, Jr., Mater. Sci. and Engr., <u>28</u>, (1977) p. 53.

257. R. E. Sanders, Jr., and E. A. Starke, Jr., Met. Trans. <u>9A</u> (1978) p. 1087.

258. E. A. Starke, Jr., Mater. Sci. Engr., <u>29</u>, (1977) p. 99.

259. S. Ikeda, Y. Izumi, and M. E. Fine, Engg. Fract. Mech. <u>9</u> (1977), p. 123.

260. P. K. Liaw and M. E. Fine, Metall. Trans., <u>12A</u> (1981) p. 1927.

261. M. E. Fine and Y. Izumi, in 4th International Conference on the Strength of Metals and Alloys, Vol. 2, Laboratoire de Physique du Solide, Nancy, France (1976), p. 468.

262. J. L. Lankford, D. L. Davidson, G. R. Leverant, J. E. Hack, and R. M. Arrowood, "Study of Fatigue Mechanisms in Aerospace Structural Materials," AFOLSR Annual Report on Contract F49 620-78-C-0022, Southwest Research Institute, February 1982.

241. T. M. F. Ronald, J. A. Hall, and C. M. Pierce, "Usefulness of Precracked Charpy Specimens for Fracture Toughness Screening Tests of Titanium Alloys," Met. Trans., 3, (1972) p. 813.

242. T. M. F. Ronald, "A Study of Tempered Martensite Embrittlement Using Standard and Subsize V-Notch Charpy Specimens," AFML-TR-68-388, 1969.

243. T. M. F. Ronald, J. A. Hall, and C. M. Pierce, "Some Observations Pertaining to Simple Fracture Toughness Screening Tests for Titanium," AFML-TR-60-311, 1971.

244. S. H. Doerr, "A Comparison of Microstructure and Properties of Equivalent Strength Ingot Metallurgy and Powder Metallurgy 7XXX Aluminum Alloys," AFWAL-TR-81-4068, 1981.

245. S. L. Langenbeck and D. L. Chellman, "Advanced Aluminum Alloys," LR-30415, (1983) pp. 5-507 - 5-541.

246. G. G. Wald, D. J. Chellman, and S. L. Langenbeck, "Advanced Aluminum Alloys," LR-30152, 1982 p. 7501.

247. J. Potter, AFWAL/FIB, Personal Communication, 1979.

248. G. Chanani, Northrop Corporation, Personal Communication, 1979.

249. D. R. Holloway, "X-Ray Diffraction Measurements of Crack-Tip Stresses as a Crack Advances Through a Single Overload Affected Zone," AFFDL-TR-79-3006, 1979.

250. J. Schijve, "Internal Fatigue Cracks are Growing in Vacuum," Engineering Fracture Mechanics, 10 (1978) p. 359.

232. Y-W. Kim and W. M. Griffith, "Annealing and Tensile Properties of Elevated Temperature P/M Aluminum Alloys," to be published in Proceedings of ASTM Symposium on Rapidly Solidified Powder Aluminum Alloys, (1984).

233. R. E. Sanders, Jr., "Compilation and Review of Available Fatigue Data for 7XXX P/M Alloys", Alcoa Report No. 56-79-AFSZ, 1979.

234. D. J. Skinner, R. Ker, M. J. Koczak and A. Lawley, "The Aging Response of a High-Strength P/M Aluminum Alloy," in Modern Developments in Powder Metallurgy; Ed. by H. H. Hausner, H. W. Antes, and G. D. Smith, MPIF, Princeton, NJ, Vol. 13, p. 483 (1981).

235. "Alcoa Stress Relieved Forgings," Alcoa Aerospace Technical Information Bulletin Series 68, No. 2, 1968.

236. R. E. Sanders and E. A. Starke, Thermomechanical Processing of Al Alloys, Ed. by J. G. Morris, TMS-AIME, (1978), p. 50.

237. R. E. Sanders and E. A. Starke, Met. Trans., 9A, (1978), p. 1987.

238. E. K. Weaver, J. J. Scutti, O. R. Singleton, and H. M. Edwards, "High Strength P/M Aluminum Mill Products, Phase II: Sinter-Seal Process Scale-Up," 8th Interim Report, Contract F33615-79-C-5161, 1983.

239. S. L. Langenbeck and J. M. Cox, "Charcterization of Fatigue Crack Growth Behavior of X7091-T7E69 Extrusion," presented at 1982 TMS-AIME Fall Meeting, St. Louis, MO (1982).

240. R. M. Hart, "Alcoa Green Letter: Wrought Aluminum P/M Alloys X7090 and X7091," Aluminum Company of America, Alcoa Center, PA, 1981.

222. A. F. Grandt, "Evaluation of a Cracked Ring Specimen For Fatigue Testing Under Constant Range in Stress Intensity", Proceedings of the International Conference on Fracture Mechanics and Technology, Hong Kong, 1976.

223. N. Bredz and C. C. Tennenhouse, Metal-Metal Oxide - Hydrogen Atmosphere Chart for Brazing or Bright Metal Processing, Welding Research, Supplement to The Welding Journal, May 1970.

224. W. R. Graff and D. C. Sargent, "A New Grain-Boundary Etchant for Aluminum Alloys," Metallography 14:69-72 (1981).

225. Metals Handbook, Vol. 8, Eighth Edition, Metals Park, Ohio, (1973), p. 120.

226. M. M. Cook and W. M. Griffith, unpublished research, AFWAL Materials Laboratory, (1978).

227. S. Hirose, Ph.D. Dissertation, Northwestern University, 1981.

228. M. M. Cook and Y-W. Kim, "A Study of the Recrystallization and Grain Growth Behavior in a High Strength Aluminum P/M Alloy X7091," Microstructural Science, 10, (1982), p. 33.

229. K. E. Buchovecky and M. R. Rearick, "Aluminum P/M Forgings", Metal Progress, February, 1972.

230. J. A. Walker and E. A. Starke, "The Microstructure and Properties of an Extruded P/M X7091 Plate, submitted to Powder Metallurgy, November 1982.

231. J. W. Bohlen, S. G. Roberts, and G. R. Chanani, "Investigation of Improved Methods for Consolidation Rapidly Solidified Aluminum Alloy Powders", Final Report, N60921-80-C-0238, 1982.

211. S. B. Chakrabortty, "A Model Relating Low Cycle Fatigue Proper-
     ties and Microstructure to Fatigue Crack Propagation Rates",
     Fatigue of Engineering Materials and Structures, 2, (1979), p.
     331.

212. E. Hainbogen and K. H. Zum Gahr, "Microstructure and Fatigue
     Crack Growth in a γ-Fe-Ni-Al Alloy, Acta Met, 24, (1976),
     p. 581.

213. A. M. Freudenthal, "Fatigue and fracture Mechanics", Engineering
     Fracture Mechanics, 5, (1973), p. 403.

214. S. R. Swanson, F. Cici, and W. Hoppe, Fatigue Crack Propagation,
     ASTM STP 415, (1967), p. 312.

215. D. F. Wilhelm, IBID, p. 363.

216. J. Schijve, IBID, p. 415.

217. L. P. Pook, Stress Analysis and Growth of Cracks, ASTM STP,
     (1971), p. 106.

218. F. A. McClintock, Fracture of Solids, Wiley, New York, p. 65.

219. G. Chanani, S. D. Antolovich, and W. W. Gerberich, Met Trans, 3
     (1972), p. 649.

220. A. Saxena and S. D. Antolovich, Met. Trans, 6A, 1975, p. 1809.

221. ASTM Standard E647, "Standard Test Method for Constant-Load-
     Amplitude Fatigue Crack Growth Rates Above 10^{-8} m/cycle," 1978
     Annual Book of ASTM Standards, Part 10, p. 662.

116

202. J. P. Bailon and S. D. Antolovich, "Effect of Microstructure on Fatigue Crack Propagation: A Review of Existing Models and Suggestions for Further Research," Fatigue Mechanisms: Advance in Quantitative Measurement of Physical Damage, ASTM STP 811, J. Lankford, D. L. Davidson, W. L. Morris, and R. P. Wei, Eds., ASTM 1983, pp. 313-349.

203. A. G. Forman, Journal of Basic Engineering, 89, 1967, pp.459.

204. N. E. Frost and J. R. Dixon, Int. J. Fract. Mech., 9.

205. K. Walker, "The Effect of Stress Ratio During Crack Propagation and Fatigue for 2024-T3 and 7075-T6 Aluminum", Effects of Environment and Complex Load History on Fatigue Life, ASTM STP 462, (1970), p. 1.

206. W. Elber, "The Significance of Fatigue Crack Closure," Damage Tolerance in Aircraft Structures, ASTM STP 486, (1971), p. 230.

207. J. Weertman, "Fatigue Crack Propagation Theories", Fatigue and Microstructure, ASM, Metals Park, Ohio, (1979), p. 270.

208. T. Yokobori, S. Konosu, A. T. Yokoburi, Jr., Fracture 1977, ICF4, D. R. M. Taplin, Ed., Waterloo Canada, Vol. 1, 1977, p. 665.

209. S. D. Antolovich, A. Saxena, and G. R. Chanani, Engineering Fracture Mechanics, 7, (1975), p. 649.

210. J. Lanteigne and J. P. Bailon, Met. Trans., 12A, 1981, p. 459.

193. J. Morrow, ASTM STP 467 (1970) p. 4587.

194. P. S. Maiya and D. E. Busch, Met. Trans A, $\underline{6A}$ 1975 p. 1761.

195. M. R. James and W. L. Morris, The Role of Plastic Deformation in Crack Initiation," Fatigue Mechanisms: Advances in Quantatative Measurements of Physical Damage, ASTM STP 811, 1983 p. 46.

196. F. Billman, Aloca Technical Center, Private Communication, 1983.

197. J. S. Santner, "Effect of Defects in Aluminum P/M," AFWAL-TR-81-4144, 1981.

198. W. Schutz, "The Prediction of Fatigue Life in the Crack Initiation and Propagation Stages", A State of the Art Survey, Engineering Fracture Mechanics, Vol. II, p. 405, Permagon Press, 1979, p. 405.

199. R. M. Pelloux, "Review of Theories and Laws of Fatigue Crack Propagation", AFFDL-TR-70-144, 1970.

200. D. Schutz and J. J. Gerharz, "Critical Remarks on the Validity of Fatigue Life Evaluation Methods Based on Local Stress Strain Behavior," Cyclic Stress-Strain and Plastic Deformation Aspects of Fatigue Crack Growth, ASTM STP 637, 1977, p. 209.

201. J. P. Gallagher, Letter to Members of Task Group E24.04 on FCGR Descriptions, 11 December 1978.

114

TABLE 9
NOMENCLATURE

Condition	Forging Strain		Cobalt		Stress Relief	
	$\epsilon = .5$	$\epsilon = 1$	0%	0.4%	No	Yes
000	X		X		X	
001	X		X			X
010	X			X	X	
011	X			X		X
100		X	X		X	
101		X	X			X
110		X		X	X	
111		X		X		X

TABLE 10

TENSILE DATA FOR CT91 CHANNEL DIE FORGINGS

FORGING*	YS Mpa	(ksi)	UTS Mpa	(ksi)	%el in 4d	%RA	MPa (psi x 10^{-6})
S1 (4) L	565.8	(82.0)	611.3	(88.6)	11.6	20.8	69.0 (10.0)
S1R (4) L	563.0	(81.6)	609.3	(88.3)	12.3	22.3	66.9 (9.7)
S3 (4) L	549.9	(79.7)	590.6	(85.6)	10.9	25.2	66.2 (9.6)
S3R (4) L	547.2	(79.3)	595.5	(86.3)	11.0	24.5	67.6 (9.8)
S4L (1) L	547.3	(79.3)	583.4	(84.6)	9.0	26.0	68.3 (9.9)
S4RL(1) L	541.7	(78.5)	592.0	(85.8)	8.5	21.9	65.6 (9.5)
S4T (5) T	527.9	(76.5)	572.0	(82.9)	9.6	18.1	68.3 (9.9)
S1T (1) T	529.9	(76.8)	578.9	(83.9)	10.4	21.9	67.6 (9.8)
S3T (1) T	541.0	(78.4)	581.7	(84.3)	10.6	18.4	60.0 (8.7)
S4RT(5) T	532.7	(77.2)	578.9	(83.9)	9.8	17.6	68.3 (9.9)
S3RT(1) T	529.9	(76.8)	580.3	(84.1)	12.8	19.3	68.3 (9.9)

( ) = replication

129

TABLE 11

ALUMINUM ALLOY CT91 AND SIMILAR ALLOYS

Alloy[a]	Product[b]	UTS MPa (ksi)	YS MPa (ksi)	%el	%RA	K_Q MPa$\sqrt{m}$ (ksi $\sqrt{in.}$)	ORIENT.[c]	REFERENCE
0% CT91	UF	570 (82.6)	523 (75.8)	10.0	25	33.9 (30.8)	T-L	THIS STUDY
CT91	UF	601 (87.1)	555 (80.4)	9.9	25.1	32.9 (29.9)	T-L	THIS STUDY
7091	UF	599 (86.8)	570 (82.5)	13.7	32	43.7 (39.8)	L-T	7
7091	UF					29.0 (26.4)	T-L	7
7091	DF	600 (87.0)	551 (79.8)	8	18	25.8 (23.5)	L-T	238
7091	DF					19.9 (18.1)	T-L	238
7091	E	579 (84)	531 (77)	13	--	36 (33)	L-T	153
0% 7091	UF	561 (81.3)	508 (73.8)	14.2	30.5	--	--	49
7091	UF	557 (80.8)	512 (74.3)	13.6	33	--	--	5
7091	UF	565 (81.9)	516 (74.9)	12.1	33	--	--	5
CT91	UF	567 (82.2)	522 (75.7)	9.0	23	--	--	105
CT91	DF	593 (86.0)	547 (79.3)	10.9	21	16.4 (14.9)	L-T	8
CT91	DF					17.8 (16.2)	T-L	8
MA87	DF	549 (79.6)	498 (72.2)	12.9	32	45.3	L-T	2

[a] all alloys heat treated to T7E69 or equivalent

[b] UF = Uniaxial Forging
DF = Die Forging
E = Extrusion

[c] first letter is direction of load application; second letter is direction of crack growth.

130

TABLE 12

TENSILE DATA FOR CT91 CHANNEL DIE FORGINGS

CONDITION*	SAMPLE	YS MPa	YS ksi	UTS MPa	UTS ksi	% el	% RA	n**
000	D3	535.4	77.6	574.8	83.3	11.2	27.0	.019
	D4	514.1	74.5	556.8	80.7	10.7	29.4	.022
	D5	536.1	77.7	580.3	84.1	10.2	25.3	.020
	DD1	535.4	77.6	579.6	84.0	11.5	25.8	.021
	DD2	534.8	77.5	578.9	83.9	10.2	26.6	.021
	AVG	531.3	77.0	574.1	83.2	10.8	26.8	.021
001	D3R	523.7	75.9	572.7	83.0	10.7	28.5	.023
	D4R	507.8	73.6	555.5	80.5	11.2	25.4	.024
	D5R	528.5	76.6	577.5	83.7	11.0	28.4	.024
	DD1R	529.9	76.8	576.8	83.6	10.0	27.7	.023
	DD2R	550.6	79.8	598.9	86.8	10.0	15.4	.022
	AVG	527.9	76.5	576.2	83.5	10.6	25.8	.023
010	TT3	558.9	81.0	603.8	87.5	10.6	25.3	.020
	TT4	561.7	81.4	603.1	87.4	10.5	23.3	.019
	TT5	557.5	80.8	600.3	87.0	10.9	28.7	.020
	WW1	556.8	80.7	601.0	87.1	10.3	23.1	.020
	WW2	559.6	81.1	603.1	87.4	9.4	24.6	.021
	AVG	558.9	81.0	602.4	87.3	10.3	25.0	.020
011	TT3R	556.1	80.6	605.1	87.7	11.0	25.9	.024
	TT4R	561.7	81.4	611.3	88.6	12.5	35.0	.022
	TT5R	549.2	79.6	602.4	87.3	10.7	27.8	.025
	WW1R	563.0	81.6	610.6	89.3	10.3	24.1	.023
	WW2R	565.8	82.0	610.6	89.3	11.7	34.8	.023
	AVG	558.9	81.0	620.0	88.4	11.2	29.5	.023

* Condition nomenclature: See Table 9
** n = strain hardening exponent

131

TABLE 12 (Cont'd)

TENSILE DATA FOR CT91 CHANNEL DIE FORGINGS

CONDITION*	SAMPLE	YS MPa	YS ksi	UTS MPa	UTS ksi	% el	% RA	n**
100	21	514.7	74.6	557.5	80.8	10.0	34.2	.020
	22	520.3	75.4	577.5	83.7	8.6	20.9	.029
	23	529.9	76.8	576.8	83.6	9.3	22.2	.023
	24	512.0	74.2	555.5	80.5	8.0	26.3	.024
	30	539.6	78.2	580.3	84.1	10.6	26.3	.019
	AVG	523.0	75.8	569.3	82.5	9.3	26.0	.023
101	21R	516.8	74.9	565.8	82.0	8.5	18.8	.024
	22R	499.6	72.4	552.7	80.1	8.3	22.4	.029
	23R	510.6	74.0	556.8	80.7	8.8	20.1	.024
	24R	506.5	73.4	556.1	80.6	10.6	25.2	.024
	30R	511.3	74.1	562.4	81.5	10.1	20.2	.025
	AVG	509.2	73.8	558.9	81.0	9.3	21.3	.025
110	15	545.1	79.0	590.0	85.5	9.0	22.3	.021
	17	569.3	82.5	610.0	88.4	10.0	23.0	.019
	18	557.5	80.8	603.1	87.4	7.5	16.8	.022
	19	567.9	82.3	620.3	89.9	11.3	21.2	.023
	20	555.5	80.5	594.1	86.1	7.5	25.8	.023
	AVG	558.9	81.0	603.8	87.5	9.1	21.8	.022
111	15R	538.2	78.0	581.0	84.2	8.4	25.7	.023
	17R	531.3	77.0	577.5	83.7	6.3	20.4	.026
	18R	547.9	79.4	594.1	86.1	9.6	25.2	.022
	19R	547.2	79.3	589.3	85.4	10.8	25.7	.020
	20R	544.4	78.9	592.0	85.8	8.9	22.9	.025
	AVG	541.7	78.5	586.5	85.0	8.8	24.0	.023

* Condition nomenclature: see Table [9]
** n = strain hardening exponent

TABLE 13

RESULTS OF TESTS USED TO DETERMINE THE APPLICABILITY
OF PRECRACKING TO FAILURE FOR CALCULATION OF K_Q

SAMPLE*	ORIENTATION	a CRACK LENGTH, cm	(in.)	K_Q MPa√m̄	ksi√in.
A1	LT	0.648	0.255	40.5	36.8
A2	LT	0.668	0.263	44.3	40.3
A3	LT	0.632	0.249	38.0	34.5
A4	LT	0.665	0.262	43.8	39.8
A5	LT	0.658	0.259	42.4	38.5
A6	LT	0.653	0.257	41.5	37.7
D1	LT	0.663	0.261	43.3	39.4
D2	LT	0.653	0.257	41.5	37.7
D3	LT	0.640	0.252	39.2	35.6
D4	LT	0.627	0.247	37.2	33.8
D5	LT	0.658	0.259	38.4	34.9
D6	LT	0.638	0.251	38.8	35.3
A7	TL	0.615	0.242	35.3	32.1
D7	TL	0.610	0.240	34.7	31.5
D8	TL	0.620	0.244	36.1	32.8

A = Forging 43R, Condition 101

D = Forging DD3R, Condition 001

133

TABLE 14
RESULTS OF FRACTURE TOUGHNESS TESTING

CONDITION	SAMPLE	CRACK LENGTH, cm (in.)		K_Q MPa$\sqrt{m}$	ksi$\sqrt{in.}$
000	TBB4	0.541	(0.213)	34.3	(31.2)
	D2T	0.511	(0.201)	31.0	(28.2)
001	D2RT	0.505	(0.199)	30.6	(27.8)
	D1RT	0.521	(0.205)	31.4	(29.2)
010	T5T	0.490	(0.193)	29.2	(26.5)
	T4T	0.513	(0.202)	31.4	(28.5)
011	TT1RT	0.528	(0.208)	32.9	(29.9)
	TT2RT	0.587	(0.231)	40.4	(36.7)
100	6TEX	0.533	(0.210)	33.4	(30.4)
	12TEX	0.569	(0.224)	37.8	(34.4)
101	9RTEX	0.546	(0.215)	35.0	(31.8)
	12RTEX	0.559	(0.220)	36.5	(33.2)
110	14T	0.508	(0.200)	30.8	(28.0)
	10T	0.523	(0.206)	32.3	(29.4)
111	13R	0.531	(0.209)	33.2	(30.2)
	14R	0.513	(0.202)	17.8	(16.2)

TABLE 15

RESULTS OF RESIDUAL STRESS MEASUREMENTS

RESIDUAL STRESS, MPa (ksi)

SAMPLE	Side 1	Side 2	Side 3	Side 4	EQUIPMENT
BB2TL	-	-310.5 (-45)	-	-310.5 (-45)	Fastress
3LT	-	-621.0 (-90)	-	-621.0 (-90)	Fastress
BB3RLT	-89.7 (-13)	-227.7 (-33)	-144.9 (-21)	-172.5 (-25)	Rigaku
BB3LT	-158.7 (-23)	-131.1 (-19)	-186.3 (-27)	-186.3 (-27)	Rigaku

135

TABLE 16

FCP DATA FOR RINGS UNSTRESS-RELIEVED

SAMPLE	CONDITION	ΔK*	da/dN**	COMMENTS
D2	000	11 (10)	27.7 (10.9)	o.k.
D2	000	5.5 (5)	3.1 (1.23)	o.k.
BB2	000	5.5 (5)	5.1 (1.29)	May be o.k.
BB3	000	7.7 (7)	5.4 (2.12)	shear lip
BB4	000	7.7 (7)	11.0 (4.33)	reduced data region o.k.
BB5	000	11 (10)	29.0 (11.4)	o.k.
D1	000	11 (10)	11.2 (4.4)	severe shear lips
T1	010	5.5 (5)	-	no data, overloaded
T3	010	7.7 (7)	13.5 (5.30)	o.k.
T4	010	7.7 (7)	4.3 (1.71)	severe shear lips
T5	010	11 (10)	12.2 (4.82)	severe shear lip
12	100	5.5 (5)	4.0 (1.56)	o.k.
12	100	11 (10)	15.0 (5.9)	o.k.
5	100	7.7 (7)	9.4 (3.7)	o.k.
9	100	7.7 (7)	9.4 (3.7)	o.k.
4	100	7.7 (7)	5.2 (2.04)	severe shear lip
3	110	5.5 (5)	-	no data, 1,060,000 cycles of no crack
14	110	11 (10)	31.5 (12.4)	growth out of plane
25	110	11 (10)	-	crack started at steep angle
26	110	11 (10)	-	machine overload/ electrical spike

* MPa√m̅(ksi√i̅n̅.)
** m/cycle x 10^8(in./cycle x 10^6)

136

TABLE 16 (Cont'd)
STRESS-RELIEVED

SAMPLE	CONDITION	ΔK*	da/dN**	COMMENTS
BB1R	001	11 (10)	-	uneven cracking - crack remained uneven
BB2R	001	5.5 (5)	2.4 (0.96)	uneven
D2R	001	11 (10)	16.3 (6.4)	
D2R	001	5.5 (5)	0.4 (0.14)	evidence of crack closure $(\Delta K_{eff} < \Delta K)$
BB3R	001	7.7 (7)	4.8 (1.9)	slight angle
BB4R	001	7.7 (7)	5.1 (2.0)	shear lips - may be o.k.
BB5R	001	11 (10)	13.0 (5.12)	severe shear lips
D1R	001	11 (10)	-	no cracking after 486,500 cycles
TT2R	011	5.5 (5)	2.2 (0.86)	o.k.
TT2R	011	11 (10)	13.5 (5.3)	o.k.
T1R	011	5.5 (5)	1.5 (0.6)	slightly uneven (0.020)
T2R	011	5.5 (5)	1.5 (0.6)	slightly uneven
T3R	011	7.7 (7)	6.9 (2.7)	
T4R	011	7.7 (7)	6.4 (2.5)	o.k.
TT1R	011	11 (10)		crack started at high angle
12K	101	5.5 (5)	1.30 (0.51)	borderline uneven - probably o.k.
12K	101	11 (10)	14.2 (5.6)	o.k.
32R	101	5.5 (5)	-	cracked one side only until failure
2R	101	5.5 (5)	0.6 (0.23)	grew across sample
4R	101	7.7 (7)	5.8 (2.3)	o.k.
5R	101	7.7 (7)	5.1 (2.0)	o.k.

*MPa$\sqrt{m}$(ksi$\sqrt{in}$.)
**m/cycle x 10^8(in./cycle x 10^6)

TABLE 16 (Cont'd)
STRESS-RELIEVED

SAMPLE	CONDITION	ΔK*	da/dN**	COMMENTS
9R	101	11 (10)	16.5 (6.5)	slight angle probably o.k.
36R	101	11 (10)	8.4 (3.3)	severe shear lip - early data o.k.
26R	111	5.5 (5)	2.9 (1.13)	crack uneven
26R	111	11 (10)	15.2 (6.0)	borderline o.k.
3R	111	5.5 (5)	1.9 (0.73)	borderline uneven
10R	111	5.5 (5)	1.5 (0.61)	some shear lips, probably o.k.
11R	111	7.7 (7)	5.1 (2.0)	some shear lip (late)
13R	111	7.7 (7)	6.6 (2.6)	o.k.
14R	111	11 (10)	8.6 (3.4)	grew at steep angle
25R	111	11 (10)	-	not enough data

*Mpa$\sqrt{m}$(ksi$\sqrt{in.}$)
**m/cycle x 10^8(in./cycle x 10^6)

138

TABLE 17
ACCEPTED FCPR DATA**

CONDITION

ΔK*	000	010	100	110
5.5 (5)	3.0 (1.2)	- -	3.8 (1.5)	- -
7.7 (7)	10.9 (4.3)	13.5 (5.3)	9.4 (3.7)	- -
11 (10)	27.7 (10.9)	- -	15.0 (5.9)	31.5 (12.4)
	29.0 (11.4)			

ΔK*	001	011	101	111
5.5 (5)	2.5 (1.0)	2.3 (0.9)	1.3 (0.5)	1.5 (0.6)
7.7 (7)	4.8 (1.9)	6.9 (2.7)	5.8 (2.3)	5.1 (2.0)
11 (10)	5.1 (2.0)	6.4 (2.5)	5.1 (2.0)	6.6 (2.6)
	16.3 (6.4)	13.5 (5.3)	14.2 (5.6)	15.2 (6.0)
	13.0 (5.1)		16.5 (6.5)	

*MPa√m̄(ksi√in.)
**m/cycle x 10^8(in./cycle x 10^6)

139

TABLE 18
PARIS LAW* CONSTANTS

THIS STUDY	A**		m
ALL SPECIMENS	198.15	(78.01)	2.97
64% forgings	130.46	(51.36)	3.15
38% forgings	299.24	(117.81)	2.80
0% Co	249.76	(98.33)	2.86
0.4% Co	120.09	(47.28)	3.23
unstress relieved	432.24	(170.17)	2.78
stress relieved	167.90	(66.10)	2.96
T-L CT Specimens			
001	5.8	(2.29)	2.62
011	7.7	(3.02)	2.52
101	11.6	(4.57)	2.28
111	7.0	(2.75)	2.58
Other Data [8]			
L-T 0% Co A Forging	5.0	(1.98)	2.23
T-L 0% Co A Forging	24.4	(9.61)	3.71
L-T 0.4% Co A Forging	110.0	(43.31)	1.86
T-L 0.4% Co A Forging	4.1	(1.61)	4.66
L-T 0% Co ABC Forging	619.0	(243.7)	2.06
T-L 0% Co ABC Forging	11.9	(4.69)	3.96
L-T 0.4% Co ABC Forging	548.9	(216.1)	2.23
T-L 0.4% Co ABC Forging	207.0	(81.5)	2.9
L-T CT91 ϵ = 0	4.0	(1.58)	5.7
L-T CT91 ϵ = 0.5	630.9	(248.4)	3.6
L-T CT91 ϵ = 0.7	513.1	(202.0)	3.9
L-T 7475 I/M	3.7	(1.44)	11.3

* $da/dN = A\Delta K^m$ ** m/cycle x 10^{12} (in./cycle x 10^{10})

140

TABLE 19

FATIGUE CRACK PROPAGATION RATES FOR HIGH STRENGTH P/M ALUMINUM ALLOYS

da/dN, * m/cycle x 10^8 (in./cycle x 10^6)

ALLOY	PRODUCT	ORIENT	ΔK MPa√m(ksi√in.)			REF
			5.5 (5)	7.7 (7)	11 (10)	
CT91	forging	T-L	5.1 (2)	17.8 (7)	76.2 (30)	2
CT91	38% forging	L-T	- (-)	1.0 (0.4)	7.1 (2.8)	8
	64% forging	L-T	- (-)	7.1 (2.8)	10.9 (4.3)	8
CT91	extrusion	L-T	2.0 (0.8)	7.1 (2.8)	- (-)	9
7091	extrusion	L-T	5.6 (2.2)	12.7 (5)	30.5 (12)	7
CT91	forging	L-T	1.3-3.8 (0.5-1.5)	4.8-13.5 (1.9-5.3)	13.0-31.5 (5.1-12.4)	This Study
CT91	forging	T-L	7.1 (2.8)	14.0 (5.5)	27.9 (11.0)	This Study

*estimated from da/dN vs ΔK curves

141
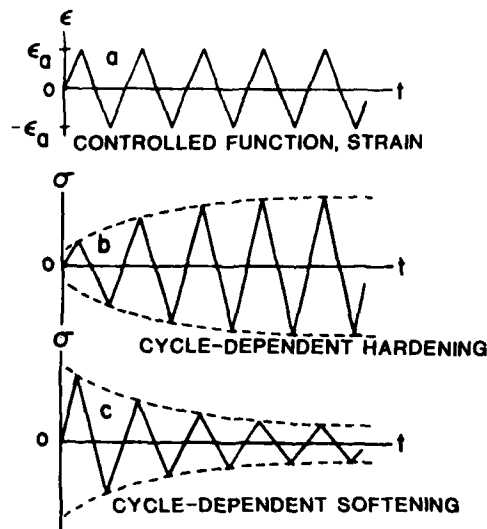
Figure 11. Cycle-Dependent Response Under Strain Control
[Reference 111 after reference 163].
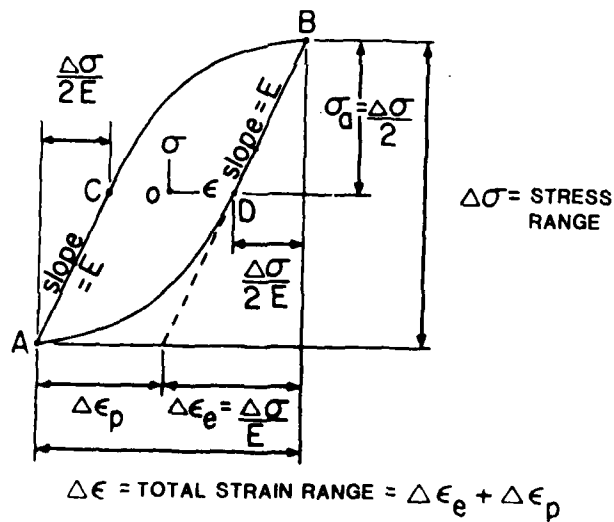
Figure 12. Schematic of a Hysteresis Loop and Associated
Quantities [Reference 111 after Reference 163].

Figure 10. Constant Amplitude Fatigue Crack Propagation Data for P/M X7091-T7E69 and I/M 7050-T76511 Extrusions and I/M 7075-T7351 Plate [153].
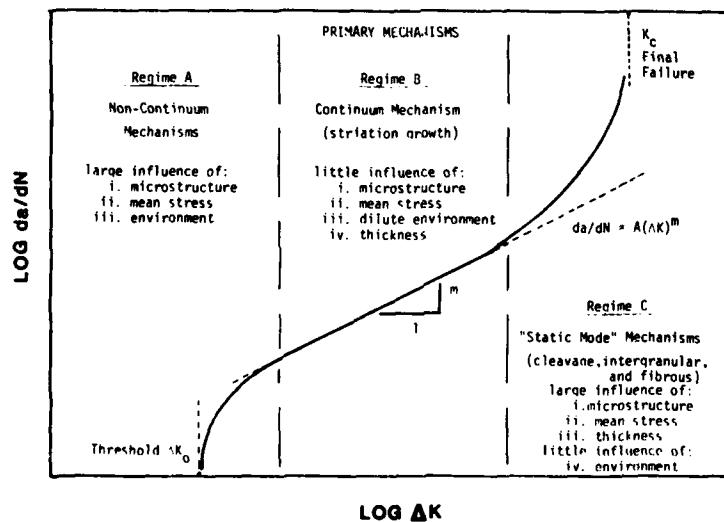
Figure 9. The Variation of Fatigue Crack Propagation (da/dN)
with Alternating Stress Intensity (ΔK) [140].
*(Author's note: Although this is generally purported,
growing evidence indicates there is an effect of
microstructure in the Paris region)
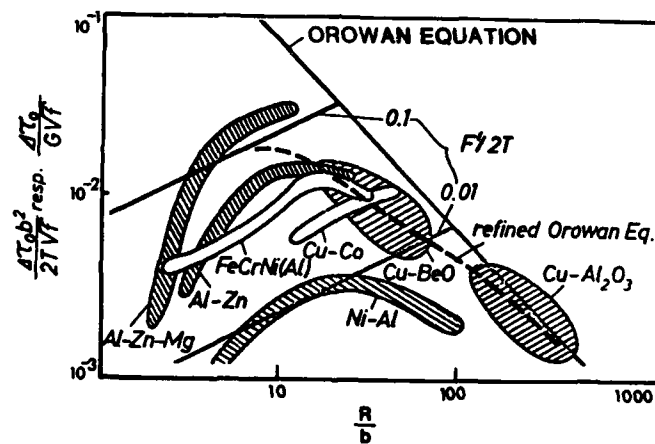
Figure 8. Normalized Critical Resolved Shear Stress vs. Particle Radius [123].
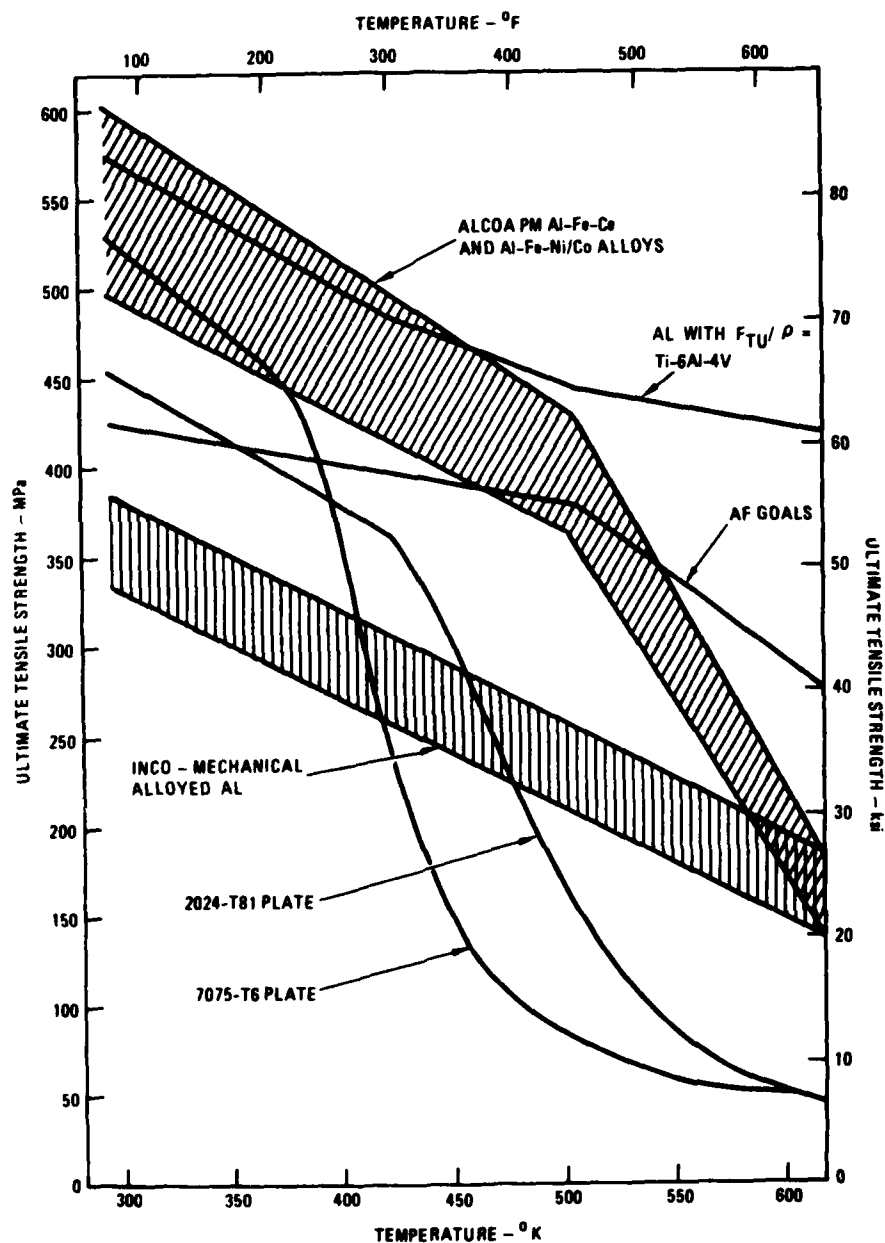
Figure 7. High Temperature Al P/M Program Goals vs.
           Capabilities of Current Materials [65].

(a)

(b)

20um

(c)
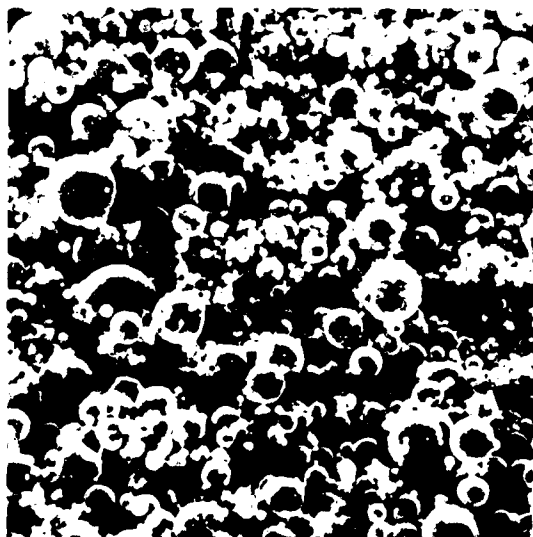
Figure 6. Shape of Atomized Powder Particles Associated with
(a) air atomization, (b) helium atomization, and
(c) centrifugal atomization [31].

150
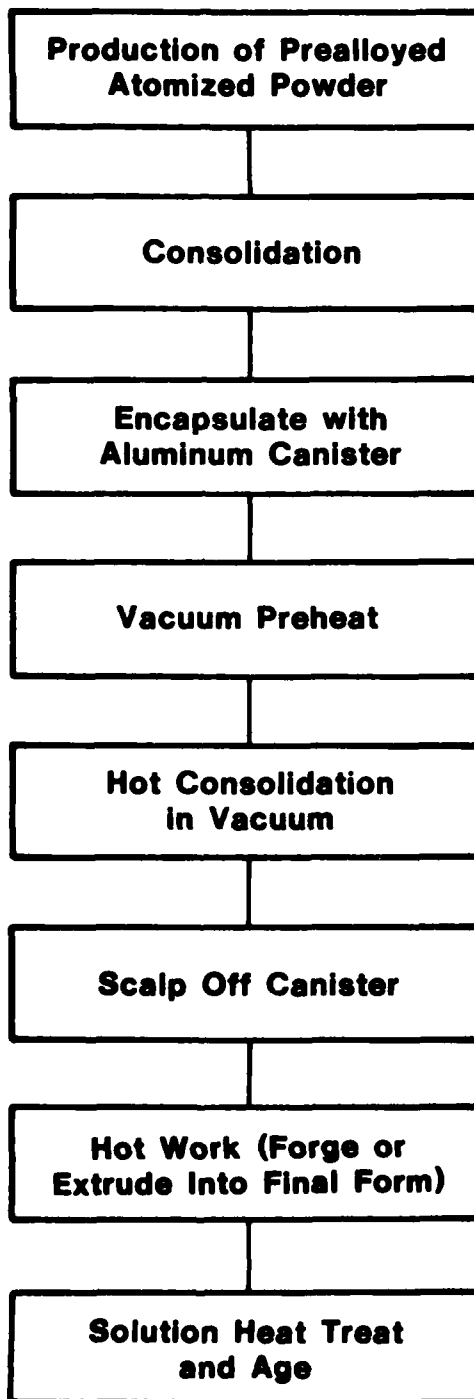
Figure 5. Consolidation Process Established Under Frankford
Arsenal Sponsorship [15].

149

POWDER   MA87   INGOT   7050

(a)   (b)

Figure 4.   Microstructures of Al Die Forgings [64].   (a) Fine
structure of P/M alloy MA87 and (b) coarse structure
of I/M alloy 7050.   Both microstructures were
originally 100x.

POWDER   MA87   INGOT   7050

Figure 3. Macrostructures of Die Forgings [63].

(a)

100um

(b)

(c)

25um

(d)
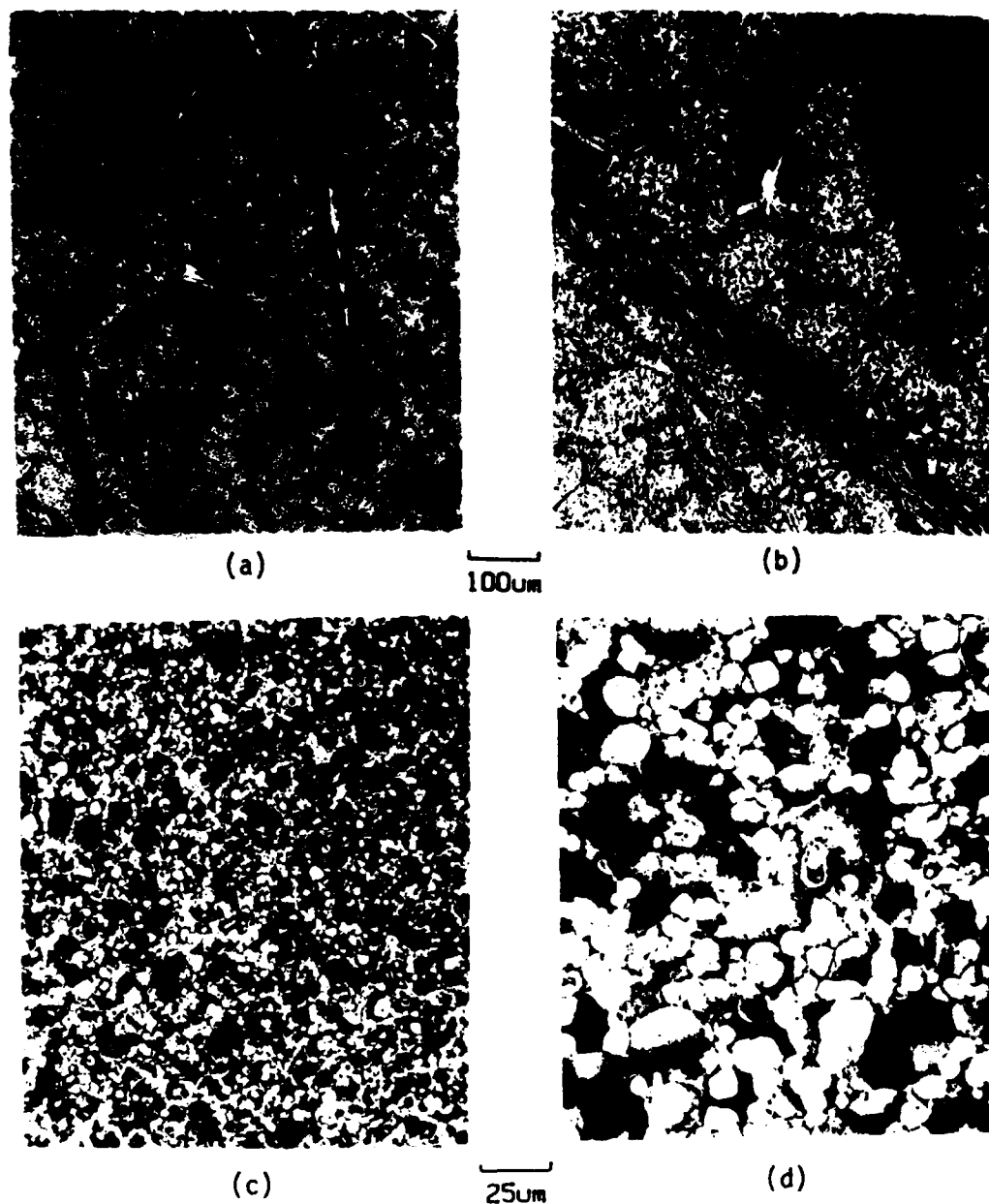
Figure 2. P/M Provides Chemical Homogeneity and Unique Alloy
Compositions [29]. These microstructures are typical of
Al P/M alloy CU78 (Al-Fe-Ce) that has been button melted
to simulate the slow solidification rates found in ingots
(a and b) and of rapidly solidified gas atomized powders
(c and d).

146
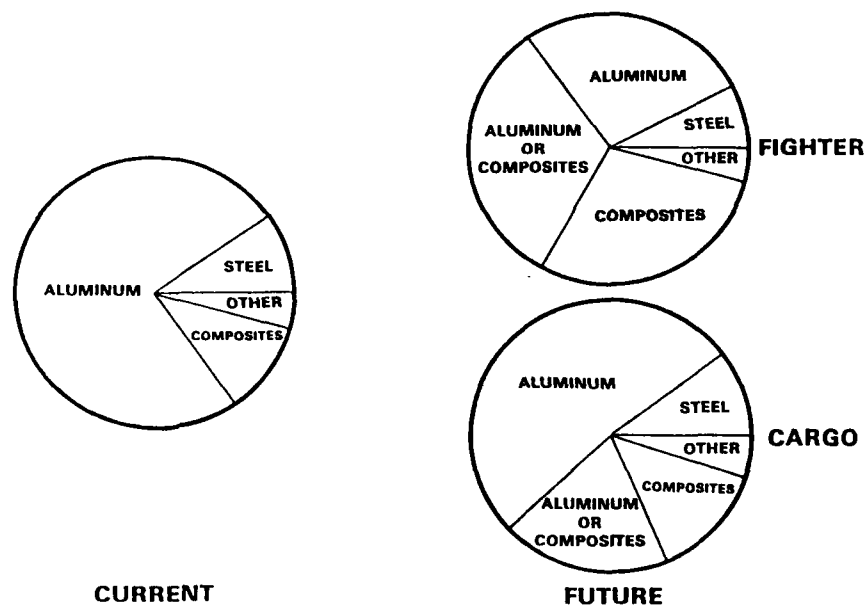
Figure 1. Materials Utilization for Current and Future Military
Aircraft [14].

145

TABLE 22
CYCLIC PROPERTIES -- $A_\epsilon = \infty$

CONDITION	n'	β_{expt}	α	β_{calc}*
00X	0.070	1.027	0.924	1.011
011	0.101	0.779	1.021	0.890
101	0.067	1.437	0.654	1.433
111	0.109	0.969	0.929	0.971
38% upset	0.082	0.917	0.965	0.958
64% upset	0.088	1.144	0.806	1.140
0 % Co	0.068	1.189	0.838	1.117
0.4% Co	0.107	0.887	0.958	0.943
All data	0.085	1.028	0.857	1.075

$$*\beta_{calc} = \frac{1}{(1 + n')\alpha}$$

TABLE 21

CYCLIC PROPERTIES -- $A_\epsilon = 0.95$

CONDITION	n'	β_{expt}	α	β_{calc}*
000	0.069	1.110	0.848	1.103
001	0.070	1.017	0.884	1.057
010	0.092	1.280	0.716	1.397
011	0.052	1.344	0.743	1.279
100	0.092	1.328	0.700	1.308
101	0.069	1.242	0.757	1.236
110	0.082	1.088	0.859	1.076
110	0.066	1.066	0.881	1.065
38% upset	0.076	1.170	0.797	1.166
64% upset	0.077	1.160	0.803	1.156
0 % Co	0.076	1.170	0.792	1.173
0.4% Co	0.077	1.143	0.807	1.151
all data	0.076	1.164	0.800	1.162

$$*\beta_{calc} = \frac{1}{(1 + n')\alpha}$$

143

TABLE 20

CALCULATED PLANE STRAIN PLASTIC ZONE SIZE FOR P/M ALLOYS

ΔK	K_{max}**	Plastic Zone Size* (mm) for σ_{ys} Shown			
		monotonic zone, r_p		fatigue zone, r'_p	
		517 MPa (75 ksi)	552 MPa (80 Ksi)	517 MPa (75 ksi)	552 MPa (80 ksi)
Mpa√m	Mpa√m				
2.2	2.4	1.14	1.00	0.29	0.25
3.3	3.6	2.57	2.26	0.64	0.57
4.4	4.8	4.57	4.01	1.14	1.00
5.5	6.1	7.39	6.48	1.84	1.62
7.7	8.5	10.58	9.28	2.65	2.32
8.8	9.7	18.68	16.38	4.67	4.10
9.9	10.9	23.58	20.69	5.90	5.17
11.0	12.1	29.06	25.49	7.27	6.37

The range of yield strengths measured in this study was approximately 75 ksi to 80 ksi

**For R = 0.1, K_{max} = 1.1 ΔK

*Calculated from: $r_p = \dfrac{1}{6\pi}\left(\dfrac{K_{max}}{\sigma_{ys}}\right)^2$ $\qquad r'_p = \dfrac{1}{24\pi}\left(\dfrac{K_{max}}{\sigma_{ys}}\right)^2$

142
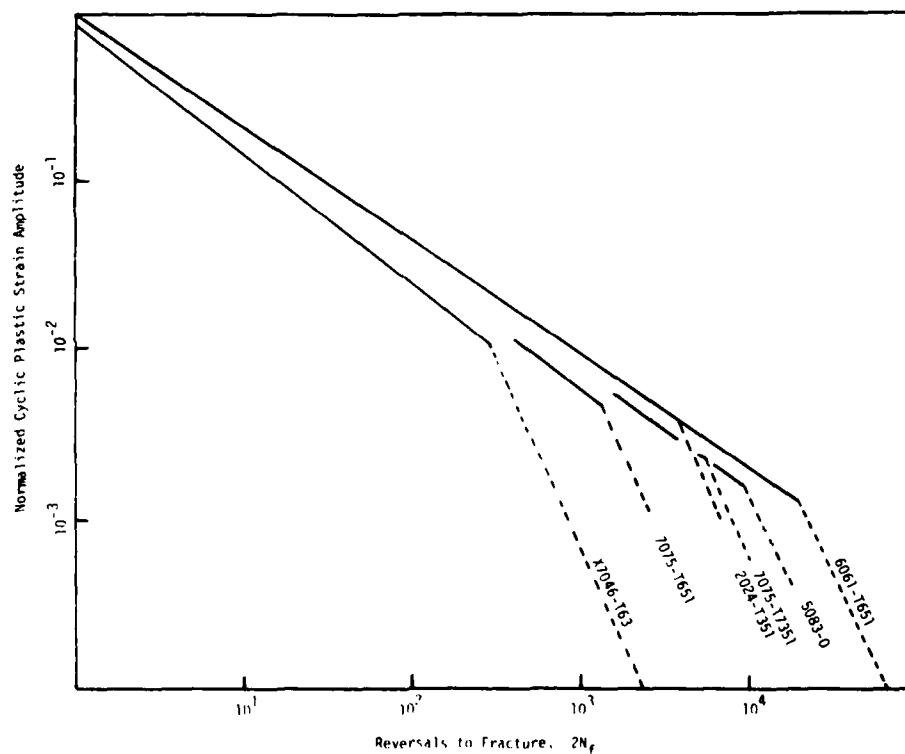
Figure 13. Dual Slope Coffin-Manson Behavior is Often
Reported for a Variety of Al Alloys [155].

156

CUT INTO 7 EQUAL PIECES. APPROX. 3.7" HIGH

FINAL HEIGHT MUST BE SUFFICIENT TO ALLOW 3.5" HIGH
FORGING BLANKS TO BE MACHINED

ID: "A" THRU "G" $\approx$ 0% Co

"S" THRU "Z" $\approx$ 0.4% Co
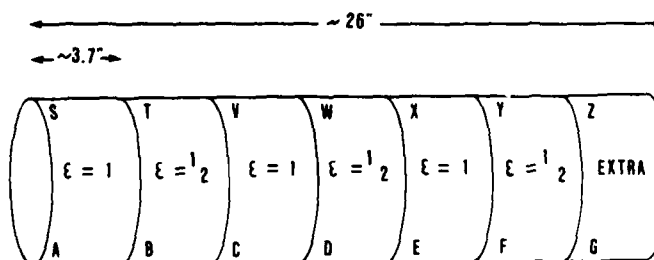
(b)

Figure 14. (a) As-Received Billets;
            (b) Cutting Plan for As-Received Billets.

157

FORGING BLANK

ε	H	W	L
1.00	1.63	3.50	2.39
0.50	0.99	3.50	3.94

ID = BILLET SECTION "D"
FORGING BLANK "5"
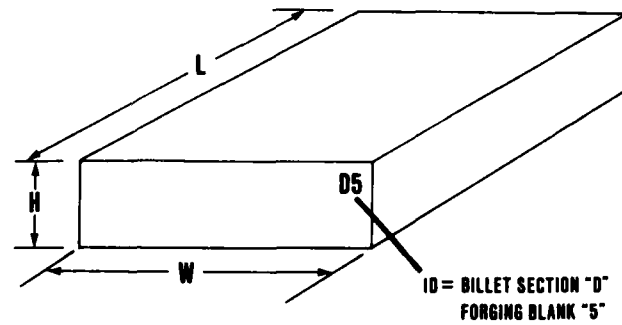
Figure 15.   Dimensions of Forging Blanks.

158

(a)

(b)
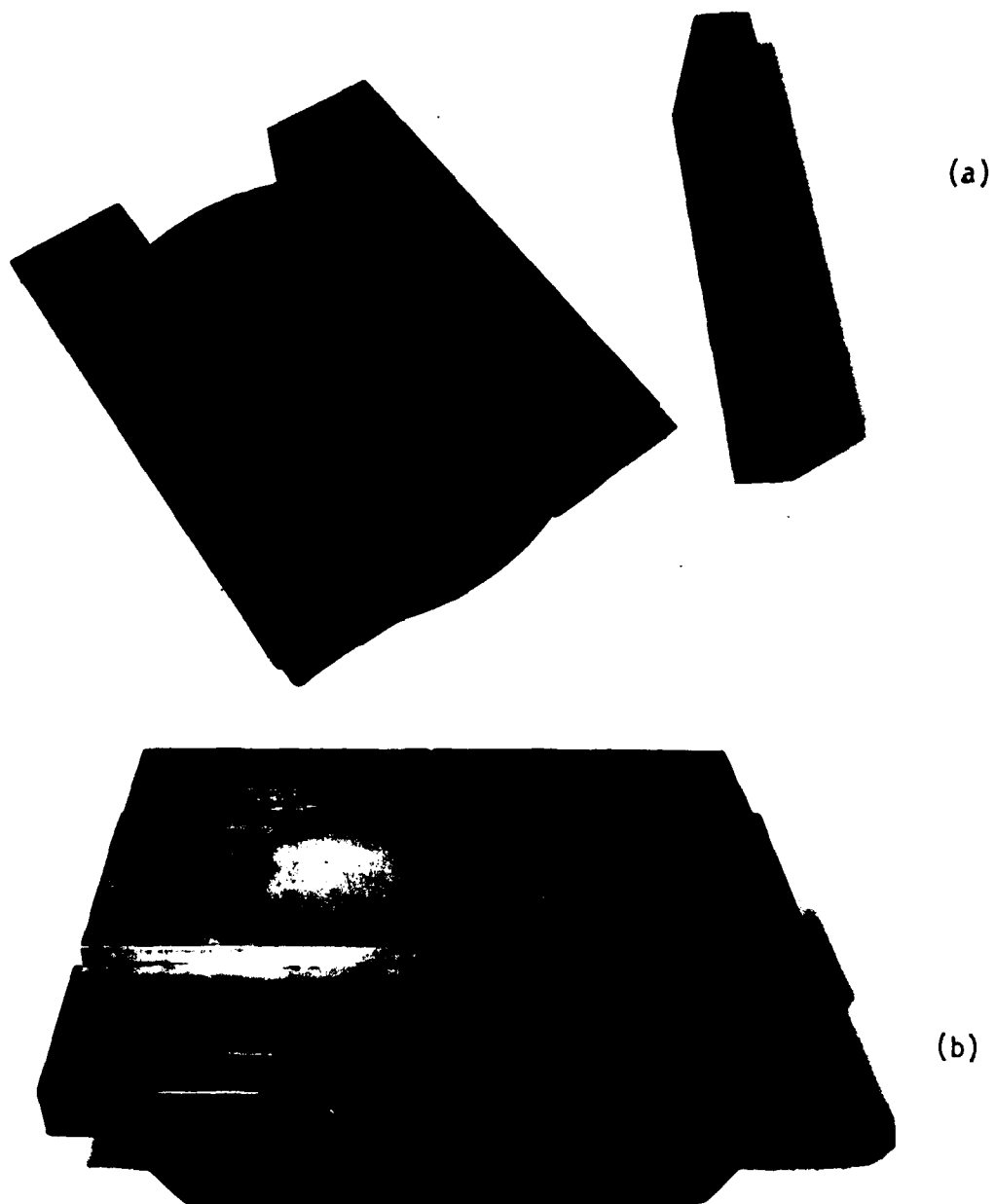
Figure 16. Channel Dies Used to Forge Material in This Study.
(a) With the die plate removed; (b) With the die
plate in place ready for forging.

FINAL FORGING:
7" LONG x 3.5" WIDE x 0.6" THICK

DON'T STRESS
RELIEVE

~7"

D5

D5R

STRESS RELIEVE

CUT INTO 2 PIECES FOR
HEAT TREATMENT, STRESS RELIEF,
AND MACHINING

~0.6"

3.5"
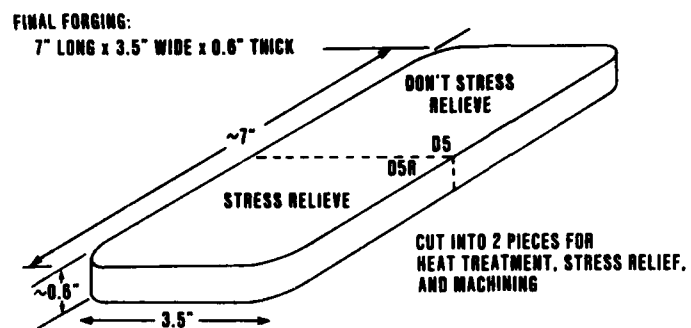
Figure 17.   Final Forging Configuration.
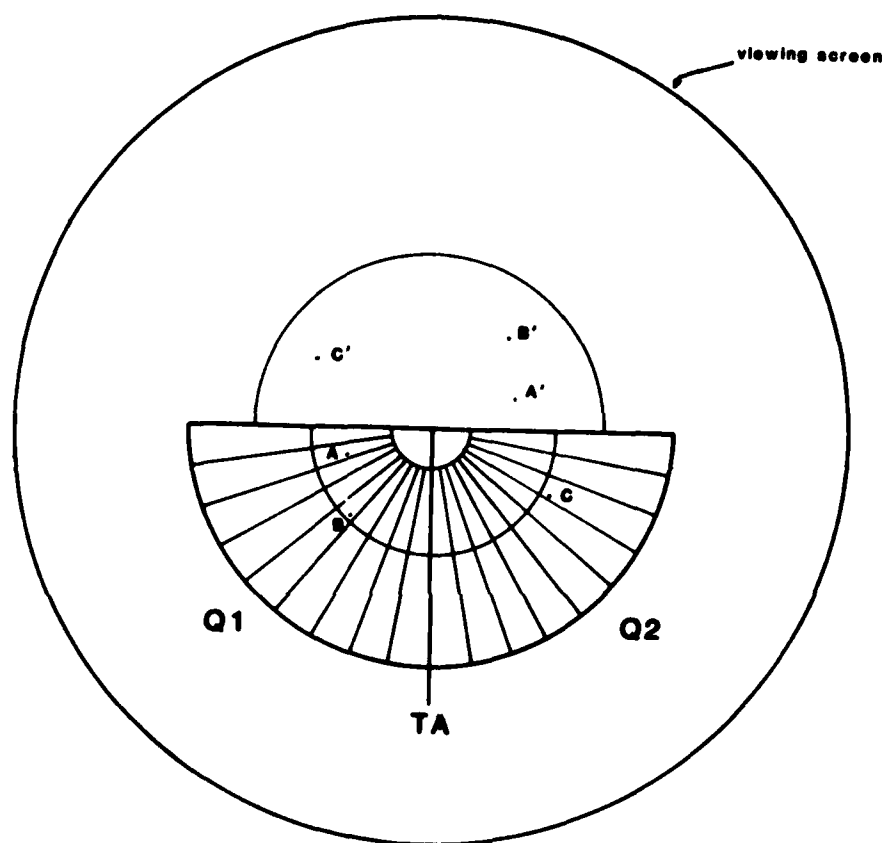
Figure 18. Schematic of the Grid Inscribed on the Transmission Electron Microscope Screen.
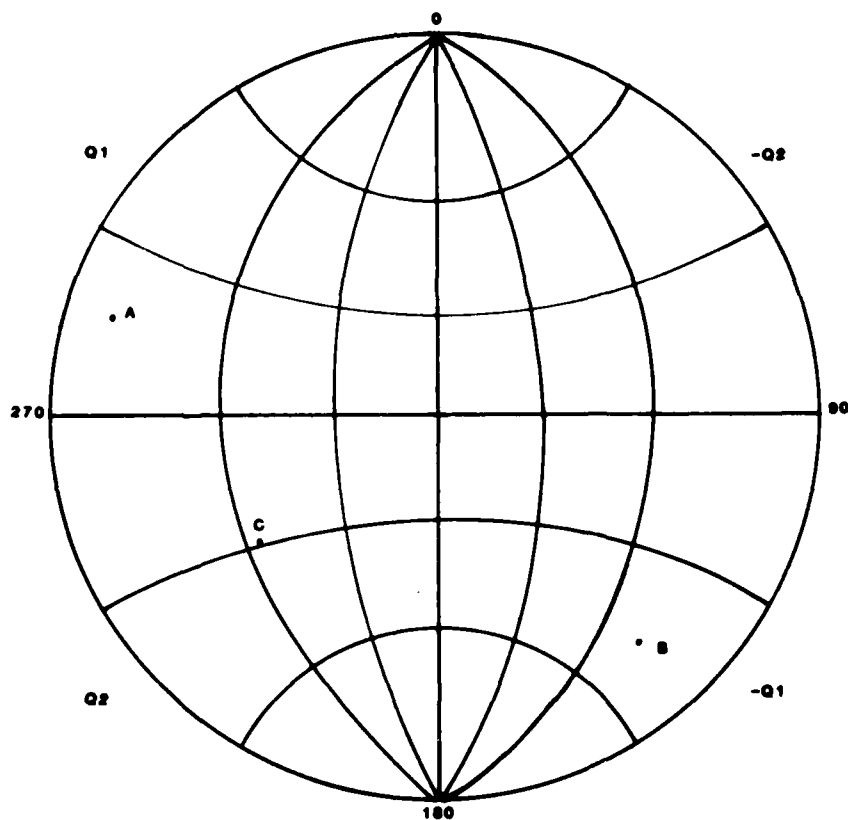
Figure 19. Example of How Spots in Figure 18 Would be Plotted on the Wulff Net.
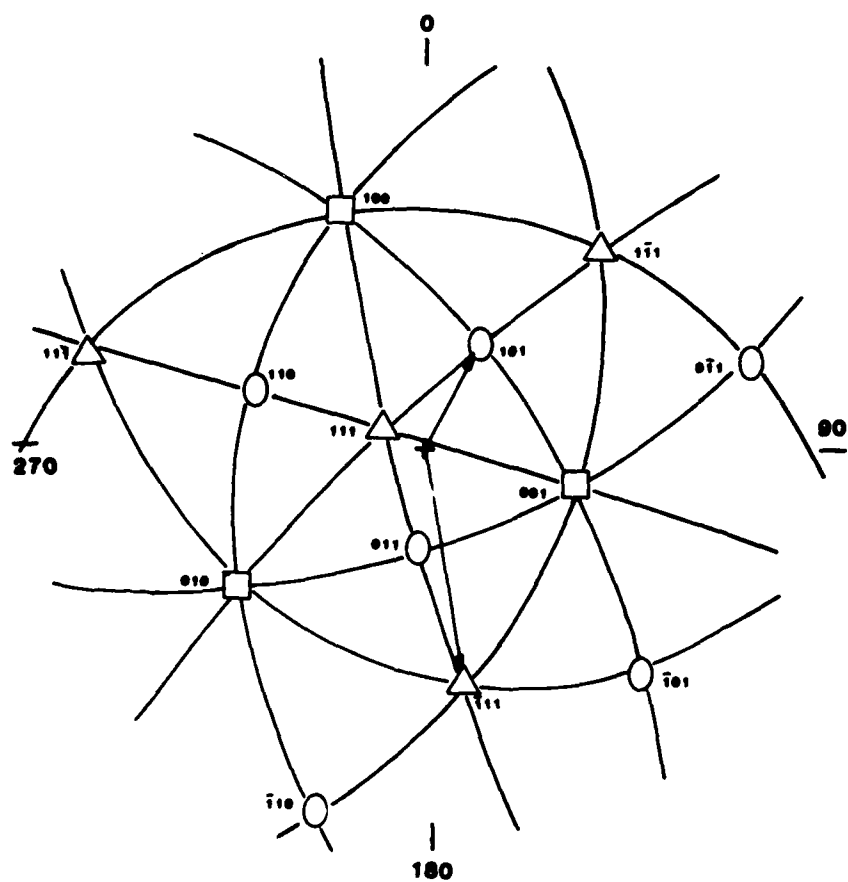
Figure 20. Example of a Completed Stereographic Projection
Based on 2-Beam Cases Found by Trial and Error.

163
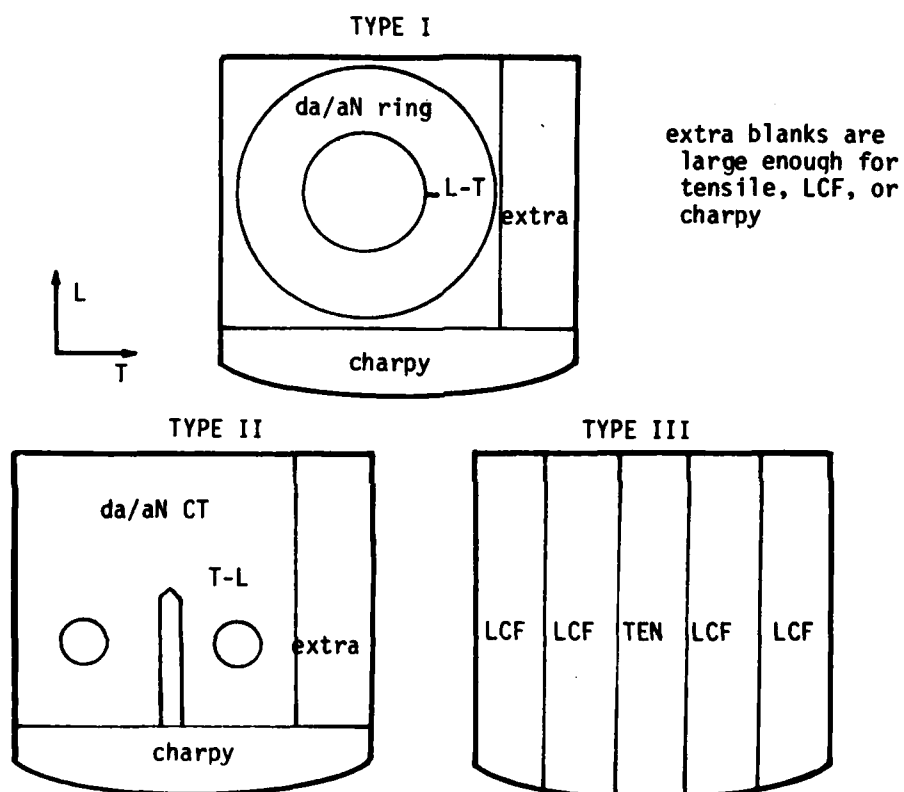
Figure 21. Specimen Layout.
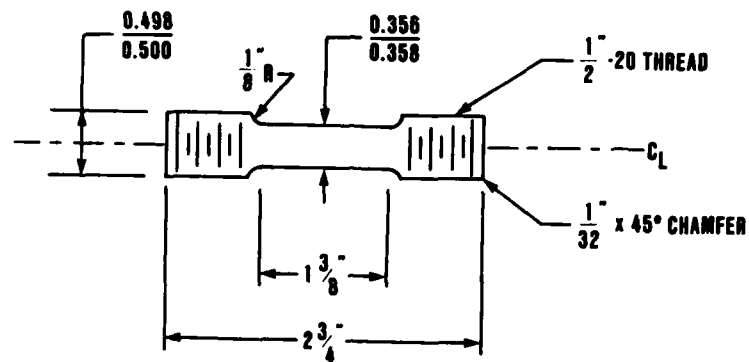
Figure 22.   Tensile Specimen.
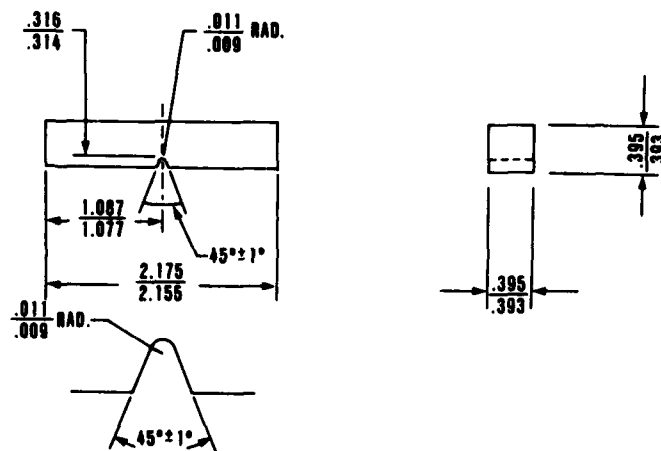
Figure 23.   V-Notched Charpy Specimen Used for Toughness Testing.
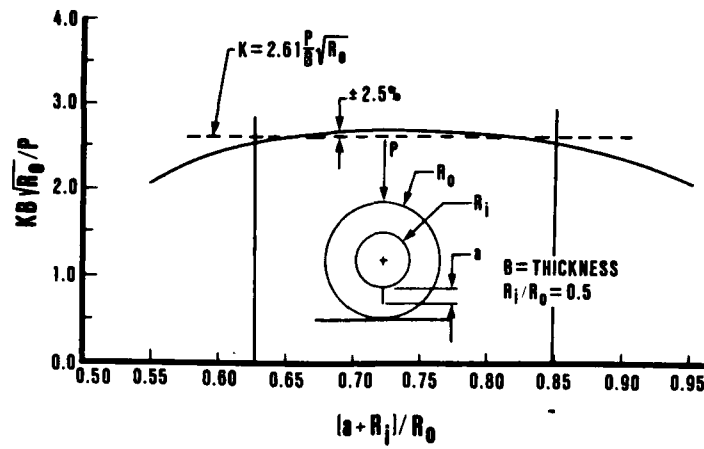
Figure 24. Stress Intensity Factor for Radially Cracked Ring in Compression [222].
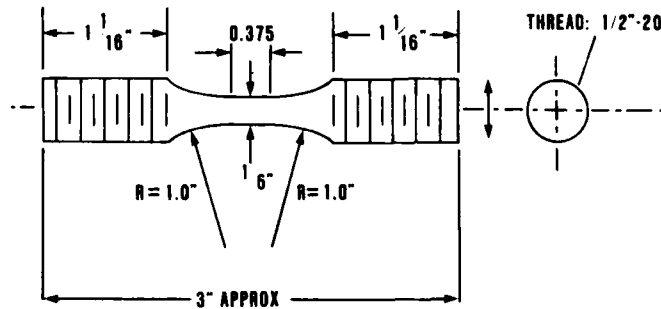
Figure 25. Low Cycle Fatigue Specimen.

166
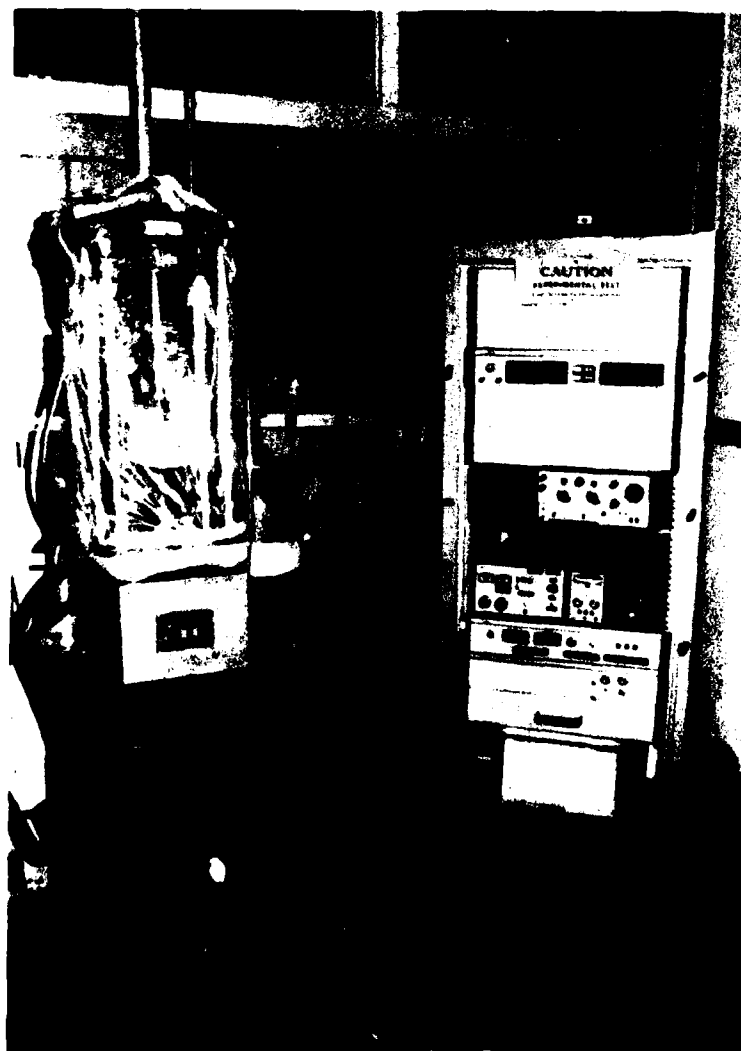
Figure 26. Overall LCF Test Set-up.
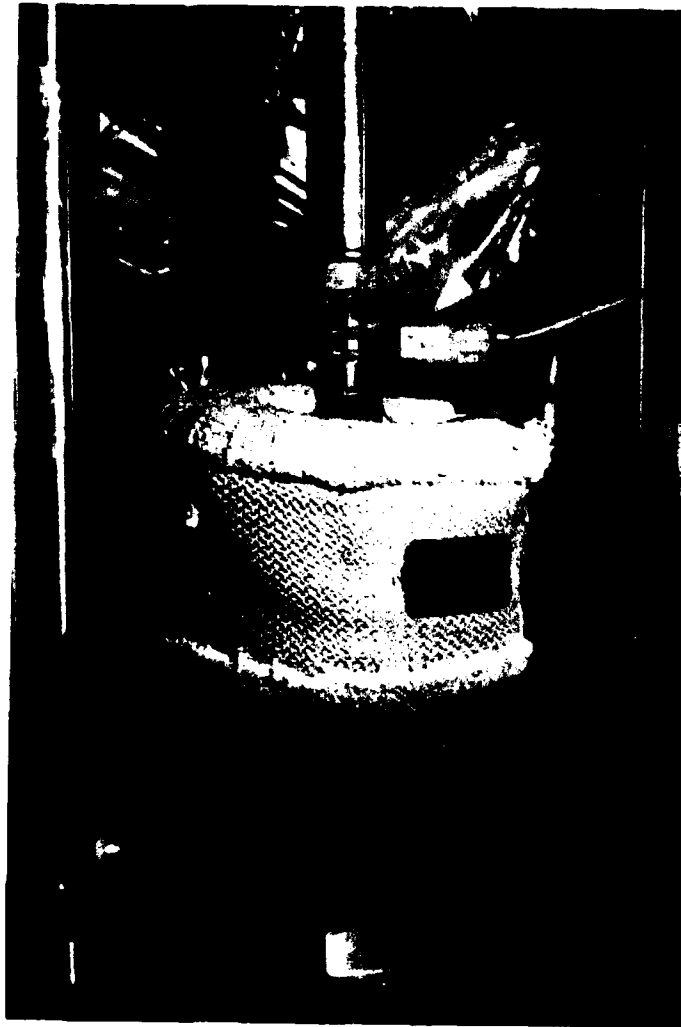
Figure 27. Close-up View of LCF Test Set-up Showing Wood's
Metal Pot and Extensometer.
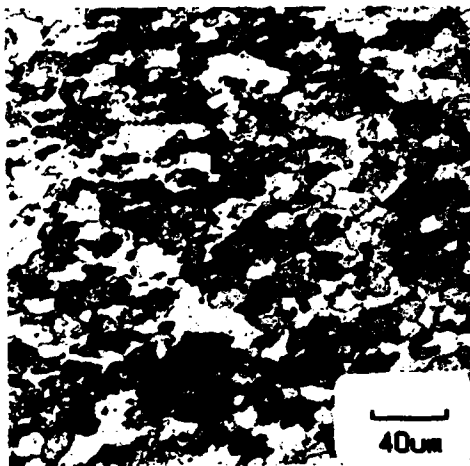
(a)

(b)
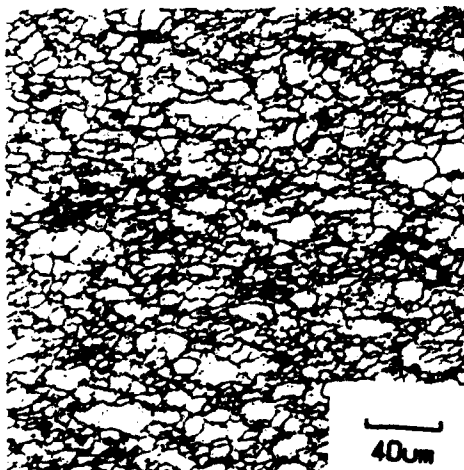
(c)
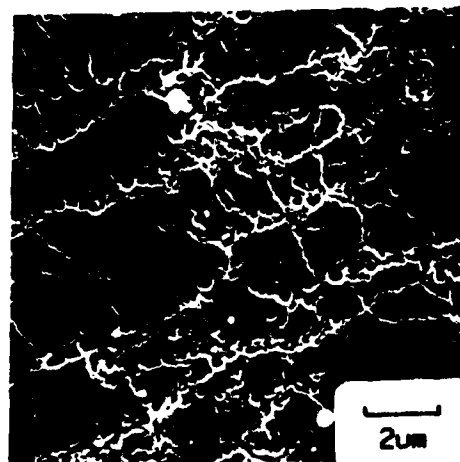
(d)

Figure 28.   Comparison of Keller's Etchant (a and b) and Graff-
Sargent's Etchant (c and d).   TS forging plane is
shown in all cases.
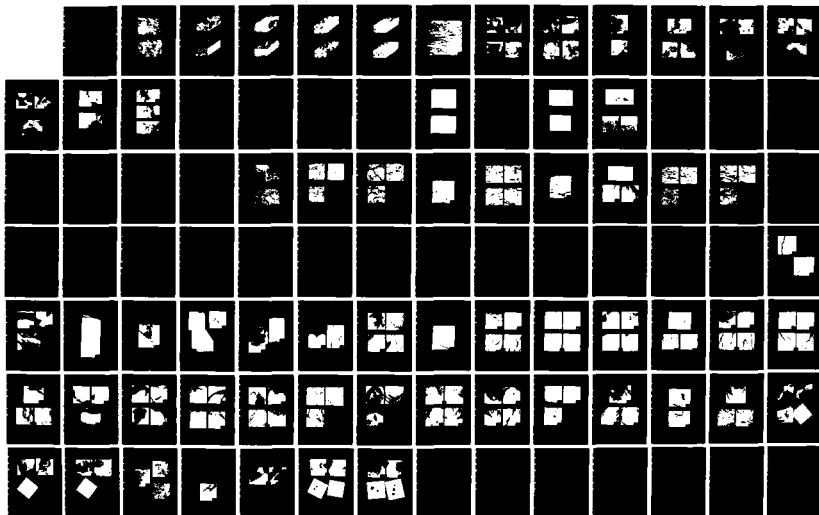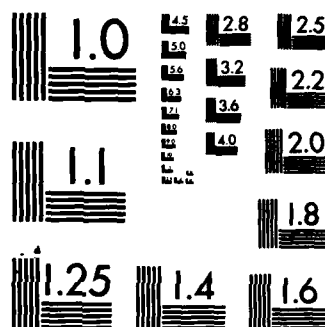
MICROCOPY RESOLUTION TEST CHART

NATIONAL BUREAU OF STANDARDS-1963-A
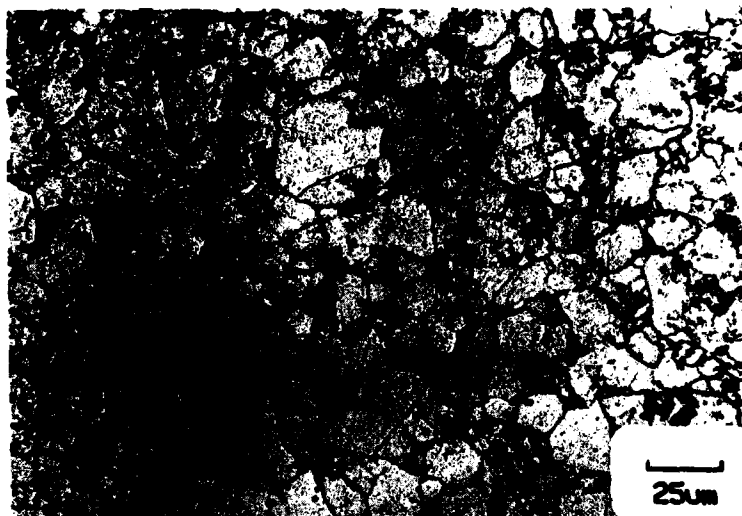
(a)
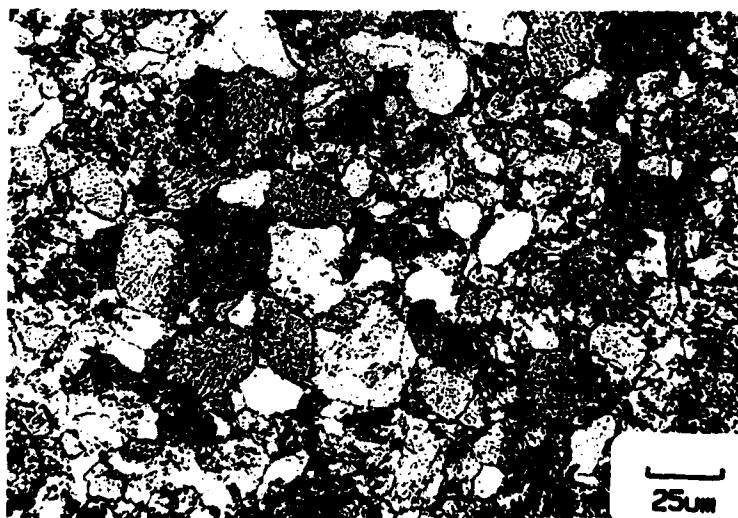
(b)

Figure 29. As-Compacted Microstructures of (a) Co-Free and
(b) 0.4% Co Variants of Vacuum Hot Pressed Billets.
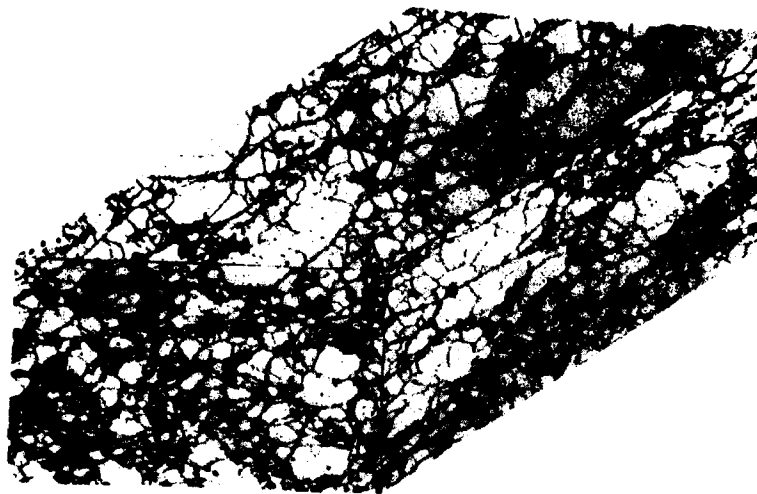
(a)

├──┤
25um
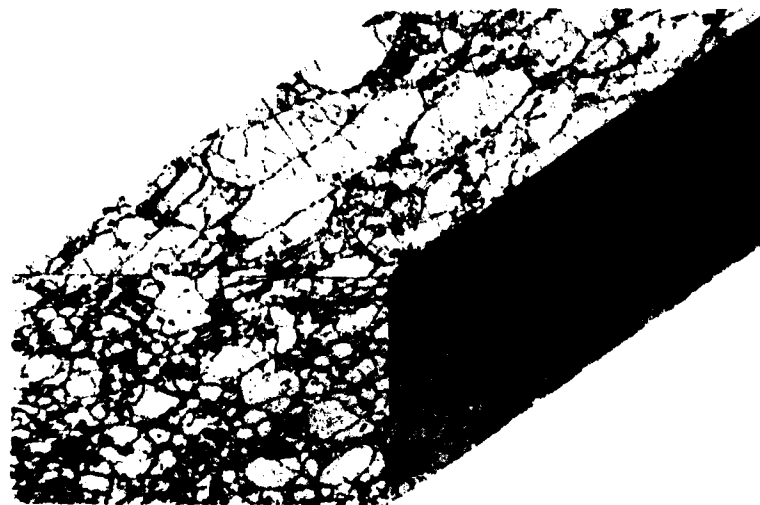
(b)

Figure 30. Optical Microstructures of Channel Die Forgings.
(a) condition 000; (b) condition 001.

(c)

25μm
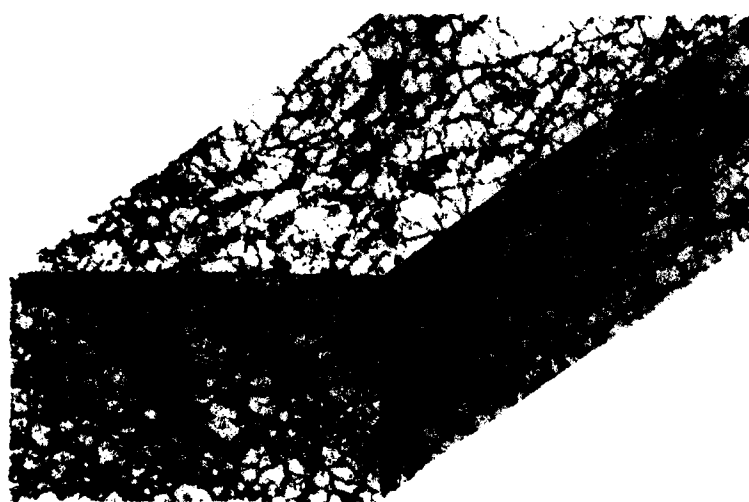
(d)

Figure 30 (continued).   (c) condition 010;   (d) condition 011.

(e)

├─────┤
25um
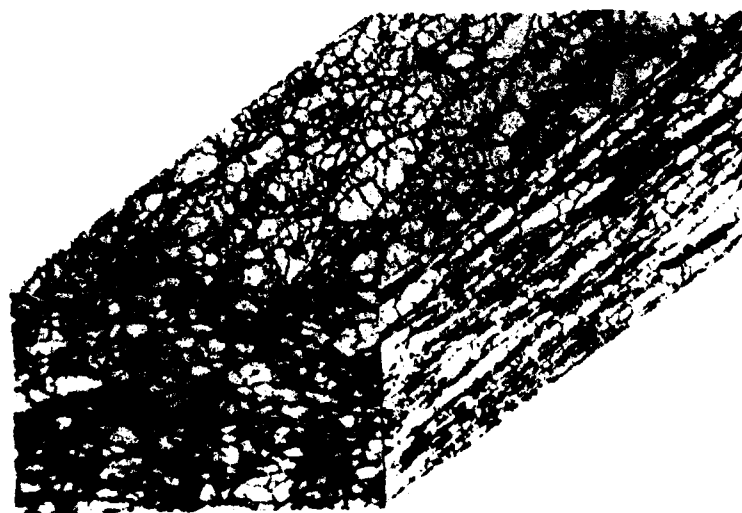
(f)

Figure 30 (continued). (e) condition 100; (f) condition 101.

(g)

25um

(h)

Figure 30 (continued). (g) condition 110; (h) condition 111.

174
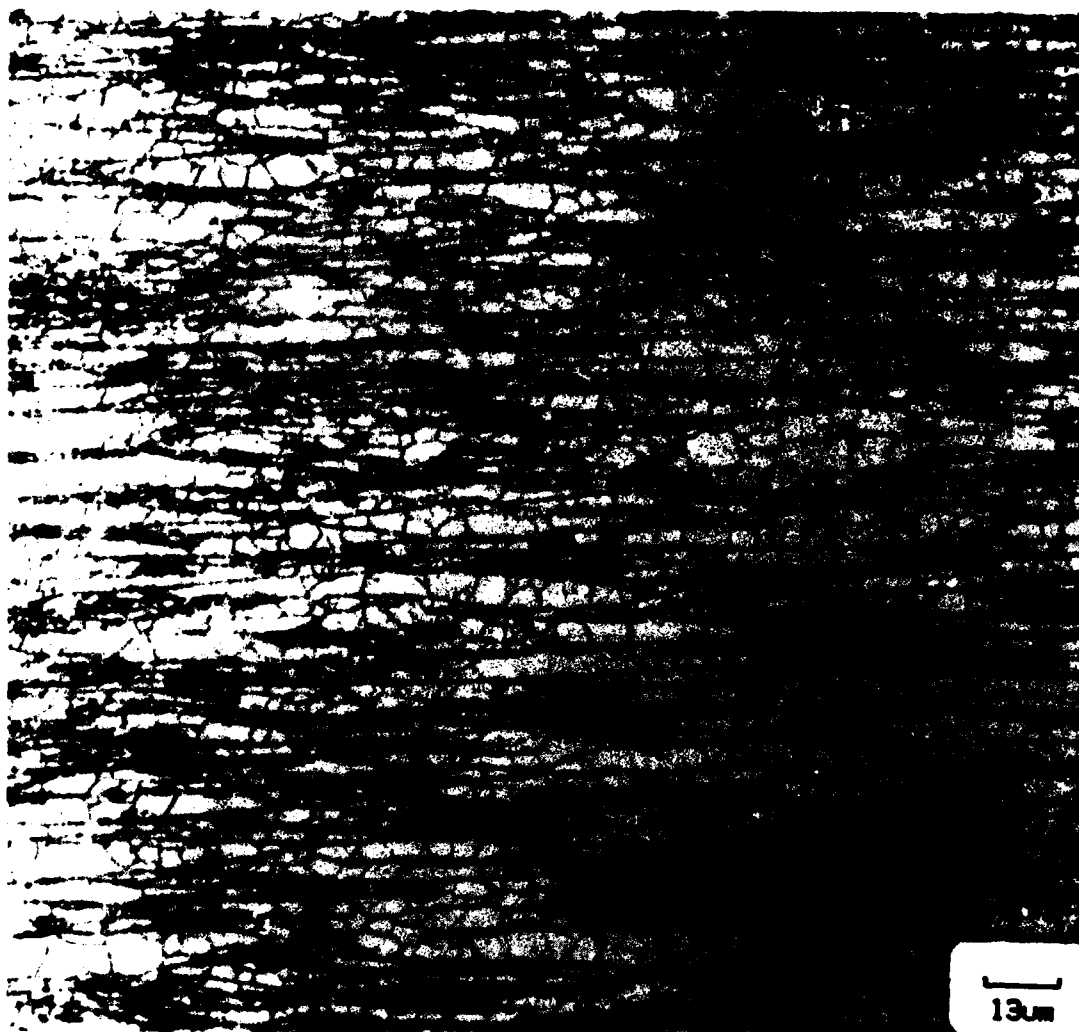
Figure 31. The "Bamboo Structure" Described in Reference 120. This structure is typical of the elongated planes of P/M alloy forgings. Note also the duplex nature of the microstructure; this is due to the wide variation in the powder particle size.

(a)   (b)

2um

(c)   (d)

Figure 32.   Typical TEM Microstructures for the Vacuum Hot
             Pressed Billets Containing 0% Co (a and b) and
             0.4% Co (c and d).

(a)   (b)
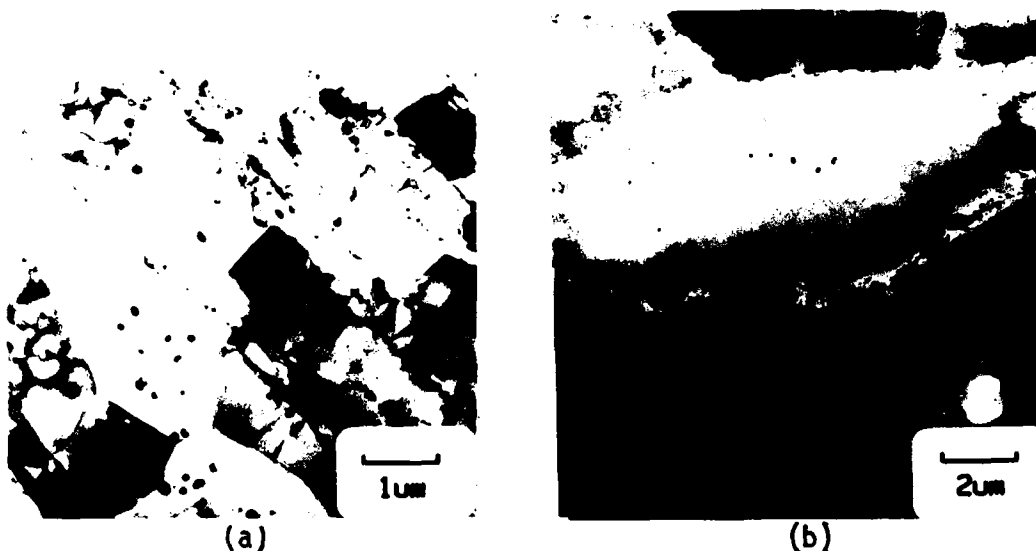
Figure 33.   The Variation in Powder Particle and Grain Size Possible in a Small Volume of Material. (a) S-L plane of a 64% upset forging, 0.4% Co, and not stress relieved. (b) T-L plane of a 38% upset forging, 0% Co, and stress relieved. These examples are typical for all cases studied.

(a)   (b)
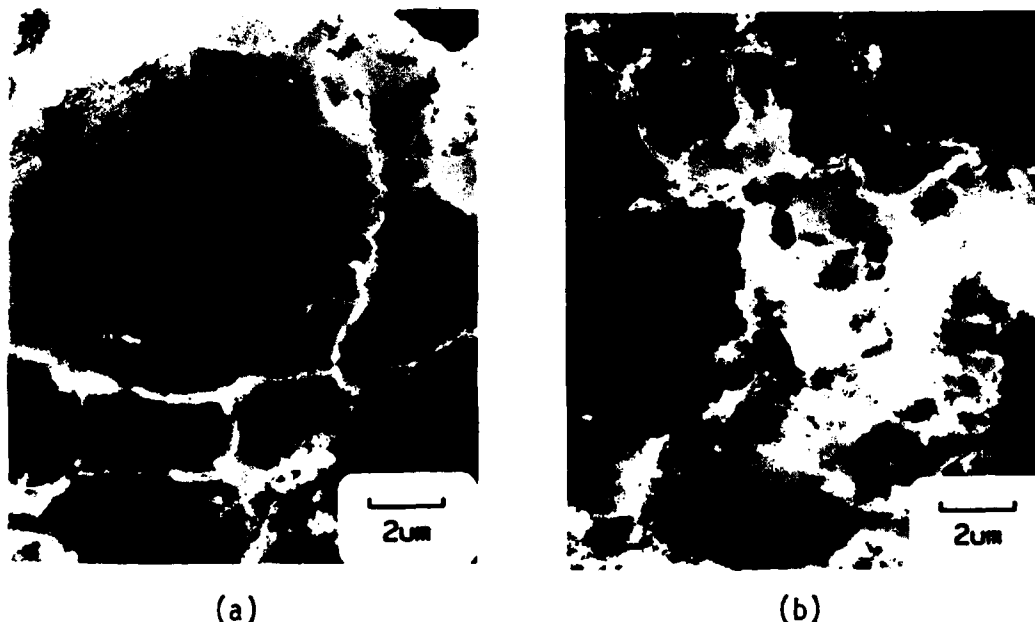
Figure 34.   Preferential Etching Due to High Oxide Content at the Original Powder Boundaries Demonstrates the Powder Size Variation Possible. This artifact of polishing differentiates between prior particle boundaries and other boundaries. (a) and (b) are from the same thin foil made from a 38% upset forging, 0% Co, and stress relieved.

177

Figure 35. The Elements of a Typical Microstructure of a CT91
Forging. (n = grain boundary $MgZn_2$, O = oxide stringer,
D = Co_2Al_9 dispersoid, C = constituent particle). The
background has a mottled appearance due to the presence
of the strengthening precipitate, η'.
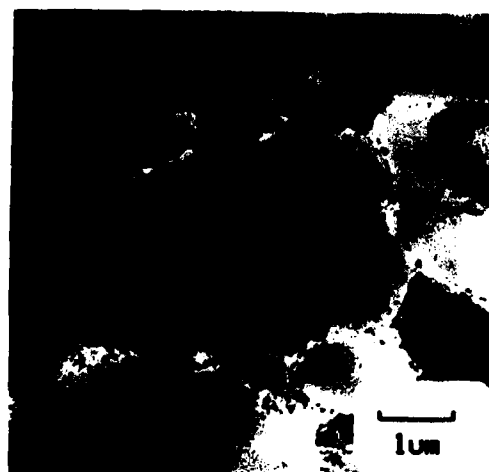
Figure 36. Typical Microstructure in the S-T Plane for a 64% Upset
Forging with 0% Co and Stress Relieved. The original
powder particle boundaries are still visible, indicating
the degree of break-up due to forging is minimal.

178

Figure 37.   Undeformed Powder Particle in a 38% Upset Forging is
              Evidence that Deformation is Insufficient to Break Up
              the Structure. This sample is a 38% upset forging,
              0% Co, and stress relieved.
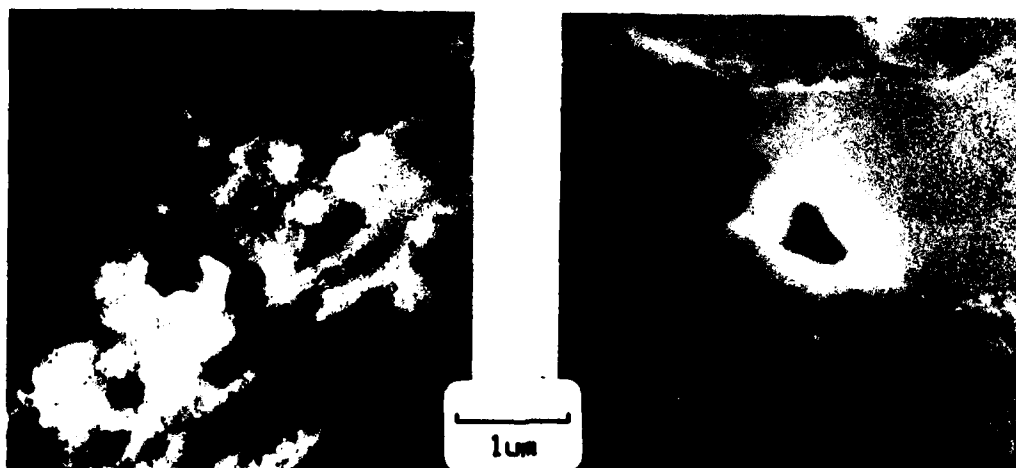
Figure 38.   Typical Constituent Particles Found in CT91 Forgings.
              (a) Mg_2Si and (b) Si or SiO_2 are found in all conditions
              studied. The constituent Al_7Cu_2Fe (not pictured) is
              found only in the Co-free variant because the Fe is
              tied up as $(Co,Fe)_2Al_9$ in the 0.4% variant. Identifica-
              tion was carried out using STEM x-ray analysis.

Figure 39. The Dispersoid Distribution Can Vary Widely in CT91
Forgings. (a) Co_2Al dispersoids outline what were
dendrites that have since been eliminated by processing;
(b) in the same foil, areas can be found where virtually
no Co_2Al_9 is seen, presumably due to the more rapid
cooling rates experienced by the smaller powder particles.
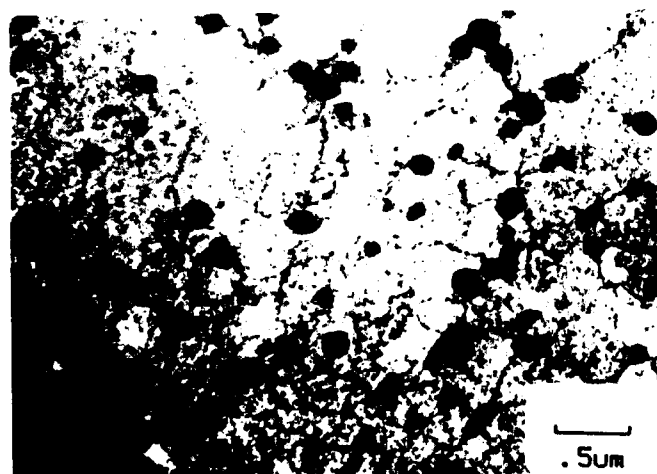
Figure 40. The Co_2Al_9 Dispersoid is not Fractured or Deformed
During Fabrication and Interacts with Dislocations.
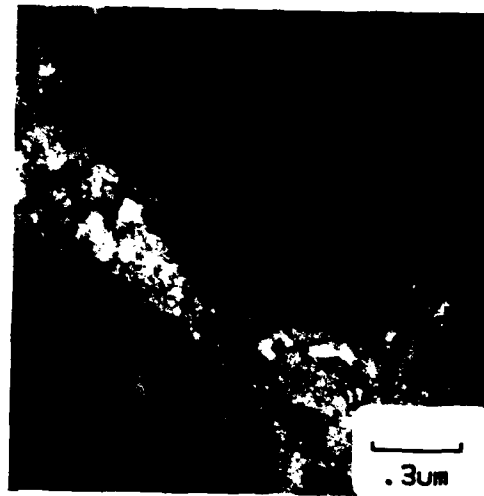
Figure 41. The Broken Oxide Films are Distributed Near the Particle Surfaces. They form continuous arrays in forged products (a and c); the arrays can be greater than 0.5 μm thick (b). (a) and (b) are the T-L plane of a 38% upset forging with 0.4% Co and no stress relief. (c) is the S-L plane of a 64% upset forging with 0.4% Co that has not been stress relieved.

181
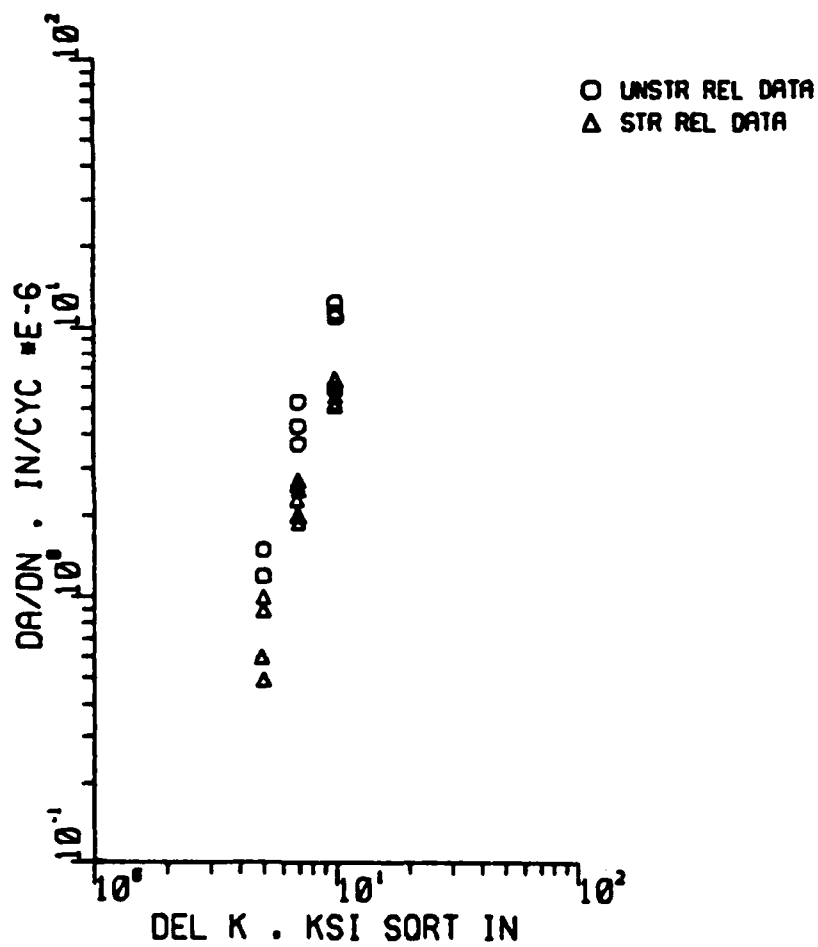
Figure 59.   Effect of Stress Relief
on FCP.
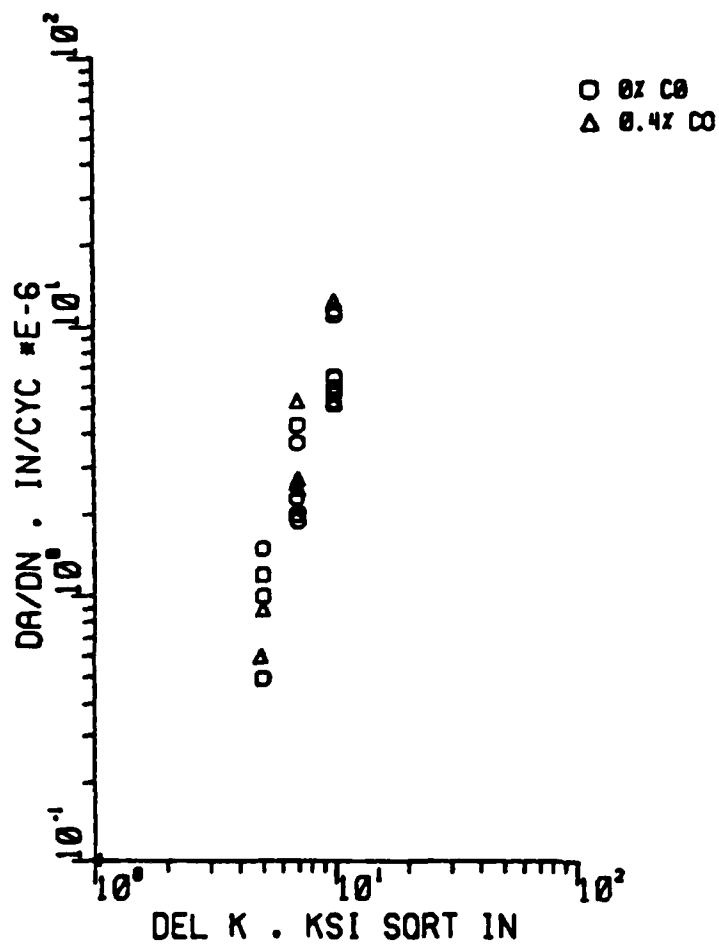
Figure 58. Effect of Co Content on FCP.
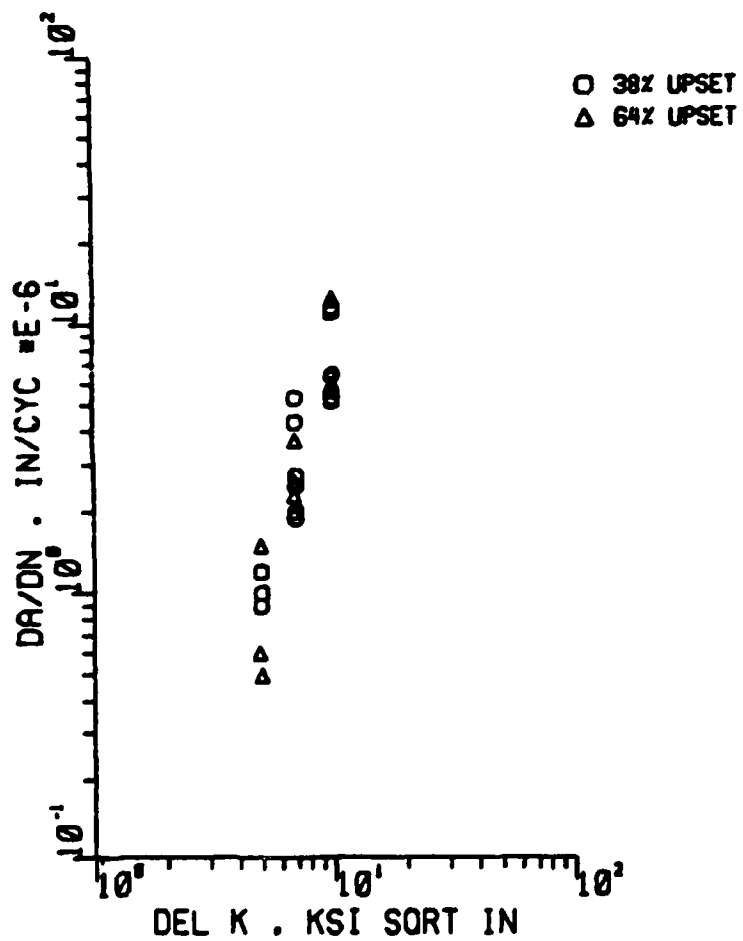
Figure 57. Effect of Forging Strain on FCP.

Figure 55. Examples of Cracks Growing out of Plane.
From the left samples are 14 (110) and
BB5 (000).
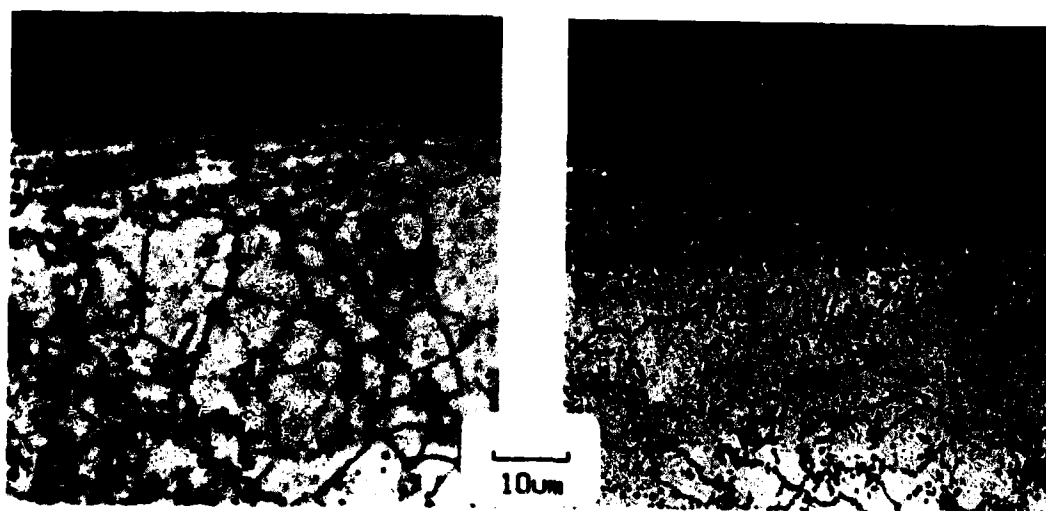
Figure 56. Microstructure at the Tip of a Ring Notch. (a) Machined
notch shows heavy surface deformation while (b) EDM'd
notch shows a layer that was remelted.
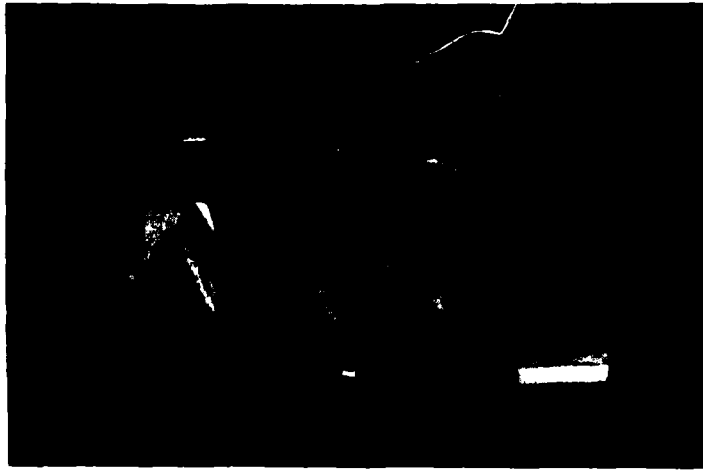
Figure 53. Examples of Shear Lips Formed in FCP Tests using Ring Specimen. From the left the samples are 4 (100), BB5R (001), D1 (000), BB4R (001).
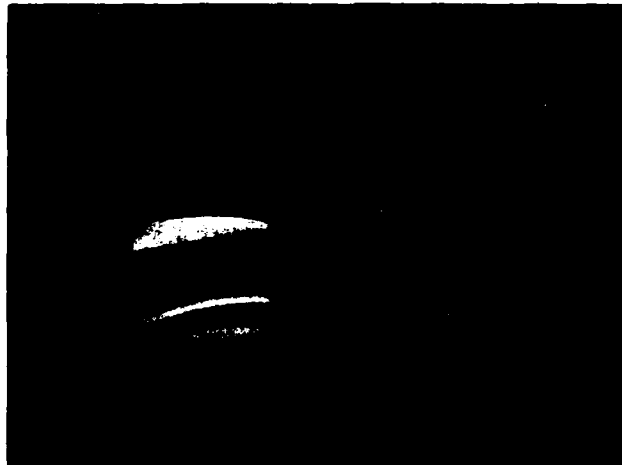
Figure 54. Examples of Eccentric Crack Growth in Ring Specimens. From the left the samples are 3R (111) and 26R (11).
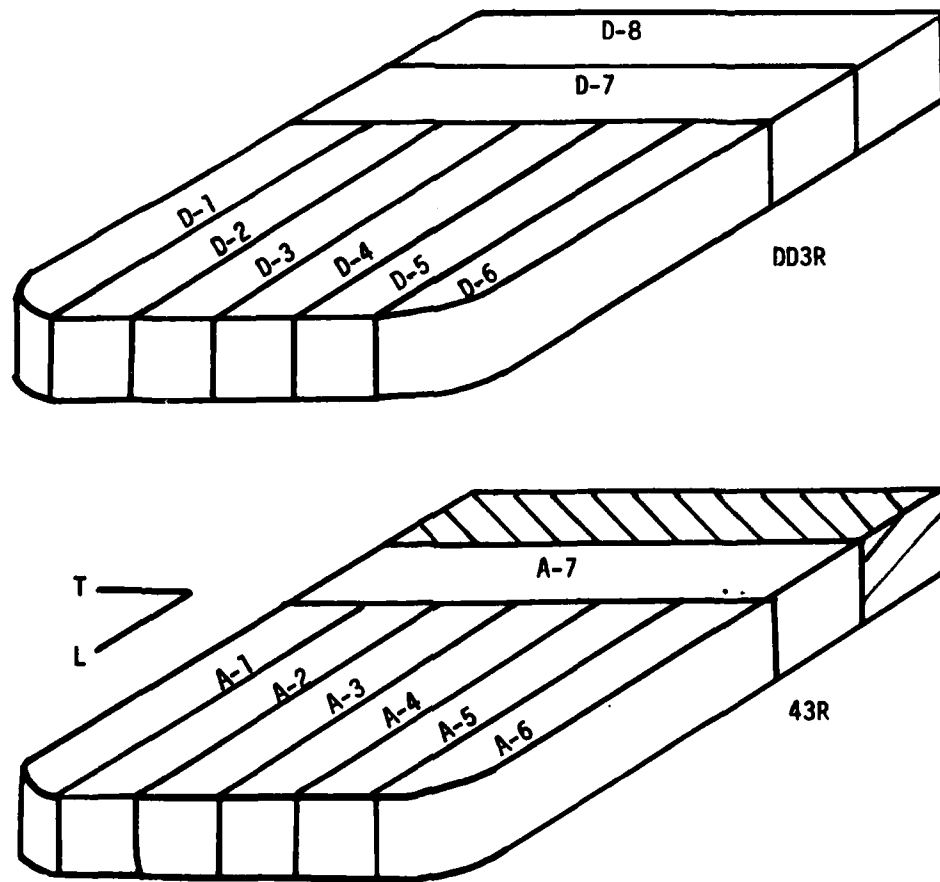
Figure 52. Schematic Showing the Arrangement of Initial Specimens
Tested by Pre-Cracking to Failure.
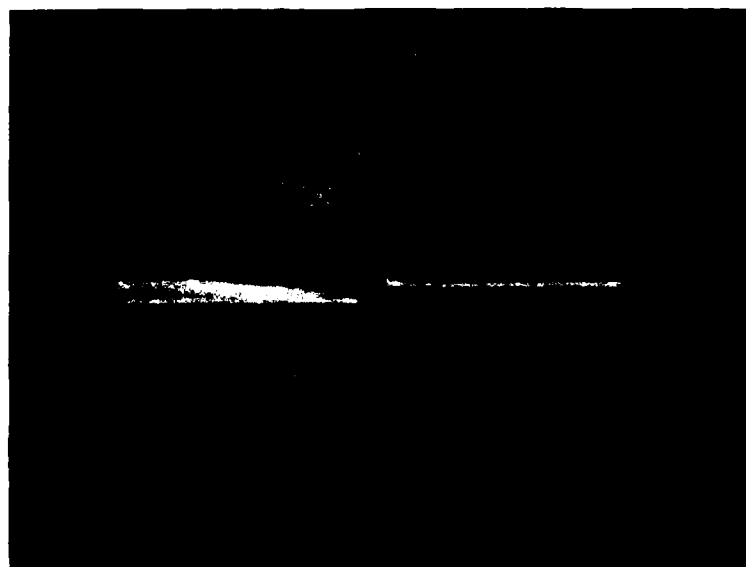
Figure 50.   Eccentric Cracking in Charpy Specimens.
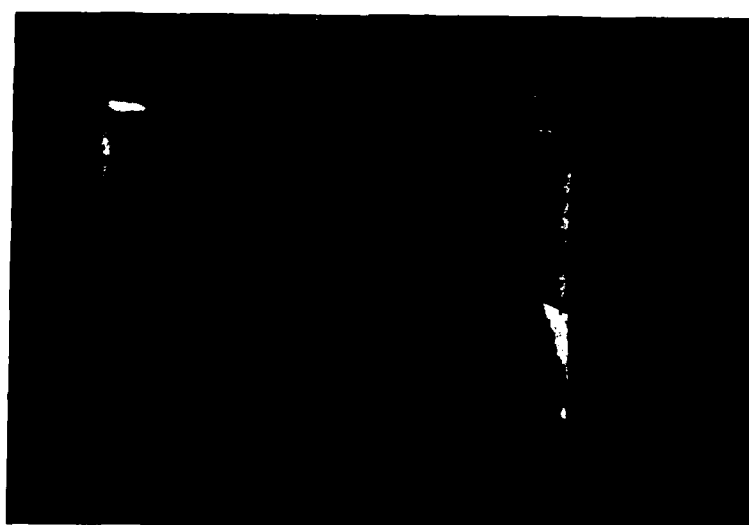
Figure 51.   Sample Failed During Pre-cracking has Even Crack Front.
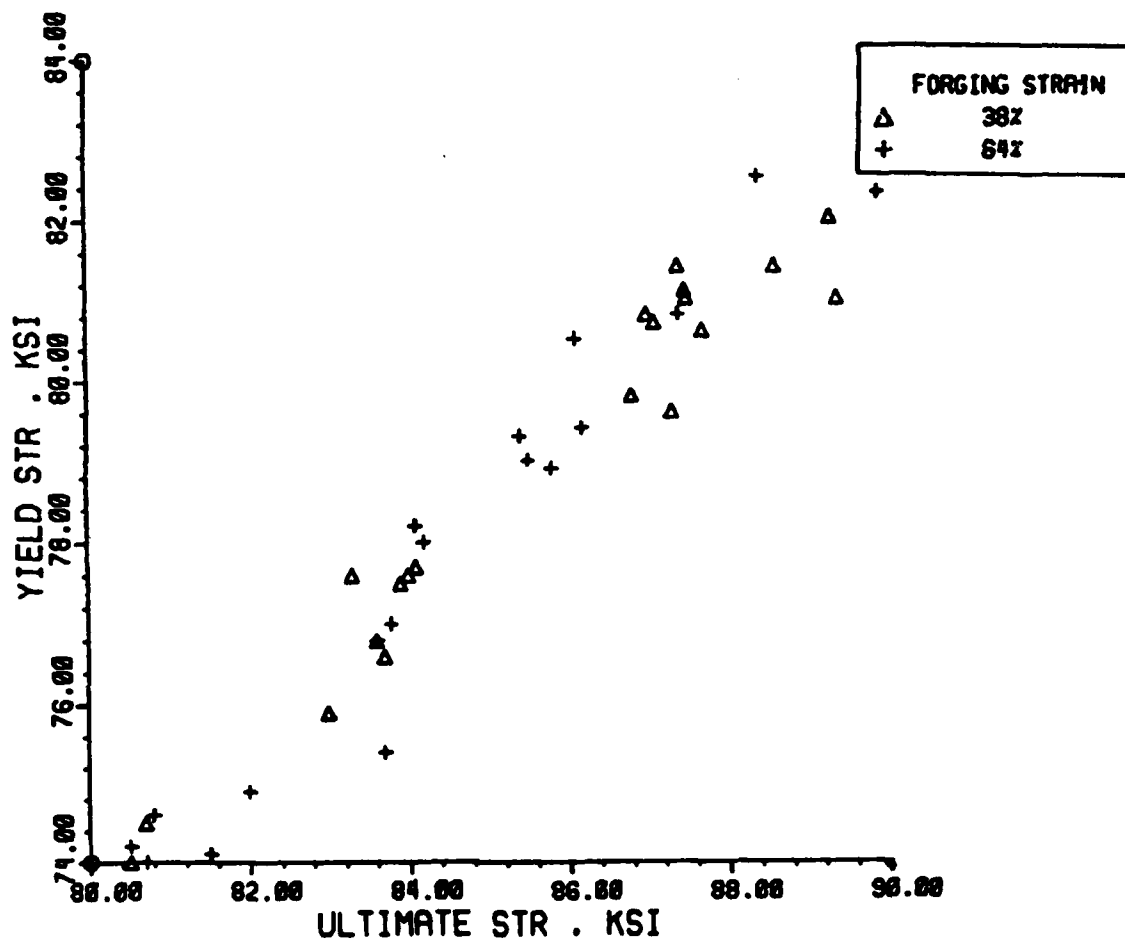
Figure 49. Effect of Forging Reduction on Strength.
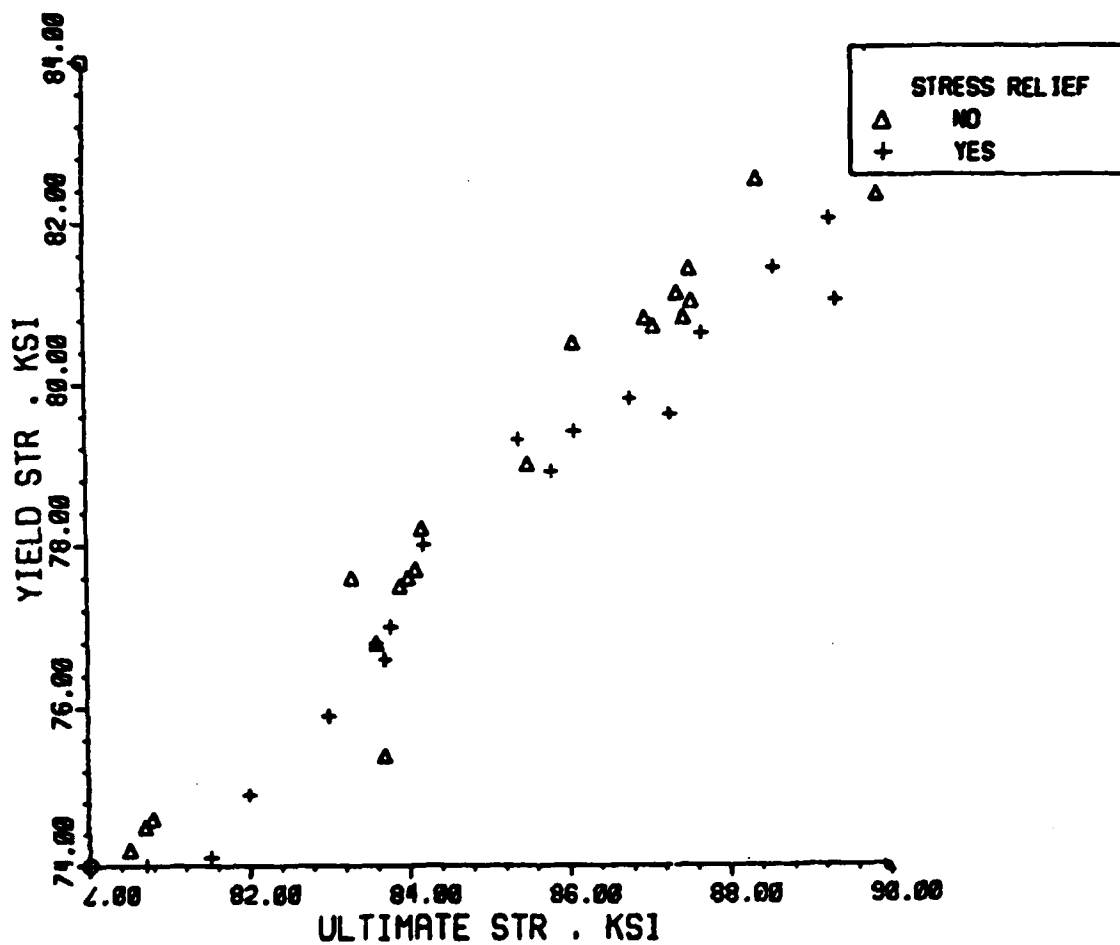
Figure 48. Effect of Stress Relief on Strength.
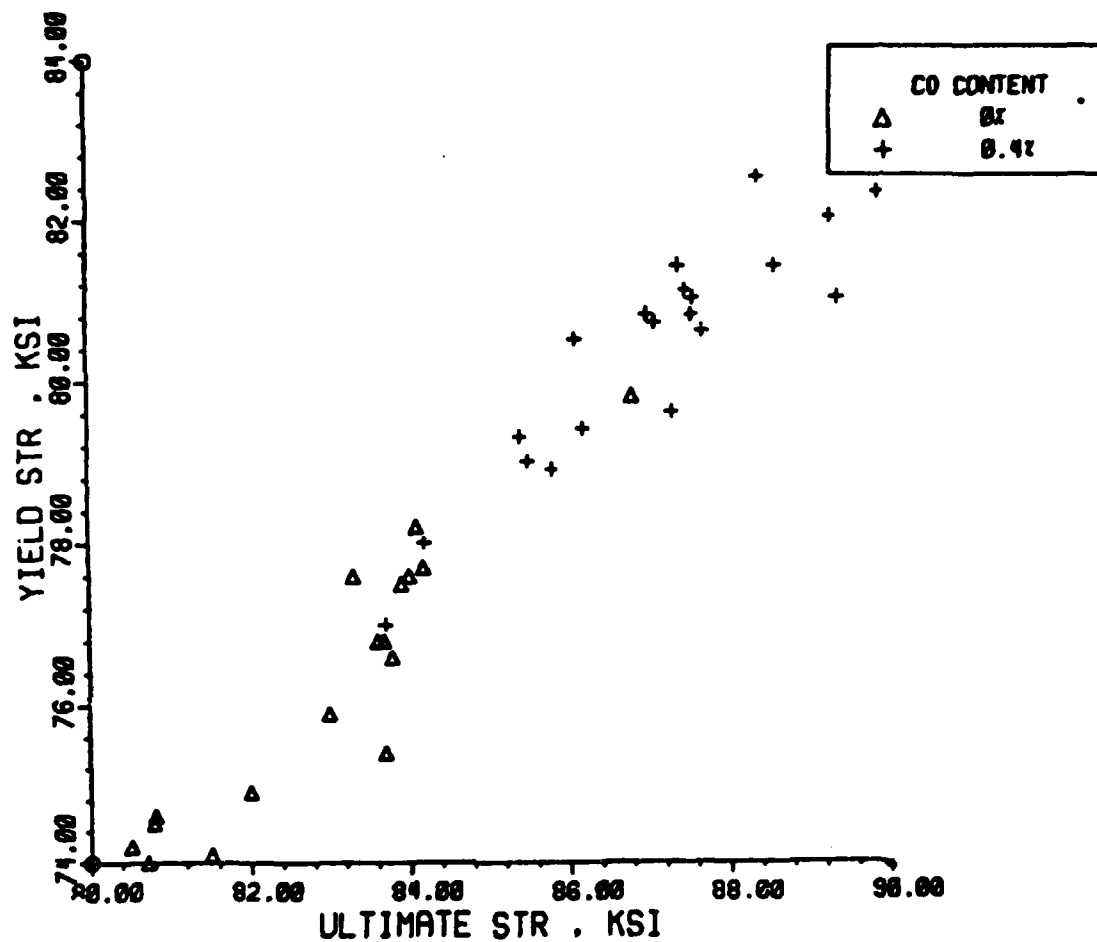
Figure 47. Effect of Cobalt Content on Strength.
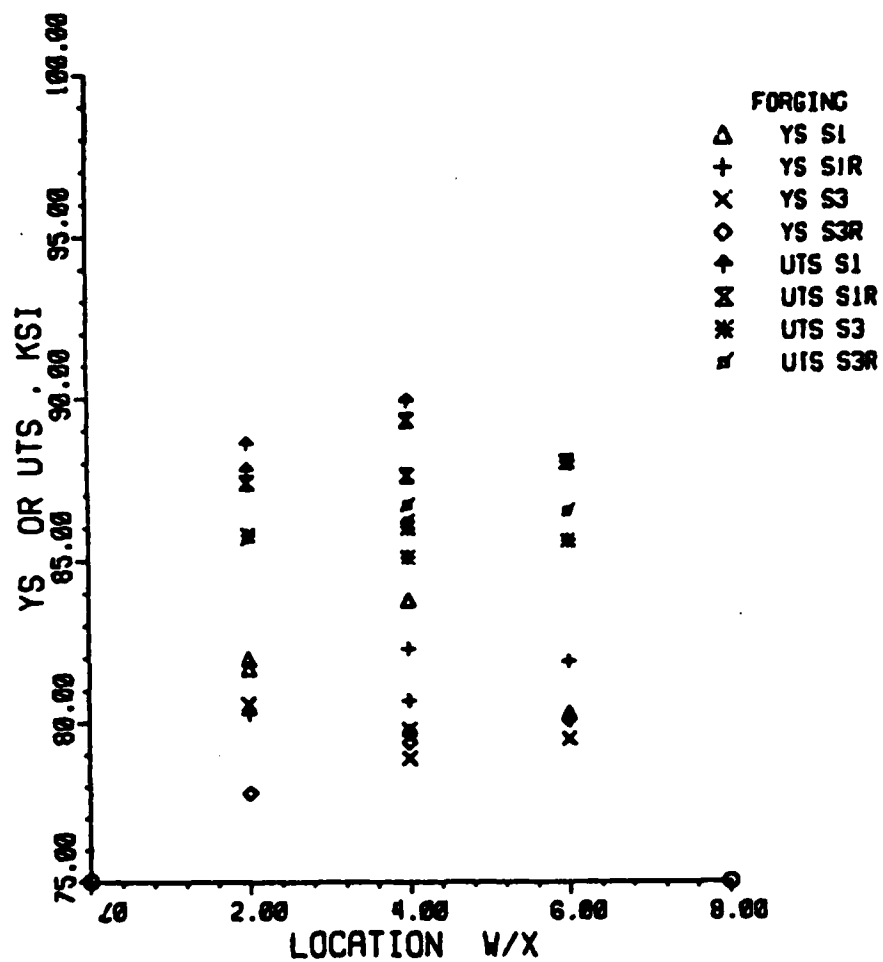
Figure 46. Yield and Ultimate Tensile Strength vs. Location in Forgings.

185
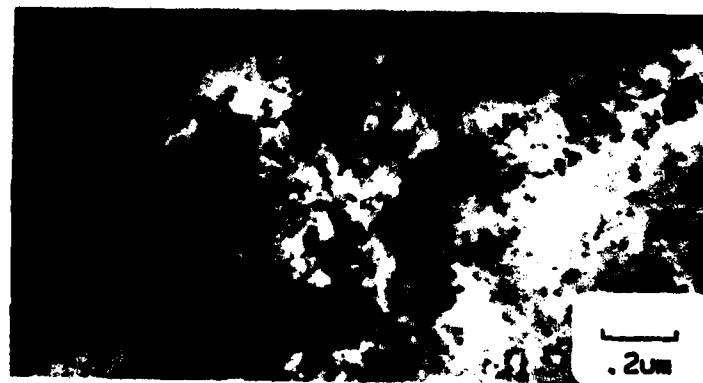
Figure 45. A Particularly Dense Oxide Array, Reaching 1.5 μm Across. (a), (b), and (c) are increasing magnification micrographs of the S-L plane of a 64% upset forging with 0% Co that has not been stress relieved.

(a)

(b)

Figure 44. Fragmented Oxides on the Surfaces of Al P/M Powders are Effective Barriers to Boundary Movement. (a) A relatively undeformed powder particle shows evidence of grain growth in the direction of the arrows; (b) at higher magnification it is clearly seen that growth is inhibited by oxide clusters. These micrographs are from the S-L plane of a 38% upset forging with 0% Co and stress relieved.

Figure 42.   Individual Oxide Arrays in CT91 Forgings. (a) T-L plane of a 38% upset forging with 0% Co and stress relieved; (b) S-L plane of a 64% upset forging with 0.4% Co and not stress relieved.
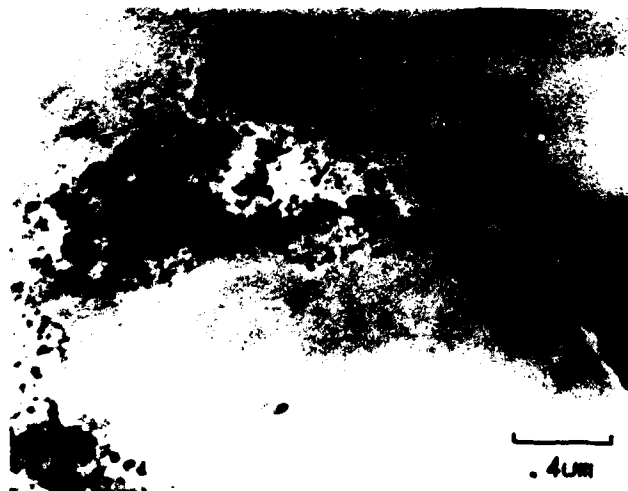
Figure 43.   The Oxides are Effective Barriers to Grain Growth.
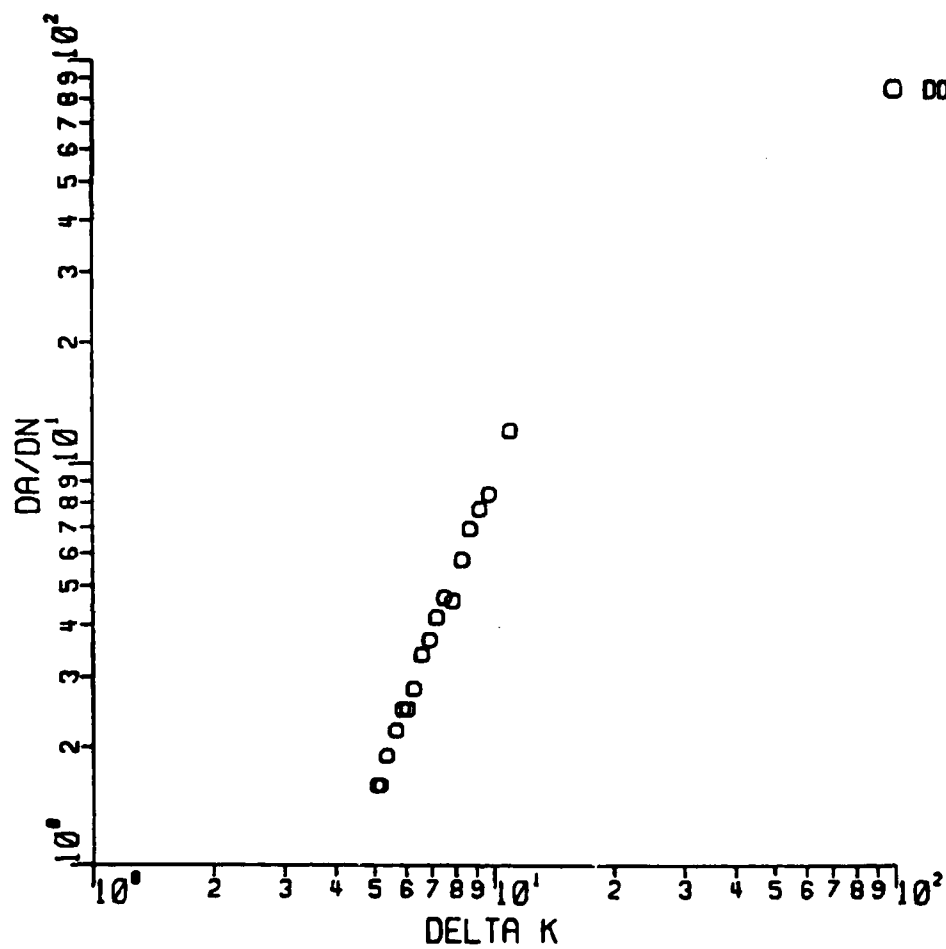
Figure 60. FCP Data for 001 Condition Using T-L CT
Specimen.

Figure 61.   FCP Data for O11 Condition Using T-L CT
Specimen.
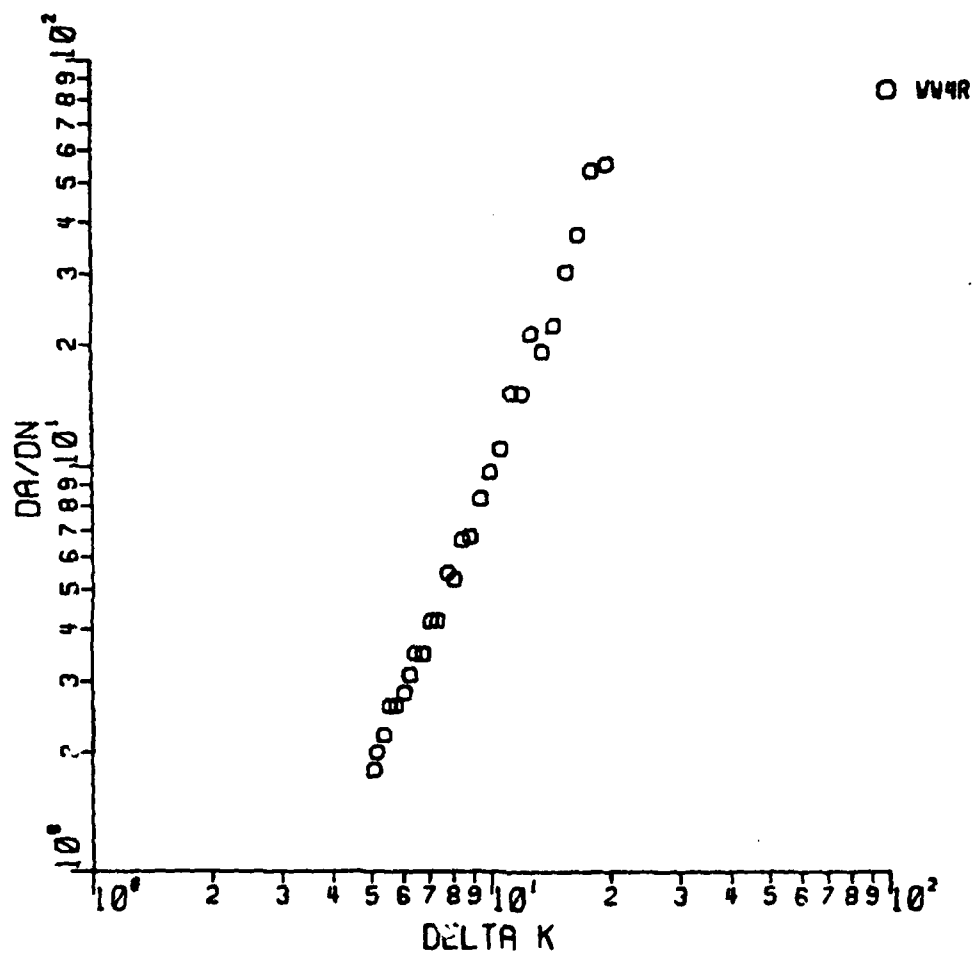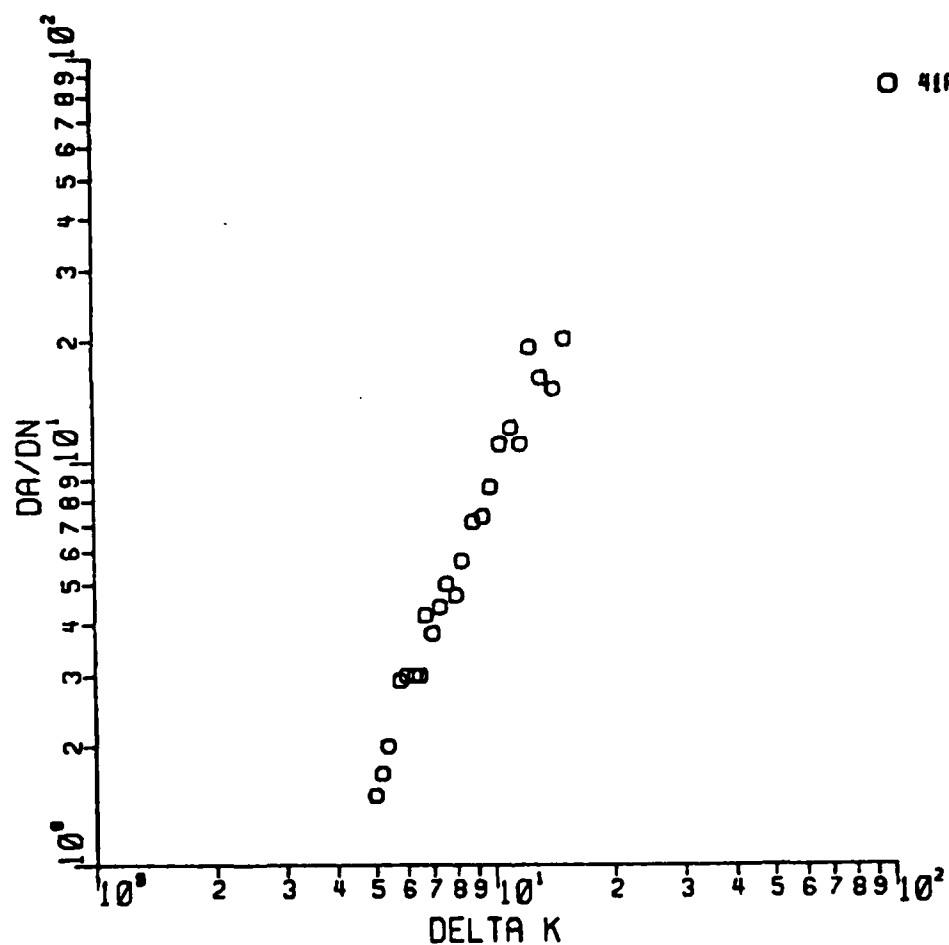
Figure 62.   FCP Data for 101 Condition Using T-L CT
Specimen.

198
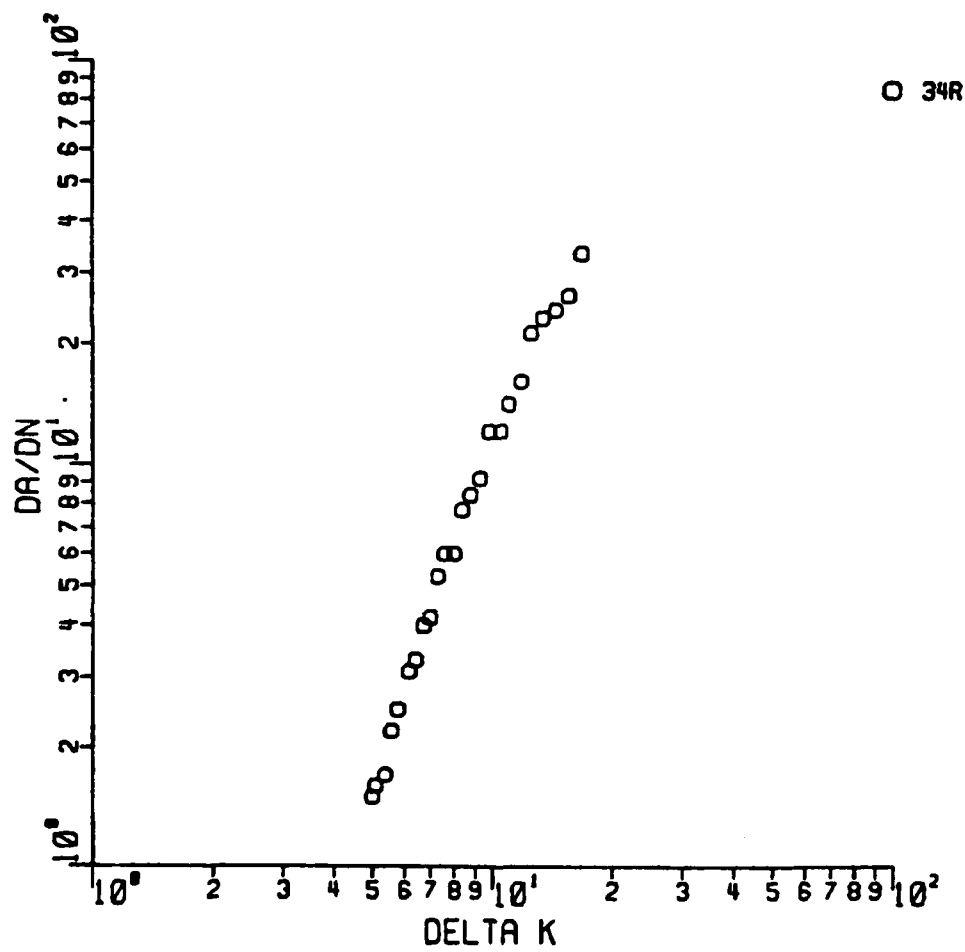
Figure 63. FCP Data for 111 Condition Using T-L CT
            Specimen.

199
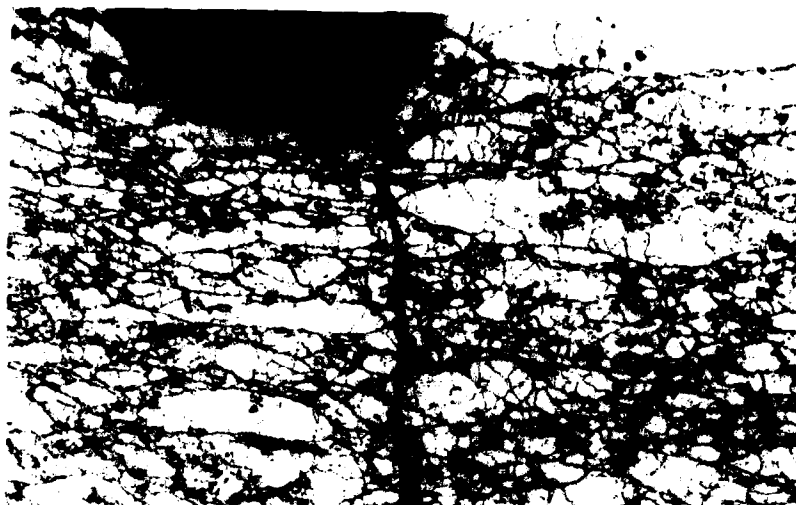
(a)

25um

(b)

Figure 64. Crack Path in Ring Specimen. (a) near the notch; (b) near the crack tip.

(a)

(b)

(c)

50um
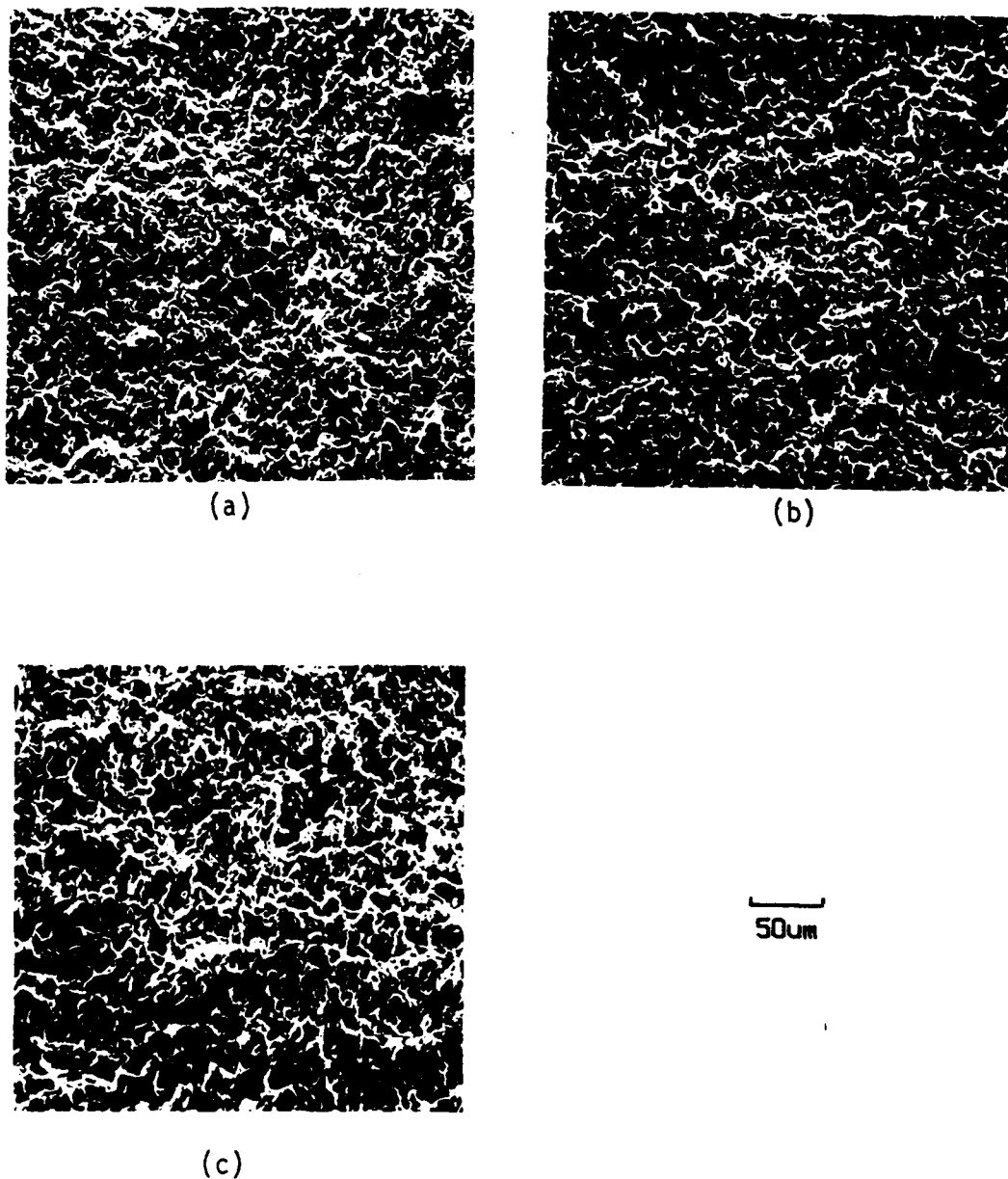
Figure 65. Representative Fractographs for L-T Ring Specimens at ΔK's
            Tested. The fracture mode is primarily transgranular.
            The fracture plane is the TS plane and evidence of the
            nearly equiaxed microstructure in that plane is visible.
            (a) 5.5 MPa√m (ΔK = 5 Ksi√in.; (b) 7.7 MPa√m (ΔK =
            7 Ksi√in.); (c) 11 MPa√m (ΔK = 10 Ksi√in.)

(a)

(b)

(c)
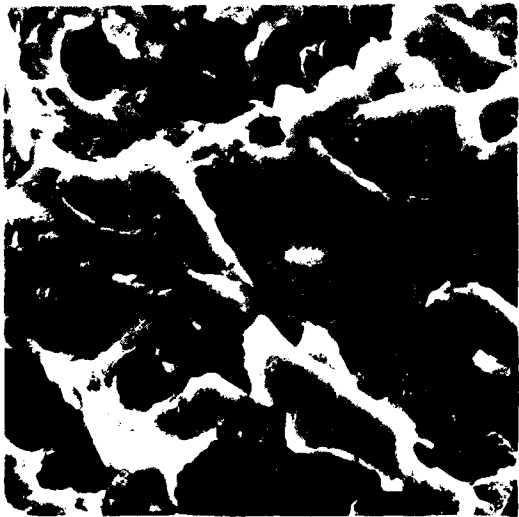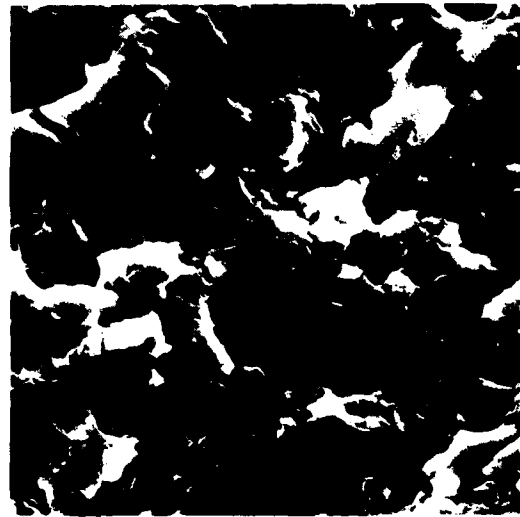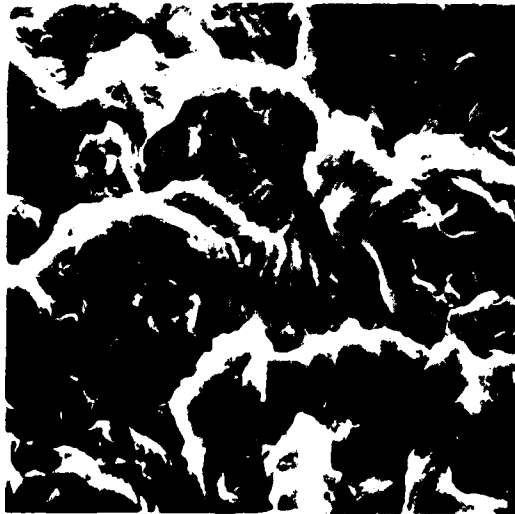
Figure 66. Striations Were Visible at all ΔK's Tested in All Conditions. Note the striation spacing increases with ΔK. In general the fracture is ductile with evidence of dimples. There are areas of brittle fracture as in (b) and evidence of secondary cracking. (a) ΔK = 5.5 MPa√m (5 Ksi√in.); (b) 7.7 MPa√m (7 Ksi√in.); (c) 11 MPa√m (10 Ksi√in.)

Figure 67. Ductile Striations are Visible in this Sample. Compare
spacing to Figure 66(c). Both are at $\Delta K = 11$ MPa$\sqrt{m}$
(10 Ksi$\sqrt{in}$.), indicating that striation spacing may
not always be a good indication of crack growth rate.
Note also the "white dots" which are reported to be
η particles [108, 227].

203

(a)
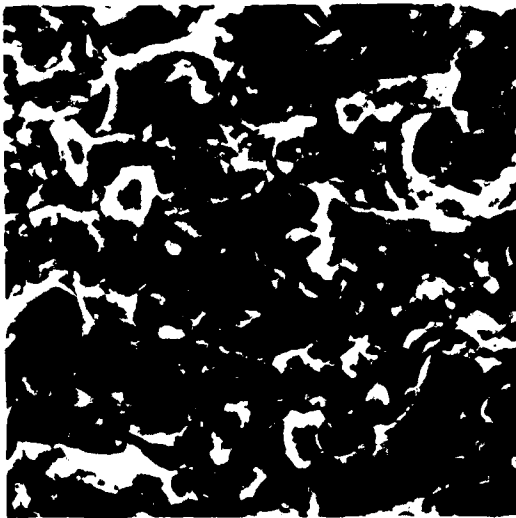
10um
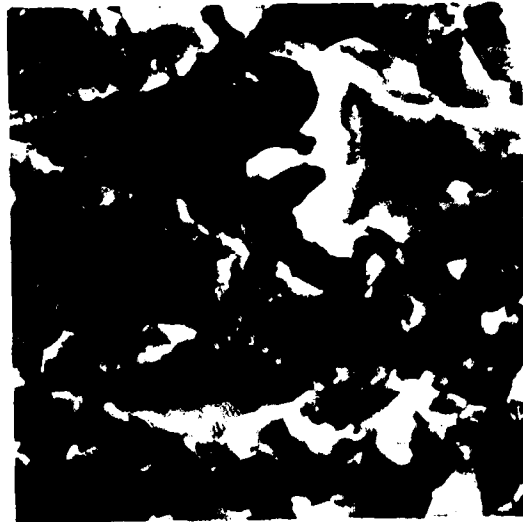
(b)

5um

(c)
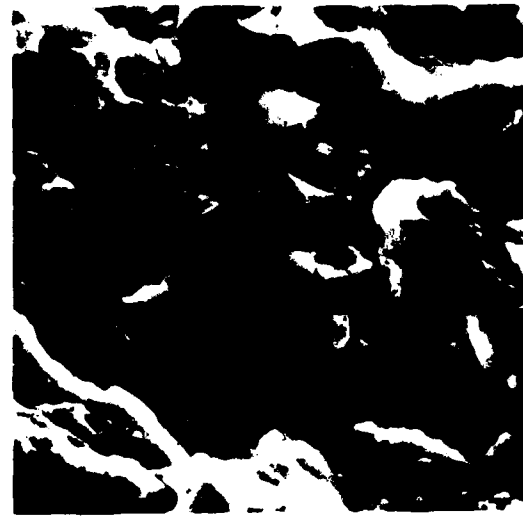
(d)

Figure 68. Evidence of the Influence of Oxide is Seen in These Fractographs.

Figure 69. An Area of Intergranular Failure, Probably at a Prior
Particle Boundary. Note the transition (arrow) from
transgranular to intergranular along a ridge.
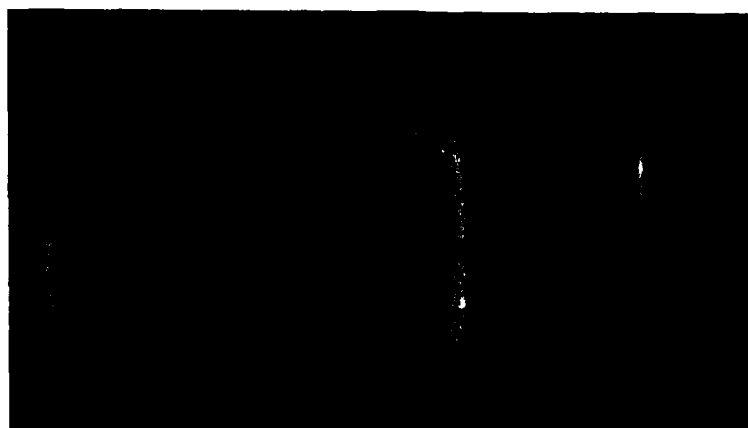
(a)
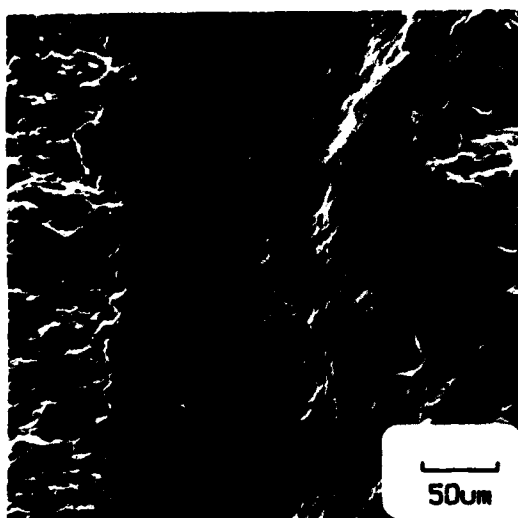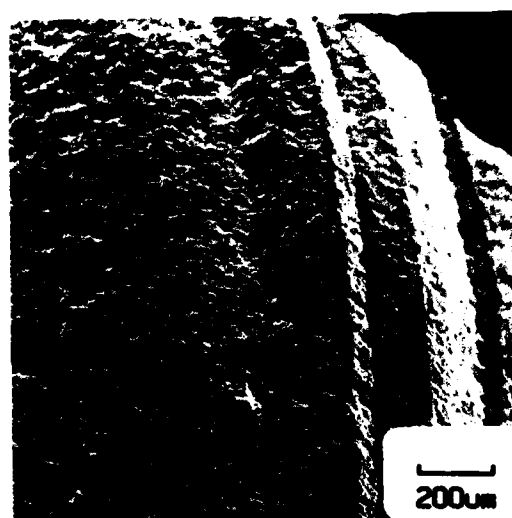
(b)   (c)

Figure 70. Evidence of Mechanical Interference in a Crack Growth
Specimen. The dark areas are probably oxides resulting
from abrasion. In (b) the deformation in the first black
band is seen. In (c), the bands are associated with the
crack front changing planes.

(a)

(b)

(c)
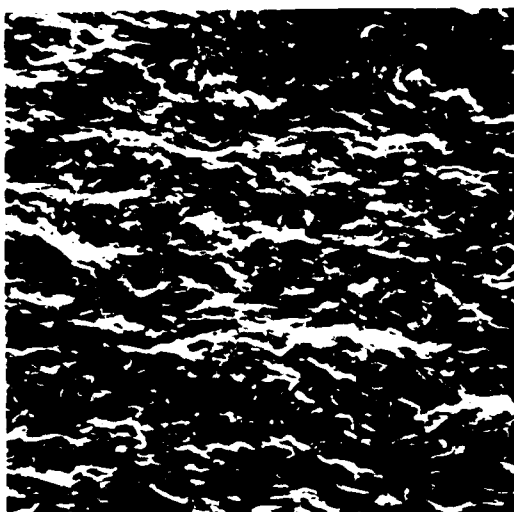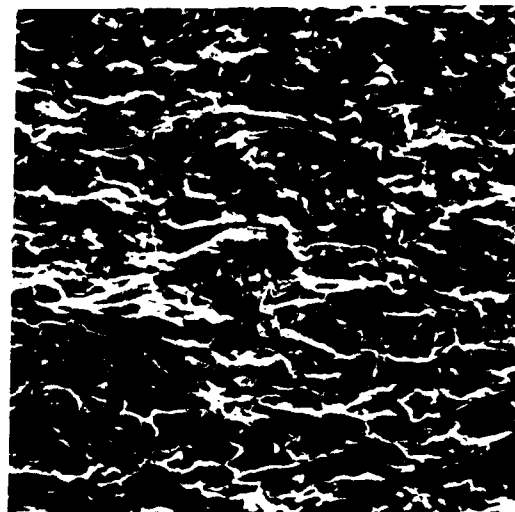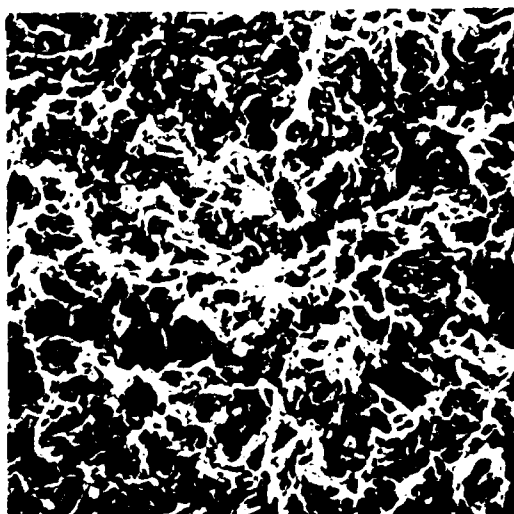
25um

Figure 71. L-T Compact Tension FCP Fracture Surfaces. The fracture
plane is L-S. Note the elongation of fracture features
similar to elongation of microstructure. This elongation
is not obvious at $\Delta K = 11$ MPa$\sqrt{m}$ (10 Ksi$\sqrt{in}$.)
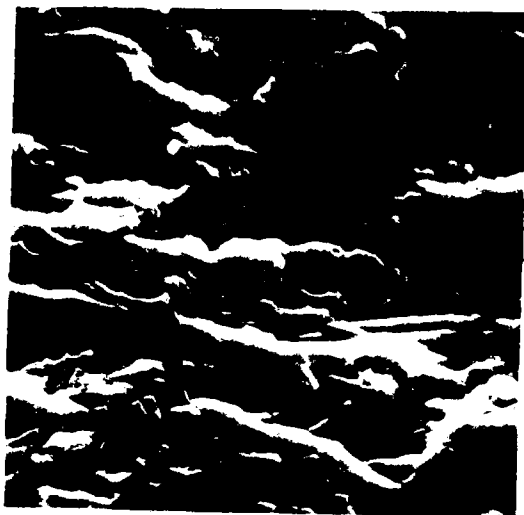
(a)
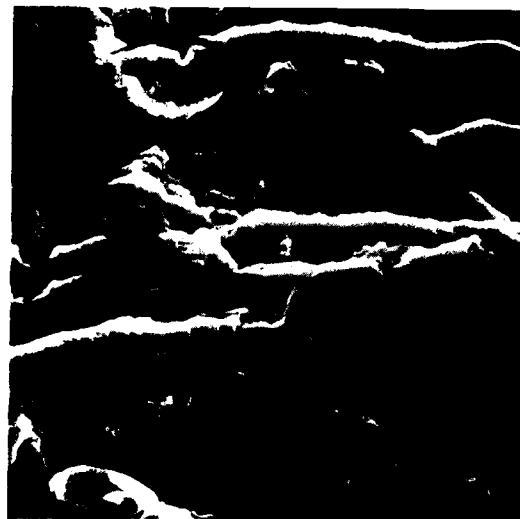
(b)
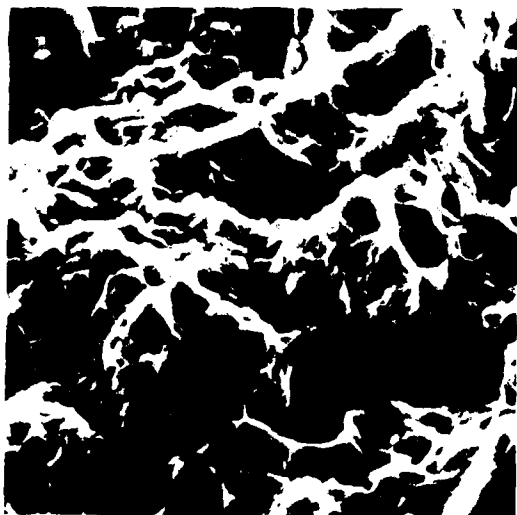
(c)

5um

Figure 72. Same as Figure 71 but Higher Magnification. Striations are rarely visible on C-T fracture surfaces. The lower ΔK's also have a more brittle appearance than was seen on ring specimens (Figures 65-67).
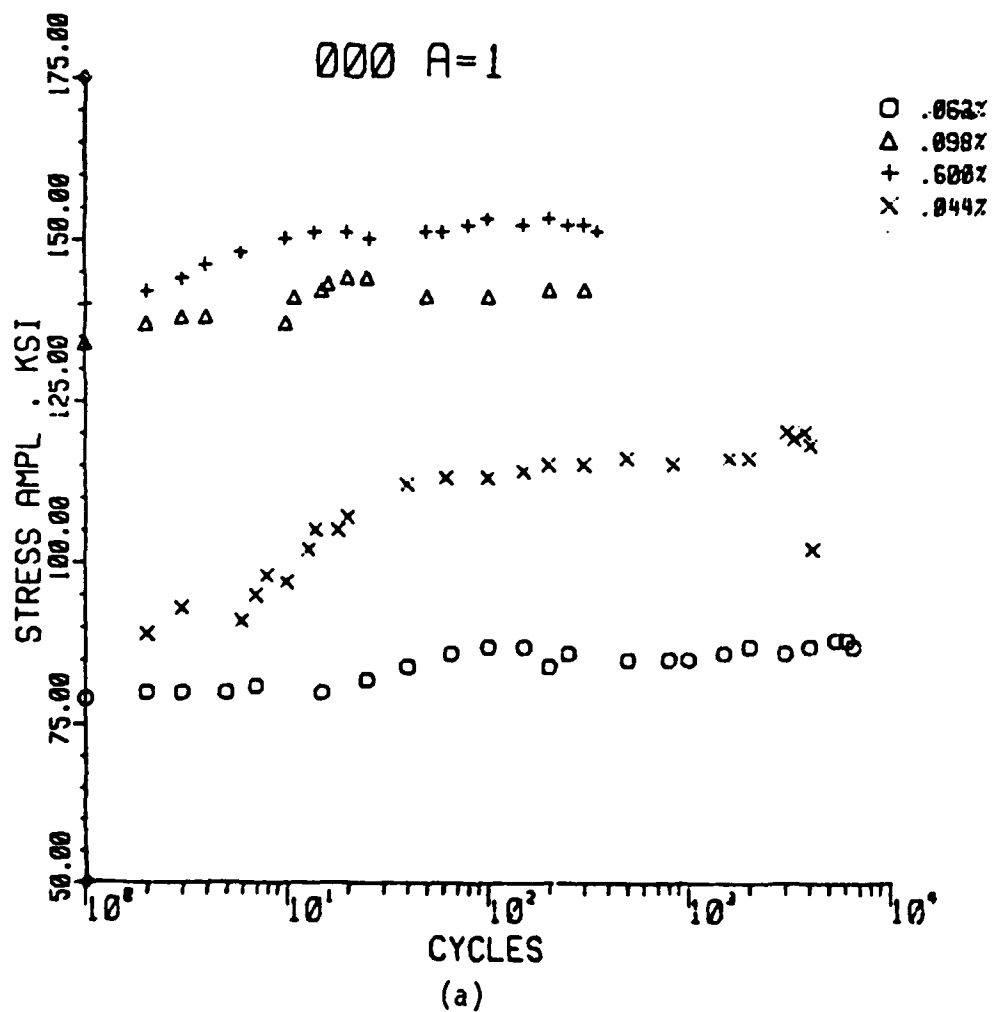
Figure 73. Cumulative Glide Plots for the Eight Conditions
Tested (A_ϵ = 0.95, Plastic Strain Control).
a. 000.
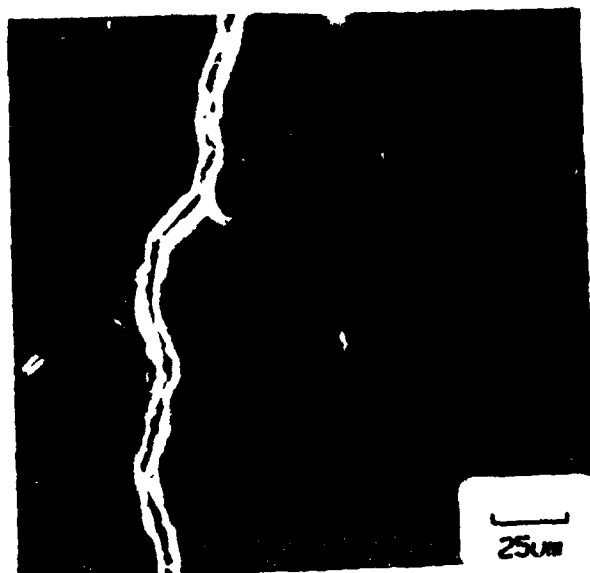
(a)

(b)

Figure 77.   Examples of Surface Cracks Found When the Test was
Stopped at Initiation. (a) Multiple cracking in 000;
(b) Debris in crack and evidence of powder particle
pull-out. Condition 000, Sample D5-2, 0.029%,
N_i = 2700.

Figure 76 (continued).   111

101 A=INF

O	.045%
△	.144%
+	.287%
X	.684%
◇	.947%
✦	1.054%

(c)

Figure 76 (continued).   101

221

011 A=INF

STRESS AMPL , KSI

CYCLES
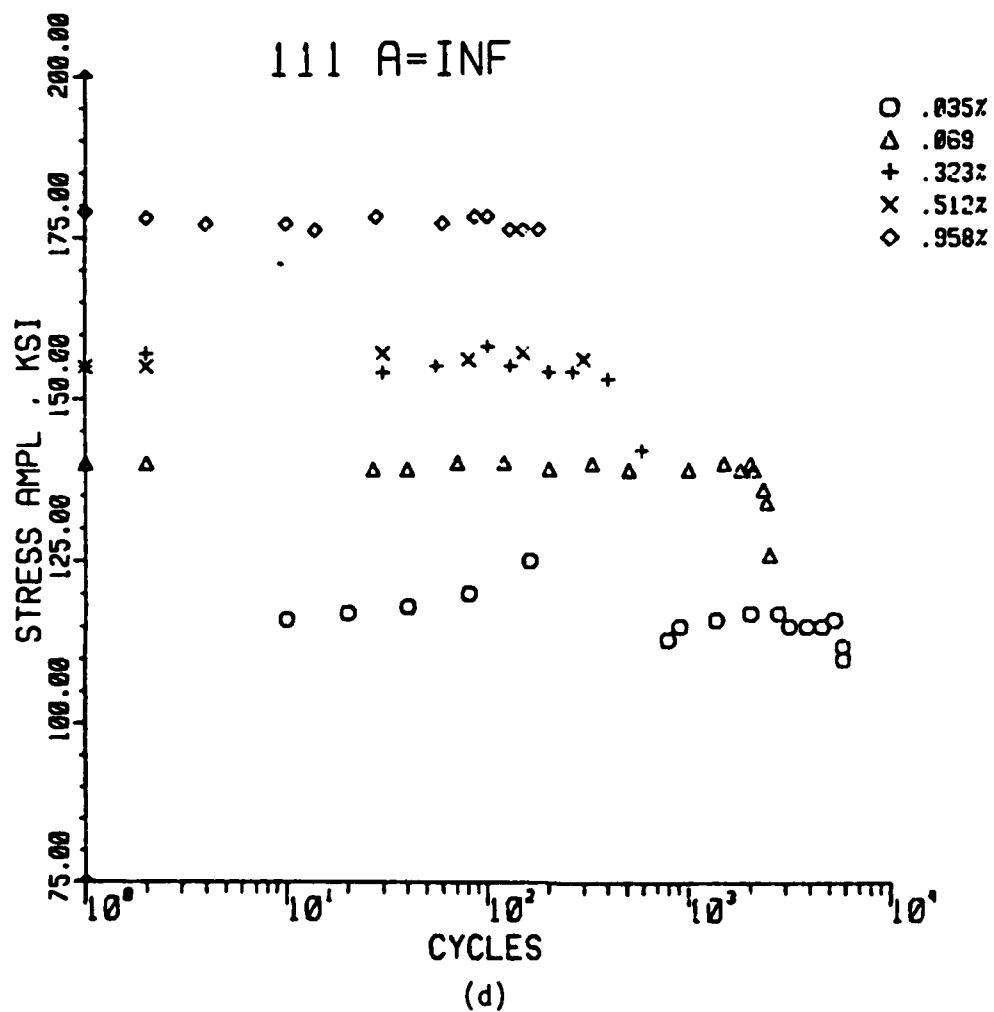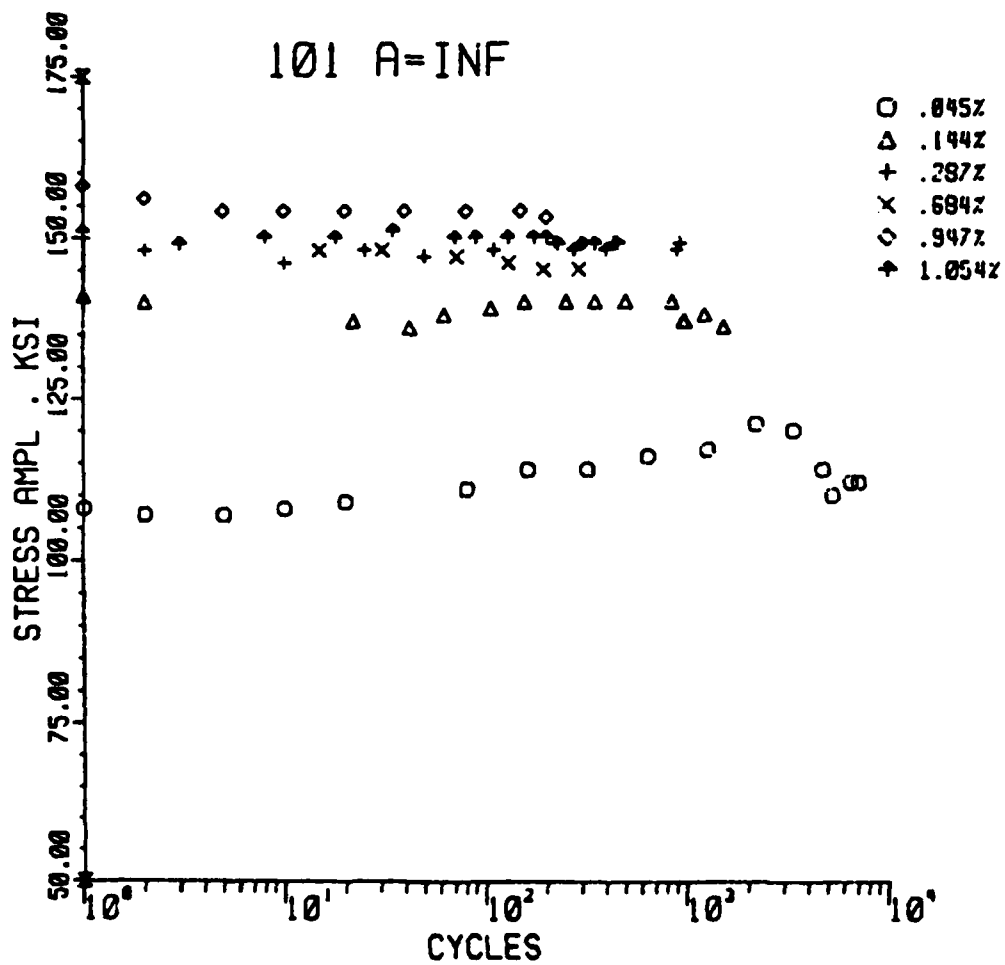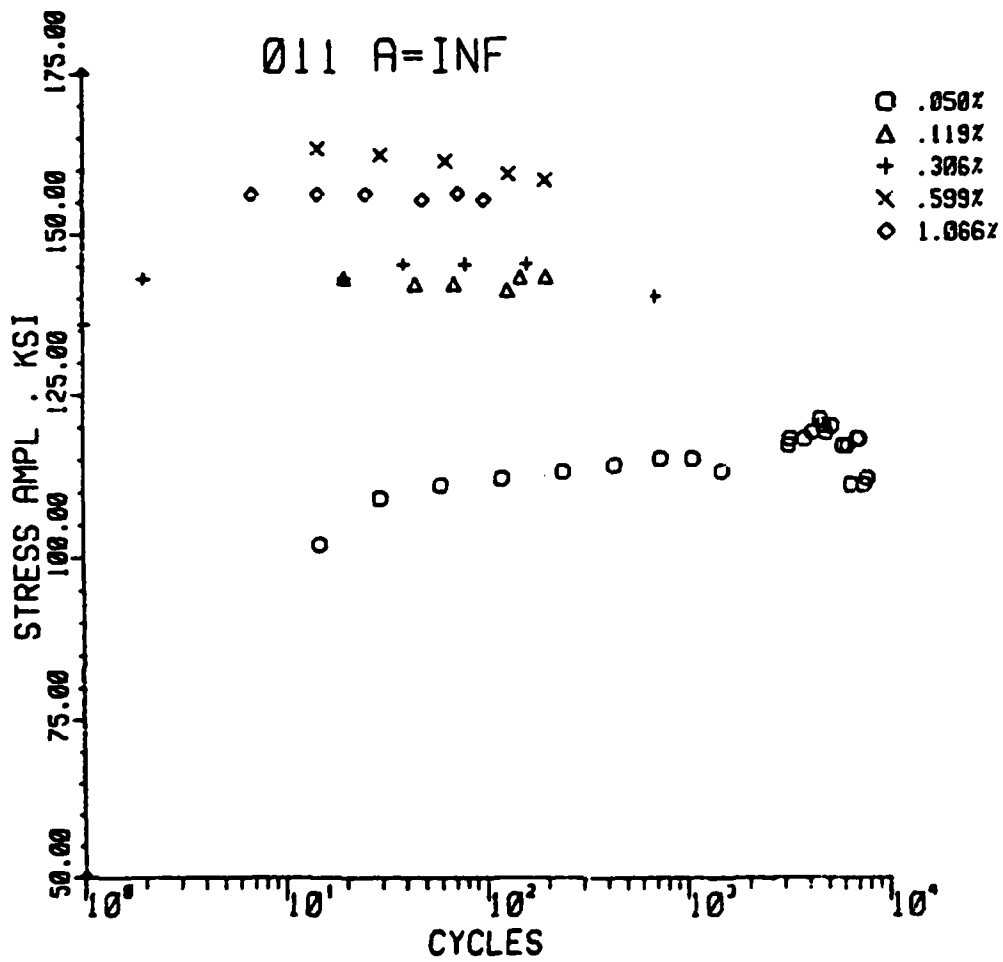
(b)

Figure 76 (continued).   011

220
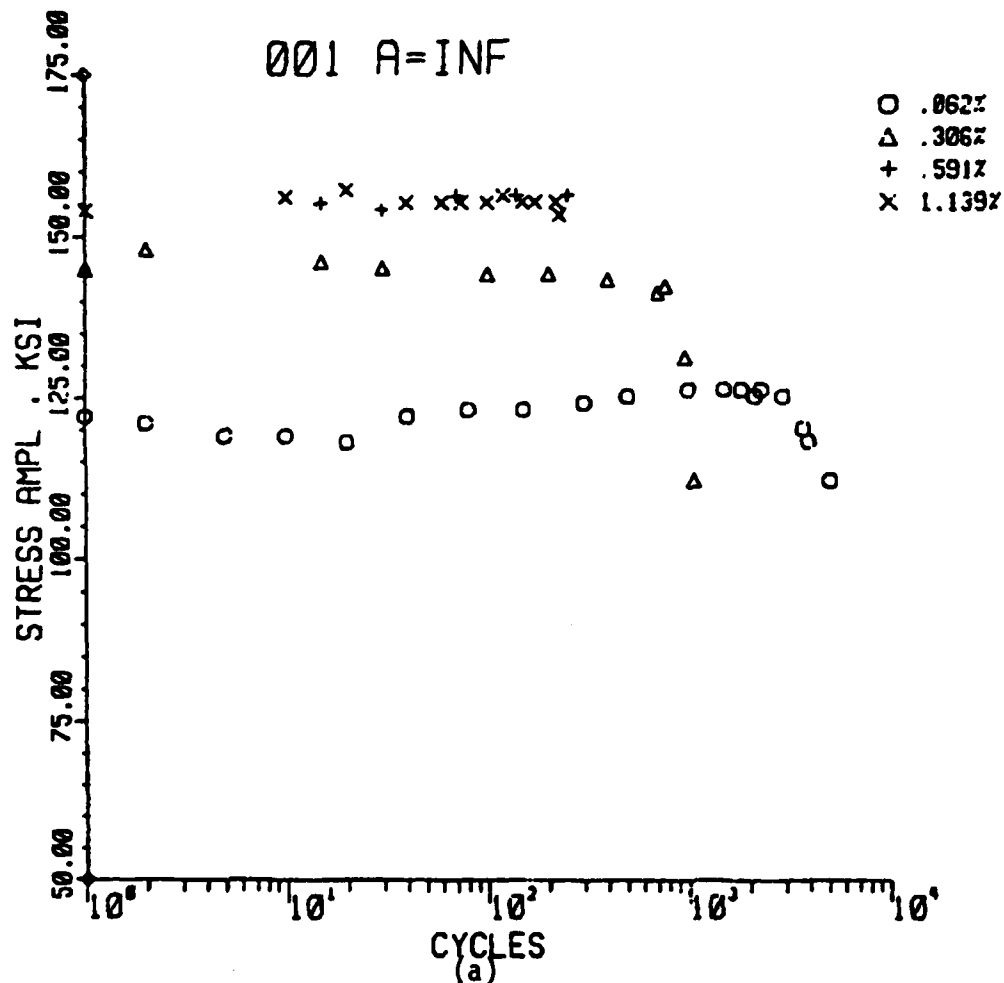
Figure 76. Cumulative Glide Plots for Specimens Tested
at $A_\epsilon = \infty$, Total Strain Control. a = 001

$$\sigma$$

$$\int_o^{\Delta\sigma_a} \varepsilon_p \, d\sigma$$

A

$$\varepsilon_p = K'(\sigma)^{1/n'}$$

$$\Delta\sigma_m$$

O   ΔW   B

$$\varepsilon_p$$

C

$$\Delta\varepsilon_p$$
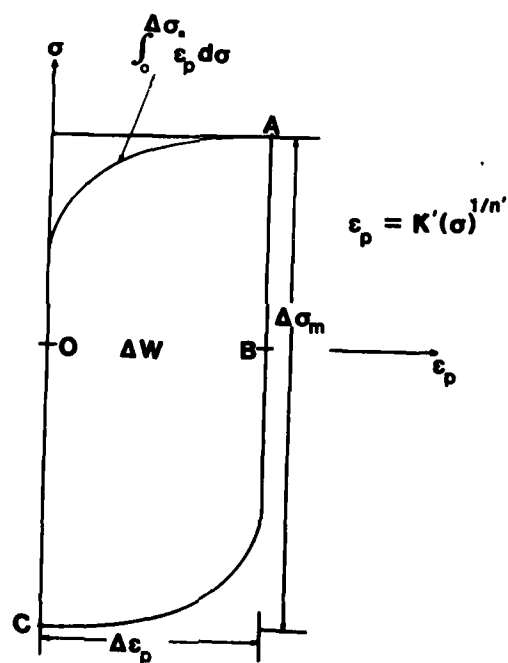
Figure 75. Idealized Hysteresis Loop of Stress vs. Plastic
Strain. The area enclosed represents the plastic
work per unit volume per cycle [173].
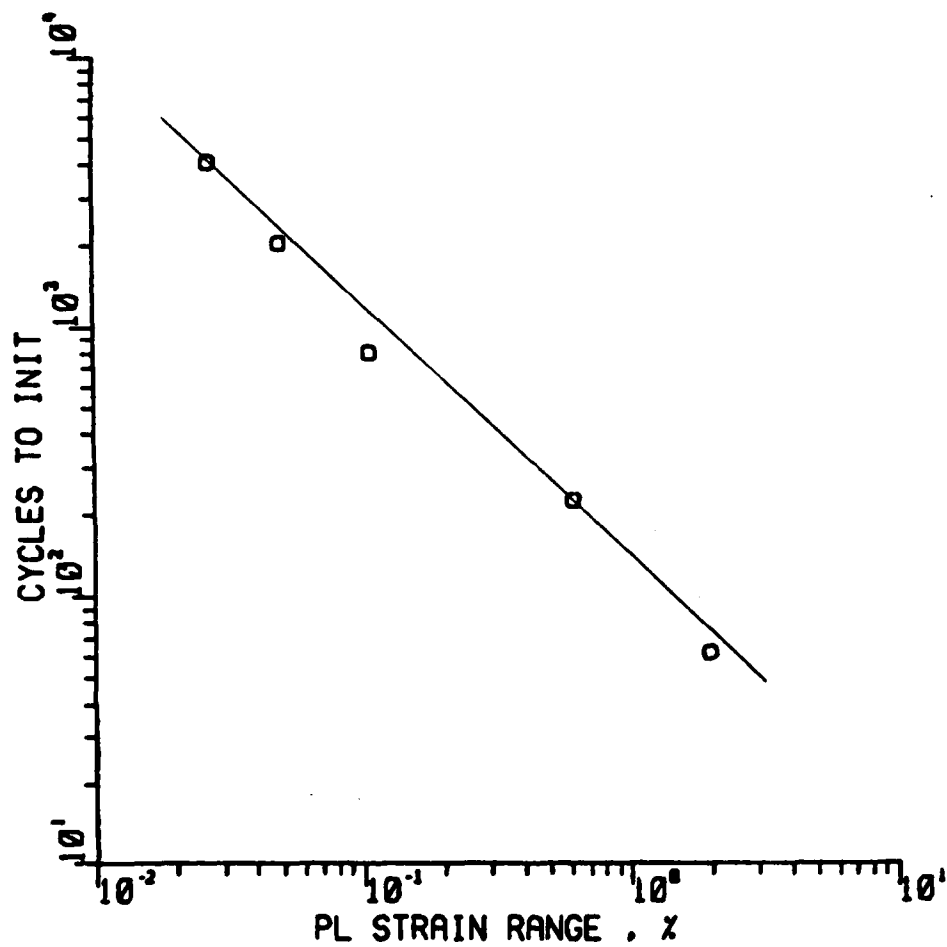
Figure 74. Typical Coffin-Manson Plot. This curve is for Condition 111 (64% upset, 0.4% Co, stress relieved). The slope is - 0.938 and $\beta = 1/m = 1.07$. There is no indication of dual slope behavior.

217

(h)
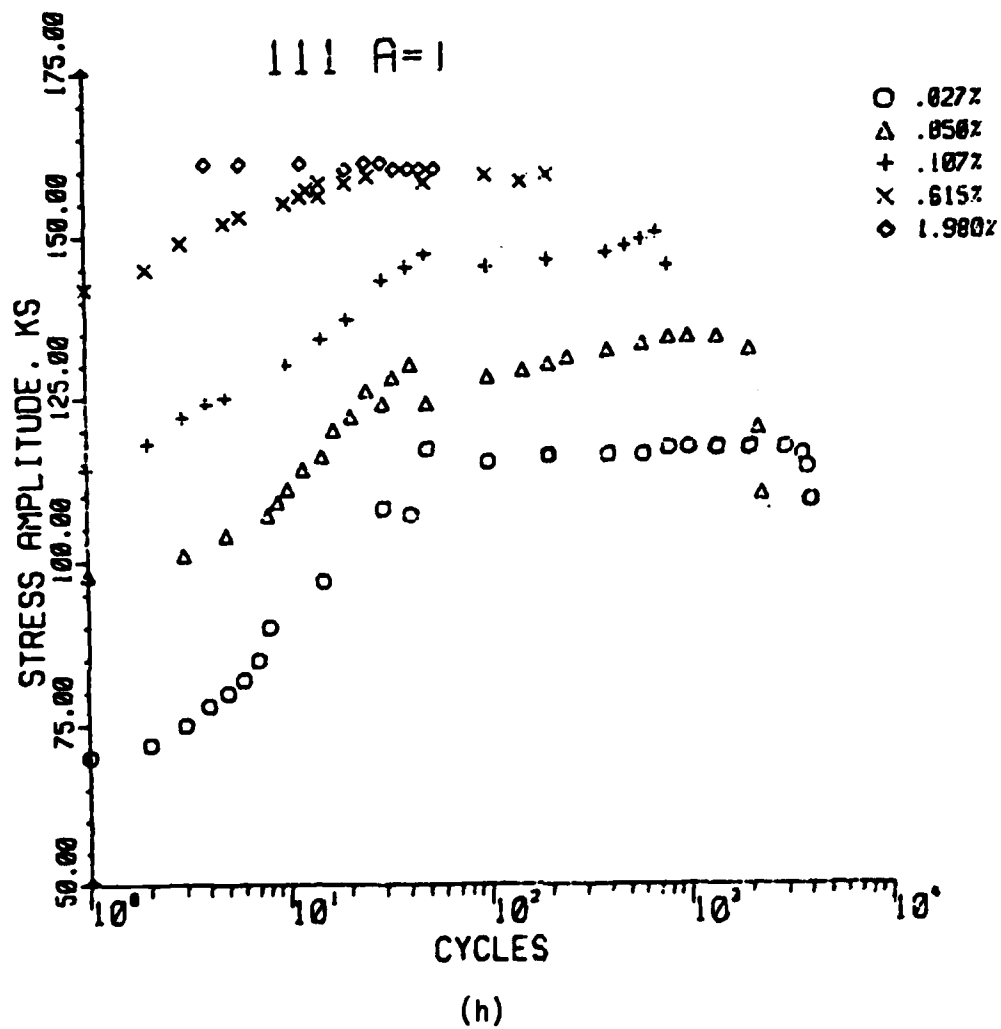
Figure 73 (continued). 111
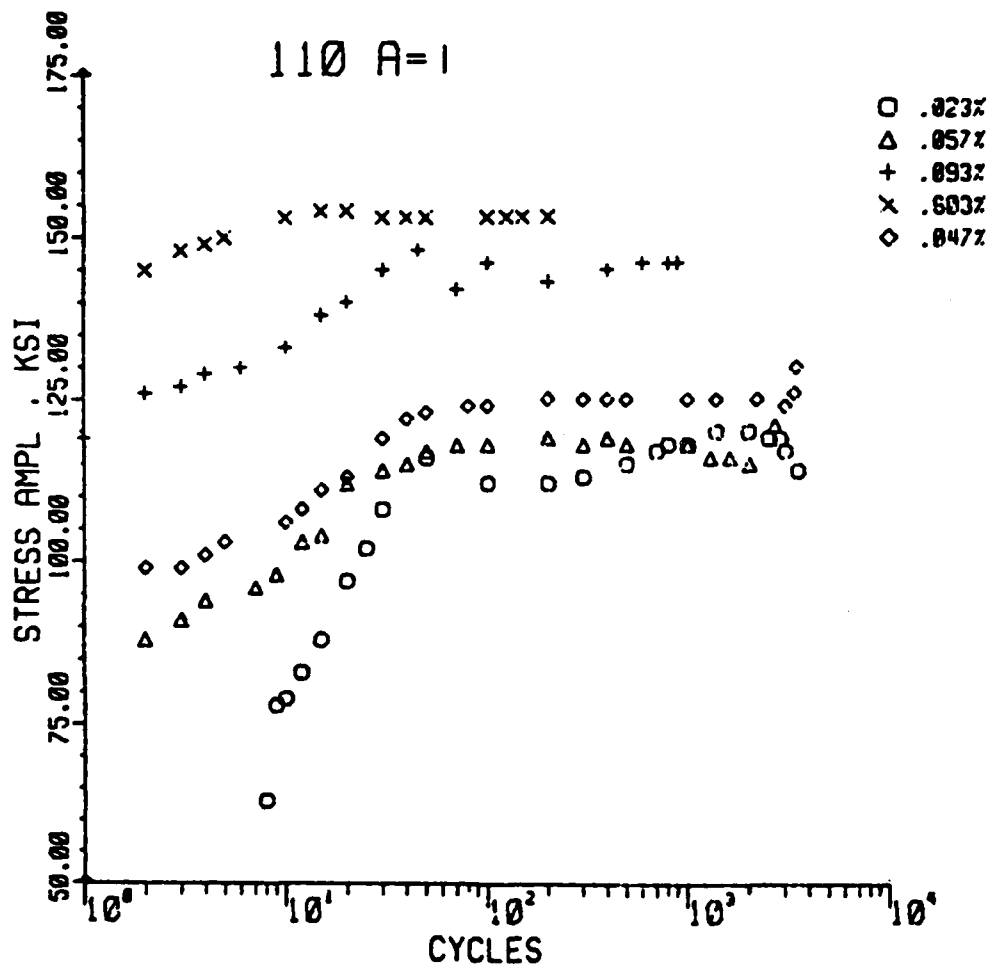
(g)

Figure 73 (continued).   110
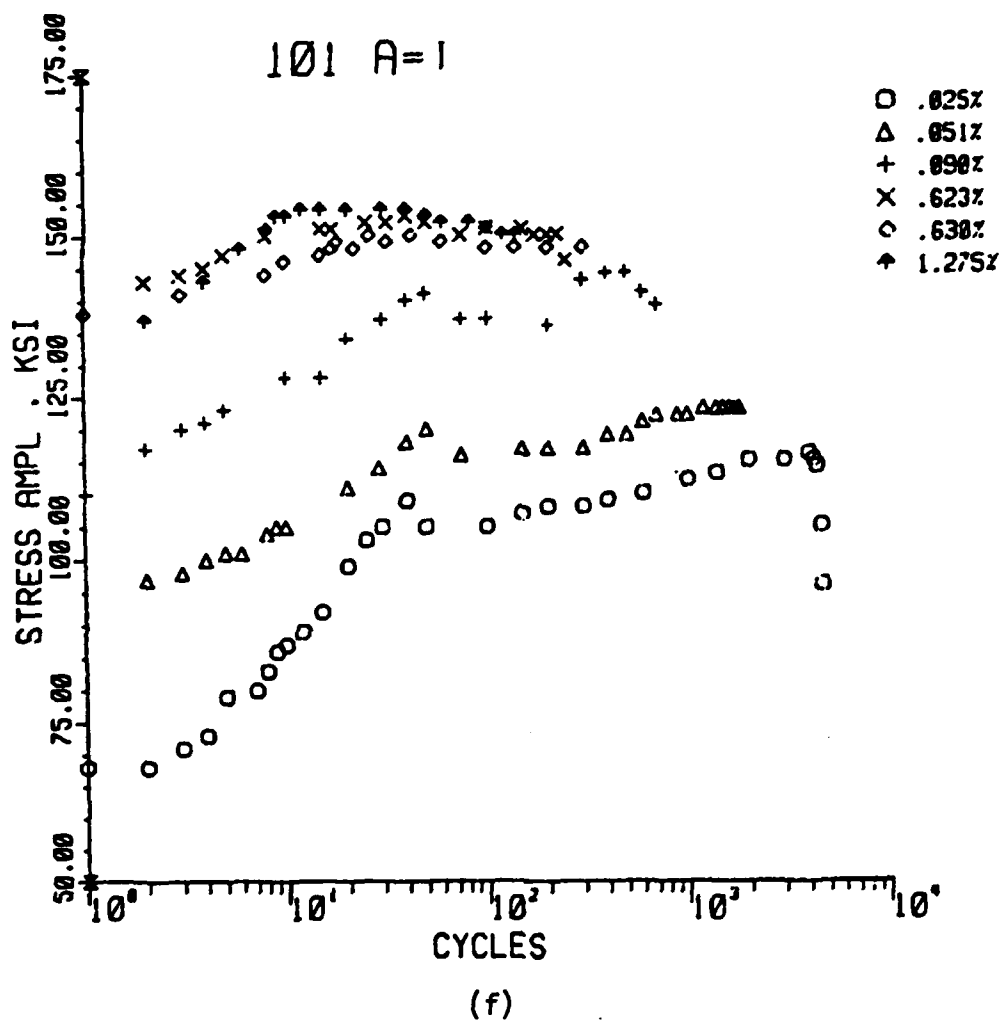
Figure 73 (continued).   101
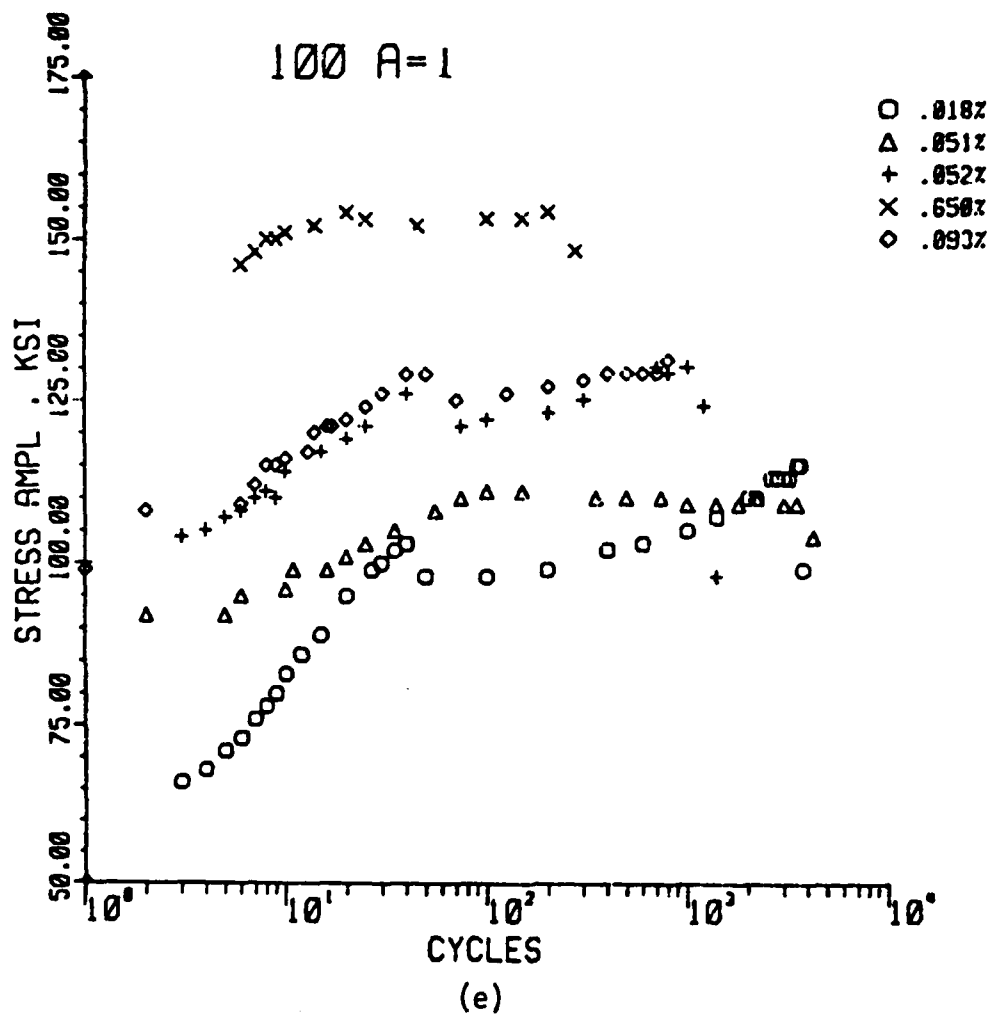
214

Figure 73 (continued).   100

213

Figure 73 (continued). 011

010 A=1

STRESS AMPL . KSI

175.00
150.00
125.00
100.00
75.00
50.00

O .022%
△ .056%
+ .049%
× .080%
◇ .585%

10⁰   10¹   10²   10³   10⁴

CYCLES

(c)

Figure 73 (continued).   010

211

001 A=1

STRESS AMPL . KSI

O .033%
△ .021%
+ .041%
X .104%
◇ .638%
✦ .585%

CYCLES
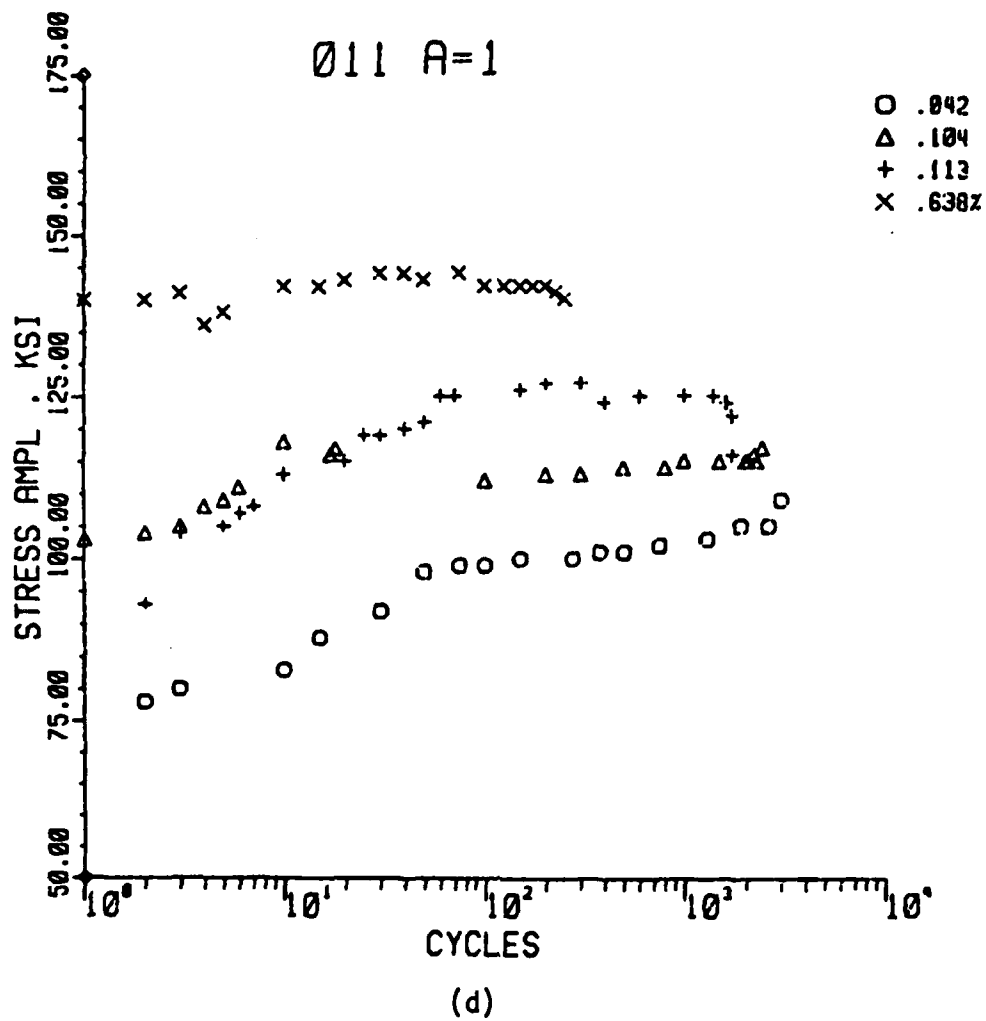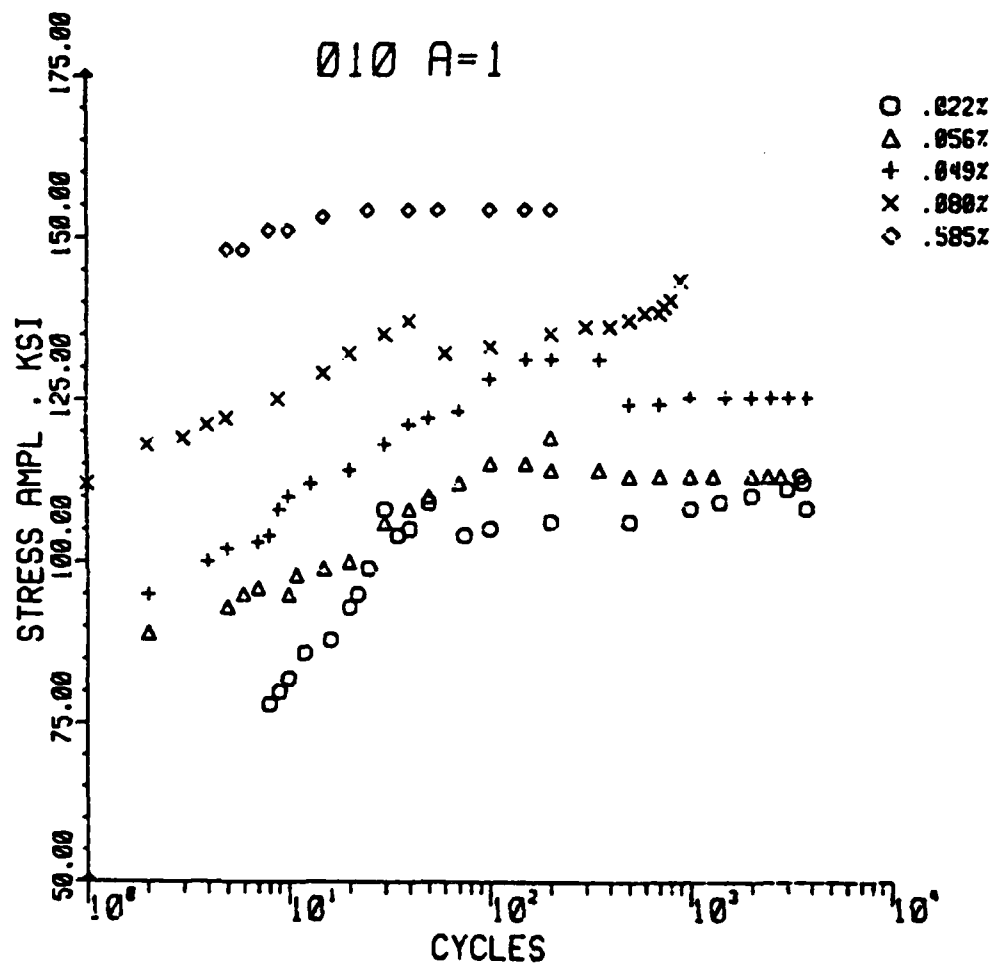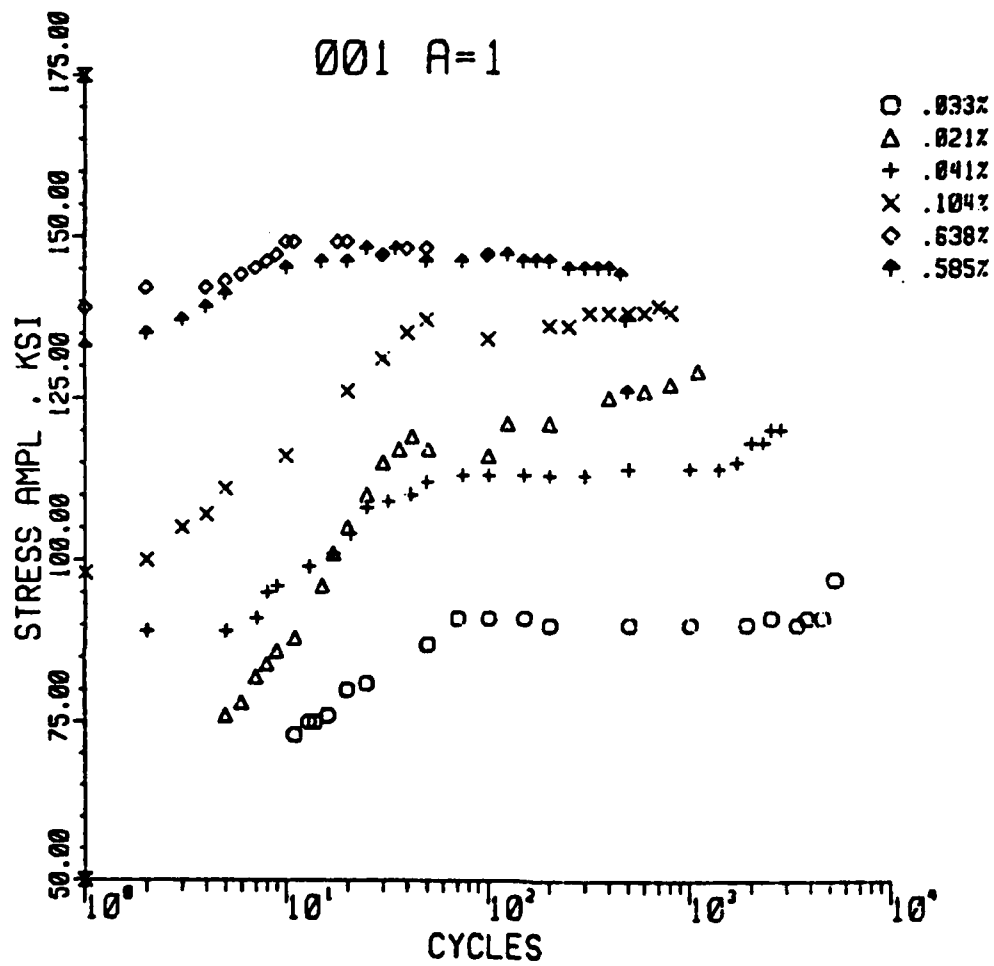
(b)

Figure 73 (continued). 001

210
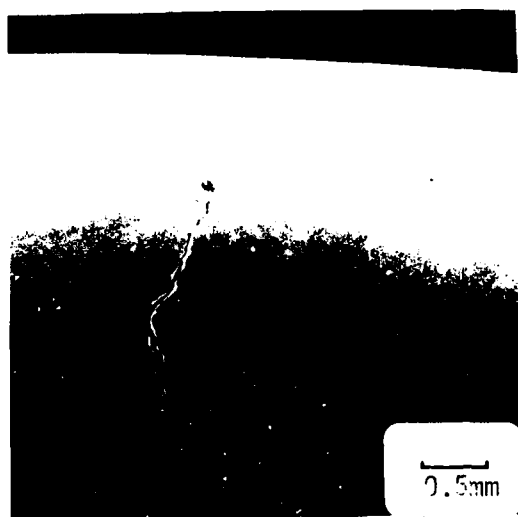
(a)
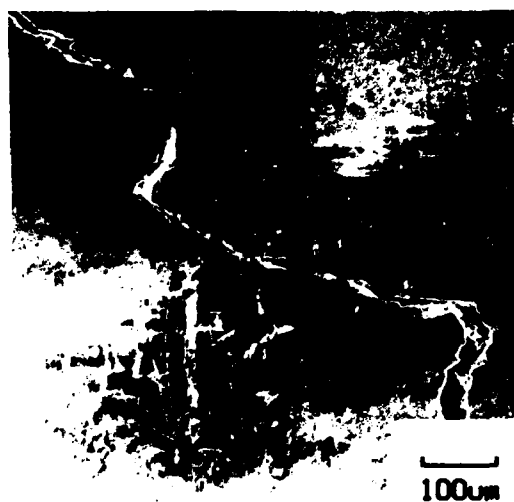
(b)
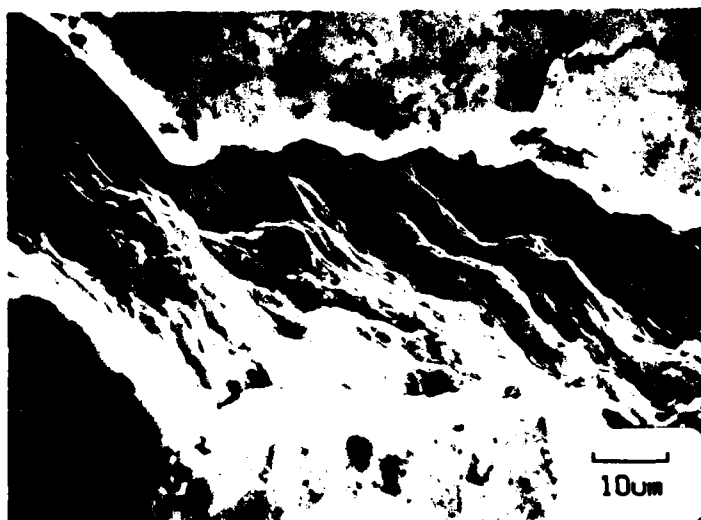
(c)

Figure 78. Typical Nature of Surface Cracking. (a) Overall view in 010. (b) Debris in crack believed at original initiation. (c) Crack away from initiation site with evidence of striations. Condition 010, Sample WW1-4, 0.024%, N_i = 1100.

224
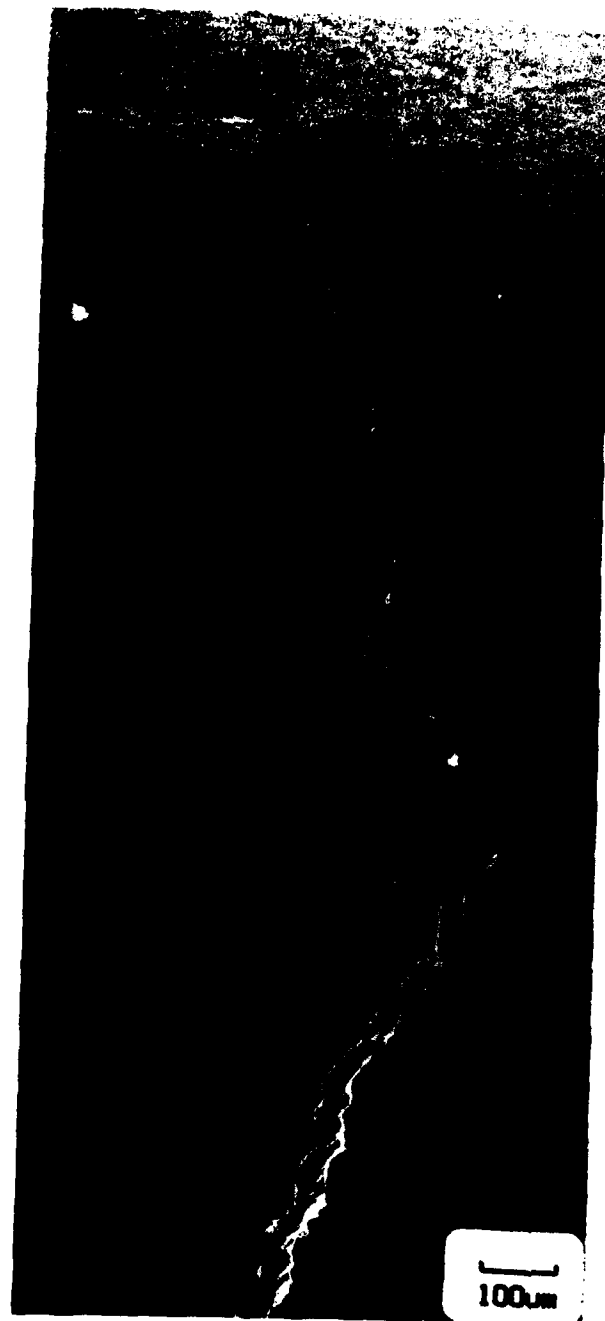
Figure 79. Same Crack as in Figure 78. Evidence of debris in crack and multiple cracking.

Figure 80. Debris is Typically Found in the Crack. Crack branches at what is believed to be an original powder particle. Condition 100, Sample 23-3, 0.570%, N_i = 447.
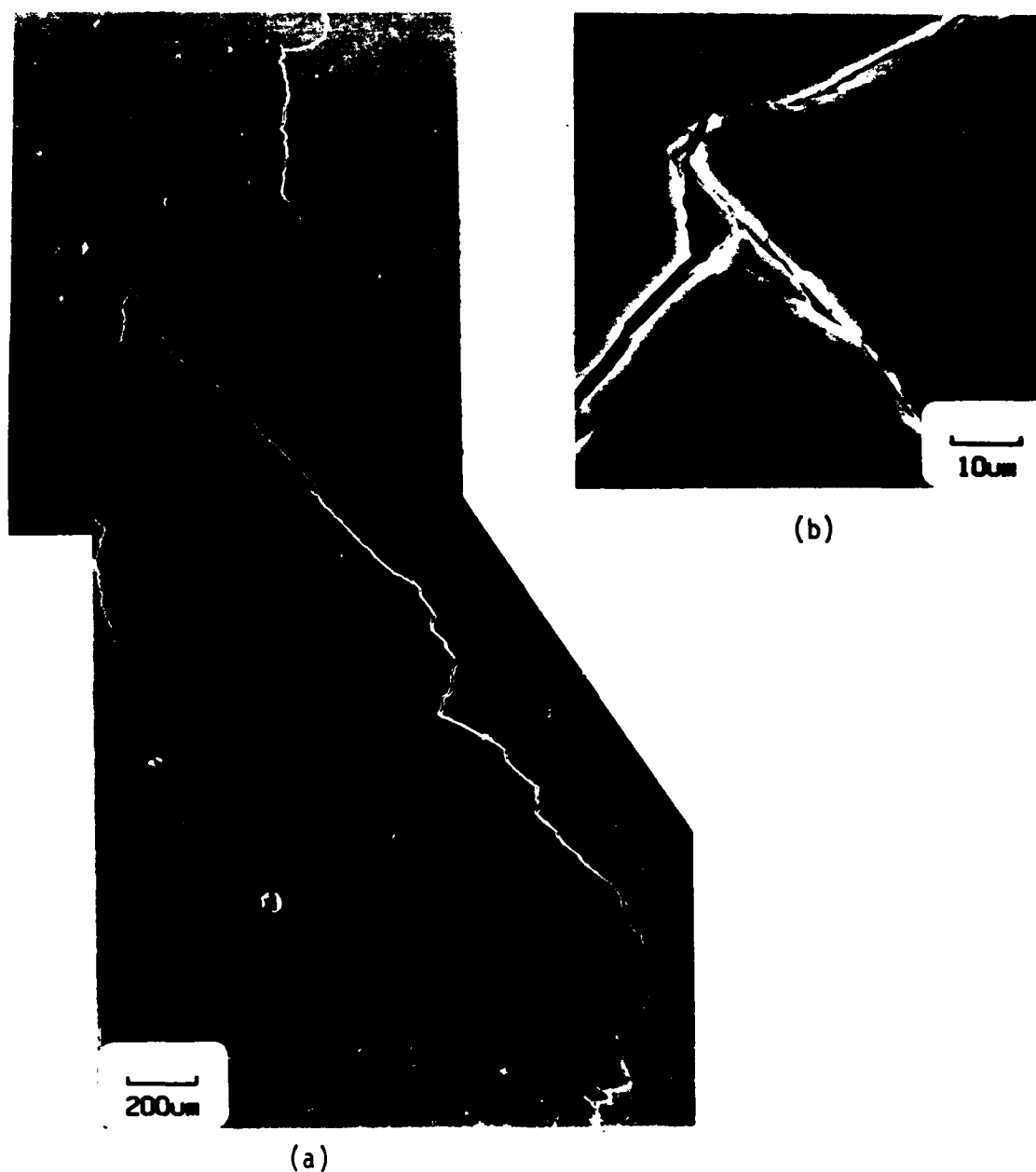
Figure 81. Another Example of Multiple Cracking. (a) Overall view.
(b) Note the significant deformation. Condition 100,
Sample 24-1, 0.035%, N_i = 2700.

227

(a)

(b)
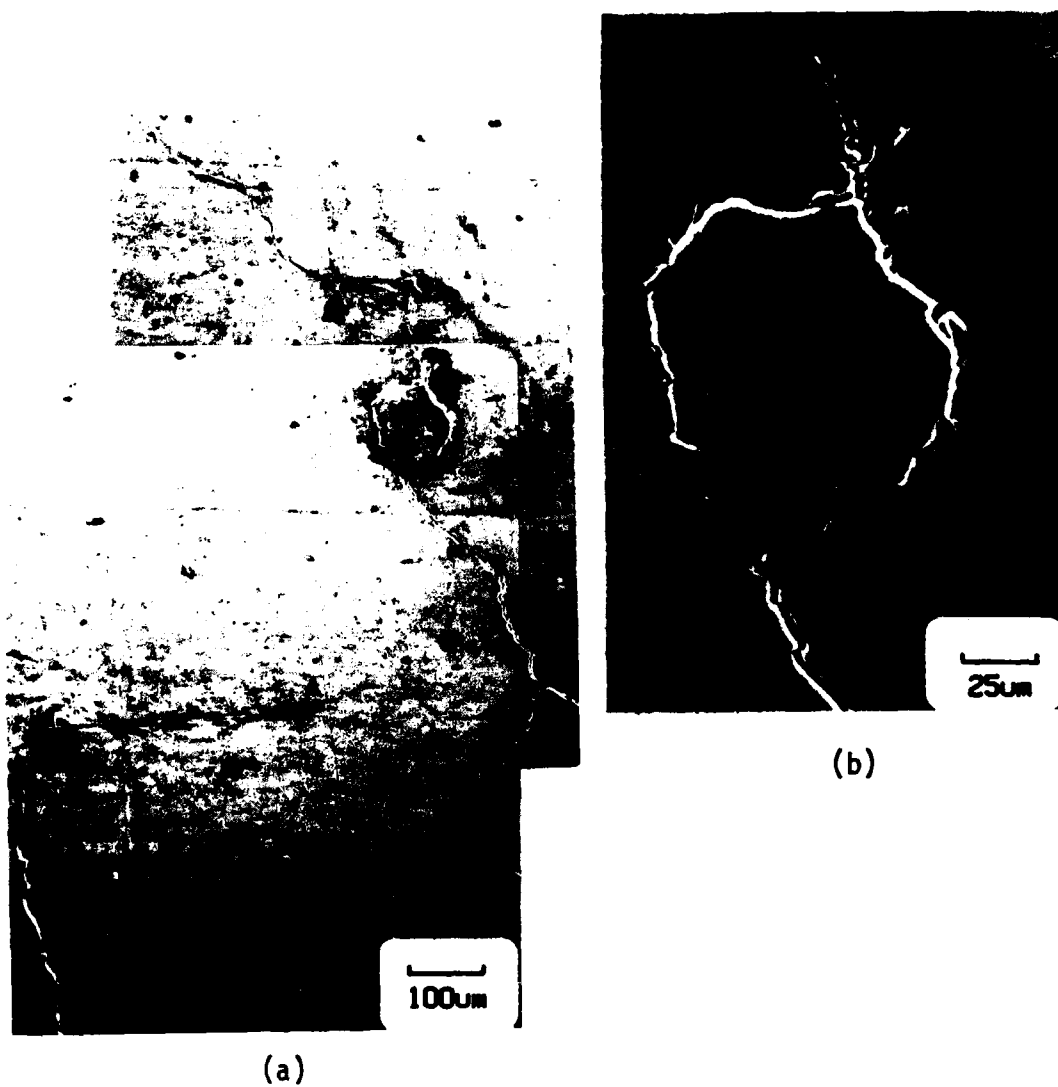
Figure 82. Surface Cracking in 110 Type Specimen. (a) Over-all view, (b) close-up of what is believed to be an original powder particle. Condition 110, Sample 19-4, 0.020%, N_i = 2515.
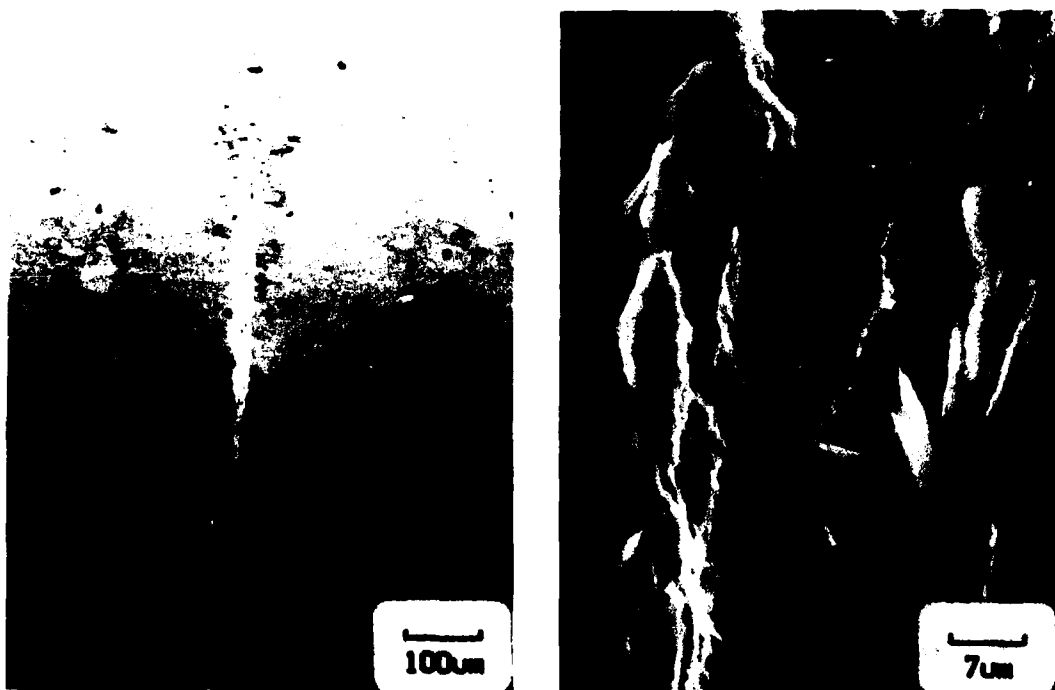
(a)

Figure 83. (a) This Initiation is not Typical and was not Associated
with the Extensometer. (b) Same as (a) but at higher
magnification. Condition 110, Sample 19-3, 0.593%,
$N_i = 277$.
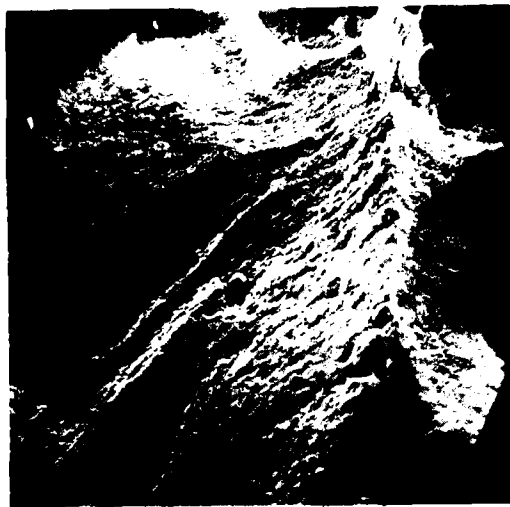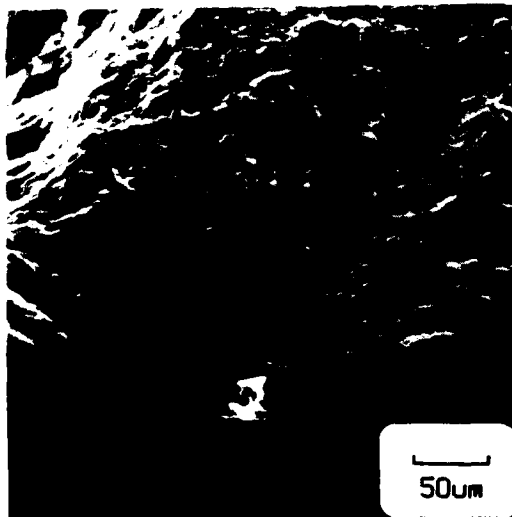
Figure 84. There are Three Kinds of Initiations Typically Found.
(a) and (b) Initiations associated with a boundary
weakness and surface instability; (c) surface particles,
and (d) subsurface particles.
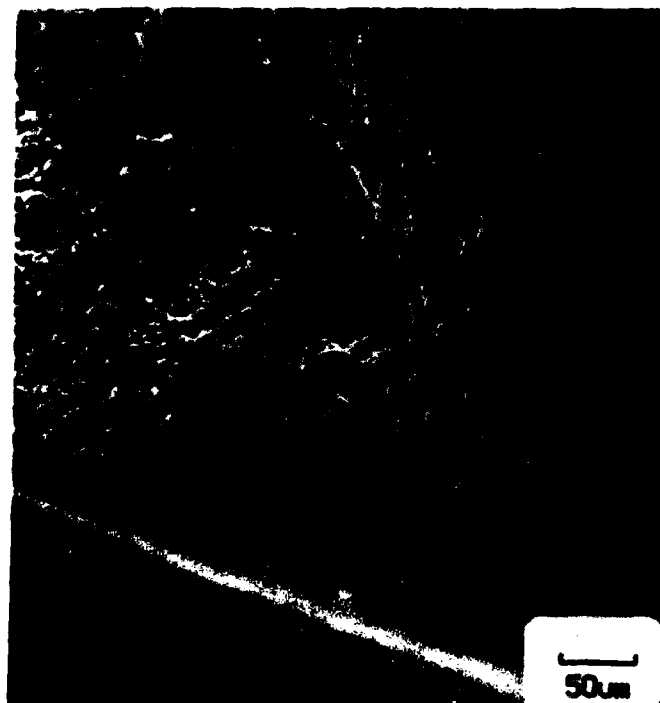
Figure 85. This is an Example of the Most Common Type of Initiation Site Found. Condition 010, TT3-1, 0.049%, N_i = 3921.
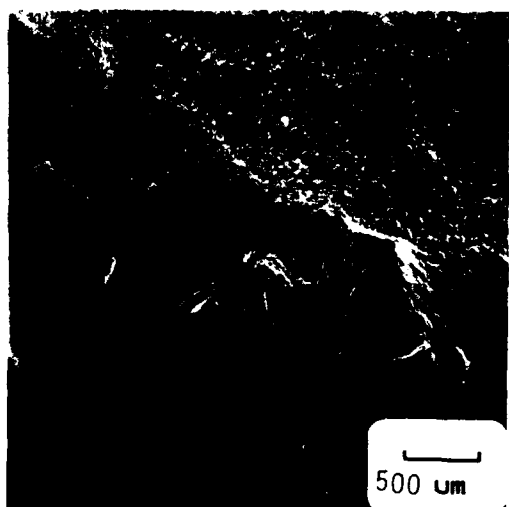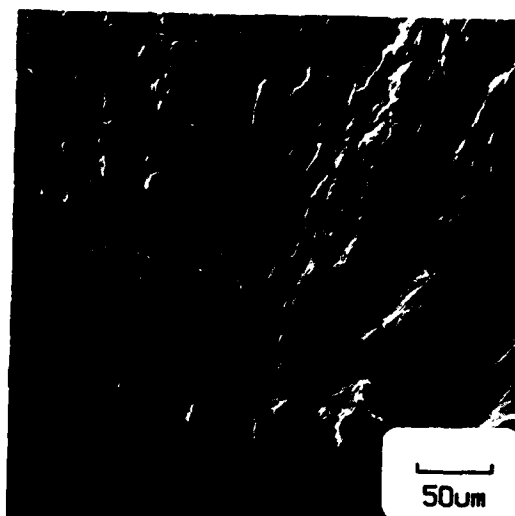
Figure 86. (a) Typical Initiation Site. (b) Higher Magnification of (a). (c) Close to the Initiation No Striations are Observed. (d) A Short Distance Away Striations are Observed. Condition 011, Sample TT4R-3, 0.042%, N_i = 3756.

232

(a)

(b)

(c)

(d)
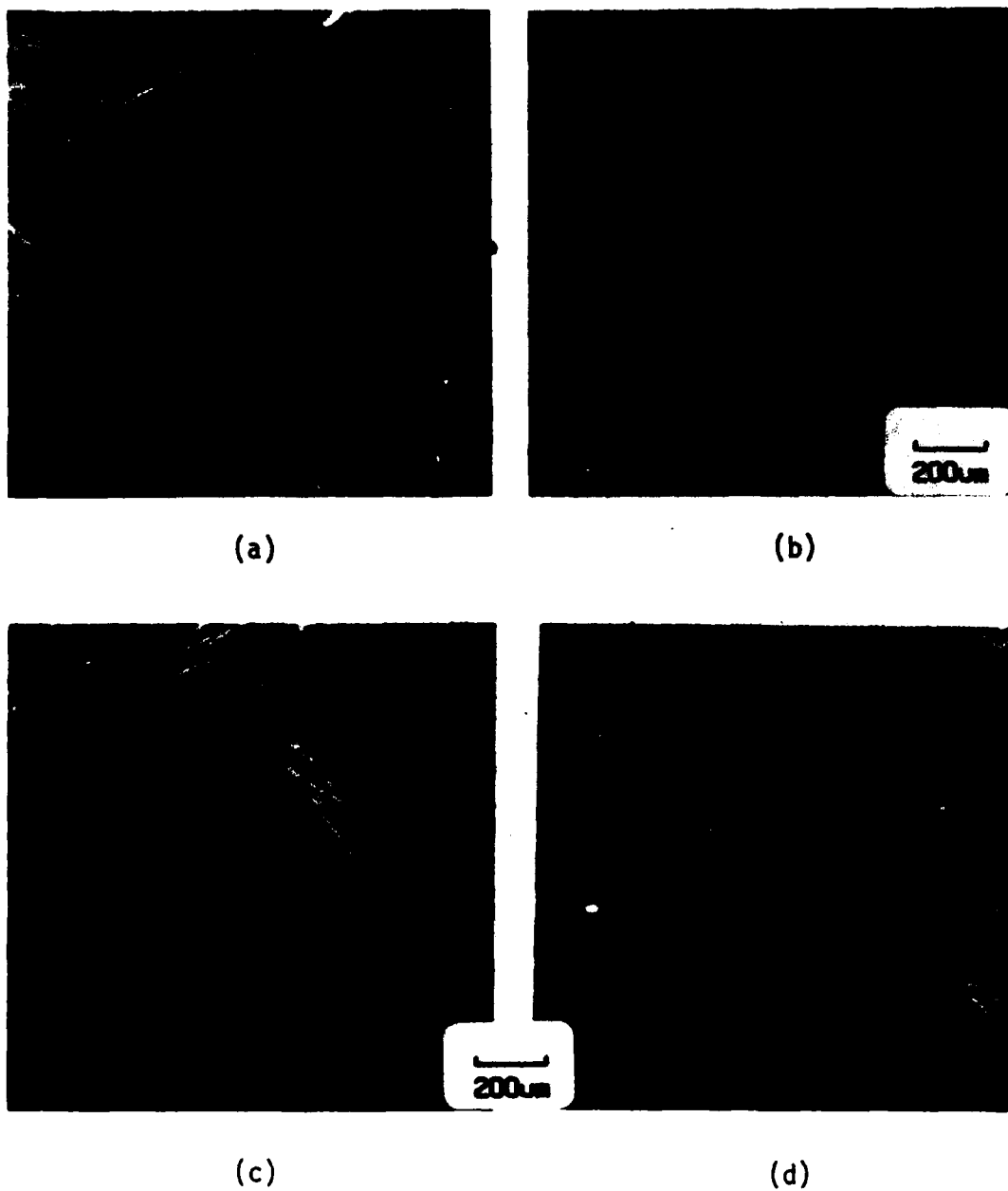
Figure 87. (a) Multiple Initiation Sites are Seen in This SEM Micrograph. (b), (c), and (d) are higher magnifications of individual sites. Condition 101, Sample 22R-2, 0.025%, N_i = 4532.
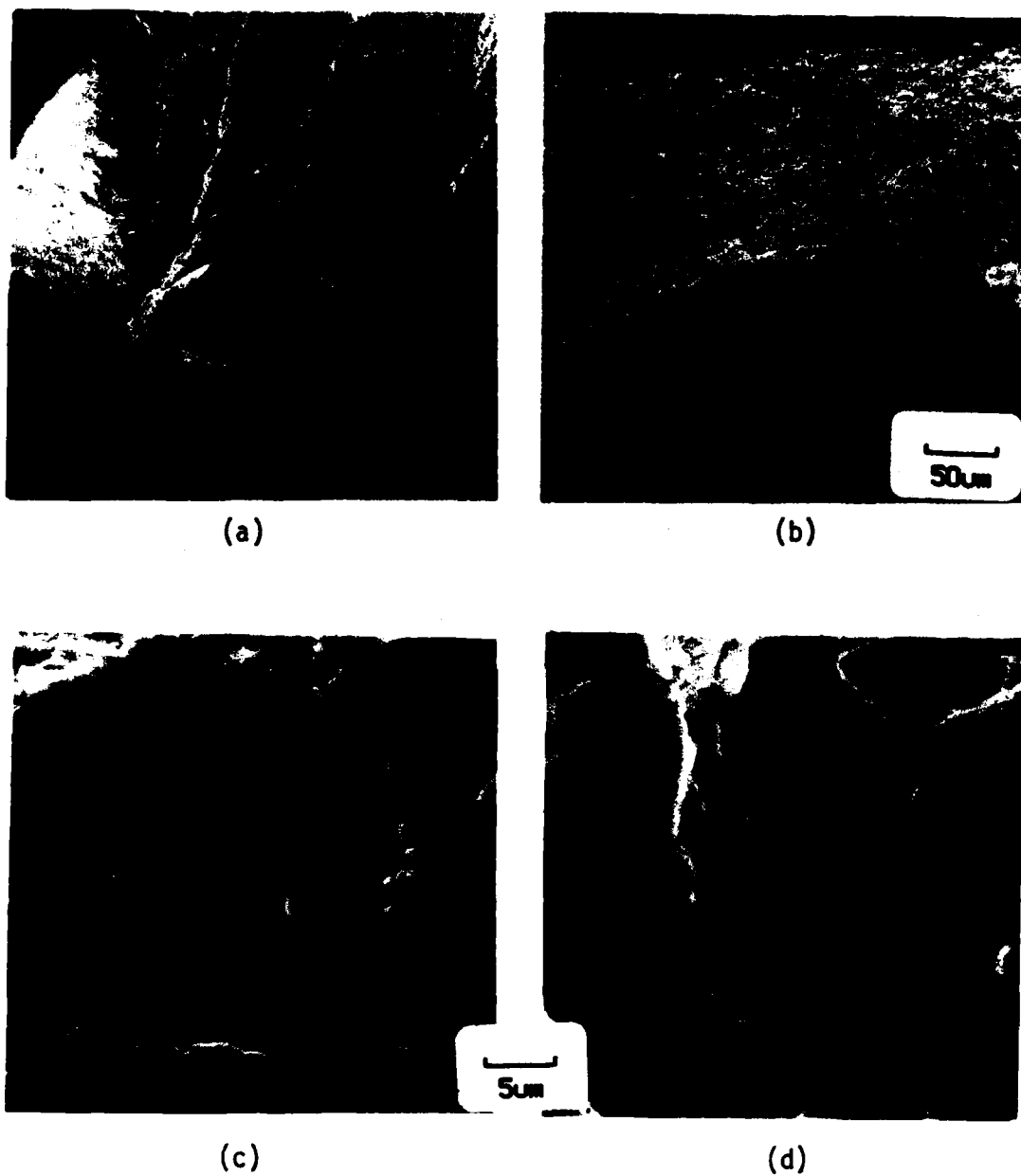
Figure 88. (a) Typical Initiation Site. (b) Higher magnification of (a). (c) No striations are found near initiation. (d) Striations are seen away from initiation. Condition 111, Sample 18R-1, 0.027%, N_i = 4050.
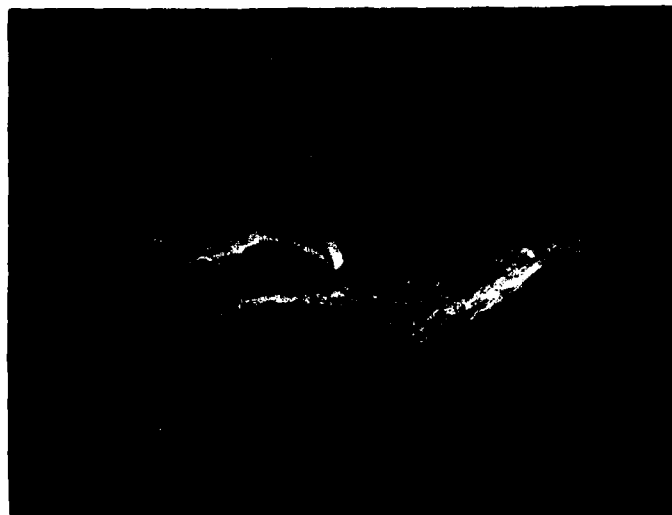
(a)
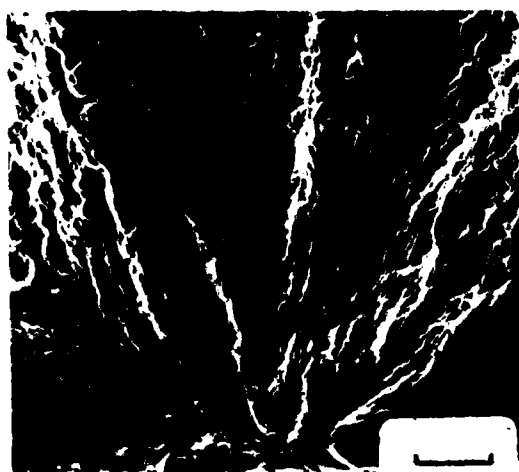
(b)
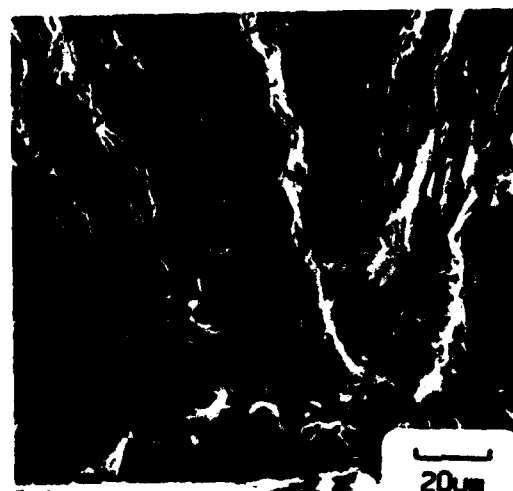
(c)

Figure 89. Typical Initiation. (a) Overall view; (b) and (c)
higher magnifications of initiation site. Condition
110, Sample 15-1, 0.023%, N_i = 3144.
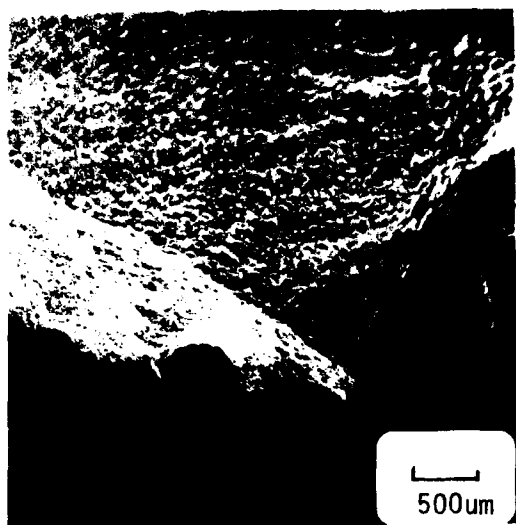
(a)
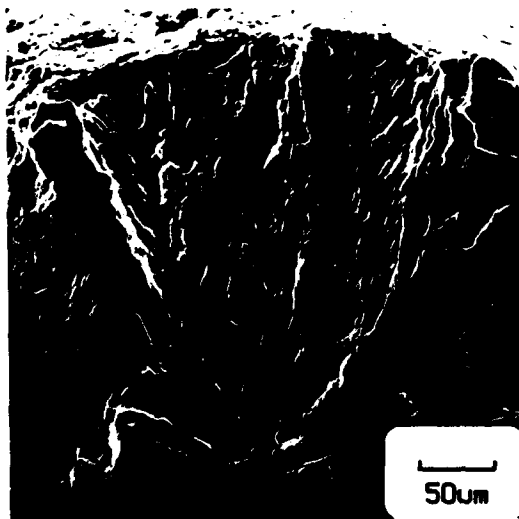
(b)

(c)

(d)

Figure 90. Same Sample as in Figure 86. (a) Typical initiation. (b) Higher magnification showing river patterns "pointing" to initiation. (c) Near initiation. (d) Near rim. Condition 011, Sample TT4R-3, 0.042%, N_i = 3756.

236
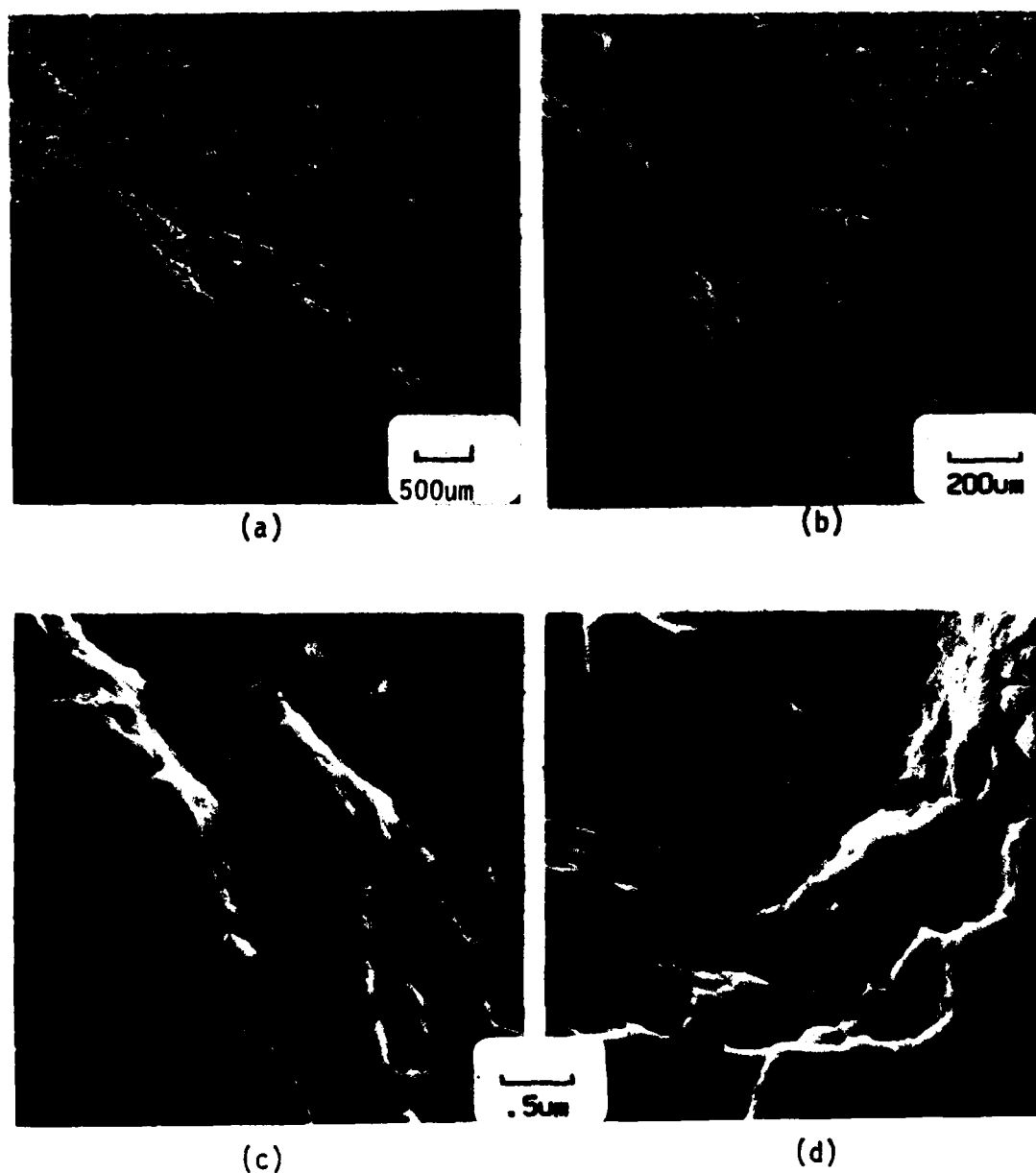
Figure 91. (a) and (b) are Typical Initiation Sites. (c) Higher
Magnification SEM Micrograph of Area seen in (b) near
surface. Note the appearance of debris, probably
indicating the oxide played a role in this initiation.
(d) Near the rim of (b) shows striations and secondary
cracking. Condition 011, Sample TT5R-1, 0.104%,
N_i = 2348.
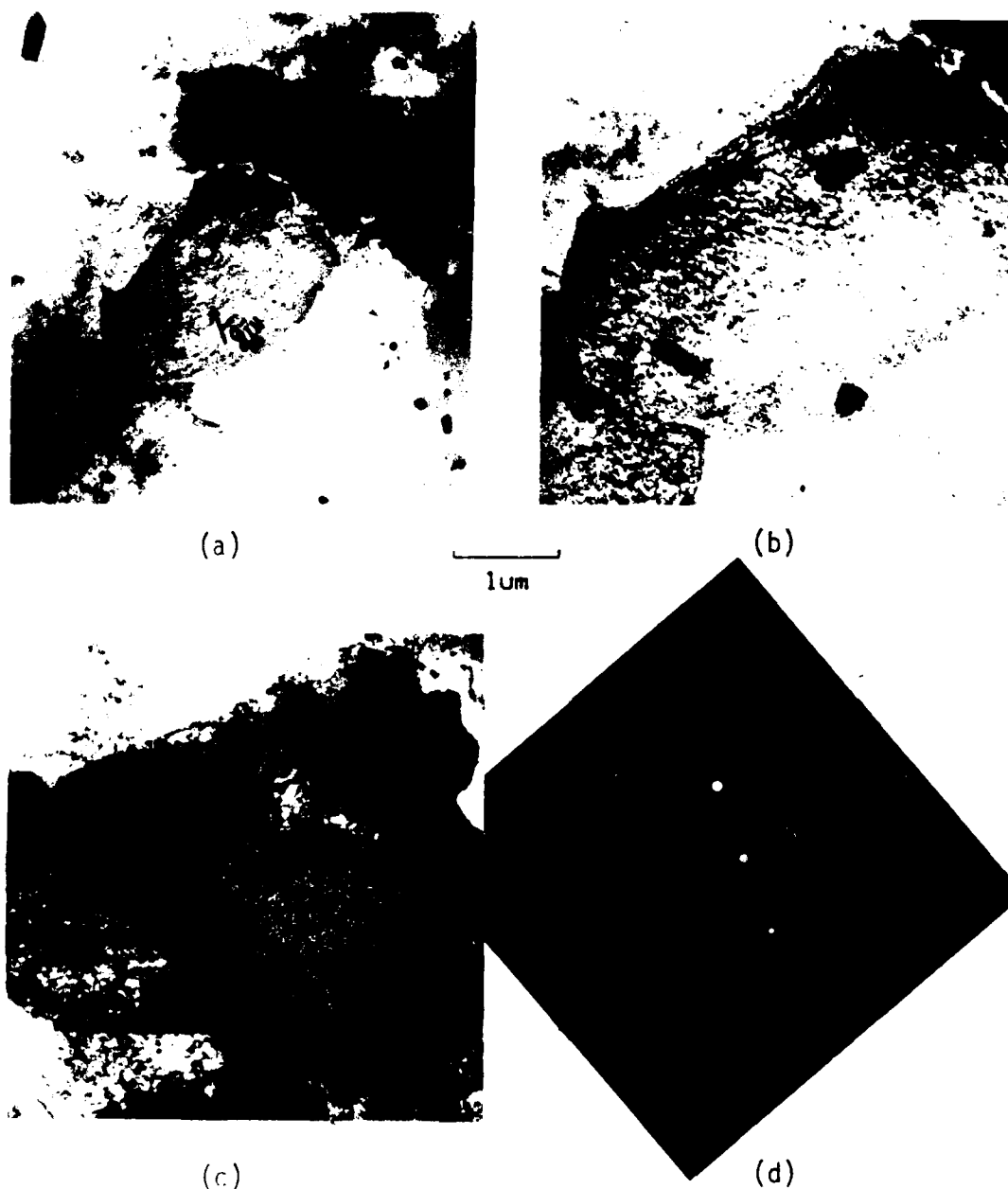
Figure 104. Typical Deformation Structure at High Plastic Strain
Amplitudes. (a) The grain is tilted so that the ($\bar{1}$11),
the plane of highest Schmid Factor, is edge on; (b) the
same grain tilted and rotated so that ($\bar{1}$11) is oblique;
(c) the diffraction pattern for (a). Note that there is
no evidence of slip band formation at high PSA. Sample
WW2-2, $\cdot\cdot$ = 0.585', N_i = 219, Condition 010.

(a)
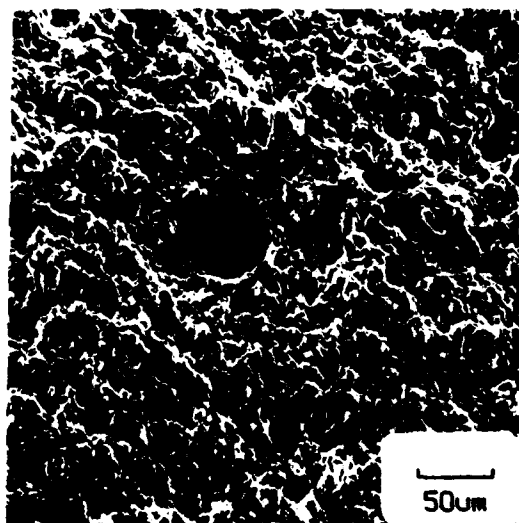
(b)

(c)

Figure 103. (a) This Subsurface Particle is Almost Unseen (Arrow).
(b) The initiation region is circular and about 30 μm
in diameter.   (c) The actual particle is only about
10 μm in size and was determined to be Mg_2Si. The life
expectancy was decreased by 67%. Condition 000, Sample
DD2-2, 0.098%, N_i = 415.

(d)

(e)

Figure 102 continued. (d) The Si-containing particle (probably
SiO$_2$ is about 60 um in size. (e) The Fe-Mn-Cr particle
is about 30 um in across.
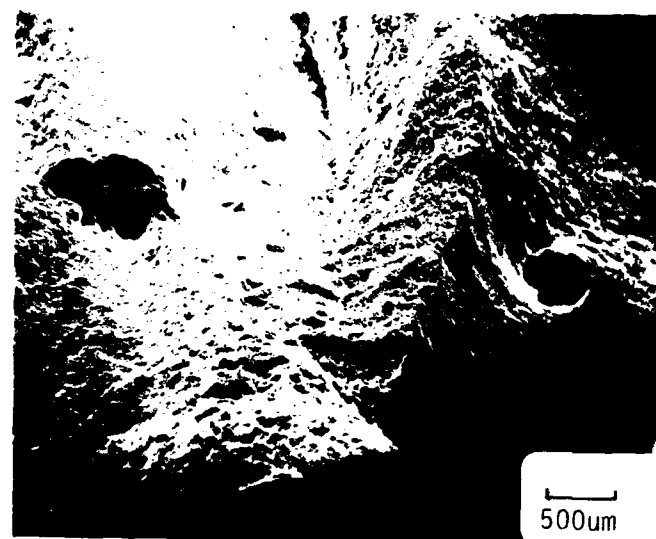
(a)
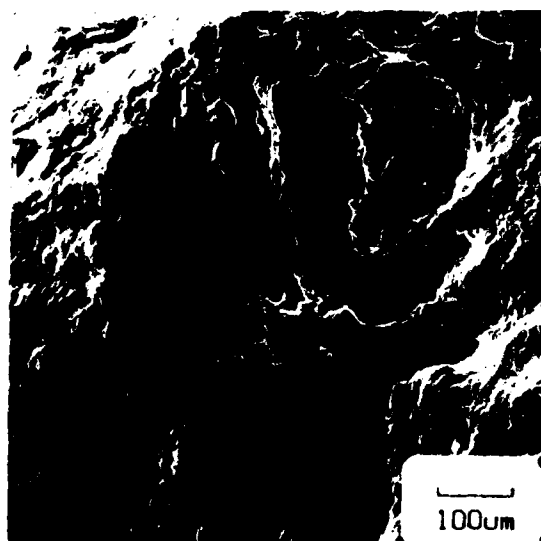
(b)
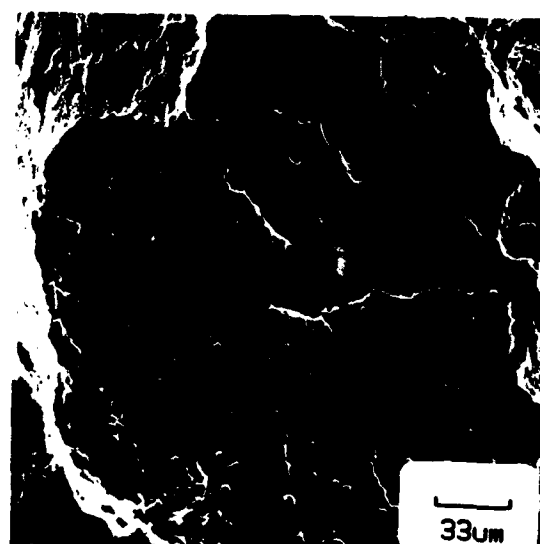
(c)

Figure 102. (a) The Very Rare Case of Multiple Subsurface Initiation, (b) an Fe-Mn-Co Particle and (c) a High Si Particle Reduced the Expected Life by about 17%. Condition 011, Sample WW1R-1, 0.111%, N_i = 1050.

248
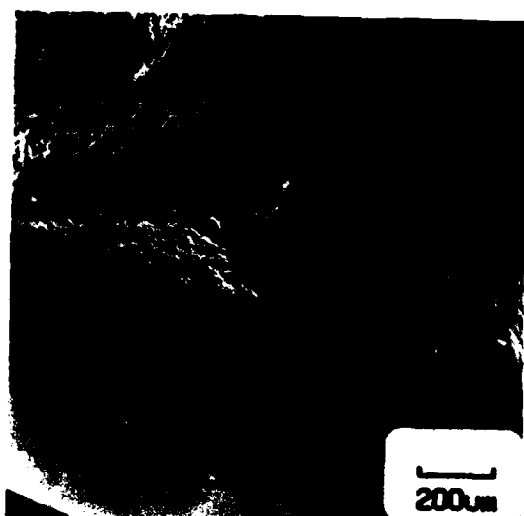
(a)
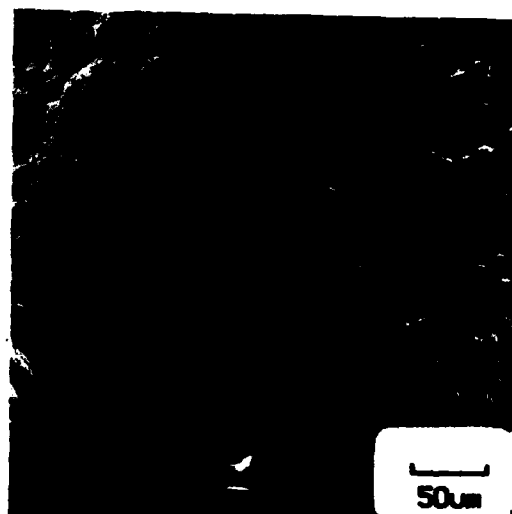
(b)

(c)

Figure 101. (a) and (b) 20 μm Particle Near Surface Caused Initiation. (c) The transition from flat and featureless to striated can be seen. Condition 111, Sample 20R-1, 0.050%, N_i = 2028.

(a)
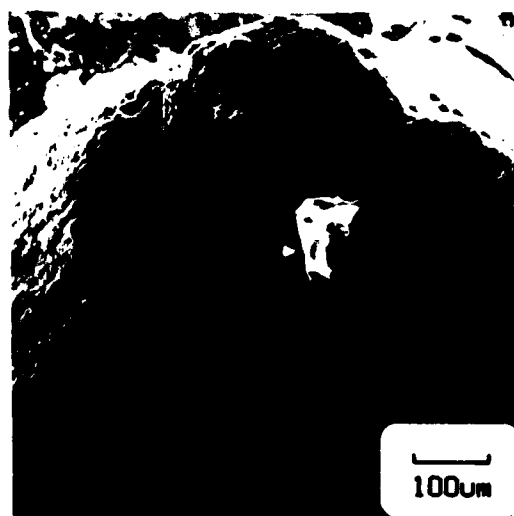
(b)
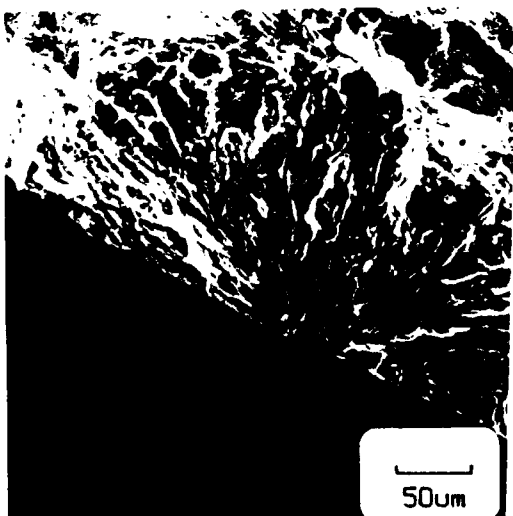
(c)
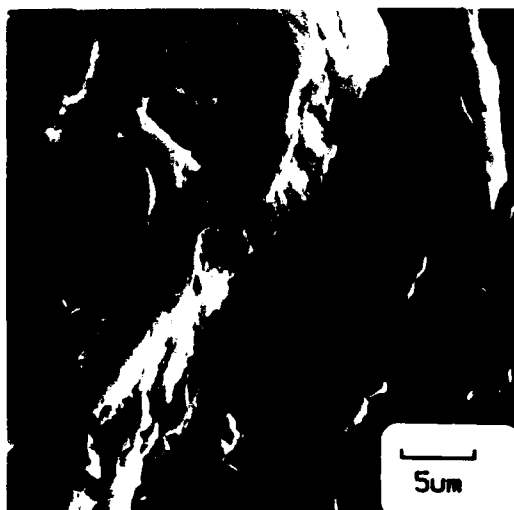
(d)

Figure 100. (a) This Fractograph Shows Both Surface and Subsurface Initiation Sites. (b) The subsurface particle contains Al, Fe, Ti and Si and is approximately 100 µm in size. (c) and (d) The typical features of a surface initiation. A 26% loss in expected life was observed. Condition 110, Sample 18-3, 0.047%, N_i = 2547.

246
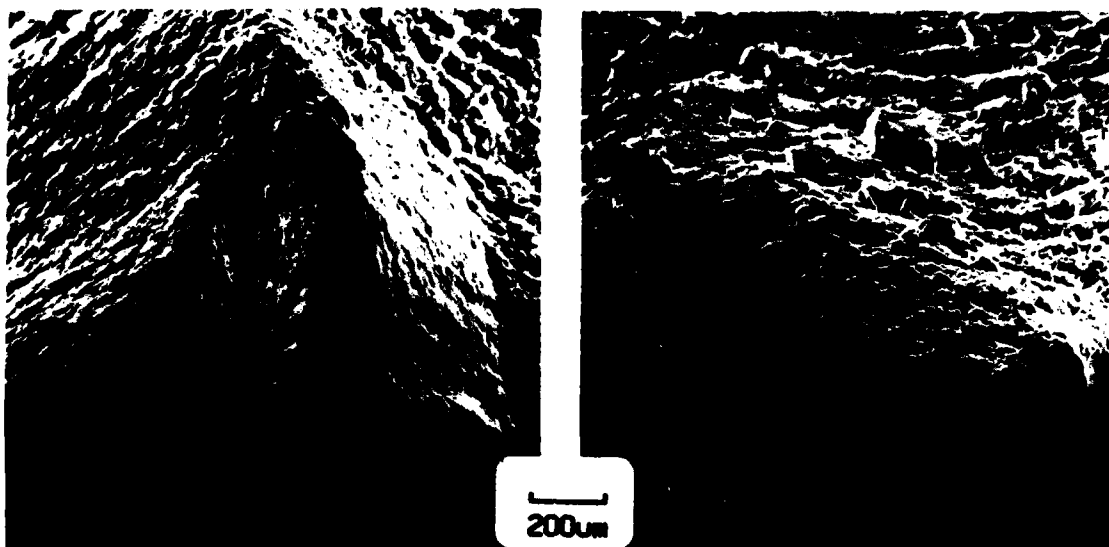
(d)

(e)

(f)

(g)

Figure 99 continued. (d), (e), and (f) The Second Initiation is Typical of the Boundary Type. (g) An initiation at a small (1 μm) Ca and Fe particle is shown. Note that no loss in expected life was observed.

245

(a)
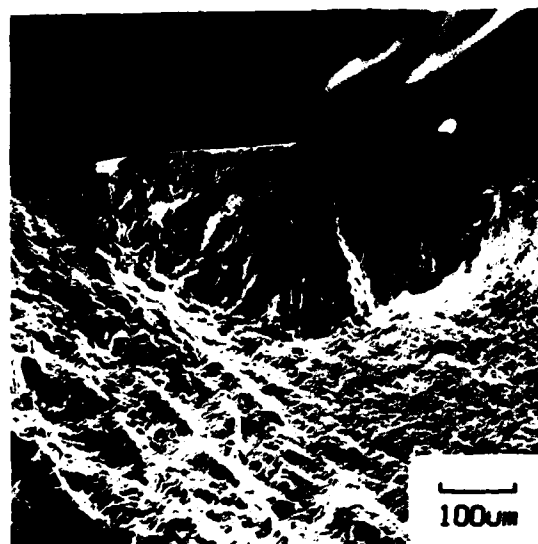
(b)

(c)

Figure 99.   (a) This Sample Shows at Least Three Initiation Sites.
(b) and (c) Show subsurface particle containing Si and
Ca about 10-20 μm in size. Condition 101, Sample 23R-2,
0.051%, N_i = 1955.

244
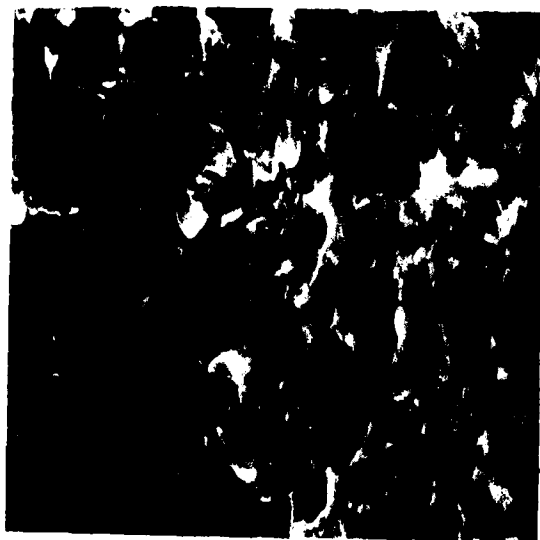
(f)

5um

(g)

Figure 98 continued. (e), (f), and (g) are SEM Fractographs Near Each
of the Three Initiation Sites Respectively, all Showing the
Flat, Featureless Regions Expected.

243

(a)

(b)
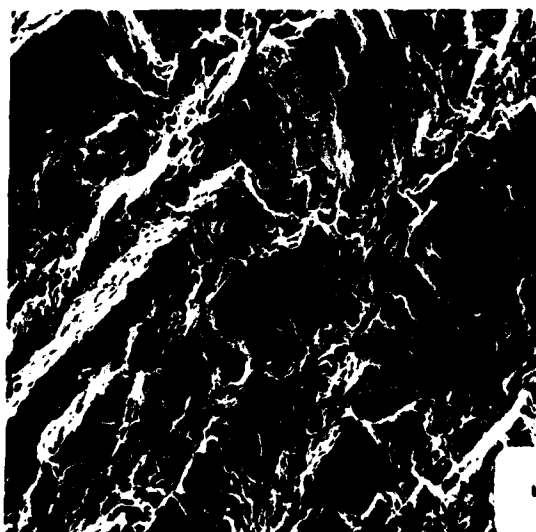
(c)
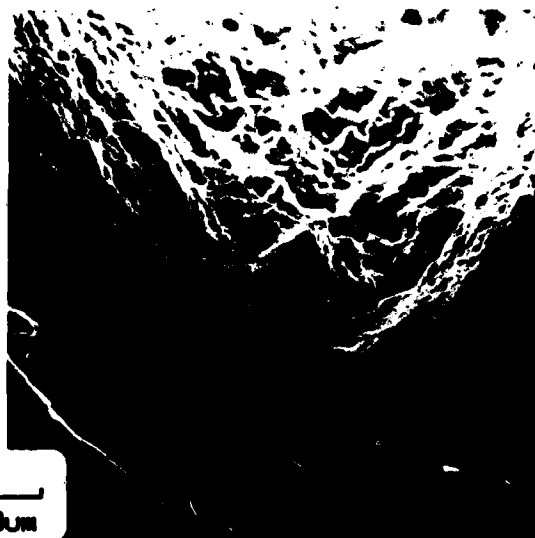
(d)

Figure 98.   Three Regions of Initiation Can be Seen in (a) and (b).
(c) and (d) are higher magnification SEM fractographs
showing secondary cracking and smearing.   Condition 001,
Sample DD2R-2, 0.585%, N_i = 225.

(a)   (b)
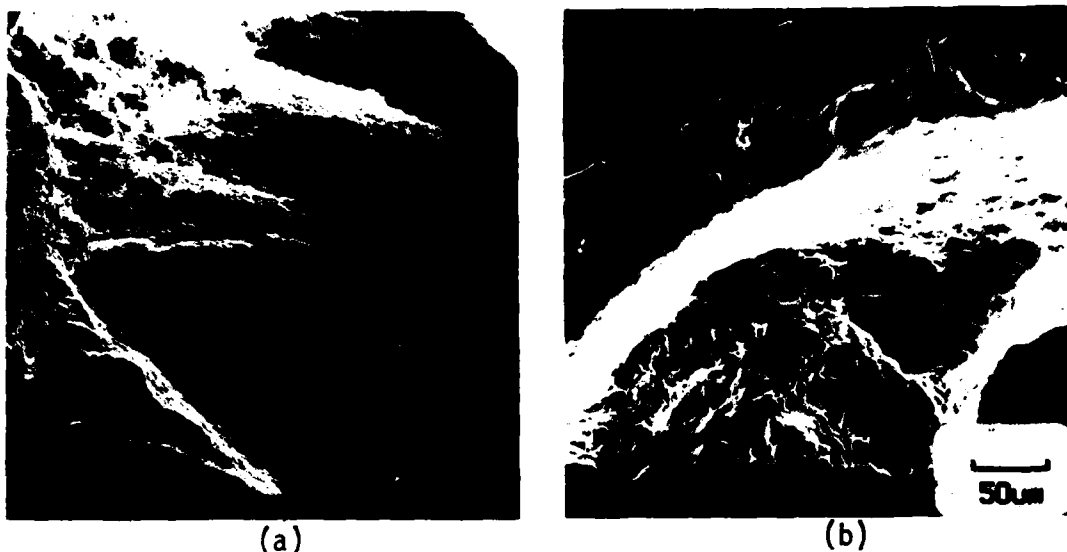
Figure 96. (a) At High Testing Strains There is Often Evidence of
Surface Smearing. (b) At high strains the initiation
area is smaller than at lower strains. Condition 111,
Sample 19R-2, 0.615%, N_i = 225.

(a)   (b)
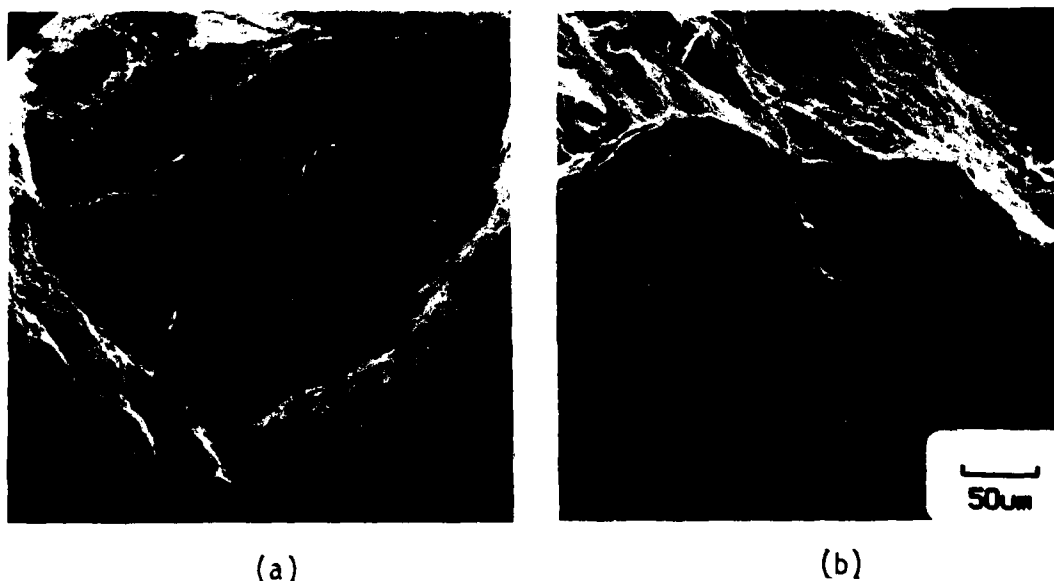
Figure 97. In Spite of Running Tests at A_ϵ=0.95, Smearing is
Occasionally Encountered in High Strain Tests. (a),
(b), and (c) are increasing magnification SEM
fractographs showing the smeared initiation site.
Condition 001, Sample DD1R-2, 0.638%, N_i = 165.

241

(a)   (b)
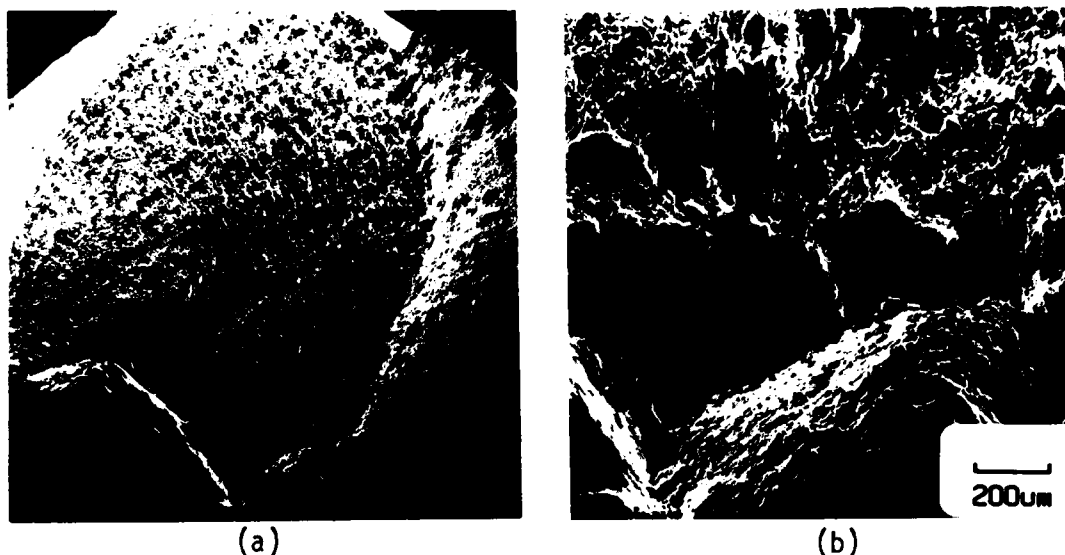
Figure 94.   (a) and (b) are SEM Micrographs of the Initiation Region. At high strains details of the initiation are difficult to see. Conditon 010, Sample TT5-3, 0.630%, N_i = 337.

(a)   (b)

Figure 95.   (a) Although Initiation Sites are more Difficult to Find in High Strain Tests, They are Present. (b) The initiation region is somewhat smaller but otherwise similar in appearance. Condition 101, Sample 23-3, 0.570%, N_i = 447.

240
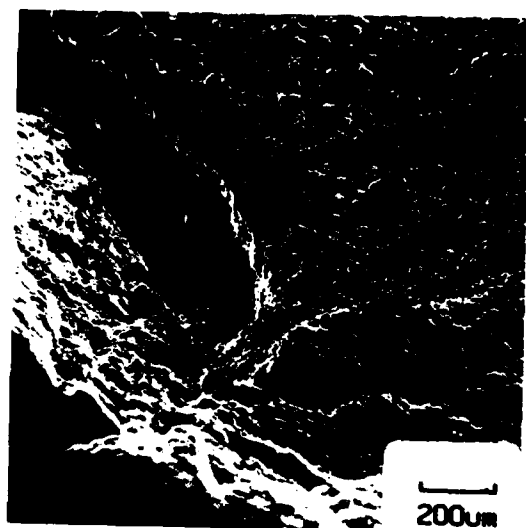
(a)

(b)

(c)

Figure 93. (a) and (b) are Typical Initiations. (c) indicates the extensometer knife edge did not cause initiation. Condition 110, Sample 15-2, 0.603%, $N_i = 211$.

(a)
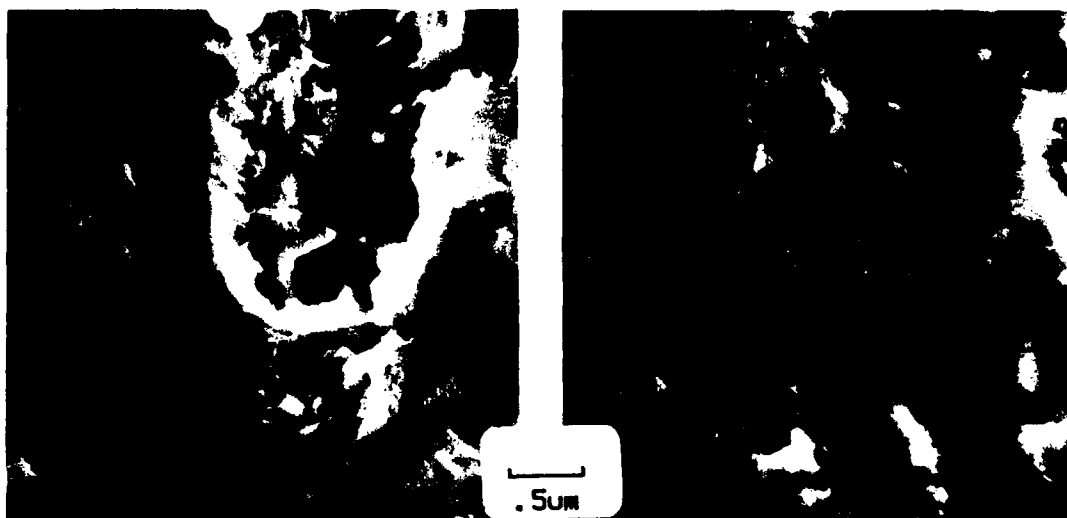
(b)   (c)

Figure 92.   Evidence of Oxide Participating in the Initiation Process
             is Shown. (a) Typical initiation, (b) near surface (c)
             100 μm from surface. Condition 011, Sample TT5R-1,
             0.104%, N_i = 2348.

238
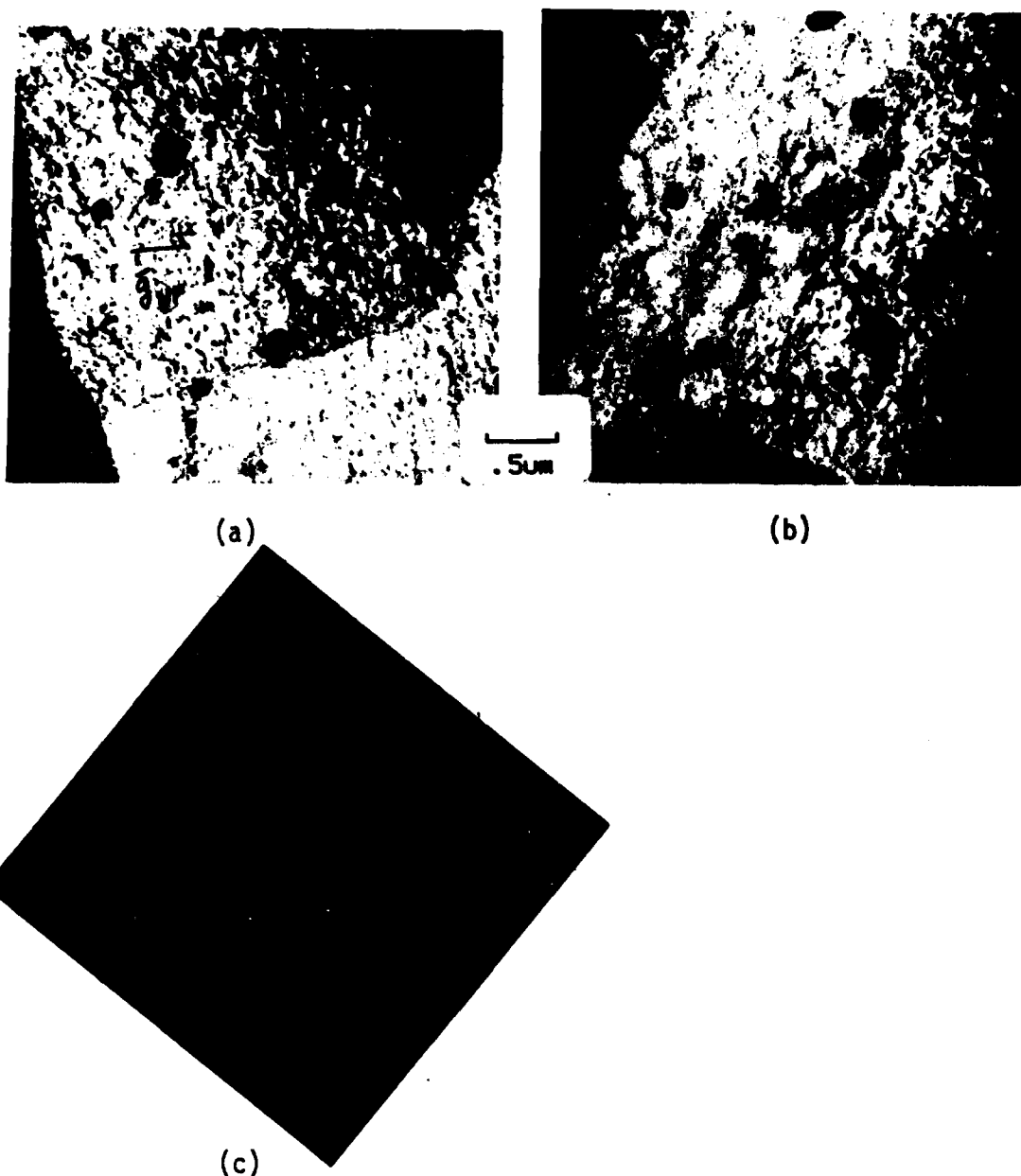
Figure 105. Typical Deformation Structure Observed at High Plastic Strain Amplitude. (a) The grain of interest is tilted so that the plane of highest Schmid Factor is edge on (M = 0.4); (b) the same grain rotated so that (001) is edge on and ($\bar{1}$11) is just off edge; (c) the diffraction pattern for (a). There is no evidence of slip band formation. Sample WW2-2, $\Delta\varepsilon_p$ = 0.585%, N_i = 219, Condition 010.

252

(a)

(b)

(c)
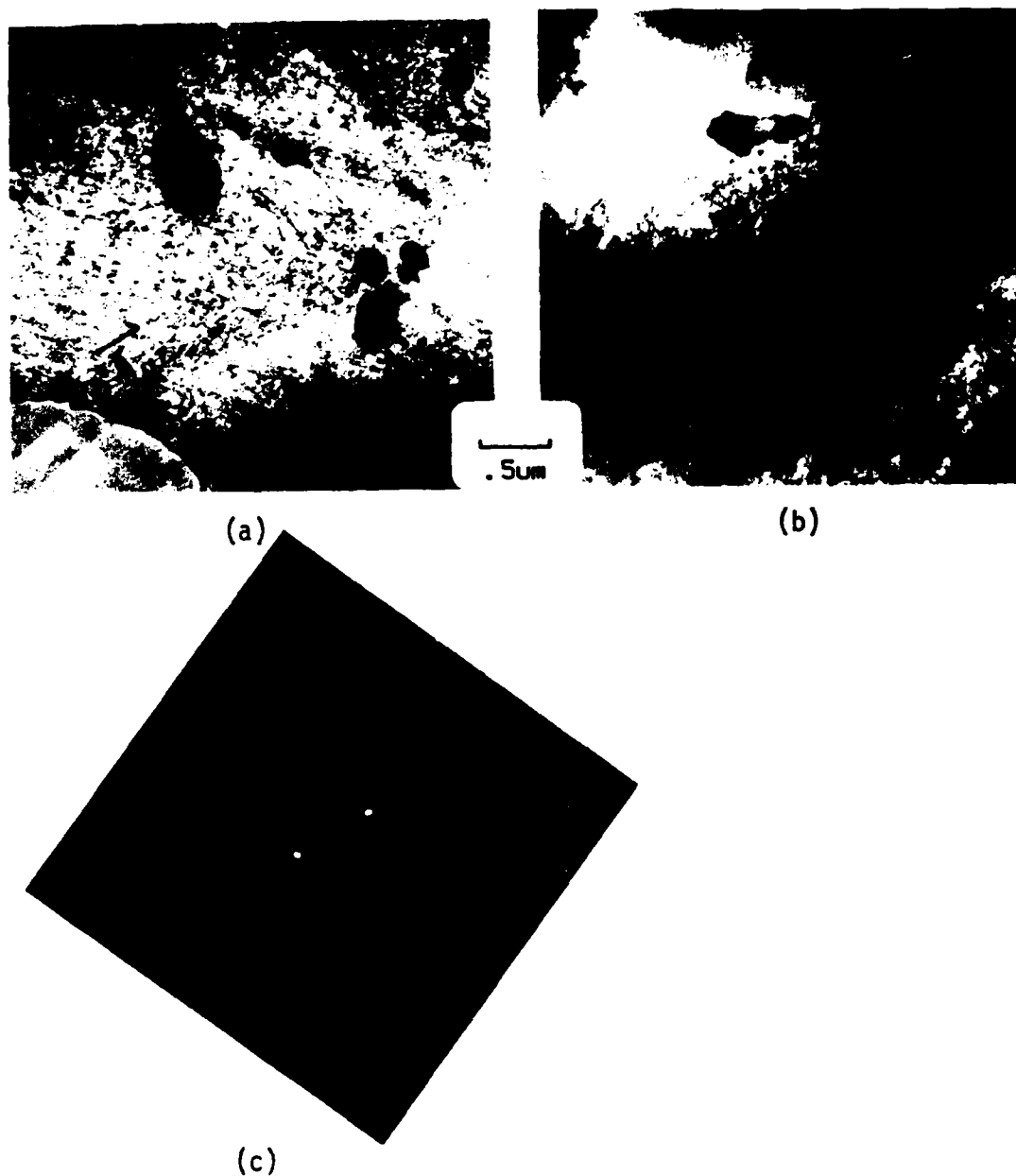
Figure 106. Typical Deformation Structure Observed at Low Plastic Strain Amplitudes. (a) the grain of interest has been tilted so that the active plane ($\bar{1}$11) is edge on (M = 0.4); (b) the same grain has been tilted and rotated so that (001) is edge on and ($\bar{1}$11) is oblique; (c) the diffraction pattern for (a). Sample TT3-2, $\Delta\varepsilon_p$ = 0.049%, N_i = 3921, Condition 010.
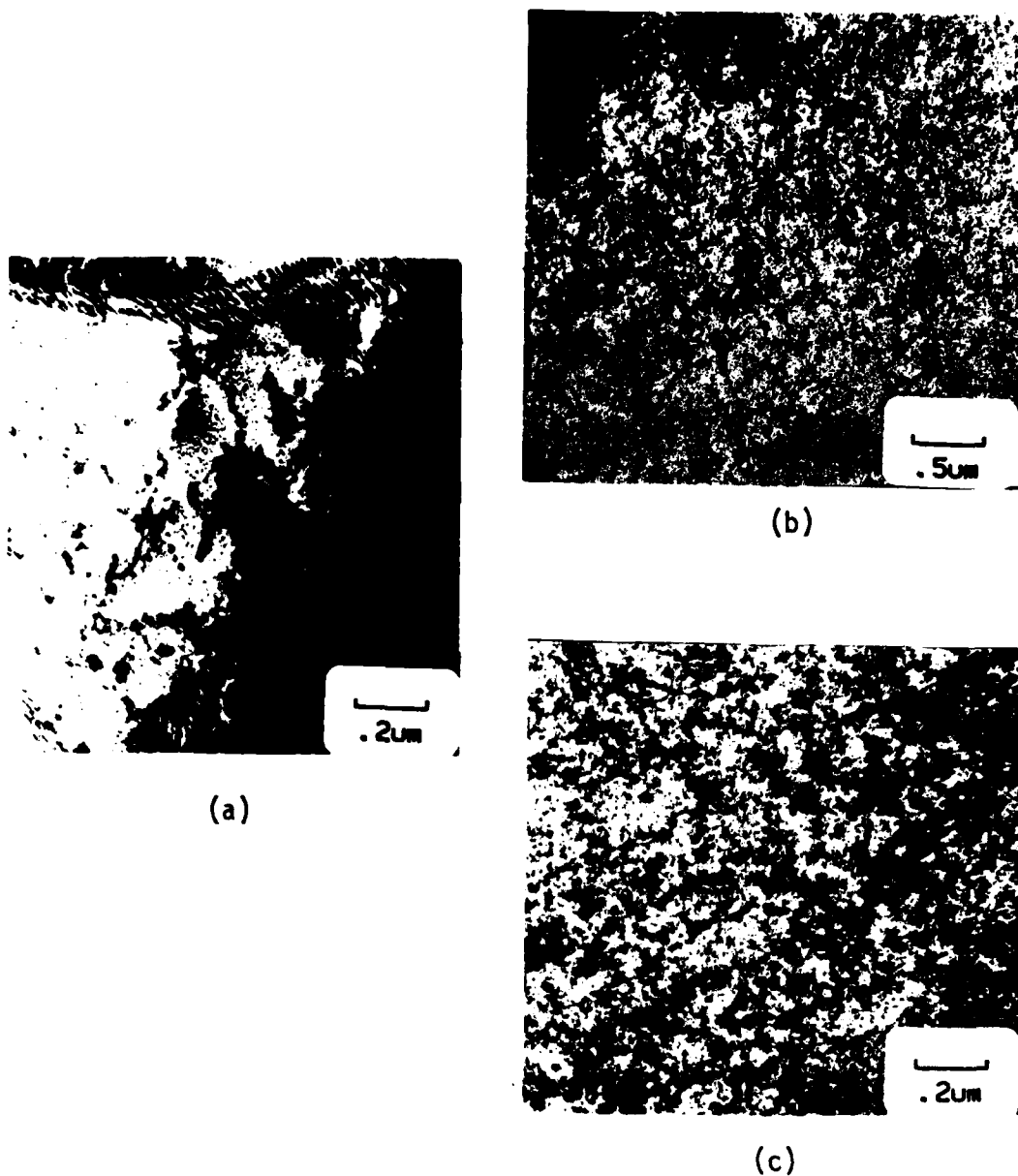
Figure 107. Occasionally Cell Formation is Observed at High Plastic Strain Amplitude. (a) Sample 30R-1, Condition 101, $\Delta\varepsilon_p = 0.623\%$ $N_i = 246$; (b) and (c) Sample DD1R-2, Condition 001, $\Delta\varepsilon_p = 0.638\%$, $N_i = 165$. In all cases the reflection is a $(\bar{1}11)$-type two-beam case.

Figure 108. Higher Magnification of the Same Grain Seen in Figure 106. Note the appearance of the beginning of cell formation.

(a)   (b)
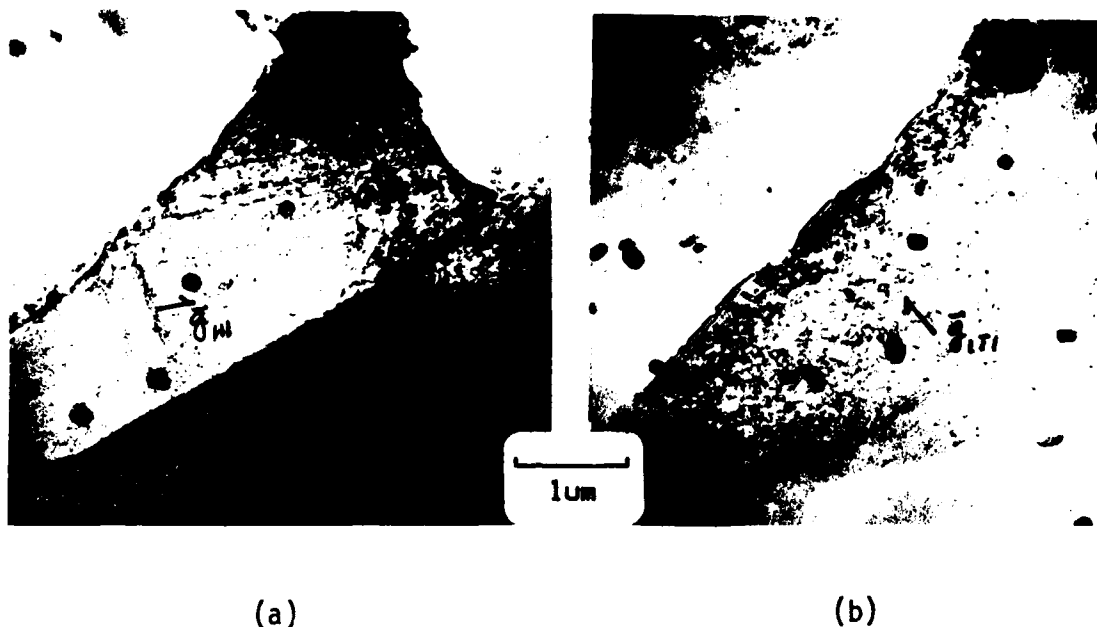
Figure 109.   Typical Deformation Structure at Low Plastic Strain
              Amplitudes When Slip Bands are Observed. (a) The grain
              is near ZA = [112] and two sets of slip bands are
              observed. (b) The same grain tilted and rotated such
              that the active slip planes are oblique. Sample
              WW2R-3, Condition 011, $\Delta\varepsilon_p$ = 0.306%, N_i = 633.
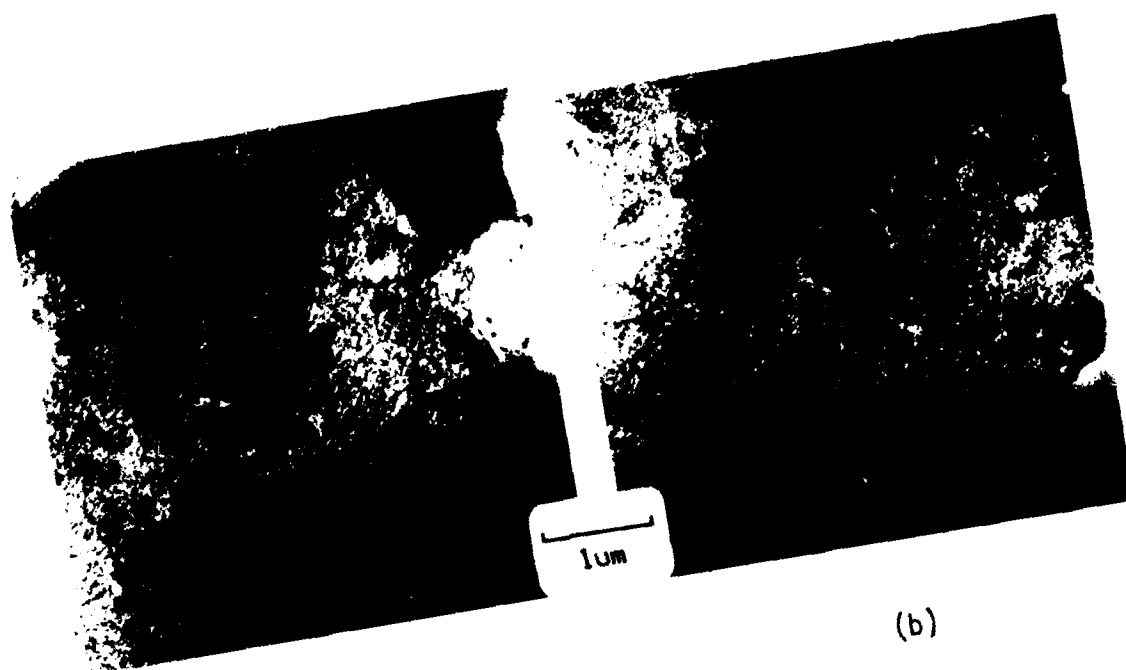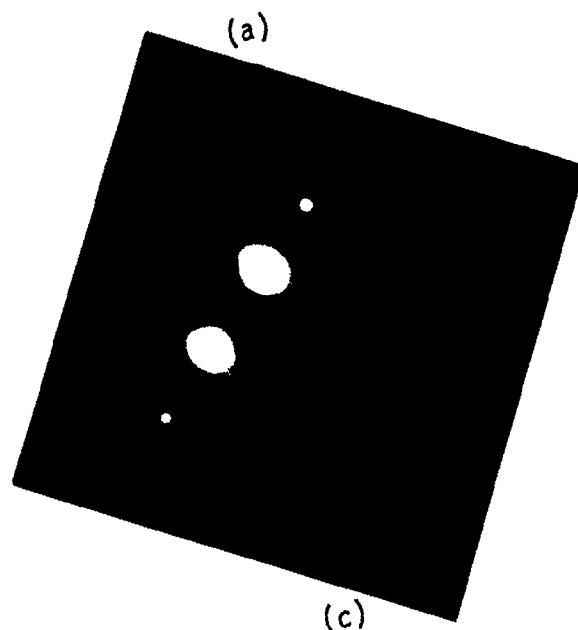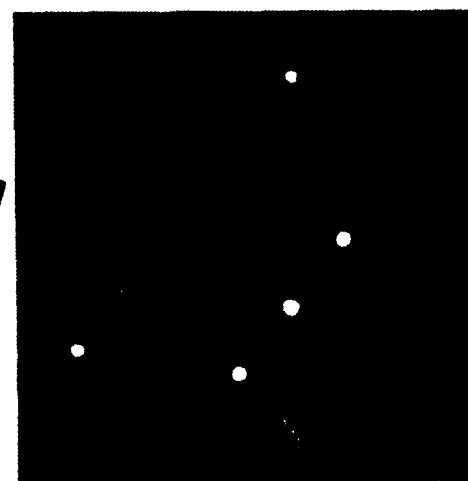
Figure 110. Typical Deformation Structure at Low Plastic Strain Amplitudes When Slip Bands are not Observed. (a) the active plane, ($\bar{1}$11), is edge on; (b) the same grain tilted and rotated near a [211] zone axis with ($\bar{1}$11) approximately 2° off edge. (c) and (d) are the diffraction patterns for (a) and (b) respectively. Sample TT3-2, $\Delta\varepsilon_p = 0.049\%$, $N_i = 3921$, Condition 010.

257
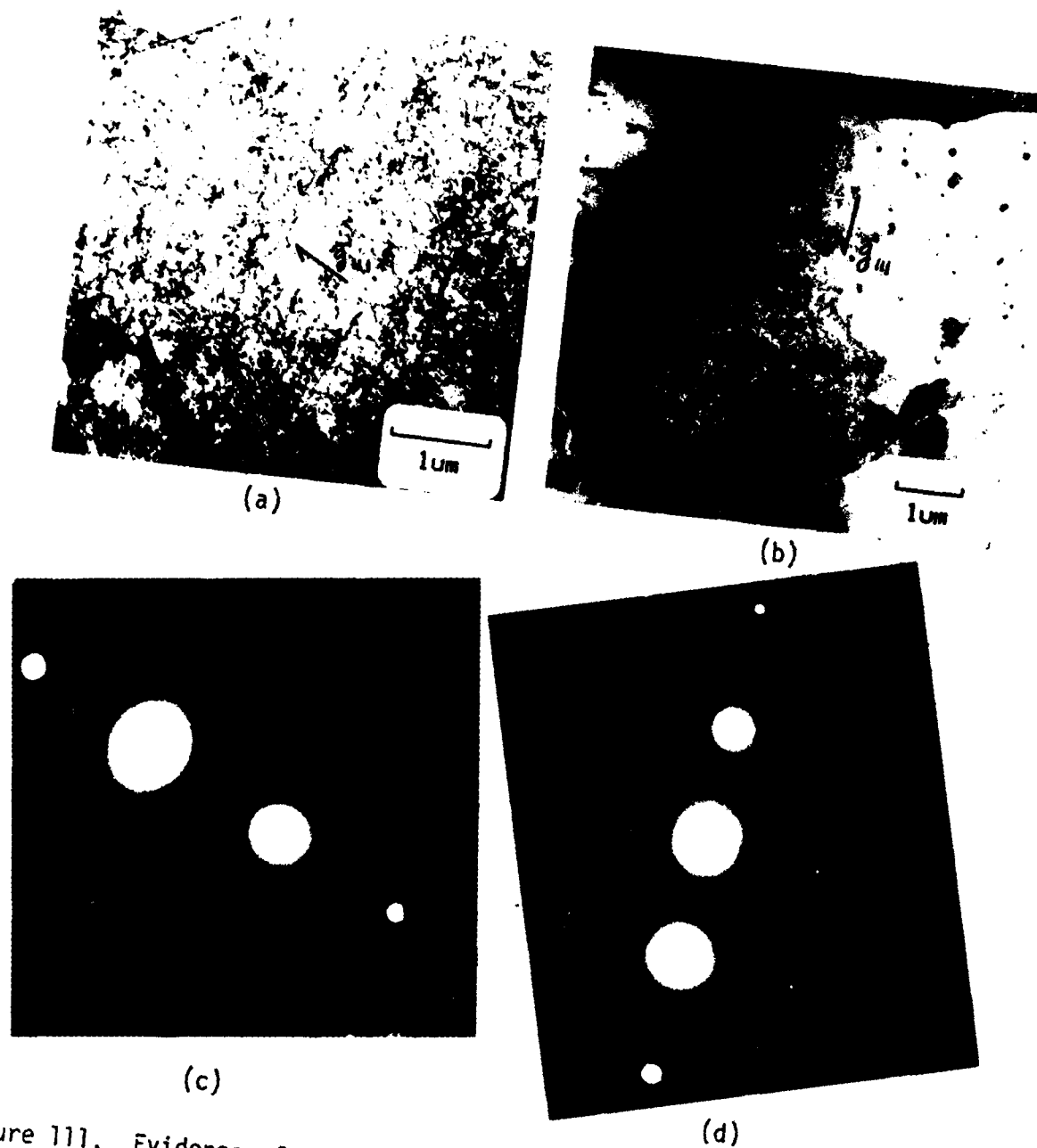
Figure 111. Evidence of Slip Band Formation at Low Plastic Strain Amplitudes in Large Grains/Subgrains. (a) This grain is greater than 6 μm across. Sample D5R-3, Condition 001, $\Delta\varepsilon_p = 0.033\%$, $N_i = 5223$. (b) This grain is about 6 x 9 μm. Sample TT4-2, Condition 010, $\Delta\varepsilon_p = 0.046\%$, $N_i = 930$; (c) and (d) are the diffraction patterns for (a) and (b) respectively. Note that the presence of Co does not prevent the formation of slip bands.

258

APPENDIX A

CYCLIC PROPERTIES

TABLE A-1

RESULTS FROM $A_\epsilon = 0.95$ LCF TESTS

CONDITION	S#	$\Delta\epsilon_t$	$\Delta\epsilon_p$	$\Delta\sigma$ Ksi	N_i	N_f	ΔW in-lb/in³
000	D4-1	1.236	0.026	127.7	2399	2399	31
	DD2-3	1.211	0.044	119.3	3945	4152	49
	D5-1	1.290	0.126	128.8	1239	1373	152
	D3-1	1.813	0.608	150.7	200	202	857
	DD1-1	1.960	0.600	152.6	225	375	856
	DD2-1(1)	0.927	0.062	87.6	6436	7310(2)	-
	DD2-2(3)	1.271	0.098	142.1	415	420	-
	D3-2(4)	1.729	0.113	82.3	-	-	-
	D3-3(6)	1.423	0.101	140.4	2300	2508	-
001	D5R-3	0.951	0.033	91.1	5223	5335	28
	DD2R-3	1.222	0.041	118.2	3025	3347	45
	D3R-1	1.379	0.104	138.0	816	827	134
	DD1R-2	1.965	0.638	147.5	165	167	879
	DD2R-2	2.138	0.585	145.4	357	526	794
	D3R-2(3)	1.189	0.021	124.6	1119	1133	-
	DD1R-1(4)	0.756	0.046	83.3	4553	4844	-

(1) Wood's Metal Problem
(2) Test Stopped Before Failure
(3) Loops Unstable
(4) Pulled Out of Grips
(5) Fracture Smeared
(6) Lock Nut Loose

TABLE A-1 (Continued)

RESULTS FROM A_ϵ = 0.95 LCF TESTS

CONDITION	S#	$\Delta\epsilon_t$	$\Delta\epsilon_p$	$\Delta\sigma$ Ksi	N_i	N_f	ΔW in-lb/in^3
010	WW1-2	1.112	.022	109.9	3720	3769	22
	TT3-1	1.115	.056	113.3	2790	2951	58
	TT3-2	1.262	.049	125.0	3921	4005	56
	WW1-3	1.436	.080	136.8	901	916	100
	TT4-1	1.983	.630	154.4	333	334	891
	WW2-2	2.070	.585	154.1	219	231	826
	WW2-1	2.105	.631	150.0	515	528	865
	TT4-2(6)	1.325	.046	134.8	930	1350	-
011	TT4R-3	1.096	.042	104.7	3756	3800	42
	TT5R-2	1.358	.047	135.8	1395	1450	61
	TT4R-2	1.360	.046	134.7	1400	1436	59
	WW1R-1	1.470	.111	137.0	1050	1074	144
	TT5R-1	1.228	.104	114.7	2348	2557	113
	WW1R-4	1.297	.113	124.6	1646	1787	134
	WW1R-3	1.395	.110	130.4	1836	1851	136
	WW1R-2	1.915	.638	141.7	250	251	859
	TT4R-1(5)	1.284	.066	111.0	3557	3587	-

(1) Wood's Metal Problem
(2) Test Stopped Before Failure
(3) Loops Unstable
(4) Pulled Out of Grips
(5) Fracture Smeared
(6) Lock Nut Loose

261

TABLE A-1 (Continued)

RESULTS FROM A_ϵ = 0.95 LCF TESTS

CONDITION	S#	$\Delta\epsilon_t$	$\Delta\epsilon_p$	$\Delta\sigma$ Ksi	N_i	N_f	ΔW in-#/in^3
100	23-1	1.089	0.018	109.6	3658	3761	18
	21-3	1.152	0.051	109.2	4085	4656	51
	21-1	1.295	0.052	129.5	1400	1536	62
	23-2	1.428	0.093	129.2	899	900	110
	22-2	2.008	0.720	152.9	267	286	1004
101	22R-2	1.158	0.025	114.6	4532	4654	27
	23R-2	1.318	0.051	122.2	1955	1956	58
	24R-1	1.304	0.090	143.6	714	723	121
	30R-1	2.115	0.623	150.9	246	252	879
	30R-2	2.048	0.630	148.1	326	332	873
	30R-3	2.655	1.275	152.3	140	142	182

(1) Wood's Metal Problem
(2) Test Stopped Before Failure
(3) Loops Unstable
(4) Pulled Out of Grips
(5) Fracture Smeared
(6) Lock Nut Loose

TABLE A-1 (Continued)

RESULTS FROM $A_\epsilon = 0.95$ LCF TESTS

CONDITION	S#	$\Delta\epsilon_t$	$\Delta\epsilon_p$	$\Delta\sigma$ Ksi	N_1	N_f	ΔW in-lb/in^3
110	15-1	1.278	0.023	120.1	3144	3150	26
	18-3	1.253	0.047	125.4	3428	3504	54
	18-2	1.273	0.057	115.9	2587	2867	61
	18-1	1.559	0.088	145.4	951	961	118
	15-2	1.913	0.603	153.1	211	215	853
	17-1(6)	1.439	0.051	143.8	831	896	-
111	18R-1	1.150	0.027	117.3	4050	4080	30
	20R-1	1.381	0.050	134.1	2028	2340	63
	17R-2	1.515	0.107	148.3	794	805	149
	19R-2	2.010	0.615	158.8	225	233	916
	18R-2	3.220	1.980	160.4	62	63	2979

(1) Wood's Metal Problem
(2) Test Stopped Before Failure
(3) Loops Unstable
(4) Pulled Out of Grips
(5) Fracture Smeared
(6) Lock Nut Loose

TABLE A-2
RESULTS FROM $A_\epsilon = \infty$ LCF TESTS

CONDITION	S#	$\Delta\epsilon_t$	$\Delta\epsilon_p$	$\Delta\sigma$ KSI	N_i	N_f	ΔW in-lb/in³
00X	WW2-4	1.378	0.075	134.2	1627	1876	94
	D5-4	1.384	0.062	125.4	2865	(2)	72
	DD2-4	1.881	0.347	147.8	606	853	479
	D5-3	2.777	1.253	158.4	83	83	1855
	D4R-2	1.864	0.306	142.6	665	1103	408
	D5R-4	2.065	0.591	155.9	265	269	861
	D3R-3	2.766	1.139	155.1	226	233	1506
	D4R-3(3)	1.184	0.030	129.0	935	1160	-
011	TT5R-4	1.172	0.050	117.4	5140	8103	53
	WW2R-3	1.872	0.306	146.4	633	755	407
	TT4R-4	2.026	0.599	159.3	219	230	867
	TT3R-3	2.768	1.066	155.5	100	104	1505
	TT3R-4	1.384	0.119	141.5	214	220	-

(1) Wood's Metal Problem
(2) Test Stopped Before Failure
(3) Unstable Loops
(4) Pulled out of Grips
(5) Fracture Smeared
(6) Locknut Loose

TABLE A-2 (Continued)
RESULTS FROM $A_\epsilon = \infty$ LCF TESTS

CONDITION	S#	$\Delta\epsilon_t$	$\Delta\epsilon_p$	$\Delta\sigma$ KSI	N_i	N_f	ΔW in-lb/in³
101	23R-4	1.167	0.045	121.1	3023	(1)	51
	22R-3(3)	1.388	0.144	139.6	1505	1530	-
	23R-3	1.862	0.287	149.2	645	1028	401
	22R-4	2.013	0.684	145.5	366	381	933
	24R-3	2.570	0.947	153.7	280	302	1364
	21R-4	2.775	1.054	149.2	445	494	1473
111	18R-3	1.181	0.035	117.2	5490	5859	37
	15R-2	1.386	0.071	138.9	2399	2548	-
	15R-4	1.869	0.275	153.4	1237	1671	380
	17R-4	1.969	0.323	154.3	549	590	449
	15R-1	1.997	0.512	156.6	316	323	723
	17R-3	2.766	0.958	176.3	176	244	1523
	20R-2	2.950	1.210	167.7	170	176	1830

(1) Wood's Metal Problem
(2) Test Stopped Before Failure
(3) Unstable Loops
(4) Pulled out of Grips
(5) Fracture Smeared
(6) Locknut Loose

265

END

FILMED

DTIC
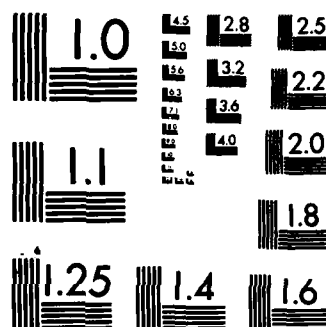
TABLE A-3
SUMMARY OF CYCLIC PROPERTIES, A = 0.95

CONDITION	n'	C.D.*	$\beta^{(1)}$	C.D.*	$\alpha^{(2)}$	C.D.*
all data	0.076	0.714	1.164	0.900	0.800	0.919
38% upset	0.076	0.665	1.170	0.864	0.797	0.889
64% upset	0.077	0.767	1.160	0.940	0.803	0.951
0% Co	0.076	0.822	1.170	0.918	0.792	0.934
0.4% Co	0.077	0.638	1.143	0.894	0.807	0.905
000	0.069	0.838	1.110	0.924	0.848	0.938
001	0.070	0.856	1.017	0.936	0.884	0.955
010	0.092	0.875	1.280	0.870	0.716	0.880
011	0.052	0.194	1.344	0.680	0.743	0.754
100	0.092	0.812	1.328	0.845	0.700	0.872
101	0.069	0.829	1.242	0.951	0.757	0.961
110	0.082	0.688	1.088	0.917	0.839	0.937
111	0.066	0.809	1.066	0.992	0.881	0.994

*C.D. = coefficient of determination

(1) β = -1/m, where m = slope of Coffin-Manson plot

(2) α = - slope of ΔW vs. N_f plot

TABLE A-4
SUMMARY OF CYCLIC PROPERTIES, A = ∞

CONDITION	n'	C.D.*	$\beta^{(1)}$	C.D.*	$\alpha^{(2)}$	C.D.*
All data	0.085	0.826	1.028	0.909	0.857	0.915
38% upset	0.082	0.896	0.917	0.945	0.965	0.956
64% upset	0.088	0.785	1.144	0.914	0.806	0.923
0% Co	0.068	0.871	1.189	0.886	0.838	0.881
0.4% Co	0.107	0.908	0.887	0.959	0.958	0.950
00X**	0.070	0.928	1.027	0.931	0.924	0.941
011	0.101	0.929	0.779	0.996	1.021	0.983
101	0.067	0.849	1.437	0.939	0.654	0.946
111	0.109	0.954	0.969	0.959	0.929	0.956

*C.D. = Coefficient of Determination

(1) β = - 1/m, Where m is Slope of Coffin-Manson Plot

(2) α = - slope of ΔW vs. N_f Plot

** Includes Data From 001 and 000 Conditions
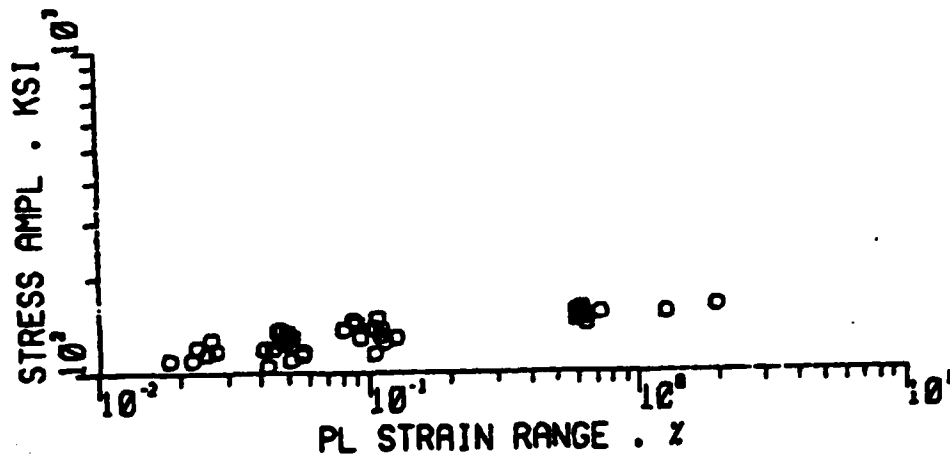
(a) All data n' = 0.076.
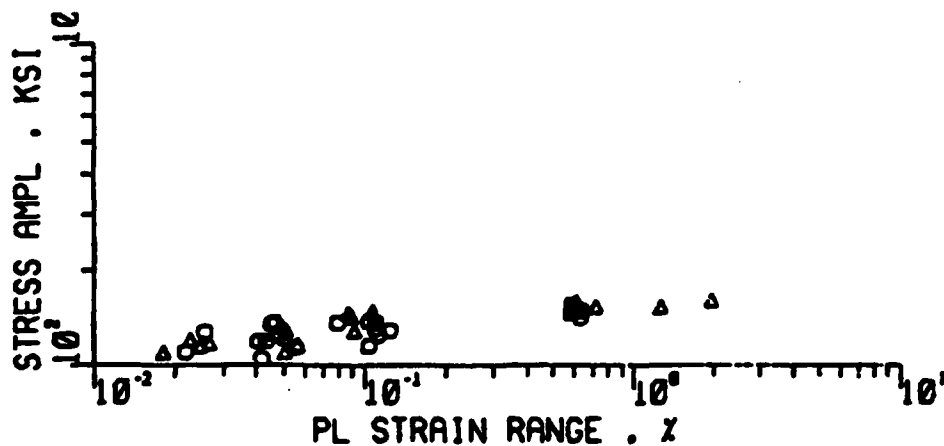
(b) o 38% upset n' = 0.076; Δ 64% upset n' = 0.077.

Figure A1. Stress Aplitude Plotted as a Function of Plastic Strain
Range for the Indicated Condition and for A = 0.95 LCF
Tests.
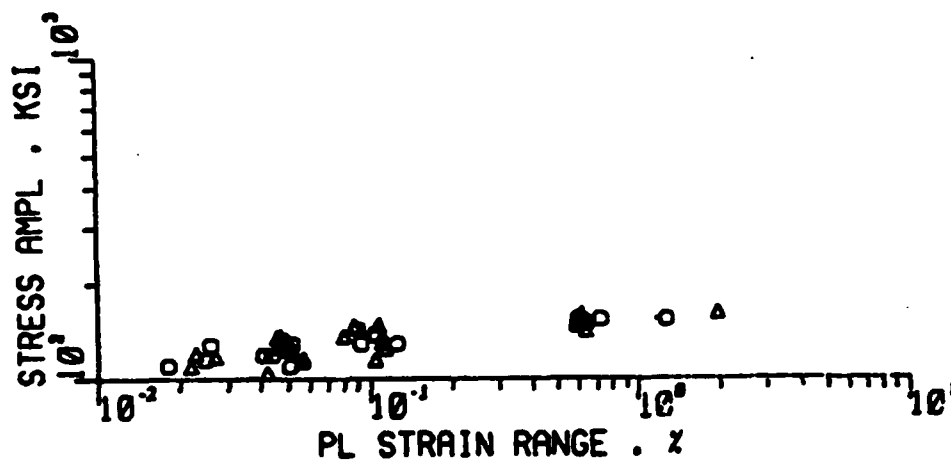
268

(c)   o   0% Co n' = 0.076; Δ 0.4% Co n' = 0.077.

(d)   o   000 n' = 0.069; Δ 001 n' = 0.070.

Figure Al Continued.

269

(e) o 010 n' = 0.092; Δ 011 n' = 0.052.

(f) o 100 n' = 0.92; Δ 101 n' = 0.069.

Figure A1 Continued.
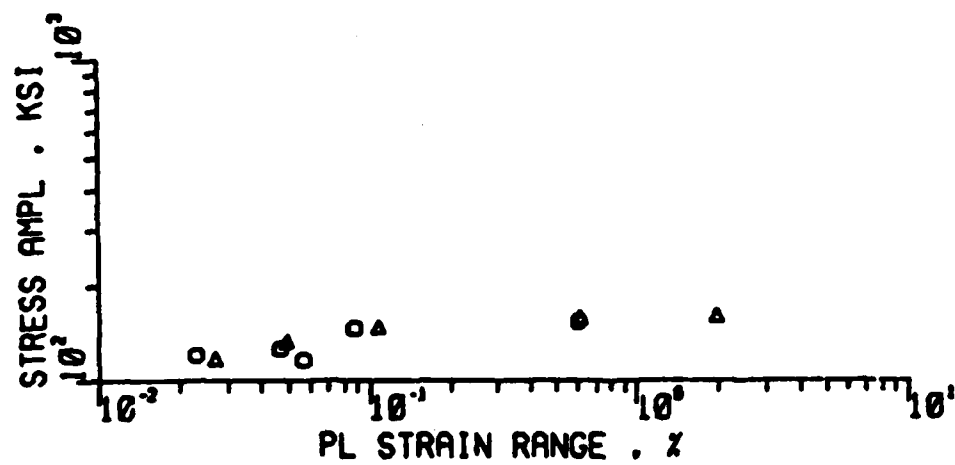
(g) o 110 n' = 0.082; Δ 111 n' = 0.066.

Figure A1 Continued.

271
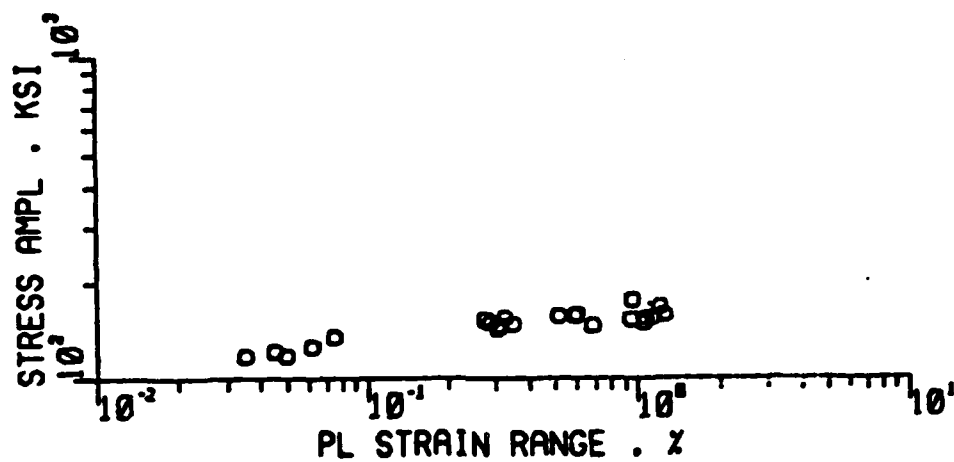
(a) o All data n' = 0.085.
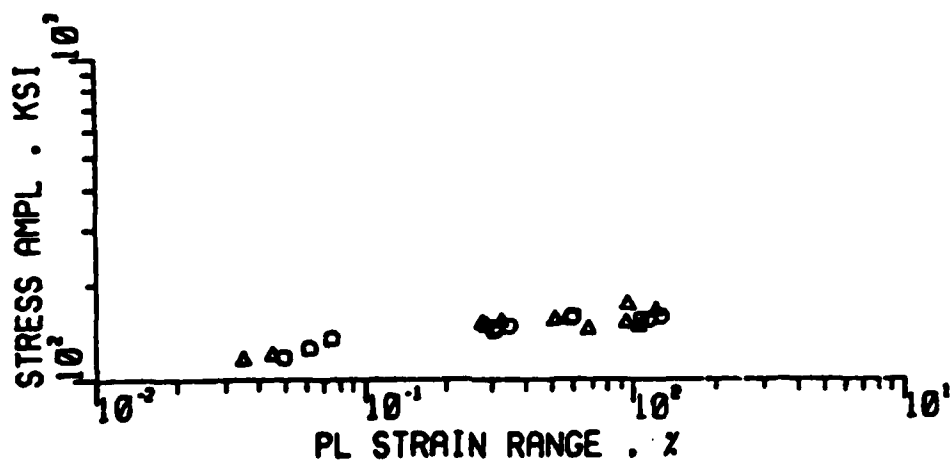
(b) o 38% upset n' = 0.082; Δ 64% upset n' - 0.088.

Figure A2. Stress Amplitude Plotted as a Function of Plastic Strain Range for the Indicated Condition and for A = ∞ LCF Tests.
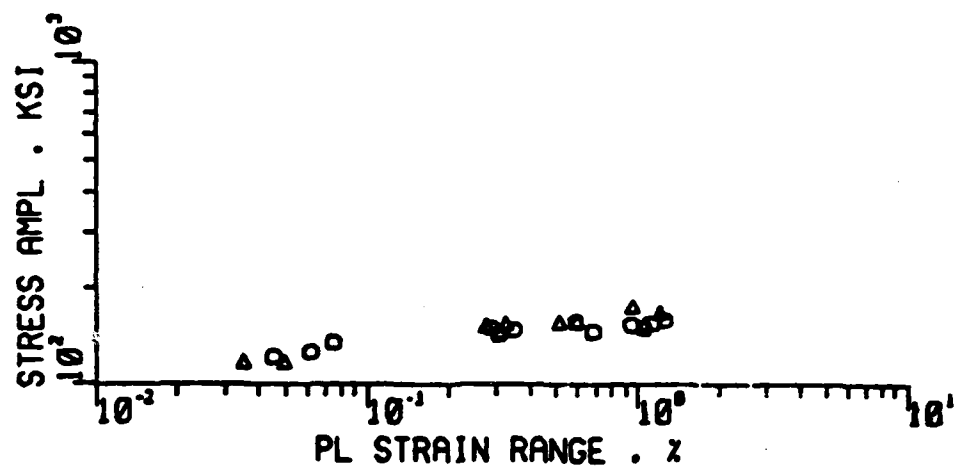
(c) o 0% Co n' = 0.068; Δ 0.4% Co n' = 0.107.
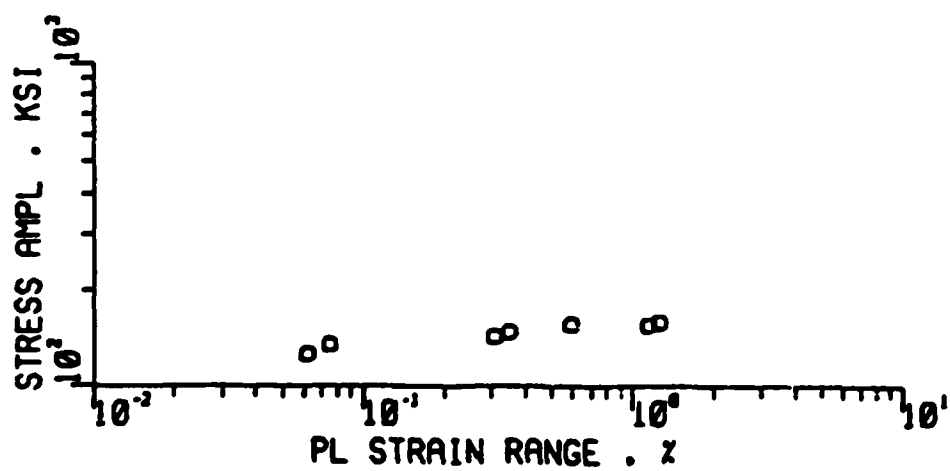
(d) o 00X n' = 0.070.

Figure A2 Continued.
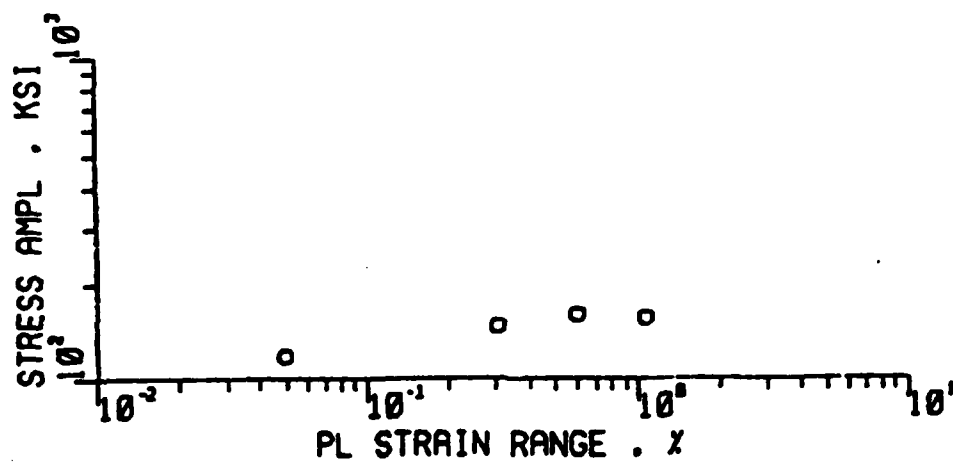
(e) o 011 n ' = 0.101.
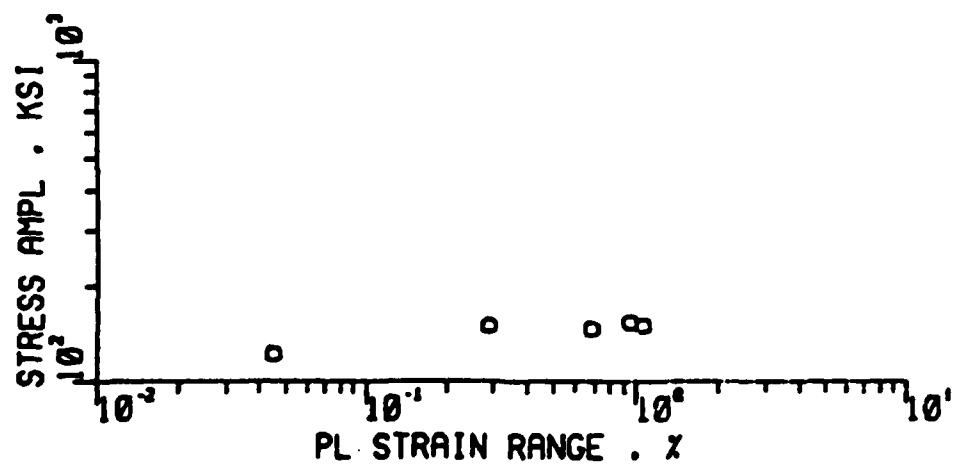
(f) o 101 n' = 0.067.

Figure A2 Continued.
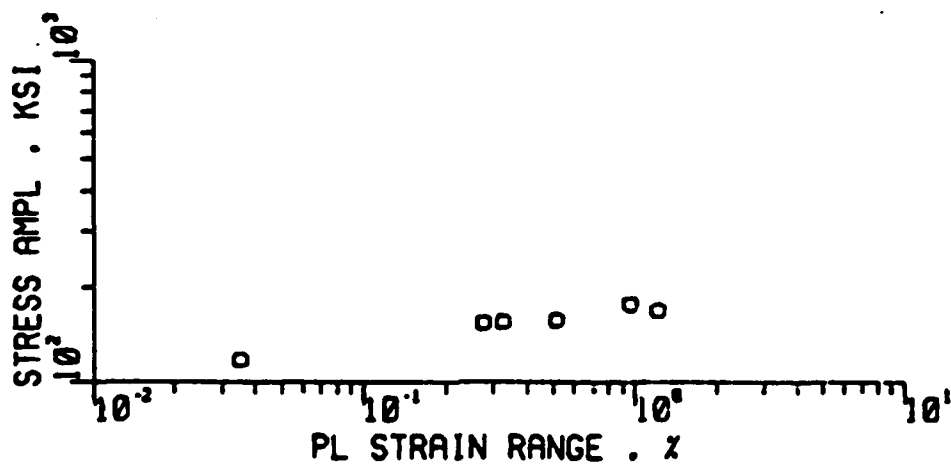
(g) o 111 n' = 0.109.

Figure A2 Continued.

Figure A3. Coffin-Manson Plot for Indicated Condition for A = 0.95 LCF Tests.
(a) o All Data m = - 0.859.

276

Figure A3 Continued. (b) o 64% upset m - 0.862; △ 38% upset m = 0.855.

277

Figure A4 Continued. (e) o 011 m = - 1.284.

291

Figure A4 Continued. (d) o OOX m = - 0.974.

290

Figure A4 Continued. (c) o 0% Co m = - 0.841; △ 0.4% Co m = - 1.127.

289
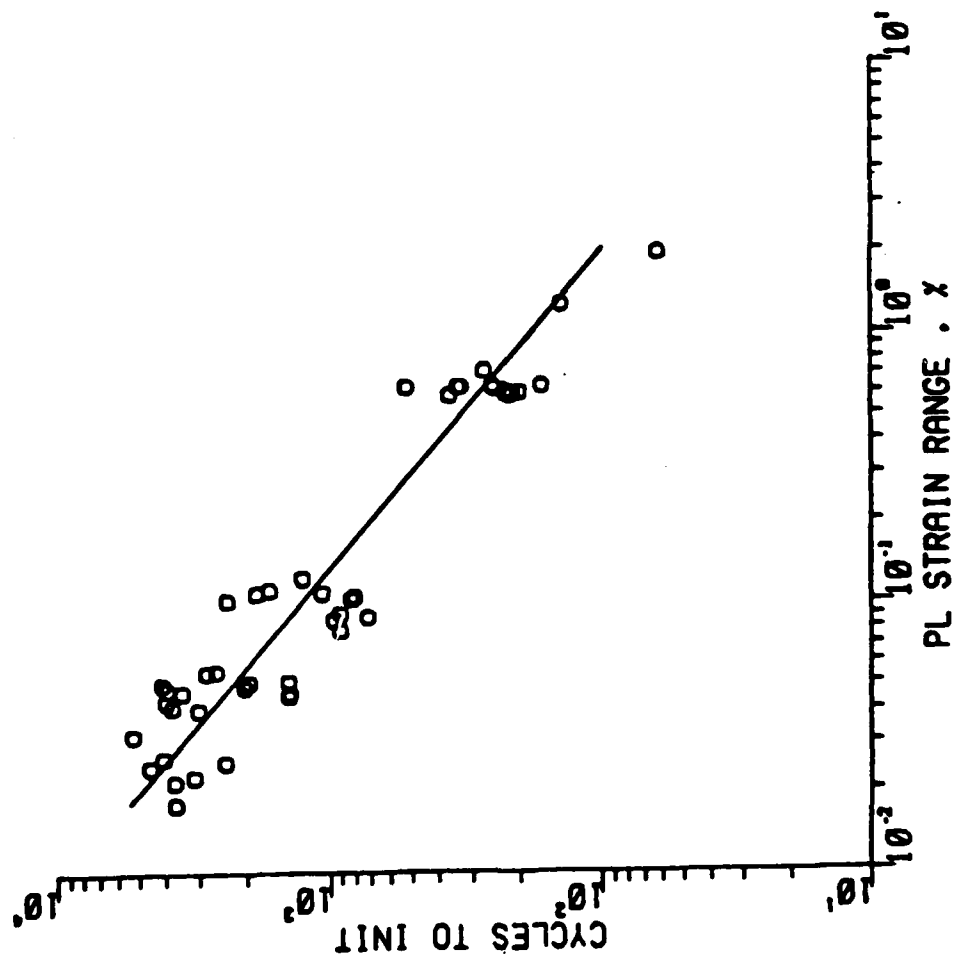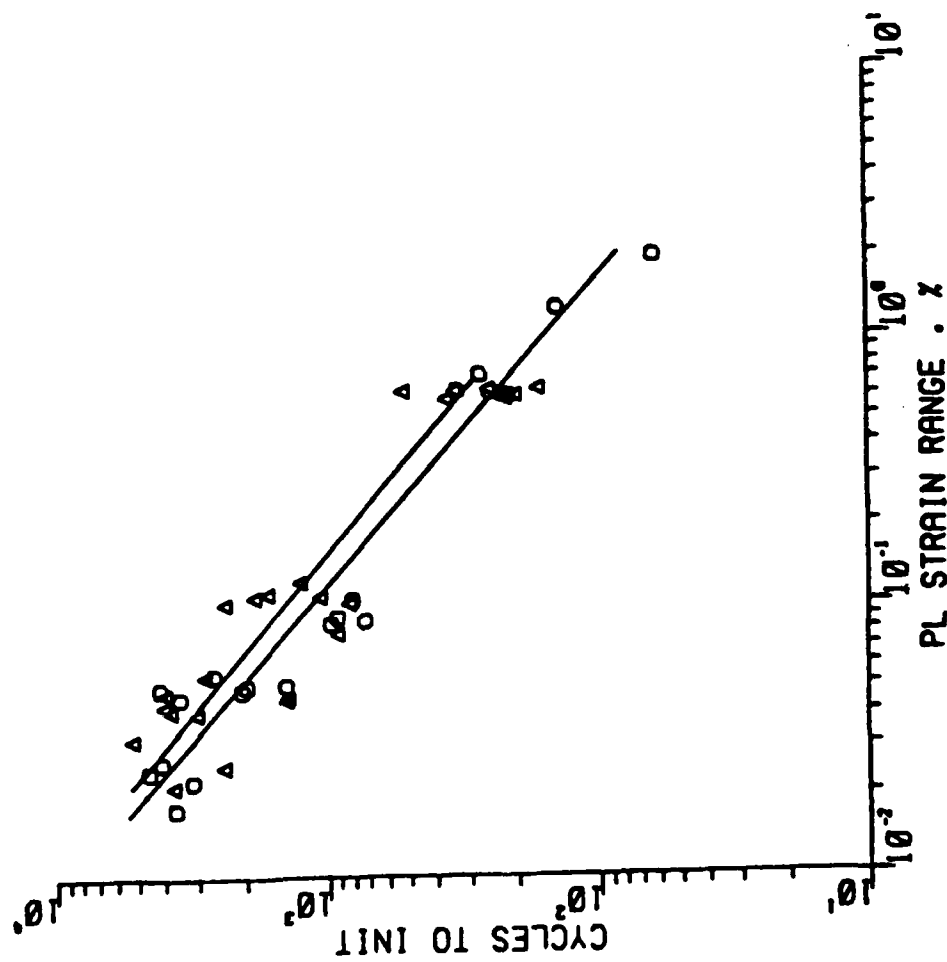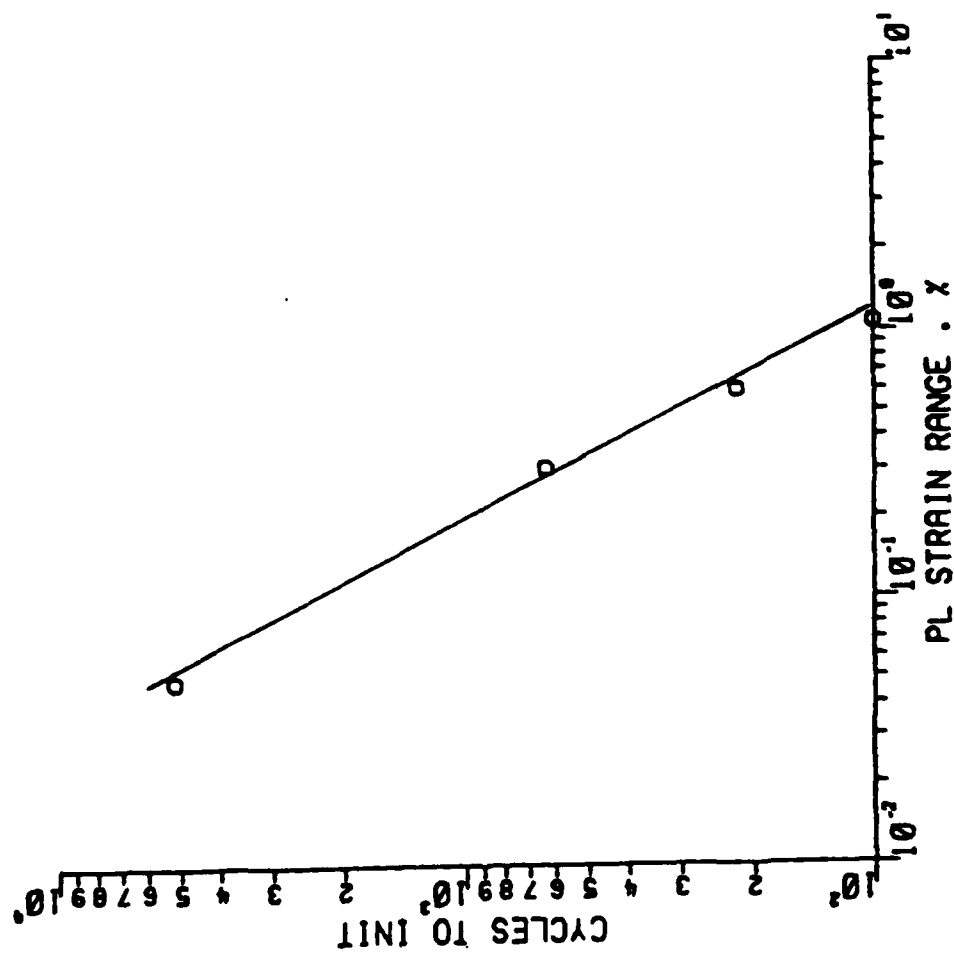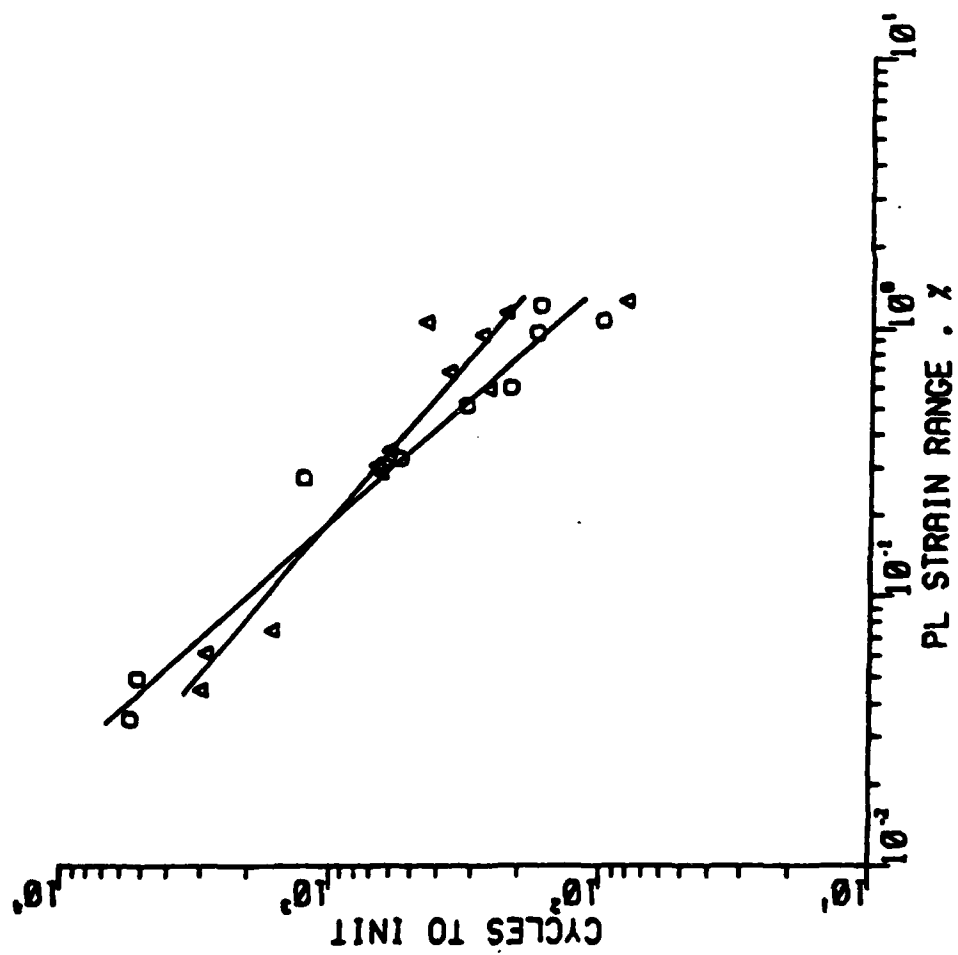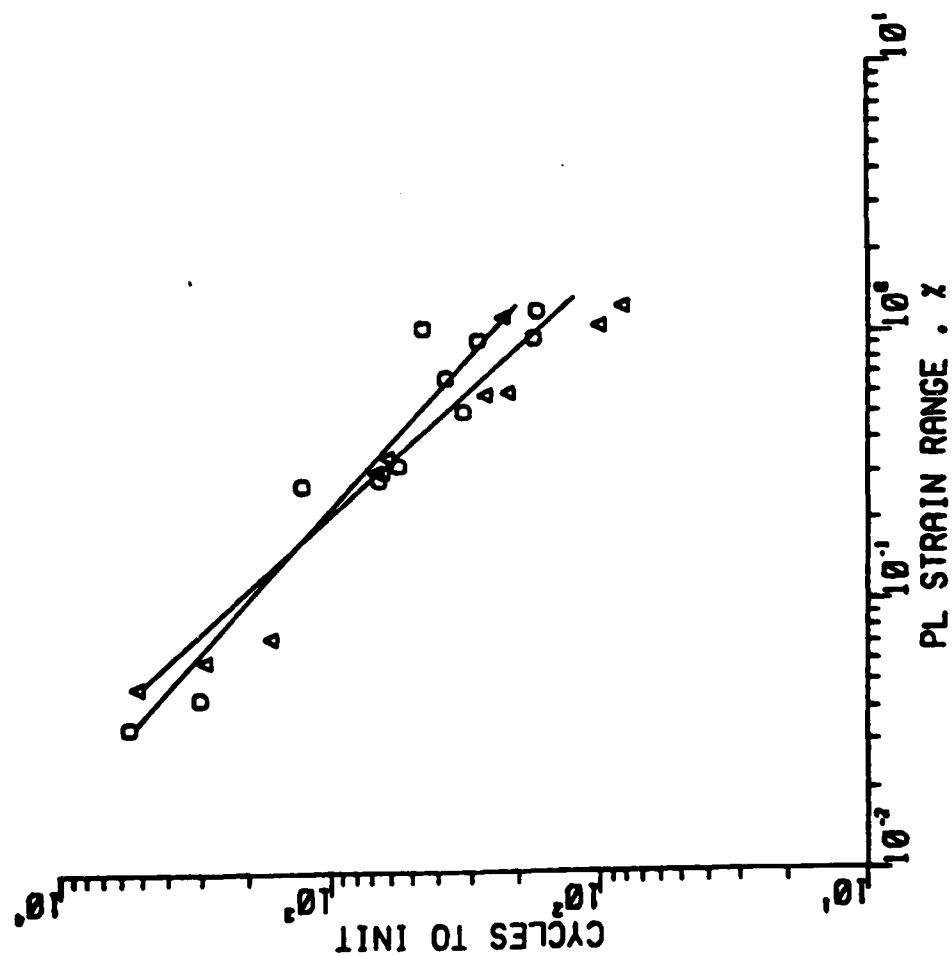
Figure A4 Continued. (b) o 64% upset m = - 0.874; △ 38% upset m = - 1.091.

288
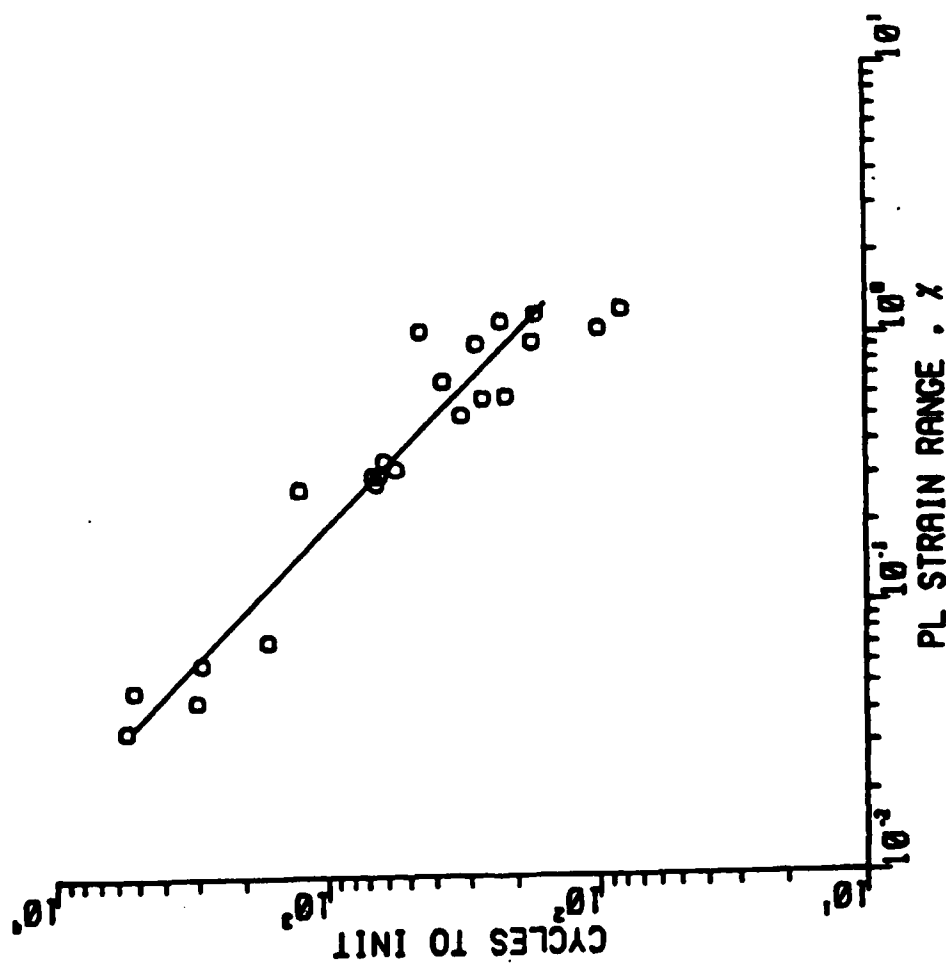
Figure A4. Coffin-Manson Plot for Indicated Condition for A = ∞ LCP Tests.
(a) o All Data m = - 0.5, 3.

Figure A3 Continued. (k) o 111 m = - 0.938.

286

Figure A3 Continued. (J) o 110 m = - 0.919.

285

Figure A3 Continued. (1) o 101 m = - 0.805.

284

Figure A3 Continued. (h) o 100 m = - 0.753.

Figure A3 Continued.   (g)   o 011 m = - 0.744.

282
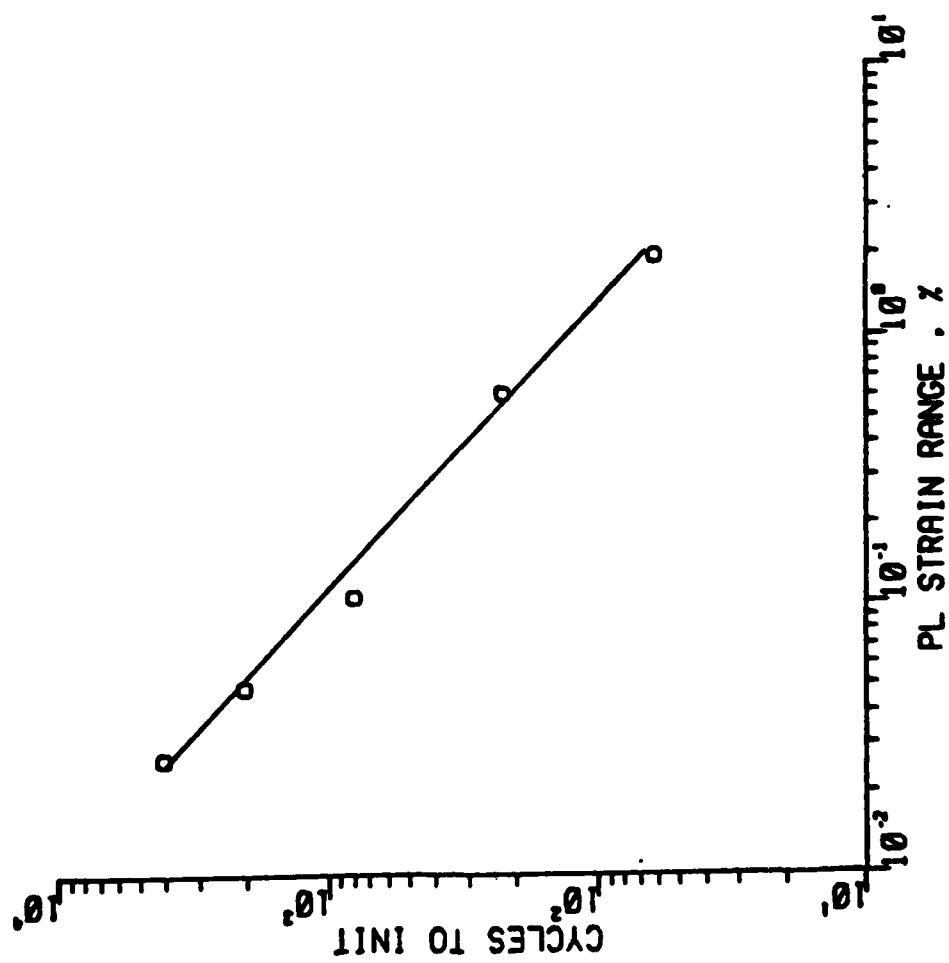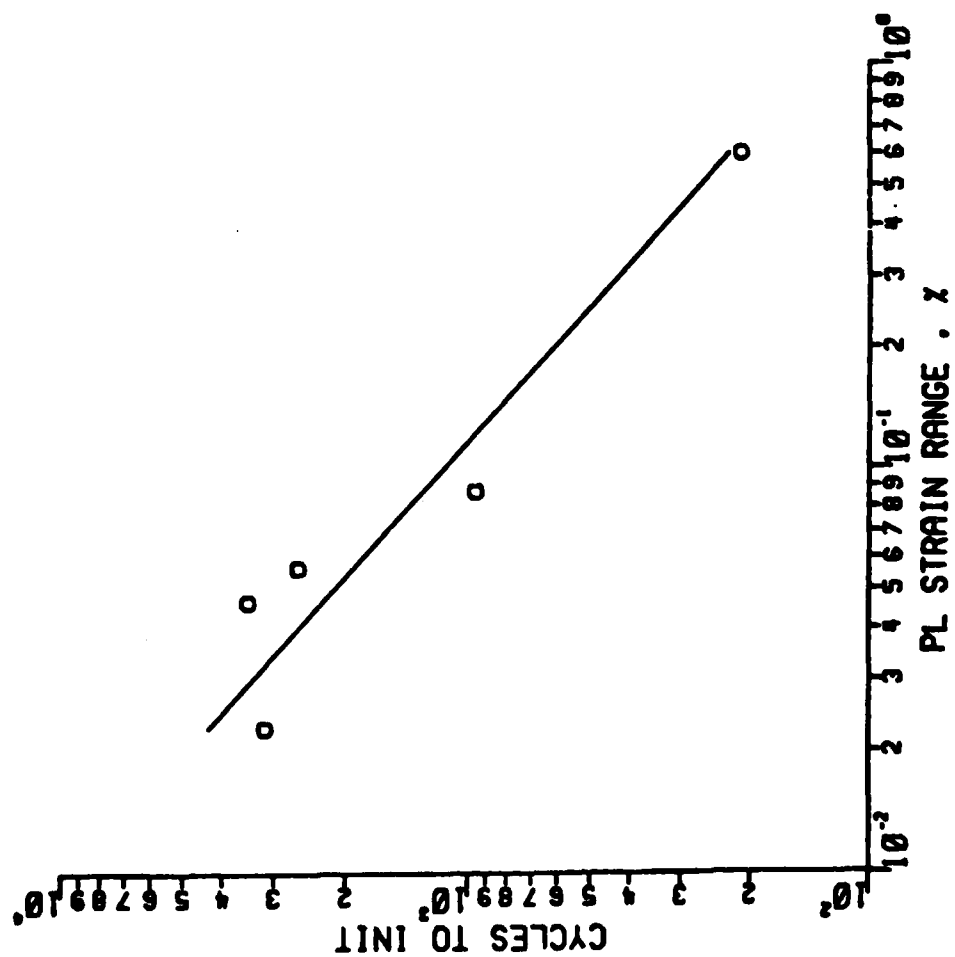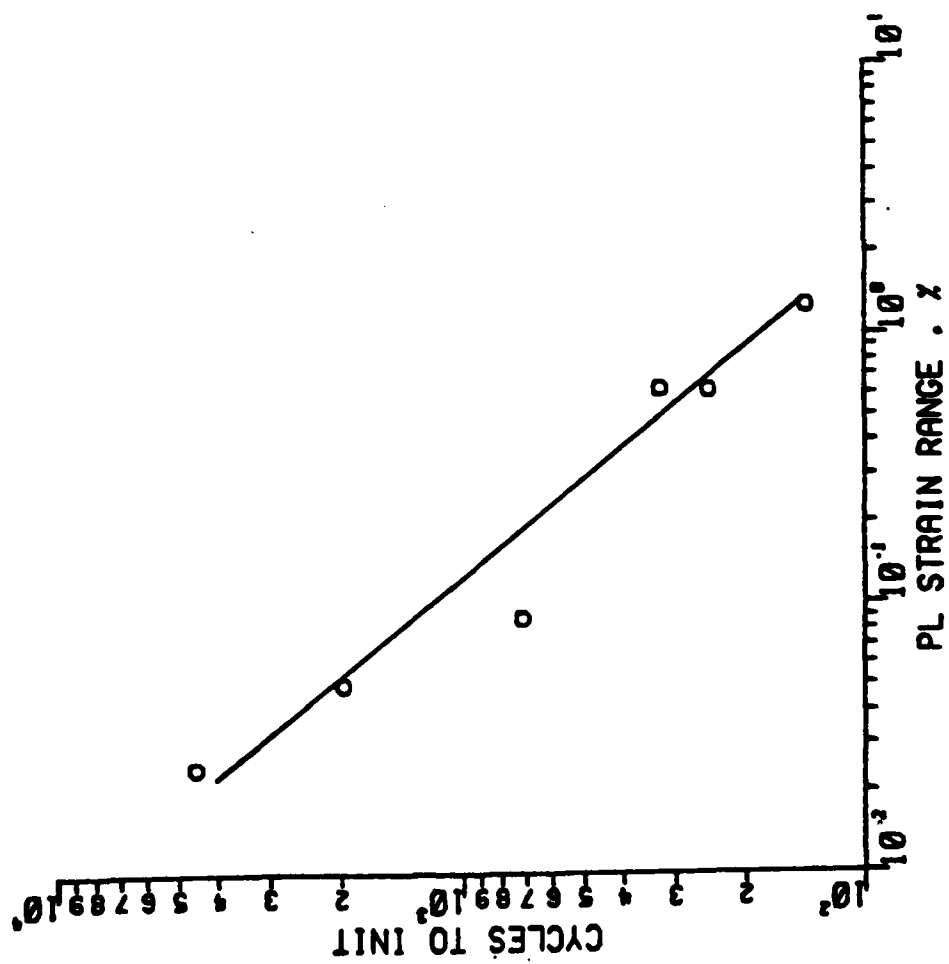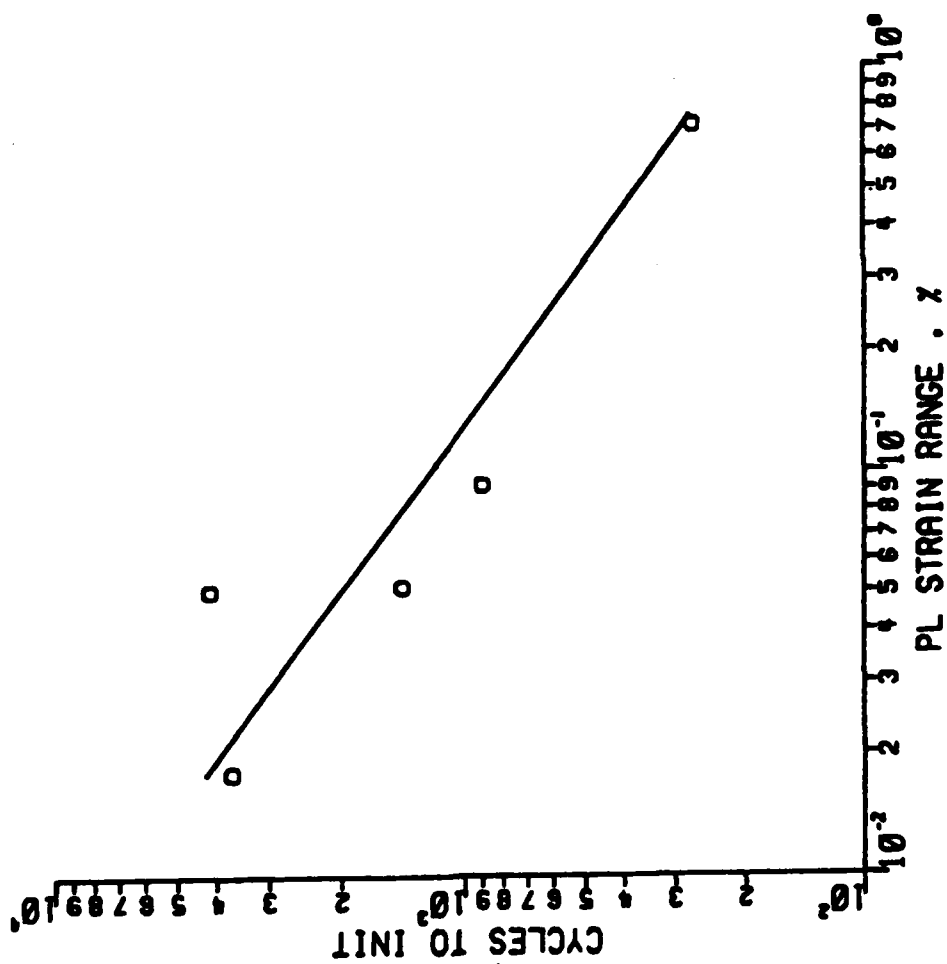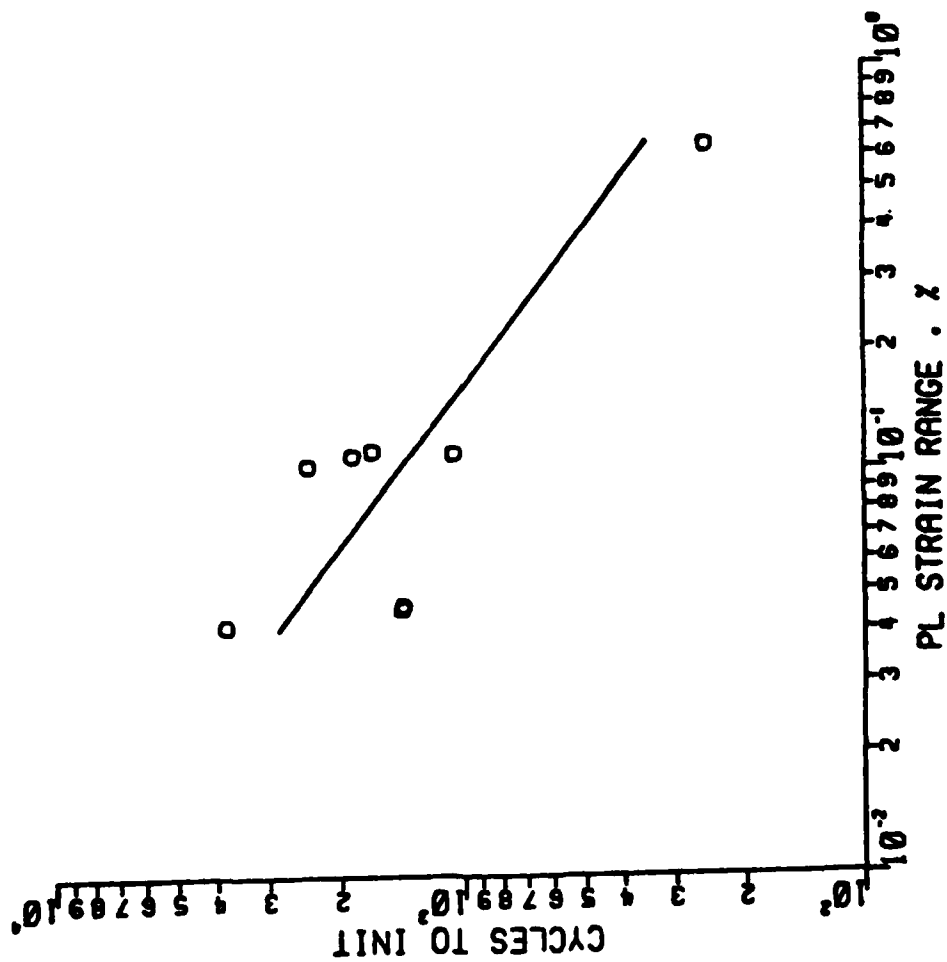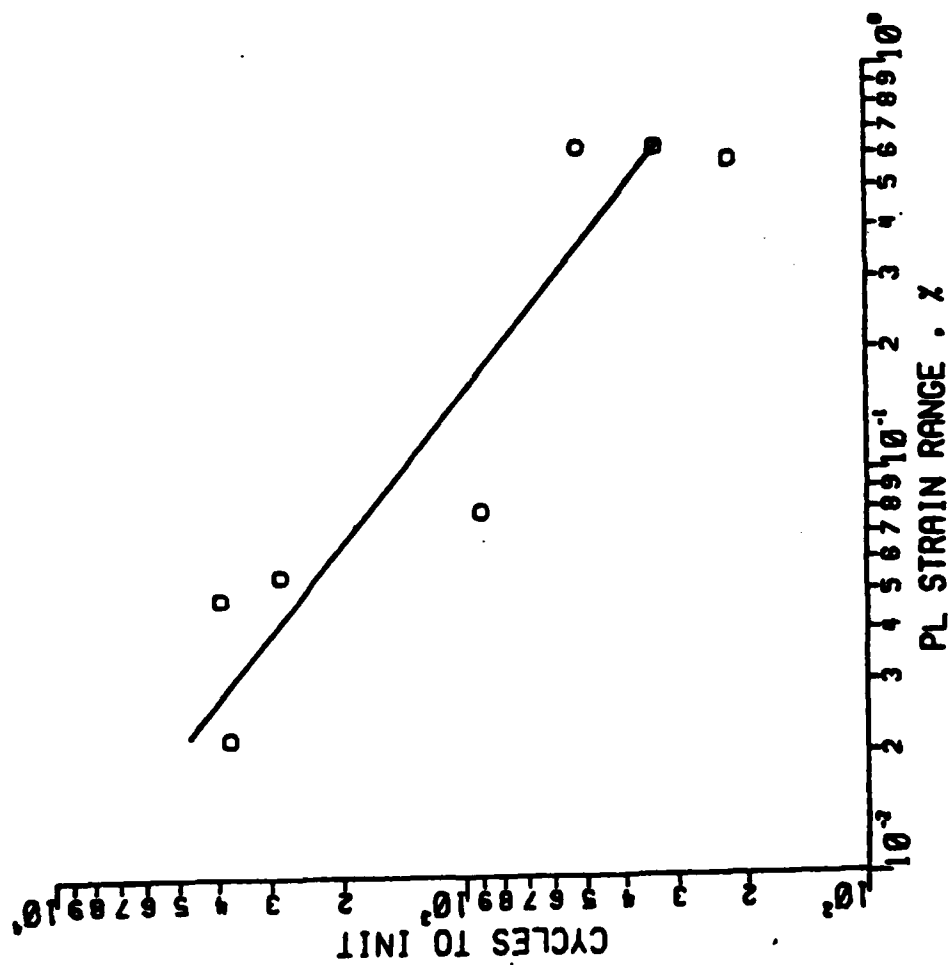
Figure A3 Continued. (f) o 010 m = ~ 0.781.

281

Figure A3 Continued. (e) o 001 m = - 0.983.

Figure A3 Continued. (d) o 000 m = - 0.901.

Figure A3 Continued. (c) o 0% Co m = - 0.854; △ 0.4% Co m = - 0.875.

278
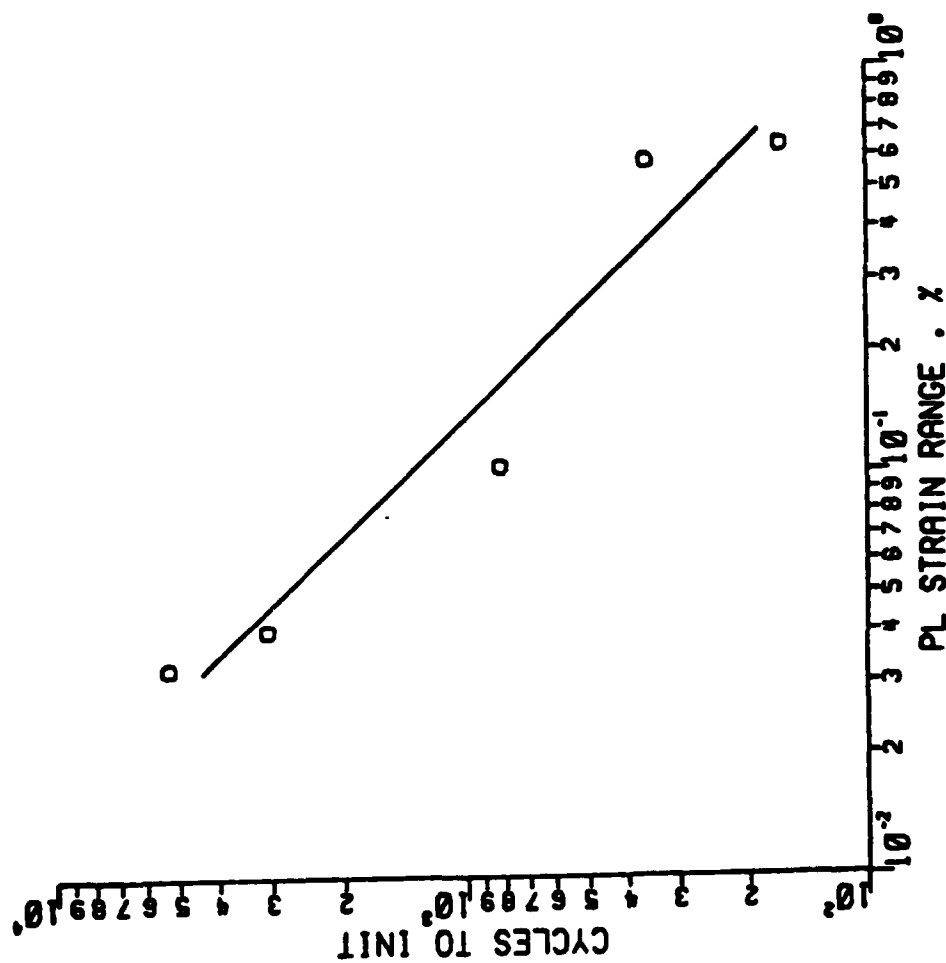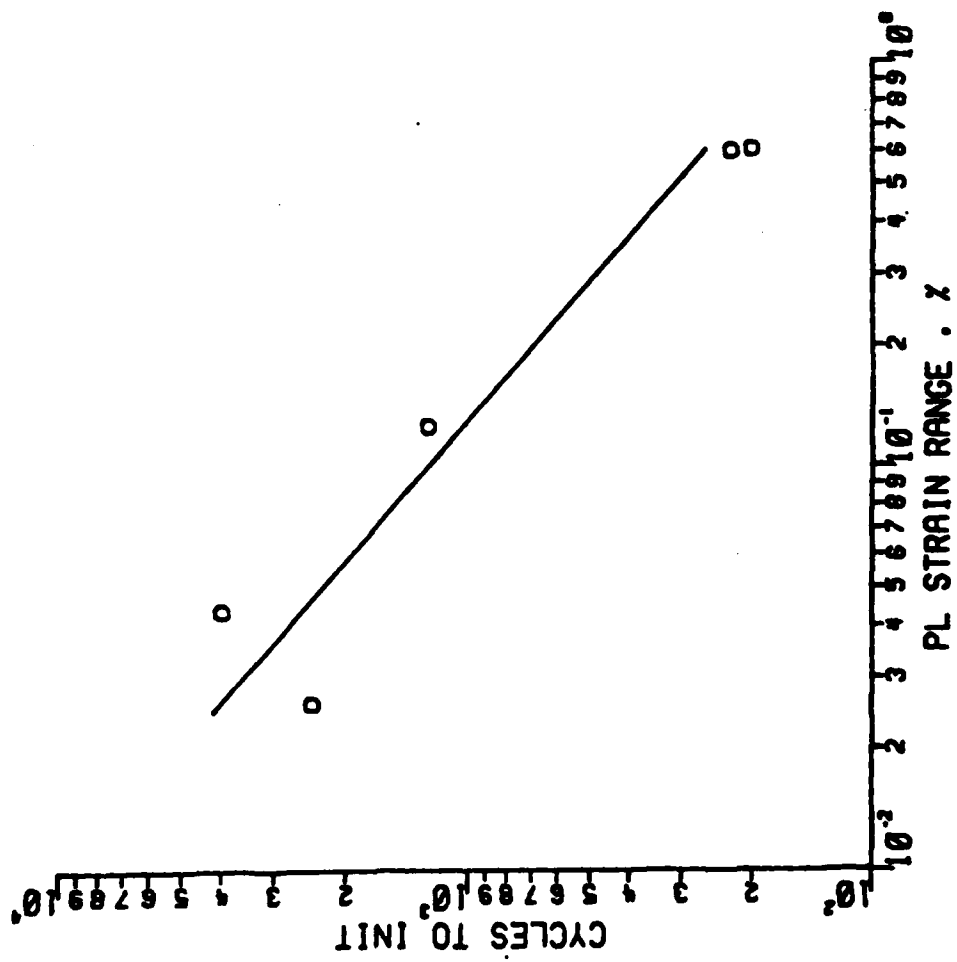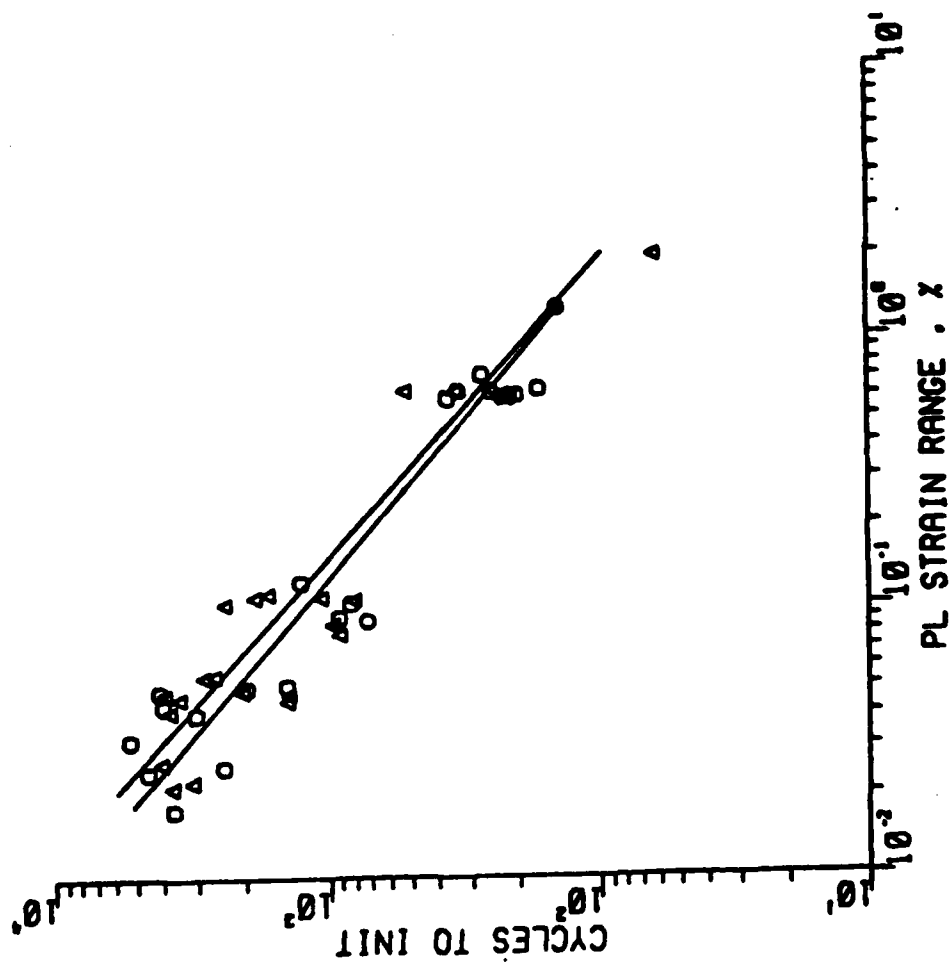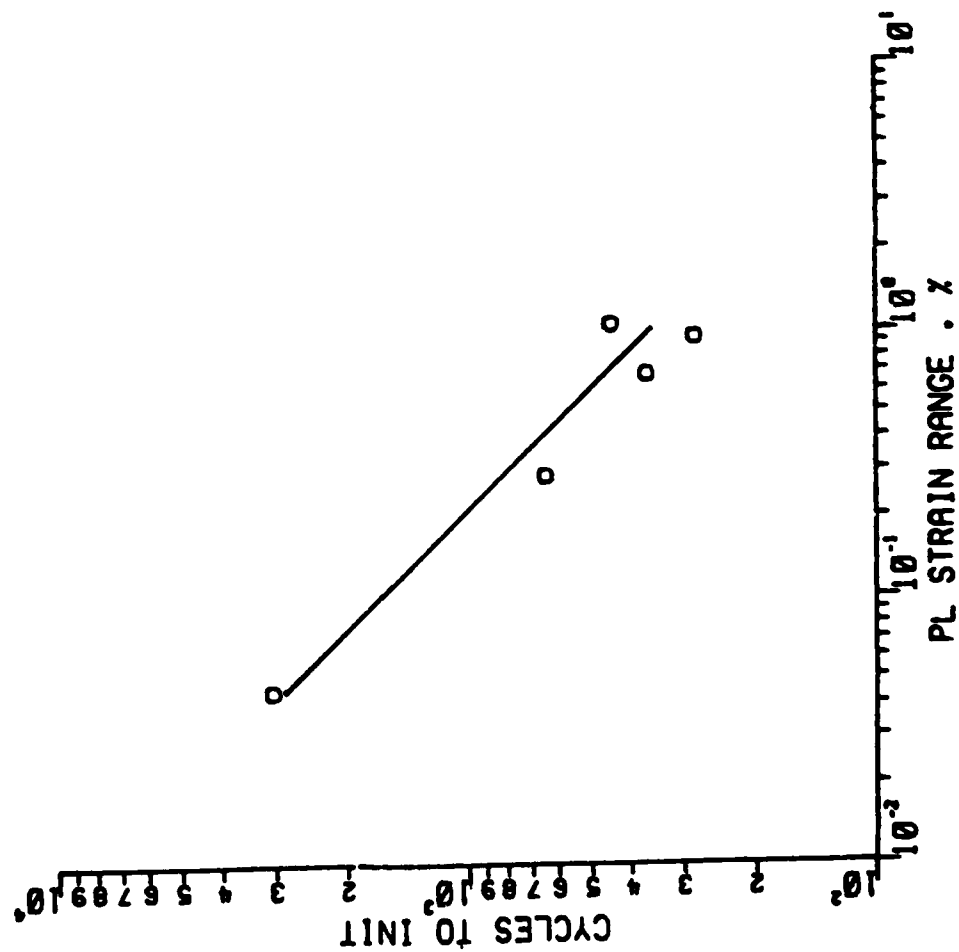
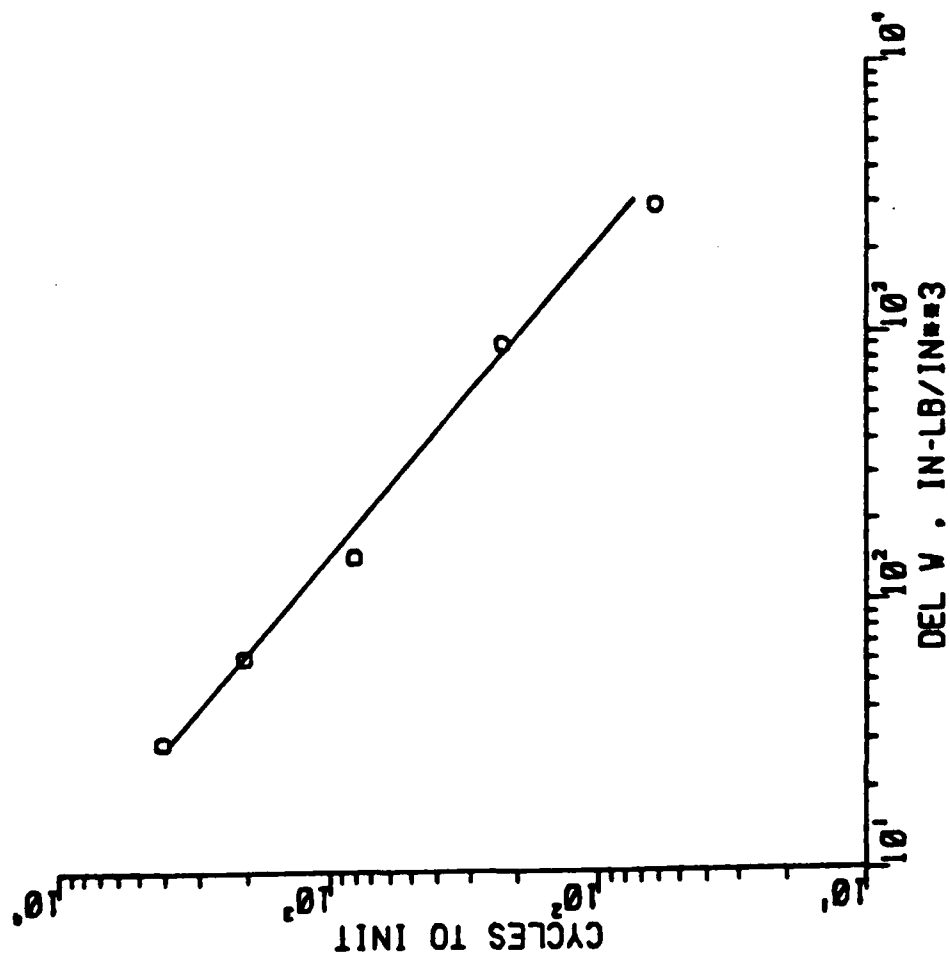Figure A4 Continued. (f) o 101 m = - 0.696.
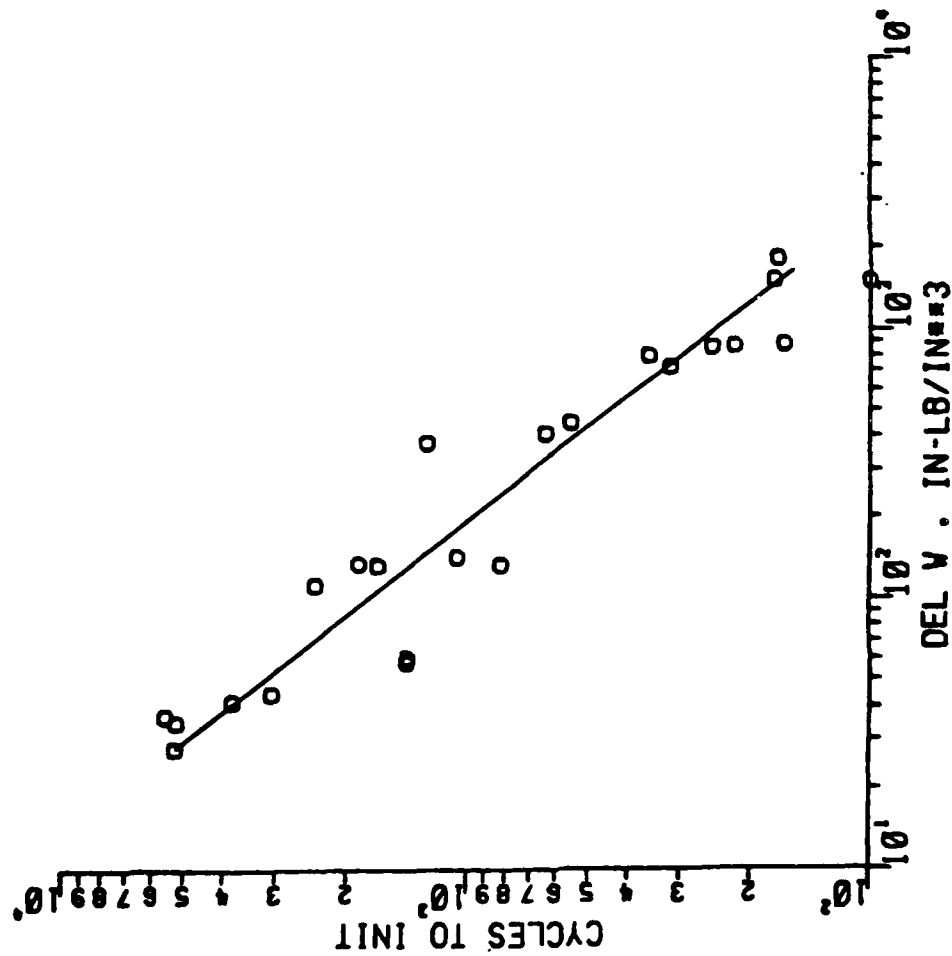
292
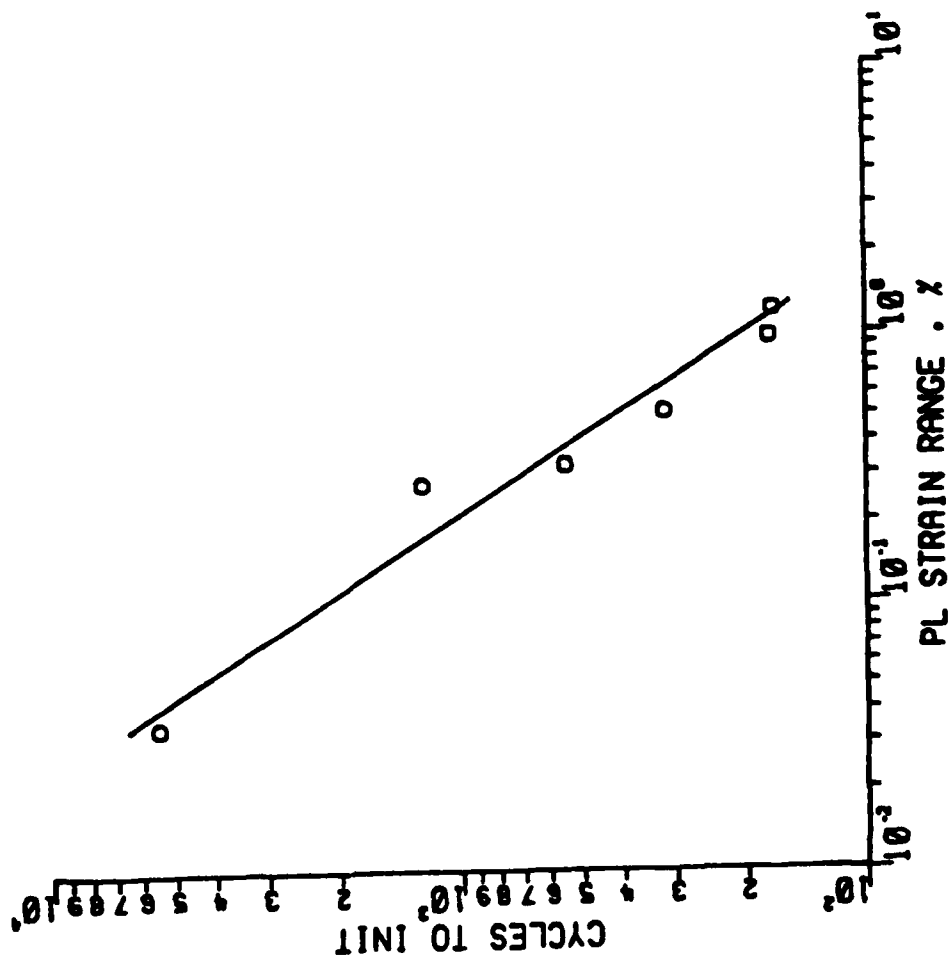
Figure A4 Continued. (g) o 111 m = - 1.032.
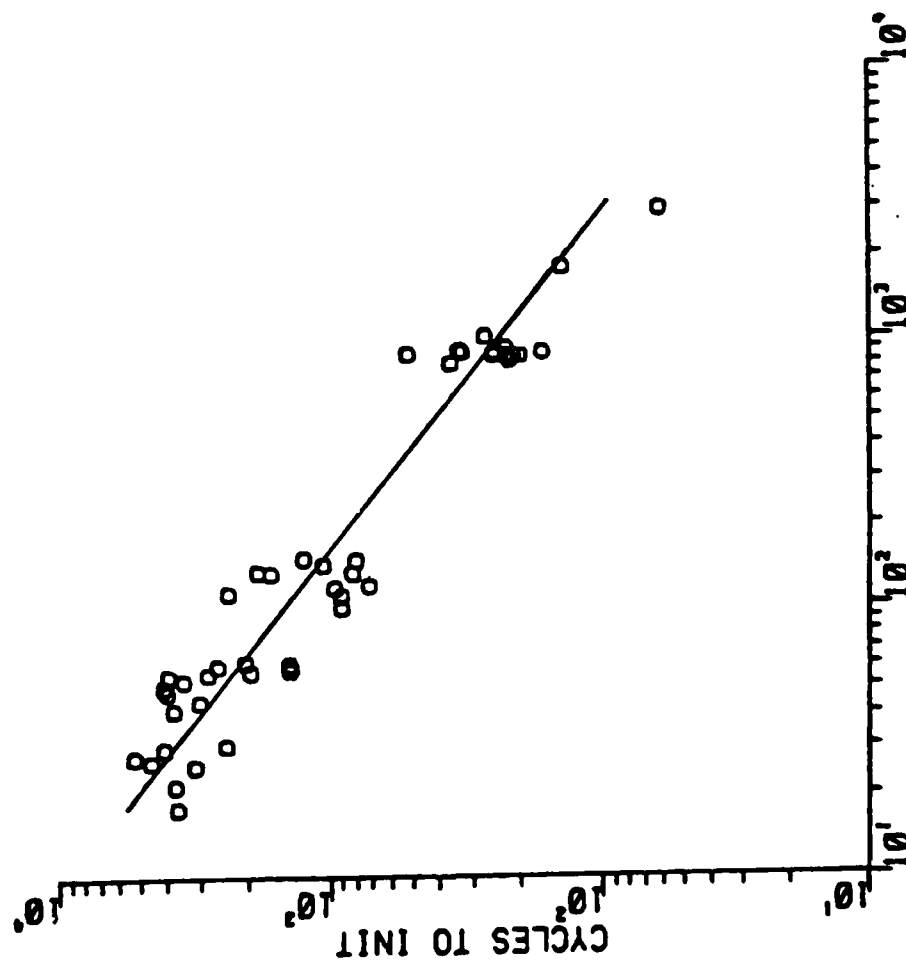
293

Figure A5. Cycles to Initiation Plotted as a Function of Hysteretic Energy, ΔW, for the Condition Indicated in A = 0.95 LCF Tests. (a) o All data m = − 0.800.

294
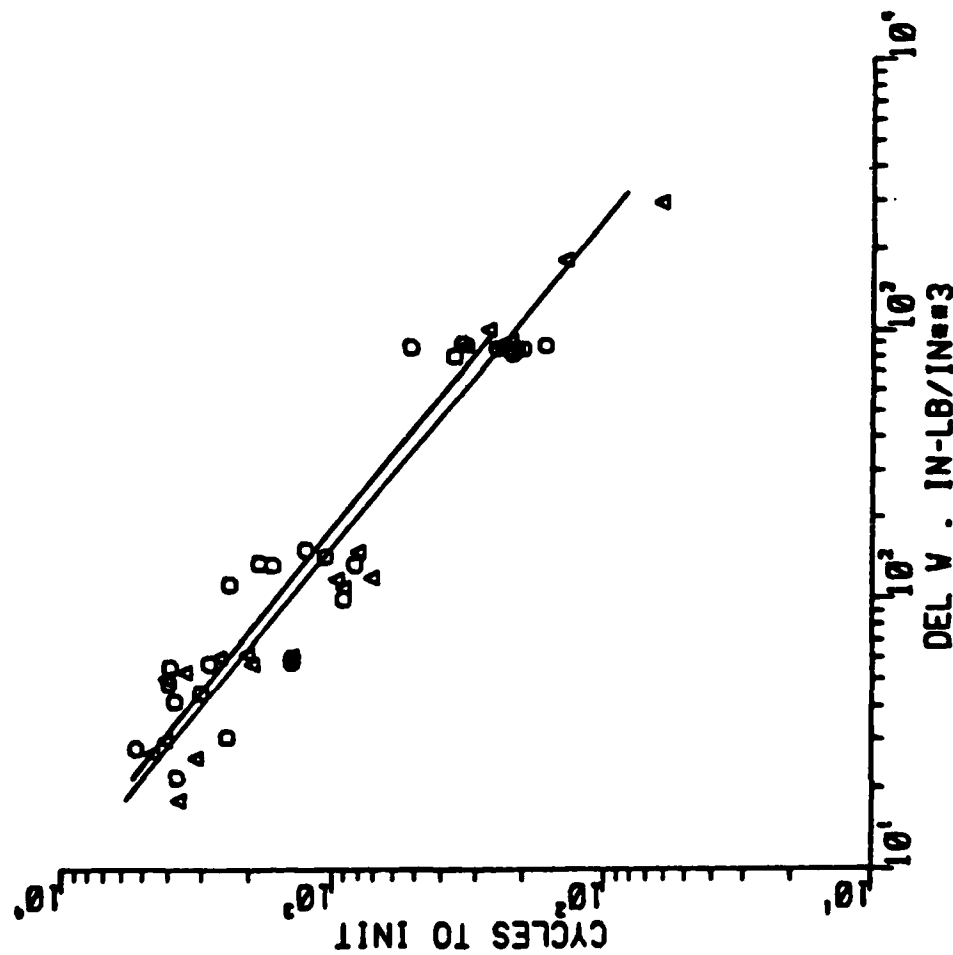
Figure A5 Continued. (b) ○ 38% upset m = - 0.797; △ 64% upset m = - 0.803.

DEL V . IN-LB/IN=3
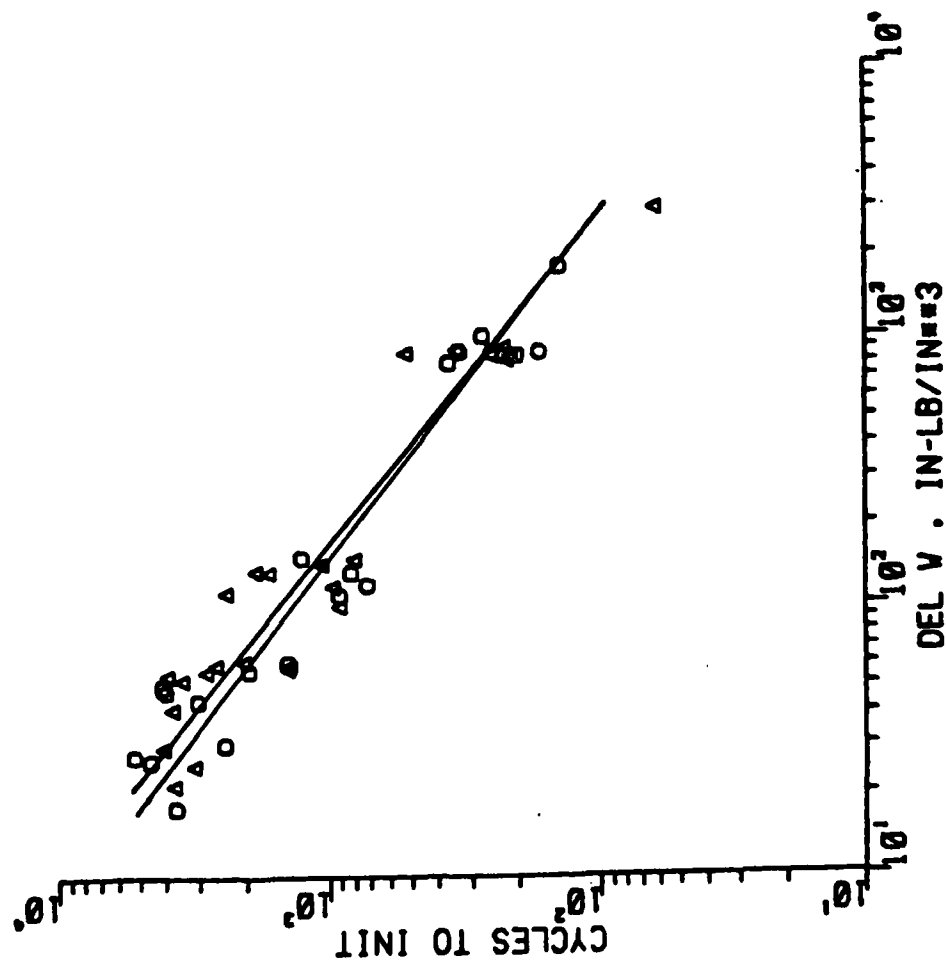
Figure A5 Continued. (c) o 0% Co m = - 0.792; △ 0.4% Co m = - 0.807.

296

Figure A5 Continued. (d) o 000 m = - 0.848.

297

Figure A5 Continued. (e) o 001 m = - 0.884.

298

Figure A5 Continued.   (f) o 010 m = - 0.716.

299

Figure A5 Continued. (g) o 011 m = - 0.743.

300

Figure A5 Continued. (h) o 100 m = - 0.700.

301
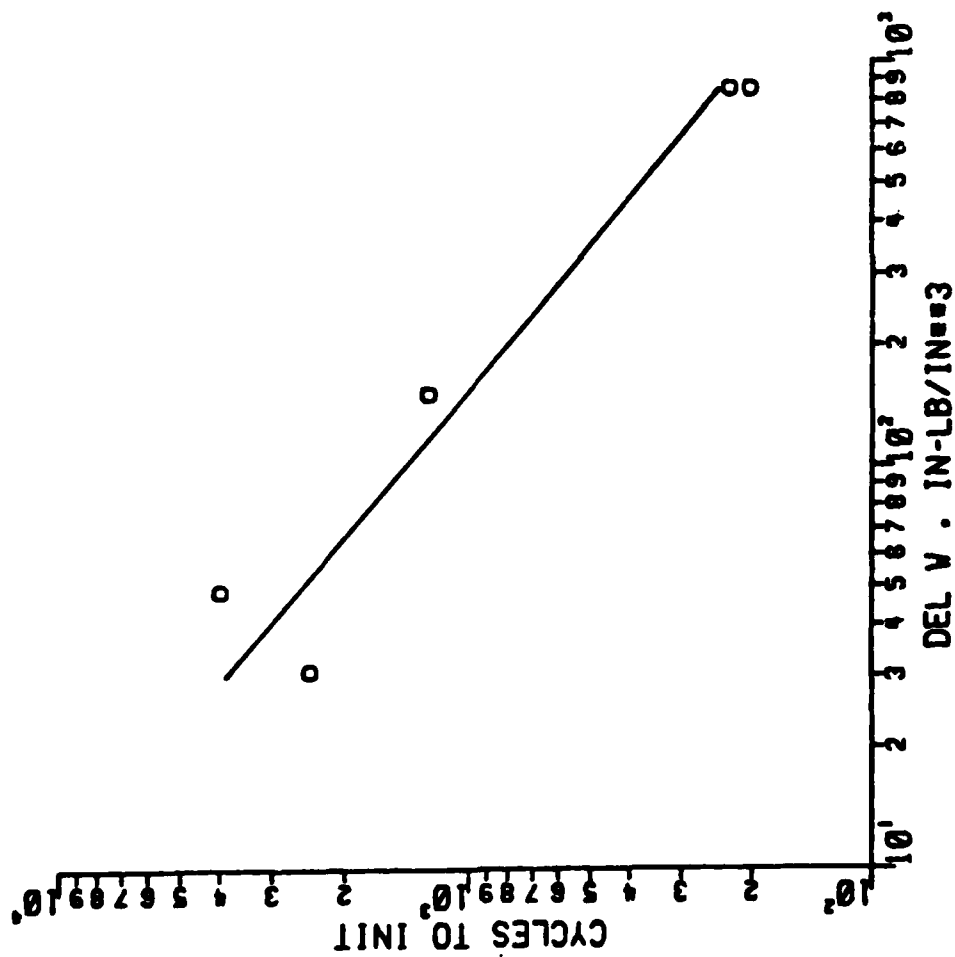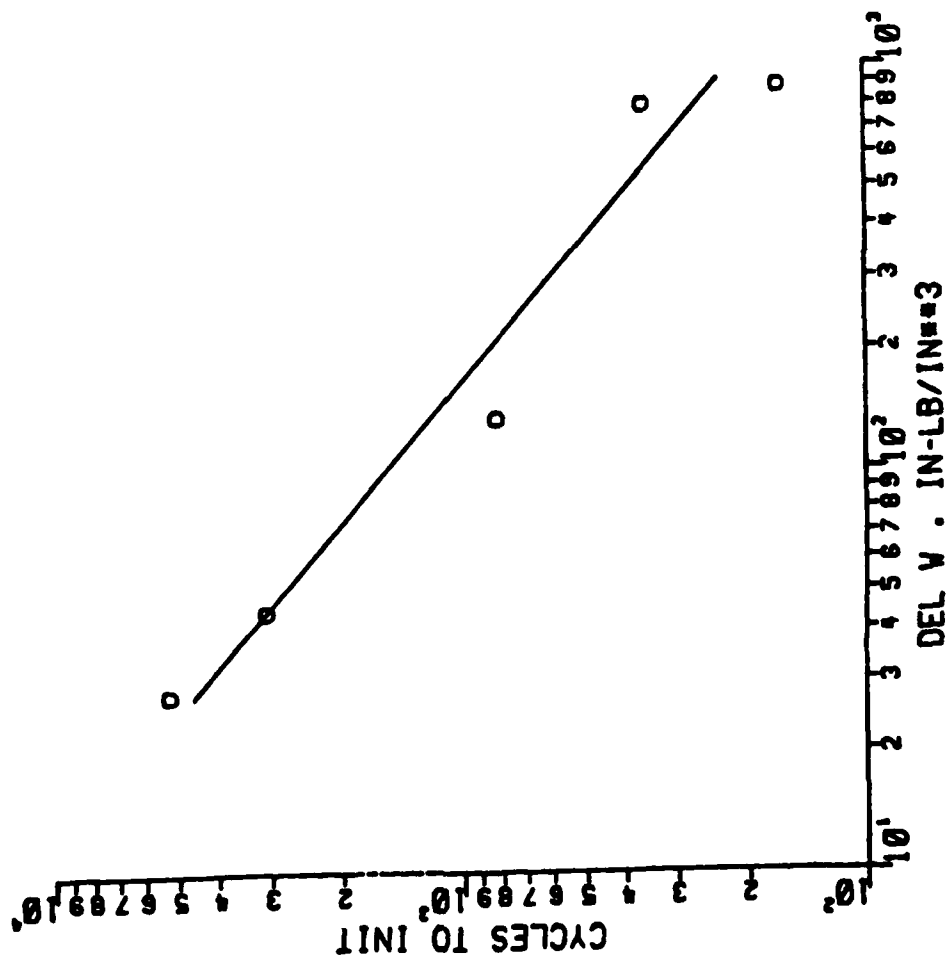
Figure A5 Continued. (f) o 101 m = - 0.757.
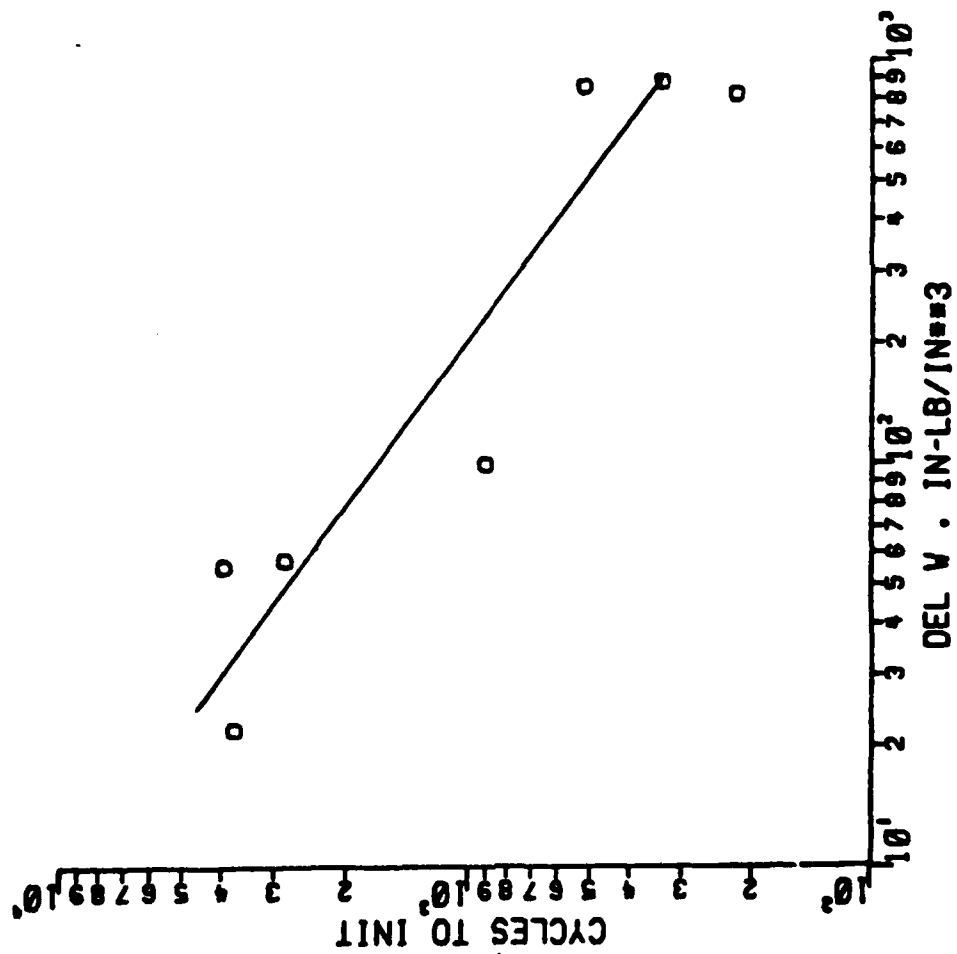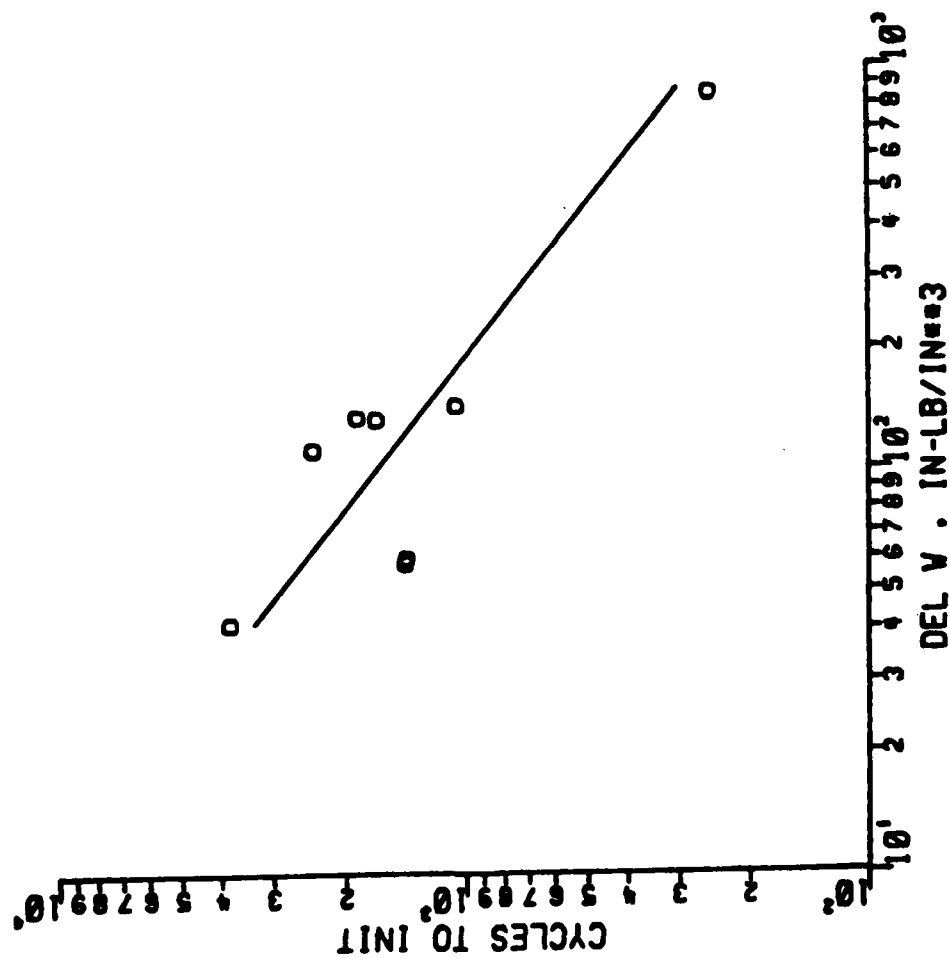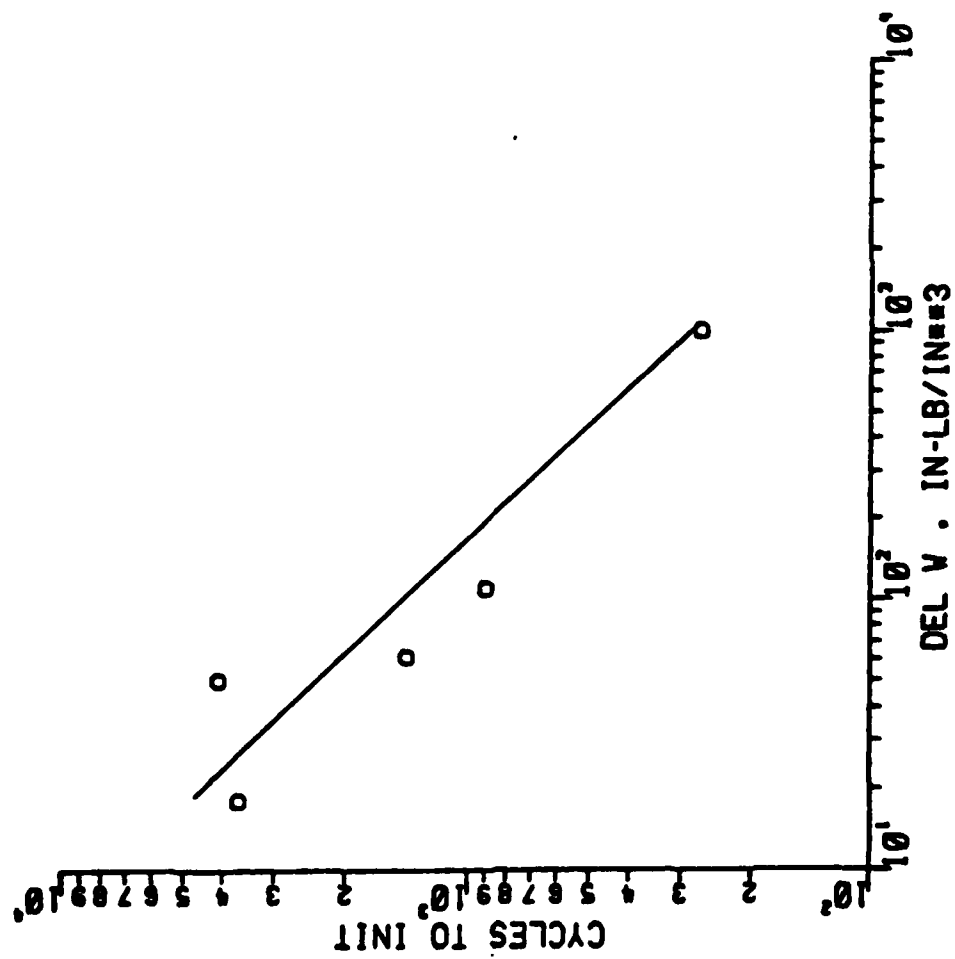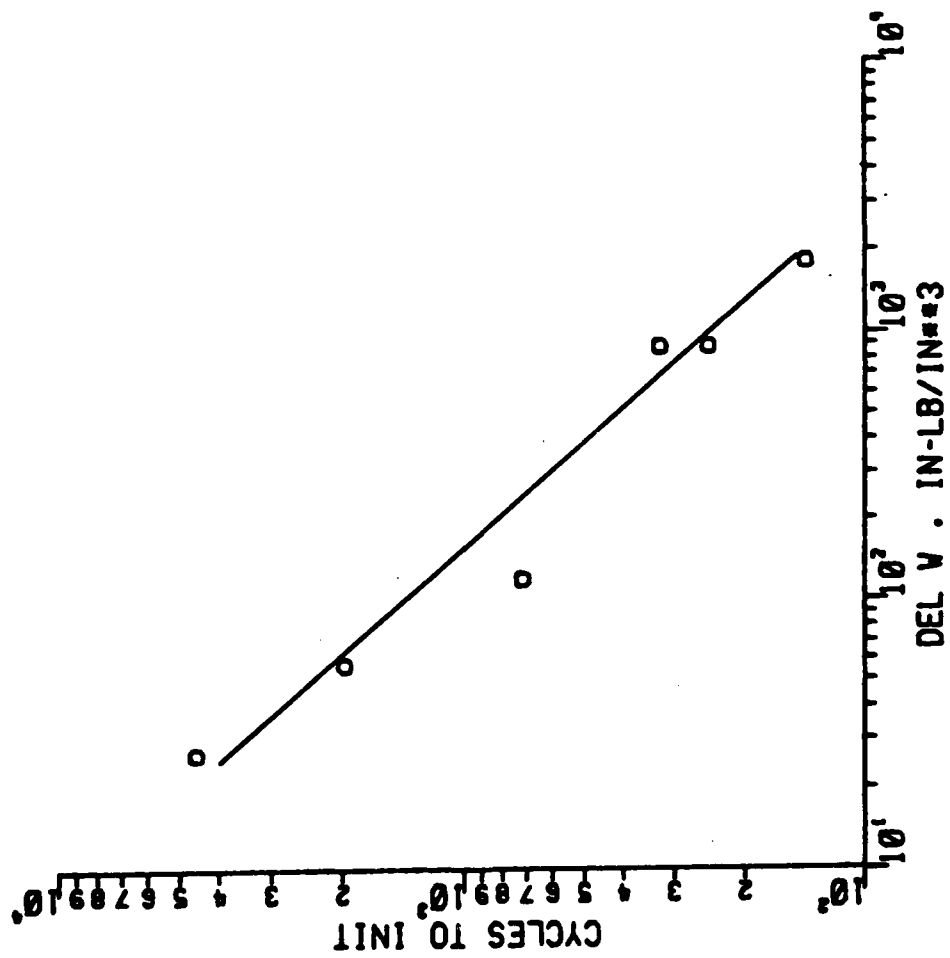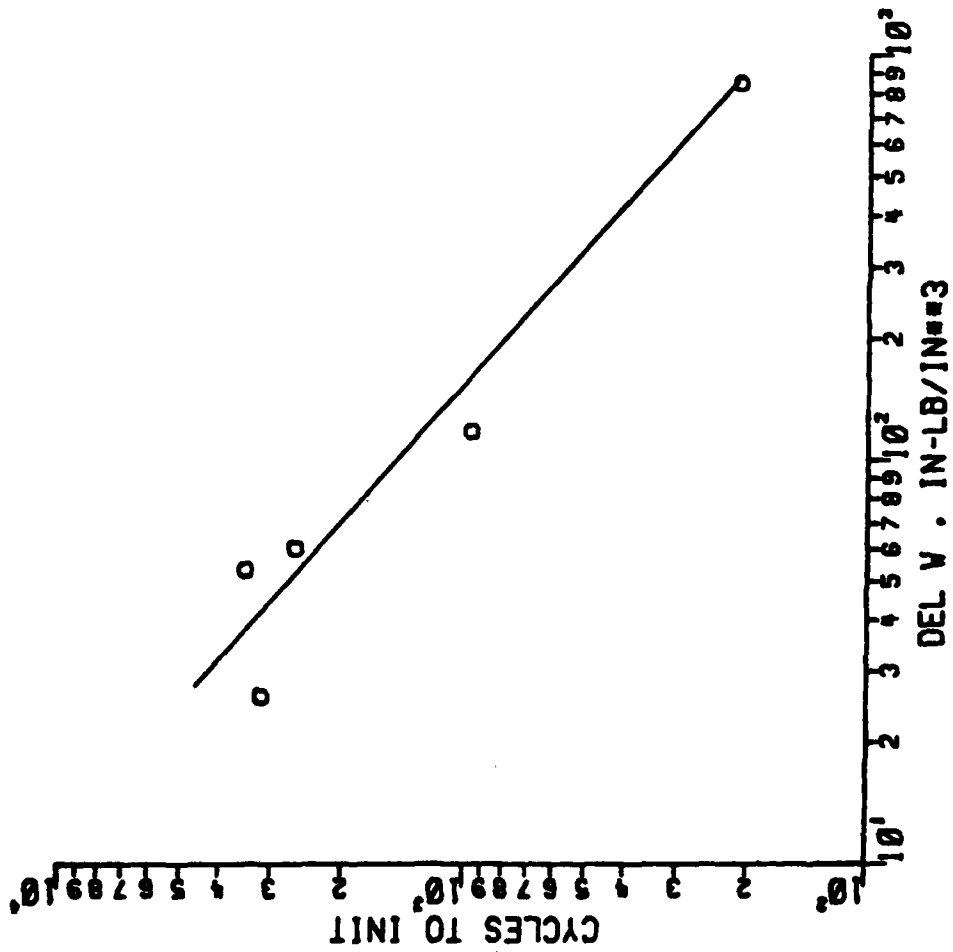
Figure A5 Continued.   (j) o 110 m = - 0.859.

303

Figure A5 Continued. (k) o -11 m = 0.882.

304

Figure A6. Cycles to Initiation Plotted as a Function of Hysteretic Energy, ΔW, for the Condition Indicated in A = ∞ LCF Tests. (a) o All data m = - 0.858.
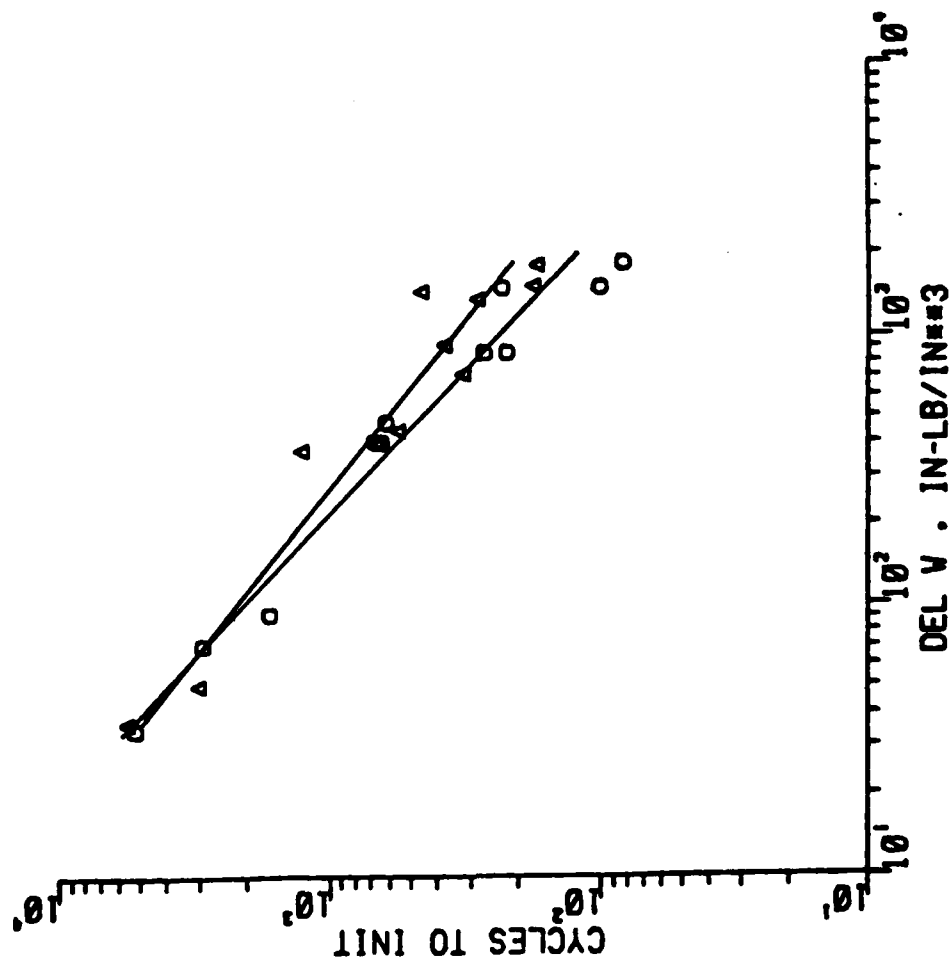
Figure A6. Continued.   (b)   o 38% upset m = - 0.965;   △ 64% upset m = - 0.806.
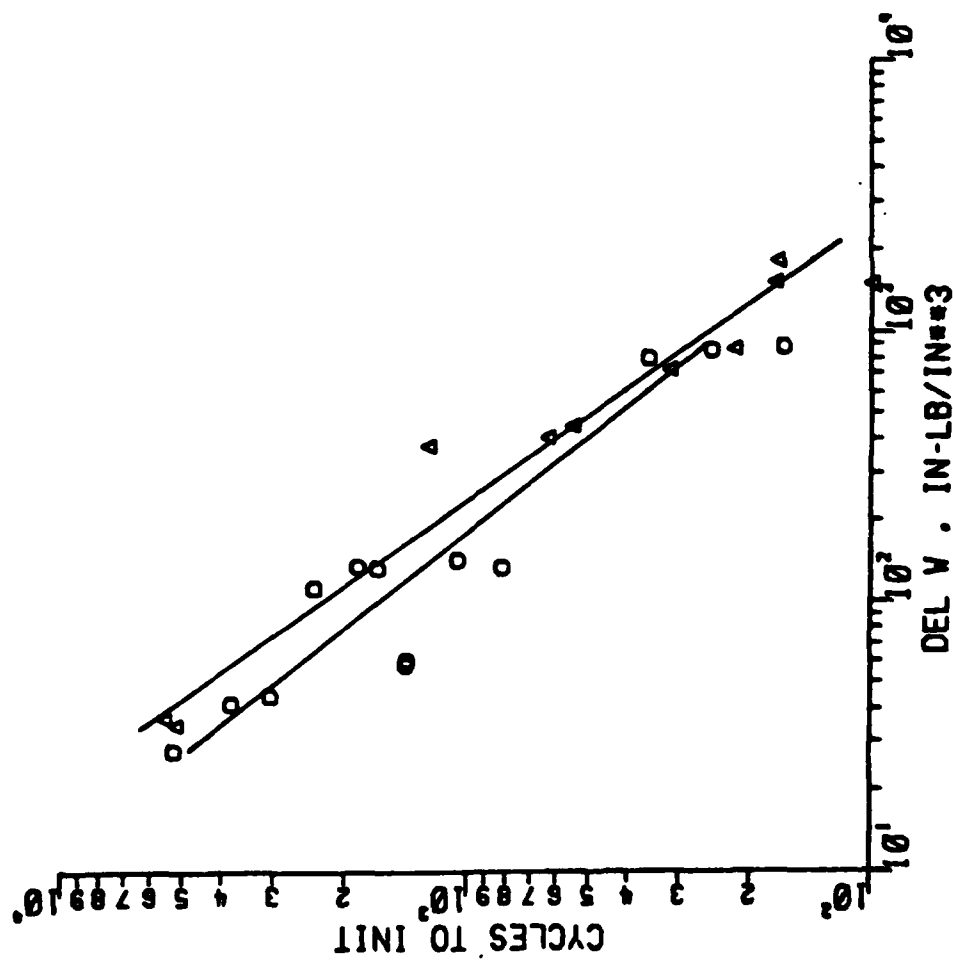
Figure A6 Continued. (c) o 0% Co m = - 0.838; Δ 0.4% Co m = - 0.958.

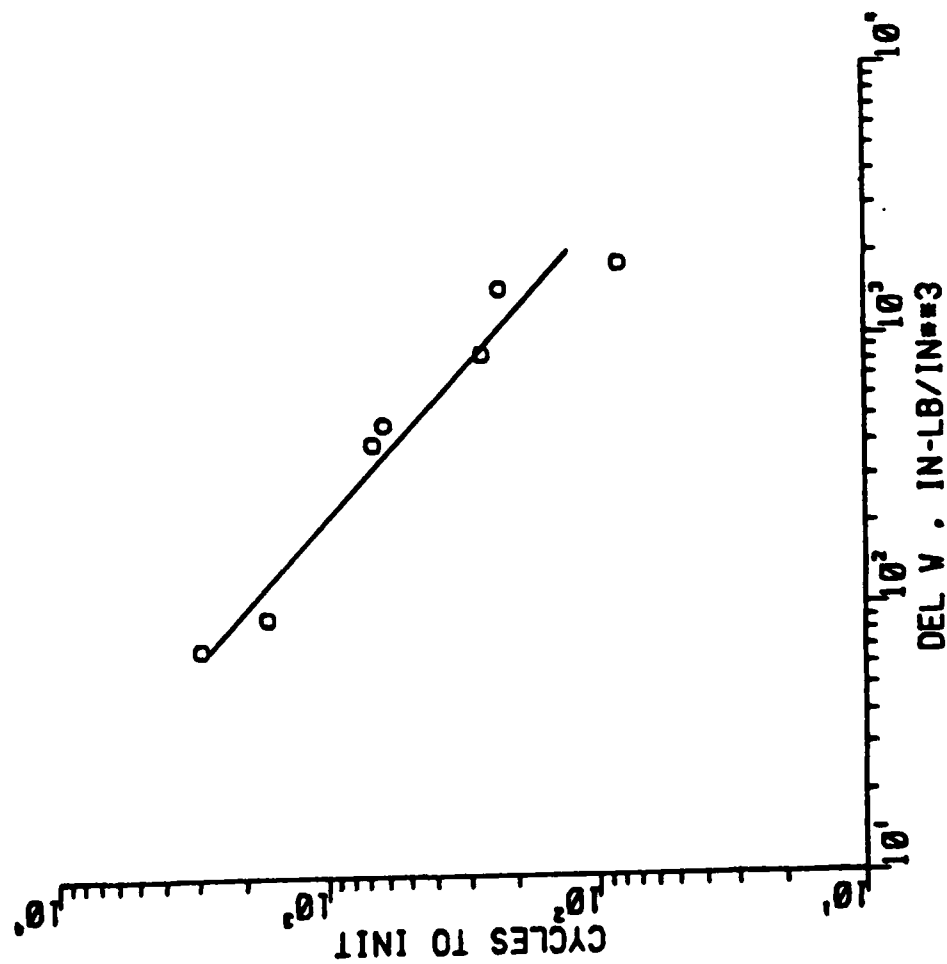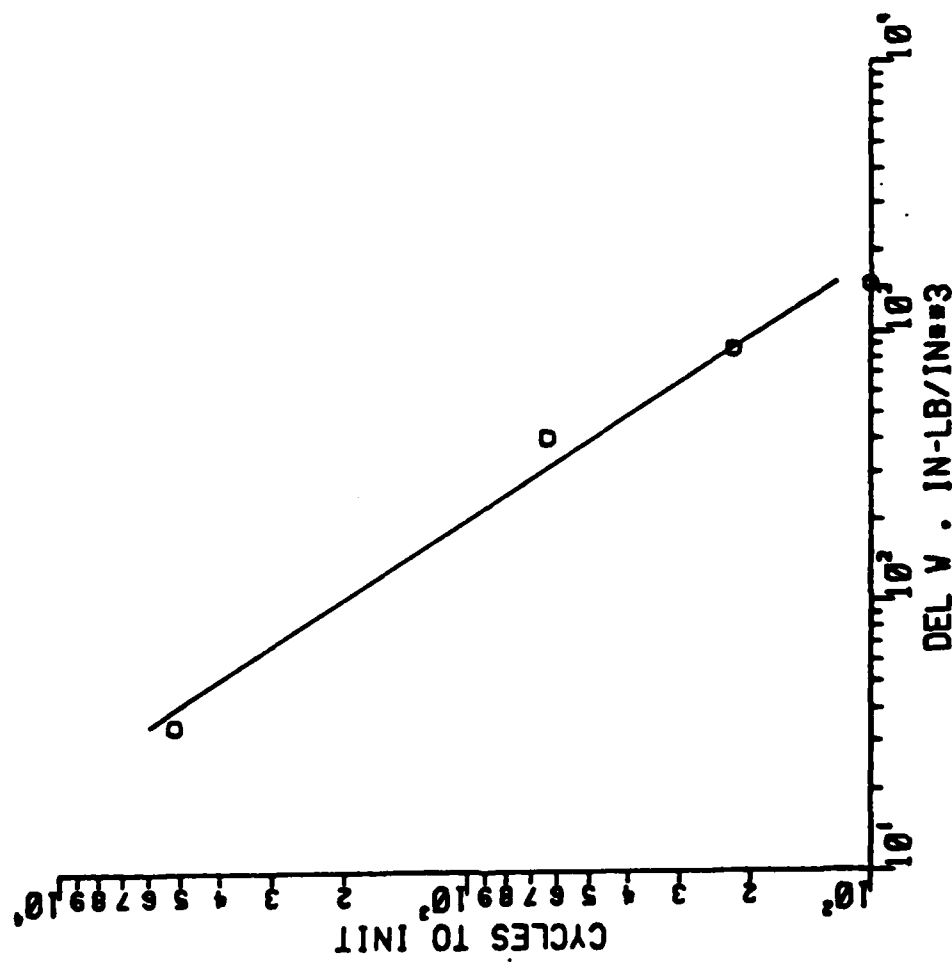307

Figure A6 Continued. (d) o OOX m = - 0.924.

308

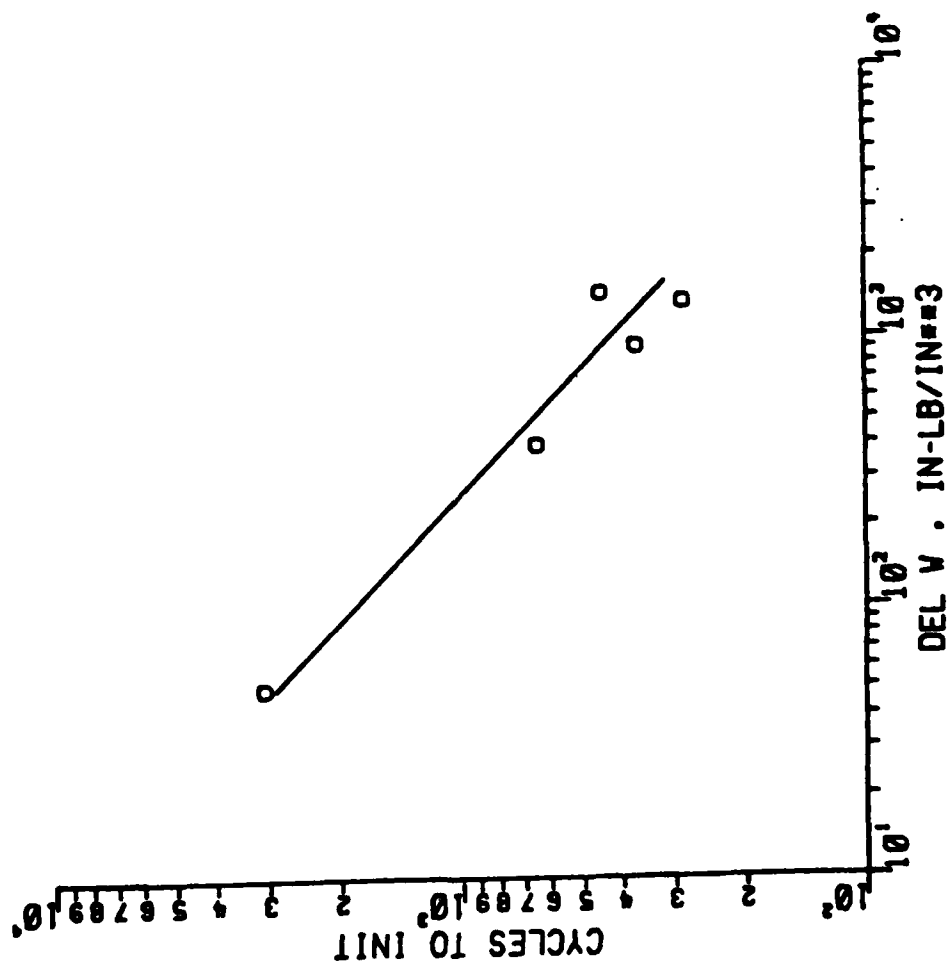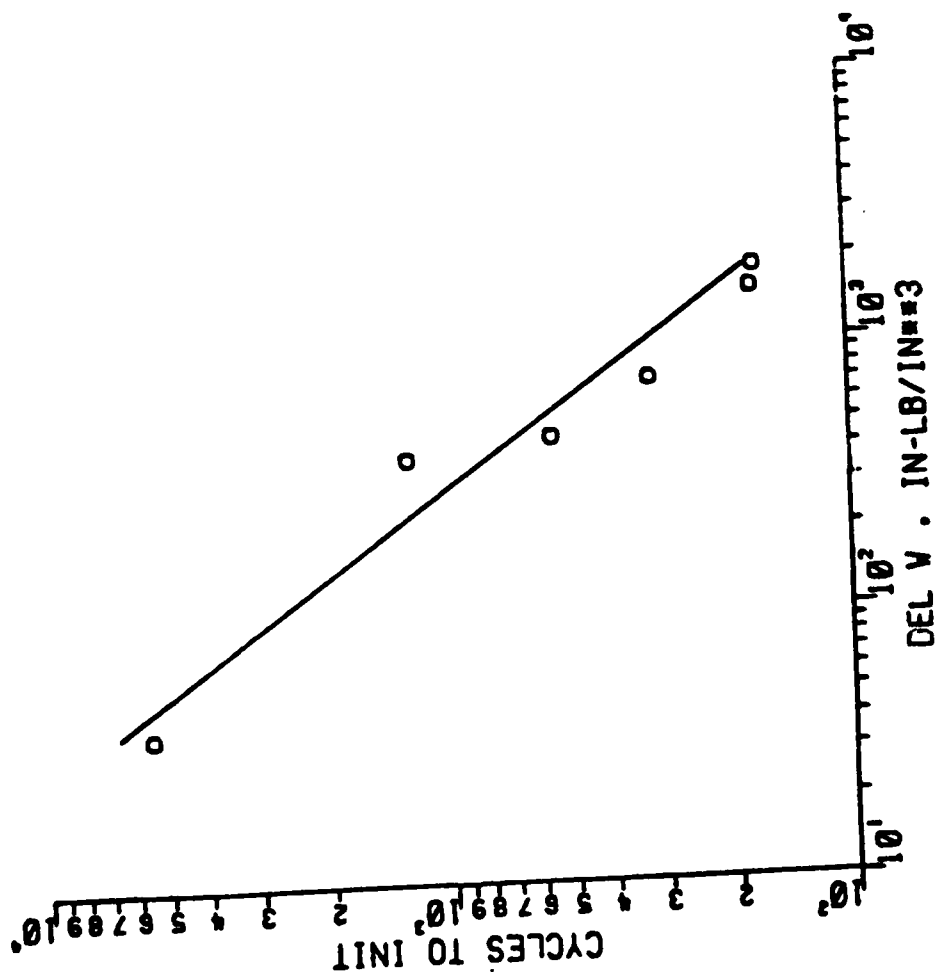Figure A6 Continued. (e) o 011 m = 1.021.

309

Figure A6 Continued. (f) o 101 m = - 0.654.

310

CYCLES TO INIT

DEL V . IN-LB/IN**3

Figure A6 Continued. (g) o 111 m = - 0.929.

311

END

FILMED

11-85

DTIC